Novel applications of airborne LiDAR and multispectral data for high-resolution geological mapping of vegetated ophiolitic rocks and sedimentary cover, Troodos Range, Cyprus

Thesis submitted for the degree of

Doctor of Philosophy

at the University of Leicester

by

Stephen Robert Grebby MPhys MSc

Department of Geology

University of Leicester

University of Leicester

June 2011

Novel applications of airborne LiDAR and multispectral data for high-resolution geological mapping of vegetated ophiolitic rocks and sedimentary cover, Troodos Range, Cyprus

Stephen Robert Grebby

Abstract

Practical and financial constraints associated with traditional field-based mapping are often responsible for the production of coarse-scale geological maps that lack detail and have inaccurately defined lithological contacts. Although remote sensing offers potential solutions to these constraints, conventional use of remotely sensed data is only effective when applied to barren terrain because just small amounts of vegetation cover can obscure or mask the underlying geological materials and structures. In this thesis, novel algorithms that utilise airborne Light Detection And Ranging (LiDAR) data and airborne multispectral imagery are applied to high-resolution geological mapping of vegetated ophiolitic rocks and sedimentary cover in the northern Troodos Range (Cyprus) with the aim of demonstrating their potential application to any geological setting. These novel algorithms involve quantification of geobotanical and topographical characteristics that are generally distinct for different lithological units, followed by automated image classification based upon these characteristics. Whilst the algorithms that individually exploit the geobotanical associations and the correlation between lithology and topography are capable of generating maps that are more detailed and have more accurately defined contacts than the existing geological maps of the study area, an integrated approach was found to significantly enhance the lithological mapping performance. Moreover, despite widespread vegetation cover, it is also shown that airborne LiDAR data and airborne multispectral imagery can be utilised to extract detailed and accurate structural information that is consistent with field-based data. Overall, the novel application of airborne spectral imagery and airborne LiDAR data has significant potential to aid accurate and high-resolution 1:5000-scale geological mapping over large areas of vegetated or non-vegetated terrain.

Acknowledgements

This research was primarily supported through a NERC CASE Studentship (NE/F00673X/1) in collaboration with the British Geological Survey University Funding Initiative (BUFI). Additional financial support was kindly provided by the Geological Remote Sensing Group in the form of a Student Travel and Fieldwork Award, and the University of Leicester Geology Department's Sylvester-Bradley Award. The airborne remote sensing data utilised in this research were acquired by the NERC Airborne Research and Survey Facility (MC04/30).

Firstly, I must start by expressing my sincere gratitude to my three supervisors ― Dr Dickson Cunningham, Dr Jonathan Naden and Dr Kevin Tansey ― for their expert support, advice and enthusiasm throughout my PhD research. Having already worked with Dickson and Kevin during my MSc degree, I was extremely grateful to have the opportunity to continue this collaboration during my PhD. Although I was already somewhat interested in pursuing the academic path prior to meeting them, it was ultimately their support and enthusiasm during my MSc research that influenced my final decision to undertake a PhD. In addition, I'm particularly grateful to Dickson for seeking the funds for the project and for involving Jon Naden of the British Geological Survey (BGS), because without Jon this PhD project would have not existed for various reasons ― most notably the fact that this project focused on remote sensing data acquired for him by the NERC ARSF. I'd also like to thank Jon immensely for his invaluable encouragement and support (both scientifically and financially through BUFI), and for providing crucial links to experts within the BGS and in Cyprus. Overall, I can't thank the three of you enough for all the support you have given me!

I also gratefully acknowledge the Geological Survey Department of Cyprus for providing a wealth of digital data and specifically Dr. Stelios Nicolaides for invaluable logistical support. Luke Bateson (BGS) and Professor Danny Donoghue (Durham University) are duly thanked for software support and advice. Prof. Donoghue deserves a special mention because he provided me with a lifeline when an original plan to borrow specialist software collapsed after a 10-month wait. I am extremely thankful to Dr. Simon Jowitt (formerly of Leicester, now of Monash University) for lending his expert knowledge of Cyprus geology, for various discussions, for help in field, and for his friendship whilst at Leicester.

Speaking of the Leicester geology crowd, there are quite a few people I'd like to mention. I thank the rest of the "old(er) school" crowd of Drs. Dan Smith, Ben Ellis, Pete Fitch, Andy Shore, Becky Williams and Jawad Afzal for your friendship and for making me feel welcome in a department that was somewhat alien to me in the beginning (with being a physicist and all that!). For those same reasons I also thank my own crop, which comprises Dave Riley, Chris Willcox and Irfan Jan. Dave, thanks for being a great mate, and I can only hope that any psychological damage as result of sharing an office with me and my sense of humour over the last few years is not long lasting! From the more recent postgrads, I'd like to thank Sam Cheyney for being an excellent mate and for listening to my frequent moaning over the years, and Laurent Darras, Alison Tasker and Mohib for being good friends and tea-break buddies! Overall, I'd like to extend my thanks to everyone in the Geology Department for providing a friendly and excellent working environment!

I now move onto my family, starting with my amazing and beautiful girlfriend Sophie Bradley, or rather Dr. Sophie Bradley as she is now known (well done by the way, I'm SO proud of you)! Being able to discuss the roller-coaster ride of PhD research with someone else who is in the same boat was of massive benefit, and so I can't thank you enough for being there to listen and support me throughout. In fact I thank you from the bottom of my heart for all the love, support and happiness you have given me over the last nine years ― my love for you is infinite and I am truly blessed to be able to call someone as special as you my girlfriend! Additionally, I am extremely thankful to Sophie's mum, Ann Bradley, for keeping me going with all those very delicious roast dinners ― especially those roast potatoes! Mum and Dad (Yvonne and Paul), I owe everything to you. Clearly, you have more than adequately provided me with all the essential skills, tools and qualities required to succeed in life. Also, if it wasn't for all the encouragement and financial support you have given me throughout my life, I would not be sat here now writing the acknowledgments for my PhD thesis! Words can not even begin to express how much I love and thank you both for everything done and given me. There are no better parents than the two of you. I hope that I make you proud.

Contents

List of Tables

List of Figures

1. Introduction

1.1 Background and rationale

Geological maps primarily portray information about the surface materials and crustal structures within a given area. More often than not, geological maps are produced at scales of 1:25,000 or smaller and therefore lack the accuracy and detail required for many developmental needs of modern society. The lack of larger scale maps can be ultimately attributed to the way in which geological information is gathered. Traditionally, this information is acquired through field-based mapping surveys, by employing strategies such as following azimuthal traverses, cross-strike transects, stream sections, ridge lines, lithological contacts, or by moving between individual isolated outcrops (Barnes & Lisle, 2004). However, this approach can be time-consuming, costly and incomplete over large areas and where terrain is geologically complex or poorly accessible (Gad & Kusky, 2007; Grunsky et al., 2009; Rogge et al., 2009). As a consequence of these practical and financial constraints, geological maps are typically produced using limited field observations, which results in the production of generalised coarse-scale geological maps that lack detail and have inaccurately defined lithological contacts (Roy et al., 2009).

Remote sensing products, such as aerial photographs and spectral satellite imagery, offer potential solutions to some of the limitations of field-based mapping because the data can provide more continuous and detailed information over large areas, thus enabling even the most inaccessible terrain to be mapped efficiently and cost-effectively. Detailed geological interpretation of aerial photographs has long been used to complement field-based mapping. However, the visual discrimination and mapping of surface materials based on image attributes such as tone, texture and drainage patterns can be subjective, difficult and time-consuming (Crouvi et al., 2006). Moreover, whilst aerial photographs offer a perspective that is useful for mapping more regional geological structures, they can be of limited use in areas with dense vegetation cover (Cunningham et al., 2006).

The availability of spectral satellite imagery resulted in a paradigm shift regarding the application of remote sensing to geological mapping. Unlike photographs, multispectral (and more recently hyperspectral) sensors predominantly measure surface reflected solar radiation in discrete wavelength intervals (or wavebands) ranging from the visible to the shortwave infrared part of the electromagnetic spectrum. Lithologies can be discriminated and mapped using spectral satellite imagery because the wavebands coincide with the same wavelength region for which the reflectance spectra of rocks exhibit unique and diagnostic spectral information (Hunt, 1977). Accordingly, two basic approaches to mapping lithologies using spectral remote sensing data have emerged. The first approach involves generating an image within which lithological contacts can be visually delineated using photogeological interpretation techniques (Rothery, 1987). Such images are typically generated by displaying combinations of the waveband images or enhanced versions of these (e.g., bands ratios, principal component bands) through the red, green and blue channels of a computer monitor (e.g., Sultan et al., 1987; Gad & Kusky, 2007; Amer et al., 2010). This approach is somewhat subjective since it relies on manual interpretation. More efficient, more objective and more detailed lithological mapping requires automated computer-based classification procedures to divide an image into distinct spectral classes, each of which represents a different lithological unit (Rothery, 1987). If spectral data alone do not enable adequate lithological discrimination, ancillary data (e.g., topography, radar, texture) can be incorporated into classification procedures to augment the accuracy of the derived map (Hutchinson, 1982; Mather et al., 1998; Chica-Olmo & Abarca-Hernández, 2000; Ricchetti, 2000; Dong & Leblon, 2004). The utility of spectral satellite remote sensing for geological mapping also extends to structural mapping since features such as faults may be expressed as lineaments in the imagery, which are defined by sharp changes in brightness or reflectance (Koike et al., 1998). Again, these can be extracted manually through visual interpretation or by employing automated mapping procedures.

Although spectral imagery acquired by classic spaceborne sensors such as Landsat TM and ASTER has been greatly exploited for geological mapping purposes, the spatial resolution of the imagery (ca. 15–30 m) restricts the ability to generate accurate and high-resolution geological maps. Nevertheless, this issue can be easily overcome by using aircraft-mounted multi- or hyperspectral sensors, which provide imagery with a spatial resolution of up to an order of magnitude greater than that acquired by satellites. Vegetation cover, however, poses a more significant problem to spectral mapping approaches because as little as 10% vegetation cover (e.g., lichen, grass, shrubs) can obscure or mask the spectra of underlying geological substrates (Siegal & Goetz, 1977; Ager & Milton, 1987; Murphy & Wadge, 1994). Thus, the utility of spectral remote sensing data is widely considered to be critically limited to only the most barren terrain (Fraser & Green, 1987). However, where the effects of vegetation prevail, indirect spectral discrimination of lithologies may be possible if geobotanical relationships with the underlying substrates are realised (Paradella et al., 1997; Leverington, 2010). Alternatively, the obscuring effects of vegetation may potentially be overcome through use of the active remote sensing technique of airborne Light Detection And Raging (LiDAR). With the capability of acquiring accurate and high-resolution (ca. 1–4 m) topographic data even through forest cover (Kraus & Pfeifer, 1998), airborne LiDAR is now established as an important tool for mapping the surface traces of faults in either vegetated or non-vegetated terrain (e.g., Harding & Berghoff, 2000; Haugerud et al., 2003; Prentice et al., 2003; Cunningham et al., 2006;

Arrowsmith & Zielke, 2009). A few studies have also suggested that it may be possible to use airborne LiDAR to discriminate lithologies through topographic differences (Wallace, 2005; Wallace et al., 2006; Webster et al., 2006a, 2006b). However, the full potential of this approach to lithological mapping is yet to be fully realised.

1.2 Aims and objectives

The main intention of this thesis is to try to demonstrate that the application of remote sensing to geological mapping need not be limited to aiding the generation of coarse-scale maps, especially those for only the most barren regions. Rather, the aim is to specifically explore the novel application of airborne LiDAR data and airborne multispectral imagery for high-resolution geological mapping using the vegetated ophiolitic rocks and sedimentary cover in the northern Troodos Range, Cyprus, as a case study. With a focus on developing and deploying algorithms for rapid high-resolution geological mapping, a number of objectives are identified in order to achieve the overall aim. These are to:

(1) determine the capability of conventional direct spectral discrimination and mapping of lithologies in vegetated terrain using airborne multispectral imagery;

(2) assess whether vegetative cover can be exploited to enable indirect spectral discrimination and mapping of lithologies through geobotanical associations;

(3) evaluate efficacy of airborne LiDAR for overcoming the potential obscuring effects of vegetation to enable the discrimination and mapping of lithologies;

(4) investigate whether the integration of airborne multispectral imagery and airborne LiDAR topographic data can further enhance the lithological mapping capabilities;

(5) examine the utility of airborne LiDAR data and airborne multispectral imagery for detailed structural mapping.

1.3 Thesis outline

This thesis comprises seven chapters, subsequent to this introduction. *Chapter 2* provides a geological and physiographical overview of both the island of Cyprus and the smaller case study area on which this project is focused. A description of the mineralogical compositions, topographic characteristics and associated vegetation types is provided for each lithological unit found within the study area. In addition, this chapter includes a structural overview of the investigated region.

The datasets utilised in this study are introduced in *Chapter 3*, with a particular emphasis on discussing the concepts of airborne LiDAR and airborne multispectral imaging, their data specifications and the pre-processing steps applied to these datasets in order to prepare them for subsequent analysis. Auxiliary datasets used in algorithm development, and the interpretation and validation of their mapping outputs are also summarised.

Previous studies have shown that vegetation cover can critically affect the ability to directly map lithologies through recognition of their reflectance spectra. *Chapter 4* assesses whether this is the case for the study area by employing a conventional spectral mapping approach. This approach involves matching representative reflectance spectra for the lithological units to the airborne multispectral image pixel spectra using automated classification algorithms.

Chapter 5 investigates the use of airborne LiDAR as a potential solution for overcoming the obscuring effects of vegetation cover, which limits the utility of conventional lithological mapping approaches to only a handful of the most barren areas. An algorithm is presented, which utilises airborne LiDAR-derived topographic data to discriminate and map lithological units based on the recognition of differences in the topographic characteristics between units.

The ability to exploit vegetation cover for the indirect spectral discrimination and mapping of lithologies through geobotanical associations is assessed in *Chapter 6*. A series of algorithms are presented which use geobotanical spectral characteristics extracted from the airborne multispectral imagery to map the lithologies. Furthermore, this chapter also presents algorithms for integrating airborne multispectral imagery and airborne LiDAR data to evaluate whether the geobotanical associations and topographical correlation can be simultaneously exploited to increase lithological discrimination and enhance the mapping performance.

Alongside lithology, crustal structures are another important constituent of geological maps. Accordingly, the utility of airborne LiDAR data and airborne multispectral imagery for detailed structural mapping is investigated in *Chapter 7*.

Finally, *Chapter 8* presents a synthesis of the main findings of the thesis research and discusses the efficacy of airborne LiDAR data and airborne multispectral imagery for high-resolution geological mapping of vegetated ophiolitic rocks and sedimentary cover in the Troodos Range, Cyprus. Recommendations and unresolved issues arising from the research are also discussed.

Chapters 4–7 of this thesis are written as discrete studies. This is particularly evident for *Chapter 5* and *6* because they comprise the published articles by Grebby et al. (2010) and Grebby et al. (2011), respectively. Inevitably, there is some degree of repetition associated with these two chapters, particularly with regard to some of the content of the chapters relating to the study area (*Chapter 2*) and datasets (*Chapter 3*).

Previous work undertaken by the author in collaboration with Dr Dickson Cunningham and Dr Kevin Tansey helped to recognise airborne LiDAR as a potential tool for overcoming the obscuring effects that dense vegetation can have on geological mapping, specifically fault mapping. This thesis represents a significant advance on this earlier work and involves adopting a multi-disciplined approach to explore not only the efficacy of airborne LiDAR to other aspects of geological mapping (i.e., lithological mapping), but also that of high-resolution spectral imagery. The research undertaken connects directly with research activities of the Leicester LiDAR Research Unit, of which the author and three supervisors are members. Moreover, this thesis represents a significant contribution towards the British Geological Survey's goal of developing accurate and high-resolution geological mapping techniques that are both cost- and time-effective.

2. A geological and physiographical overview of Cyprus and the study area

2.1 Cyprus

2.1.1 General overview

The island country of Cyprus (Fig. 2.1) is located in the northeastern corner of the Mediterranean Sea — 75 km south of Turkey, 105 km west of Syria, 380 km north of Egypt and 380 km east of Rhodes — at approximately 33° E; 35° N. It covers an area of approximately 9200 km^2, making it the third largest island in the Mediterranean Sea after the Italian islands of Sicily and Sardinia. Cyprus has a typical Mediterranean climate, characterised by a hot (or warm at higher altitudes) dry season from mid-May to mid-September and a mild rainy season from November to mid-March. Its close proximity to the southwest Asian land-mass makes it one of the hottest parts of the Mediterranean during summer. The average annual precipitation for the island is approximately 500 mm, with annual totals ranging from 300 mm for inland plains to 1100 mm for the highest altitudes of the Troodos Range (Pashiardis & Michaelides, 2008). Cyprus receives an average of 11.5 hours of bright sunshine per day (≤ 11 hours per day in the mountains) during the summer months, reducing to 5.5 hours per day (~ 4 hours per day in the mountains) in December and January (Koroneos et al., 2005).

Situated in a tectonically complex zone, the formation of Cyprus is associated with the subduction of the African plate beneath the Eurasian plate during the closure of the Tethys Ocean (Gass & Masson-Smith, 1963; Robertson & Xenophontos, 1997). The present form of the island is the result of a complex combination of geological processes including sea-floor spreading, marine sedimentation, thrusting, uplifting and subaerial erosion. Structurally and topographically, Cyprus is divisible into four domains that form a series of roughly parallel east–west trending belts (Fig. 2.2). From north-to-south, these are: the Kyrenia (or Pentadaktylos) Range, the Mesaoria Plain, Troodos ophiolite complex and the Mamonia Complex.

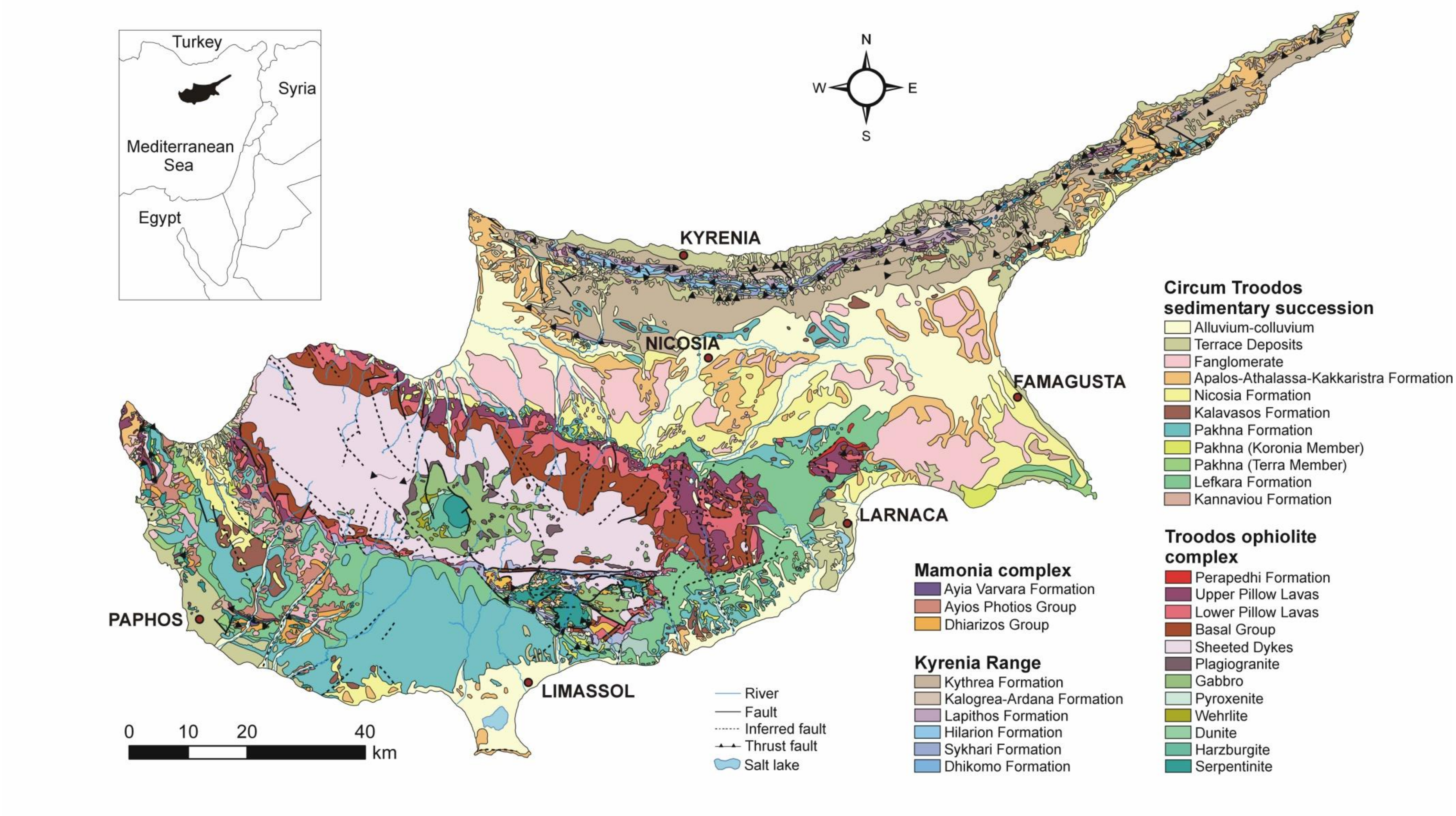

Fig. 2.1. Location and geological map of Cyprus (geological domains are shown in Fig. 2.2). Digital data was provided by the Cyprus Geological Survey Department.

2.1.2 Geological domains

2.1.2.1 Kyrenia Range

The Kyrenia or Pentadaktylos Range is a rugged, steep-sided mountain range that varies in altitude between 800 m and 1024 m as it curves along the northern coastline of the island. To the north of the range lies a thin (≤ 5 km) strip of coastal plain and to the south, the Mesaoria Plain. The Kyrenia Range, which is considered to form part of the southernmost arc of the Tauro-Dinaric Alps (Gass & Masson-Smith, 1963), was formed through the southward thrusting of allochthonous slices of recrystallised limestones over younger autochthonous marine sediments of Cyprus, followed by continual uplift (Adamides, 1984; Robertson & Xenophontos, 1997). The allochthonous rocks of Triassic to Cretaceous age consist of thinly-bedded micaceous marbles of the Dhikomo Formation, massive to thickly bedded dolomitic limestones of Sykhari Formation and massive to thickly bedded marbles of the Hilarion Formation (Constantinou, 1972). Chalks and marls — with intercalated lavas — of the Lapithos Formation and sandstones, siltstones and marls of the Kythrea Formation comprise the primary autochthonous sedimentary units of the Kyrenia Range.

2.1.2.2 Mesaoria Plain

The Mesaoria Plain is the area of flat low-lying land situated between the Kyrenia Range to the north and the Troodos Range to the south, and extending from Morphou Bay in the west of the island to Famagusta Bay in the east. A series of autochthonous sediments of Upper Miocene to Recent age constitutes the Mesaoria Plain. These sediments include radiolarian marls, chalks, cherts, calcareous marls and gypsum belonging mostly to the Athalassa and Nicosia Formations, overlain by Pleistocene to Holocene conglomerates, sands, silts and gravels derived through rapid erosion of the Troodos ophiolite following its uplift (Adamides, 1984; Poole & Robertson, 1991).

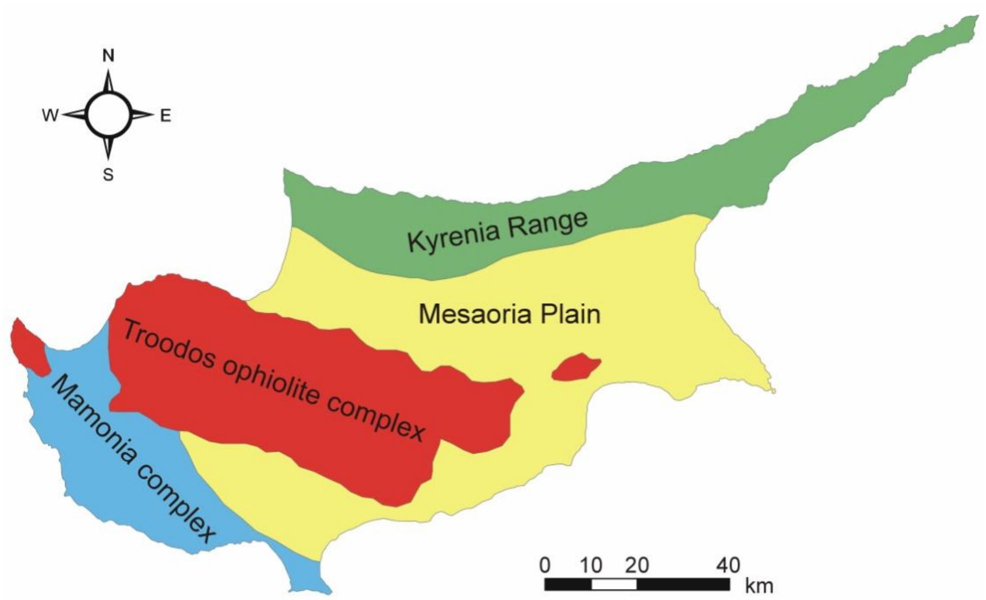

Fig. 2.2. Generalised map of the four geological domains of Cyprus. Digital data was provided by the Cyprus Geological Survey Department.

2.1.2.3 Troodos ophiolite complex

Cyprus is dominated both topographically and geologically by the Troodos Range or Massif, which is situated in the centre of the island and exhibits a dome-like structure centred on Mt. Olympus (1952 m). The range consists of the Troodos ophiolite complex (Fig. 2.3), which is an uplifted slice of oceanic crust and lithospheric mantle that was created through sea-floor spreading (Gass, 1968; Moores & Vine, 1971). The ophiolite stratigraphy includes a mantle sequence comprising dunites, harzburgites and a serpentinite diapir exposed at the highest elevations. This mantle sequence is stratigraphically overlain by a largely gabbroic plutonic complex, a sheeted dyke complex, extrusive lavas and oceanic sediments at decreasing elevations along the slopes of the range (Varga & Moores, 1985). The topographic inversion of the ophiolite stratigraphy has been attributed to a combination of uplift and erosion (Searle, 1972);

the uplift possibly due to the protrusion of the serpentinite diapir (Gass & Masson-Smith, 1963; Poole & Robertson, 1991).

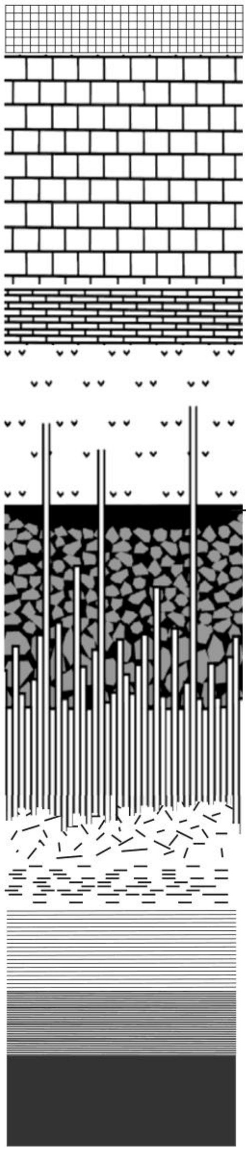

Fig. 2.3. Stratigraphy of the Troodos ophiolite complex and associated sedimentary cover sequences (after Adamides, 1984).

The extrusive lavas of the ophiolite are divided into three separate units: the Basal Group, Upper Pillow Lavas and Lower Pillow Lavas (Robertson & Xenophontos, 1997). The Basal Group represents a transition from the underlying sheeted dyke complex (100% dykes) to the overlying pillow lavas. Consisting of both dykes and screens of pillow lavas, the definition of the Basal Group is somewhat subjective. In general, it contains at least 50% dykes, but more commonly has a dyke abundance of 80–90% dykes (Bear, 1960). The pillow lava sequence was traditionally divided into the Upper Pillow Lavas and the Lower Pillow Lavas according to mineralogy, colour and dyke abundance (Wilson, 1959; Gass, 1960). The Lower Pillow Lavas are predominantly characterised by basaltic andesites, whereas the Upper Pillow Lavas are mainly olivine-bearing basalts. However, the Upper and Lower Pillow Lava division is difficult to apply in the field (Govett & Pantazis, 1971) and an unconformable or transitional boundary between the two lava units has led to uncertainty over this division (Boyle & Robertson, 1984). Furthermore, geochemical overlap between the two units has led to the divide being interpreted as a metamorphic discontinuity (Gass & Smewing, 1973; Smewing et al., 1975). Regardless of this division, the pillow lavas sequence is crucial to mineral exploration on Cyprus, as it hosts virtually all the Troodos volcanogenic massive sulphide deposits (Constantinou, 1980).

Sedimentary rocks most closely associated with the Troodos ophiolite complex are of Campanian to Miocene in age and belong to the Perapedhi, Lefkara and Pakhna Formations. The pillow lava sequence is directly overlain by the iron and manganese-rich sediments or umbers of the lower Perapedhi Formation. These umbers were precipitated from black smoker fluids before drifting, oxidising and accumulating in topographic lows on the sea floor (Robertson & Xenophontos, 1997). Well-bedded pink radiolarian shales and mudstones form the upper parts of the Perapedhi Formation. In the absence of the sediments of the Perapedhi Formation, the pillow lavas are unconformably overlain by the Lefkara Formation (Constantinou, 1972). This unit comprises chalks, marls and cherts representing late Cretaceous to early Miocene marine sedimentation (Kähler & Stow, 1998). Miocene marls, chalks, gypsum, calcarenite and reef limestone constitute the overlying sedimentary units of the Pakhna Formation (Adamides, 1984).

2.1.2.4 Mamonia complex

Lying adjacent to the Troodos ophiolite complex and associated sedimentary cover in southwestern Cyprus, the Mamonia Complex is an allochthonous unit (Lapierre, 1968) comprising a diverse and structurally complex assemblage of igneous, sedimentary and metamorphic rocks, ranging in age from Middle Triassic to Upper Cretaceous (Robertson & Woodcock, 1979). The origin of the Mamonia complex is the subject of an ongoing debate. However, a recent study suggests that it represents a remnant of intra-oceanic within-plate volcanism and sedimentation, which was tectonically emplaced onto the Troodos ophiolite complex during Maastrichtian time (Lapierre et al., 2007). The rocks of the Mamonia complex are divided into the Dhiarizos Group, Ayios Photios Group and Ayia Varvara Formation. The Dhiarizos Group includes Triassic pillow lavas, minor intrusives with overlying volcaniclastic siltstones, radiolarian mudstones and reefoidal limestone breccia (Swarbrick & Robertson, 1980), whereas the Ayios Photios Group is an entirely sedimentary unit that reflects the shallow to deep water evolution of the basin (Bailey et al., 2000). Siltstones, radiolarian mudstones, carbonates and quartzose sandstones are the main constituents of the Ayios Photios Group (Swarbrick & Robertson, 1980). The metamorphic rocks comprising the Ayia Varvara Formation are of greenschist and amphibole facies and include metavolcanics and metacherts (Robertson & Xenophontos, 1997).

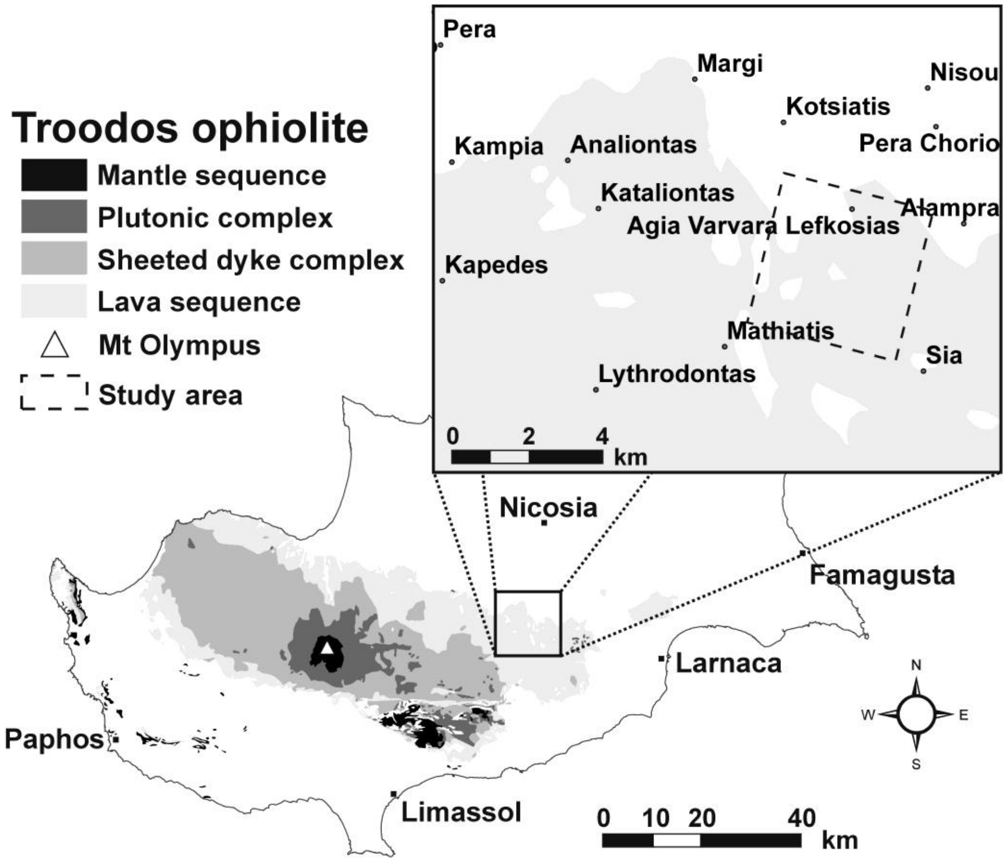

Fig. 2.4. Simplified geological map of the Troodos ophiolite showing the location of the study area.

2.2 The study area

2.2.1 General overview

The focus of this study is a 16 km^2 area located in the northern foothills of the Troodos Range, about 21 km south of Nicosia and 24 km west of Larnaca, at 33.4° E; 35.0° N (Fig. 2.4). This area encompasses the general contact between the lava sequence of the Troodos ophiolite and associated Cretaceous to Miocene sedimentary cover, and also includes more recent cover sequences. It has topographic relief on the order of 200 m, with elevation ranging between 250 m and 450 m. This particular study area was chosen due to its complex landscape, which arises through a combination of variable geology, diverse topography and widespread, heterogeneous vegetation cover. Furthermore, because the area is only sparsely populated, the landscape is predominantly natural with the exception of the disused Mathiati mine with spoil tips in the southwest and the small village of Agia Varvara Lefkosias in the north. Small-scale agricultural activity also occurs throughout the study area, but is generally confined to the northwest. Accordingly, the size and complexity of this study area provides an excellent opportunity to efficiently and rigorously evaluate the efficacy of novel and alternative remote sensing-based approaches to high-resolution geological mapping.

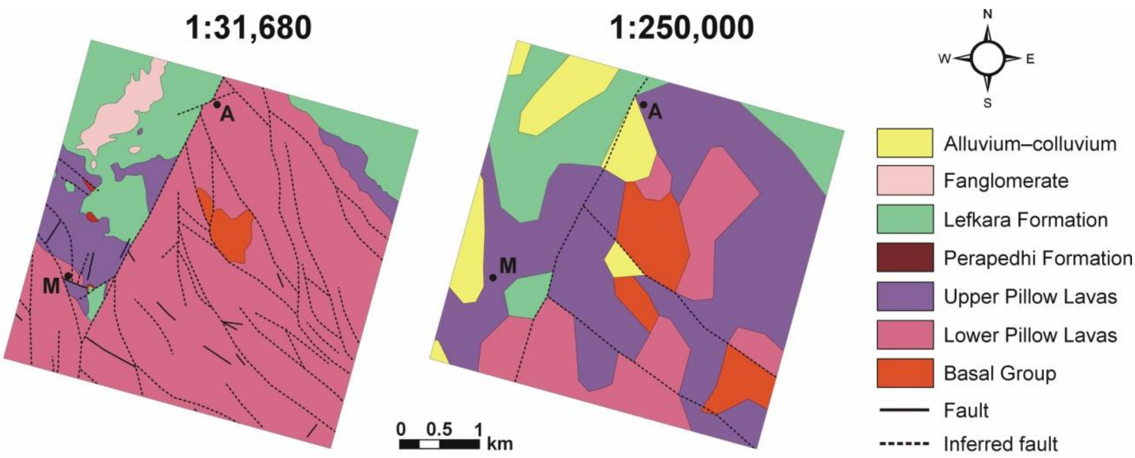

Fig. 2.5. Existing geological maps of the study area at 1:31,680 and 1:250,000 scales. M — Mathiati mine, A — Agia Varvara Lefkosias village. Digital geology provided by the Cyprus Geological Survey Department.

2.2.2 Geological and physiographical characteristics

2.2.2.1 Existing geological maps

Two existing geological maps of Cyprus cover the study area at both local and regional mapping scales (Fig. 2.5). The 1:31,680-scale map is the product of a mapping campaign undertaken in the 1950's and early 1960's, whereas the 1:250,000-scale map is the more recent version, revised in 1995. Regardless of scale, the two maps exhibit some obvious geological differences. This can be ultimately attributed to an amalgamation of the limited area covered during fieldwork, the subjectivity associated with the employed mapping techniques and some degree of ambiguity in defining some of the lithological units (e.g., Upper and Lower Pillow Lavas). To avoid the ambiguity surrounding the validity of the divide, the pillow lavas are treated as a single unit in this study (Fig. 2.6).

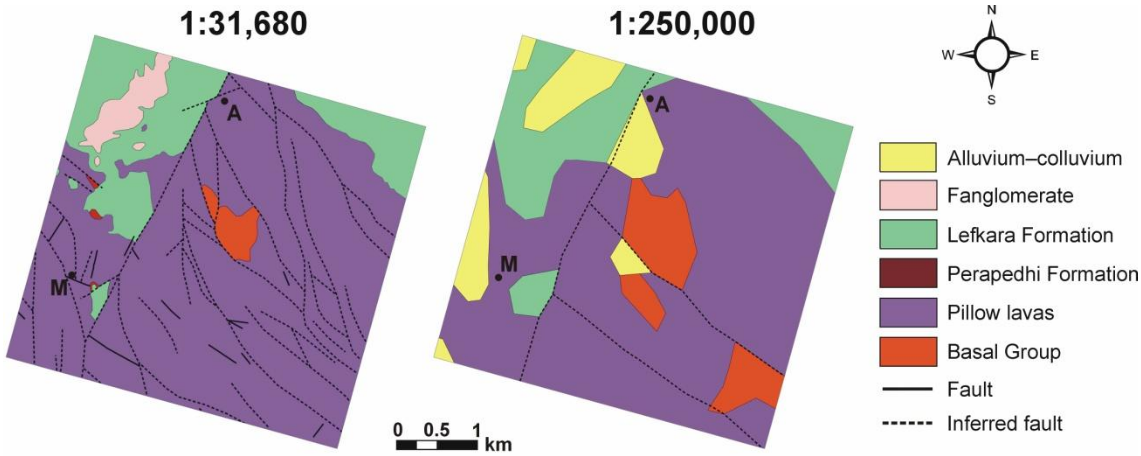

Fig. 2.6. Refined existing geological maps of the study area portraying the pillow lavas as a single unit. M — Mathiati mine, A — Agia Varvara Lefkosias village. Digital geology provided by the Cyprus Geological Survey Department.

From observations made within the study area, the more recent 1:250,000-scale geological map (see Fig. 2.6) generally appeared to be the most accurate with regards to lithology. Consequently, the lithological classification portrayed by the 1:250,000-scale map was adopted in this study. Thus, the study area was considered to comprise four lithological units — alluvium–colluvium, the Lefkara Formation, pillow lavas and the Basal Group.

2.2.2.2 Lithological units

Petrological and physiographical descriptions of the four lithological units found within the study area are provided below. Although the physiographical descriptions are based on observations made during this study, the petrological descriptions of the units are based on those provided by Gass (1960) following geological mapping of the study area and the surrounding region during the mapping campaign in the 1950's and 1960's.

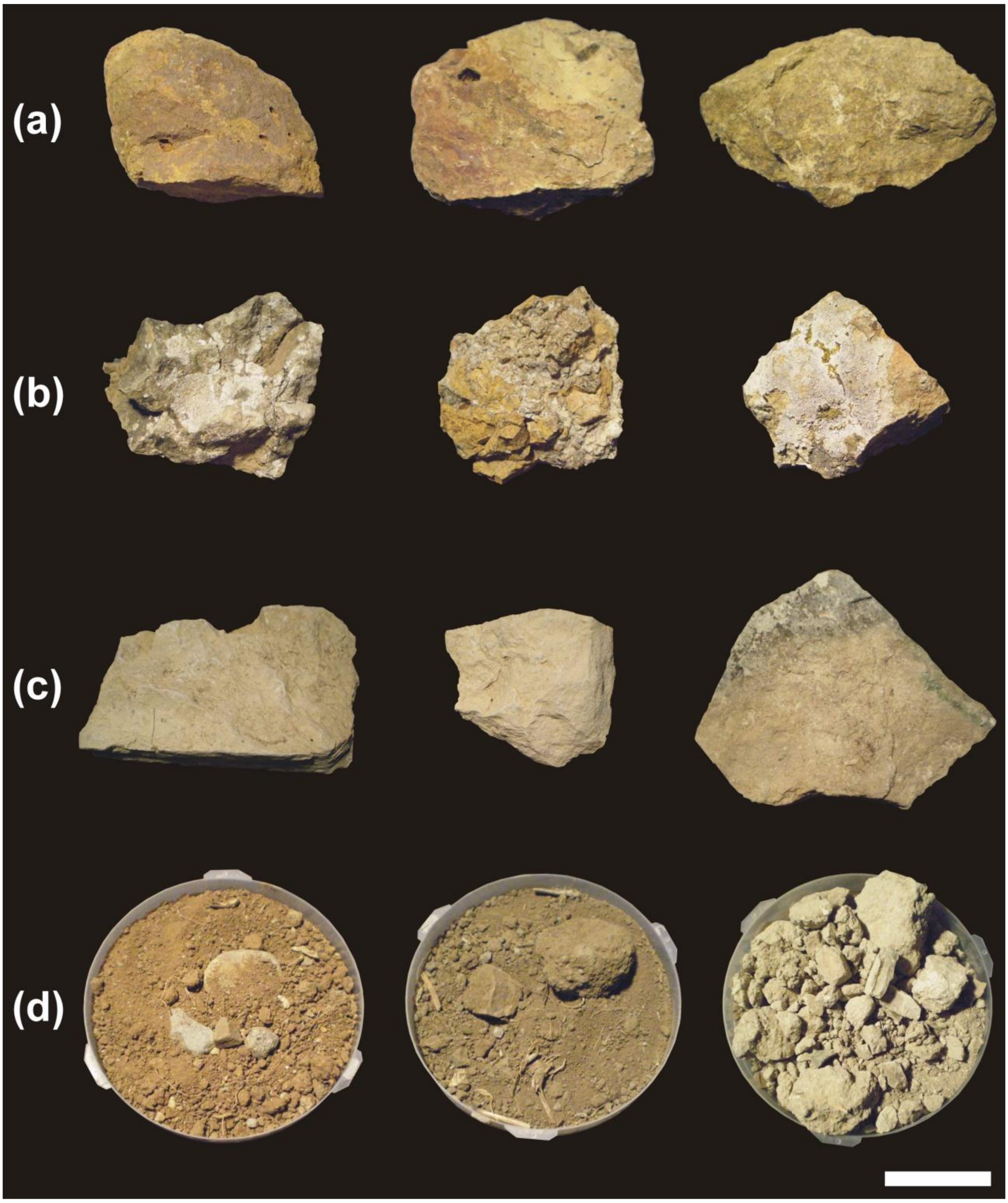

Fig. 2.7. A selection of samples of the four lithological units found within the study area. **(a)** Basal Group, **(b)** pillow lavas, **(c)** Lefkara Formation and **(d)** alluvium–colluvium. Scale bar = 5 cm.

Basal Group

As previously mentioned, the Basal Group is essentially the transitional unit between the underlying sheeted dyke complex and the overlying pillow lava sequence. With sheeted dykes forming around 90% of the total rock, it is the presence of up to 10% pillow lava screens that distinguishes the Basal Group from the sheeted dyke complex. Highly sodic plagioclase is the primary constituent of both the pillow lava screens and intrusive rocks, which is the result of metasomatism probably associated with saussuritisation and uralitisation of the original plagioclase and clinopyroxenes, respectively (Gass, 1960). The pillow lava screens of the Basal Group are typically keratophyre, quartz-keratophyre rocks and greenstones, whereas the dykes are mostly keratophyre, quartz-keratophyre, and albite-microdiorite. The main mineral constituents of Basal Group rocks include quartz, albite, diopside, epidote, actinolite, chlorite, calcite, goethite (limonite) and magnetite. Relic hypersthene and plagioclase, belonging to the andesine–labradorite range, are also present. The occurrence of goethite (limonite) as a common alteration mineral is most likely to be responsible for the orange-red colour of the rocks (Fig. 2.7a).

Basal Group outcrops, mostly confined to the centre and southeast of the study, are distinguishable from pillow lava country in the field through their distinctive relatively high topography and steep relief (Fig. 2.8). These topographic characteristics probably arise because of the increased resistance to erosion in comparison to the pillow lavas due to the higher dyke abundance. Vegetation commonly found growing on Basal Group rocks can be broadly described as garrigue or maquis, predominantly comprising scrubby short dry grasses, short-to-medium height shrubs and scattered small trees (see Fig. 2.8). Green grass is also observed growing on Basal Group rocks, albeit less frequently. Overall, it is estimated that up to 75% of the surface area of Basal Group outcrops is covered by vegetation.

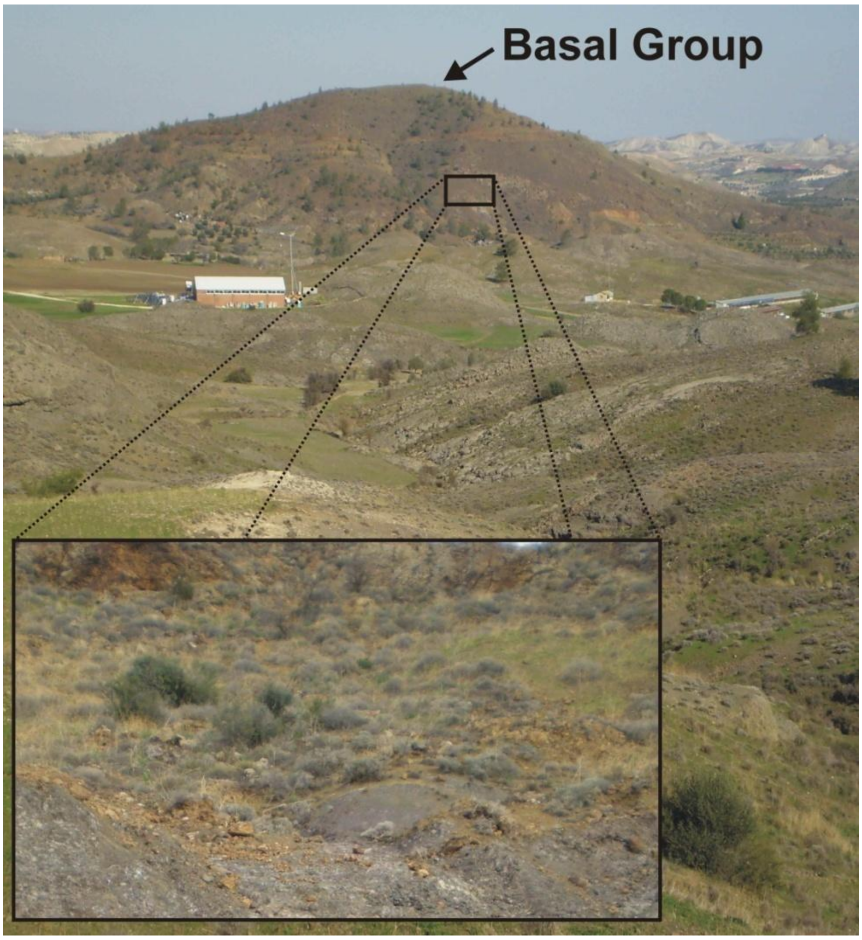

Fig. 2.8. Field photographs showing the physiographical characteristics of Basal Group outcrops in the study area.

<u>Pillow lavas</u>

Irrespective of the nature or existence of a division in the sequence, there are essentially two pillow lava end-members. The pillow lava end-member typically found occurring at a lower stratigraphic level is generally andesitic to basaltic in composition. The main minerals of this end-member are plagioclase — both labradorite and andesine — diopside and magnetite. Large vesicles in the pillows are often completely or partially infilled by minerals such as quartz, opal, calcite, chlorite, celadonite, goethite (limonite) and natrolite to form amygdales. These pillow lavas are more commonly cut by feeder dykes. The higher stratigraphic pillow lava end-member is characterised as basalts and olivine basalts, again primarily comprising plagioclase, diopside and magnetite, with plagioclase taking the form of labradorite. Olivine in this pillow lava end-member is commonly altered to calcite — which also occurs as extensive veining often stained pink due to the presence of disseminated hematite. Montmorillonite, quartz and the zeolite analcime constitute additional alteration and amygdaloidal minerals of this pillow lava end-member. On the whole, rocks of the pillow lava sequence vary in colour from grey to red-brown depending on the extent of weathering and alteration (Fig. 2.7b).

Fig. 2.9. Field photographs showing the physiographical characteristics of the pillow lavas in the study area. Note that the white colouration on pillow lavas in the inset photograph is lichen growth.

Pillow lava country comprises the majority of the study area, with the exception of the area to the northwest. The topography associated with pillow lavas is also distinctive and is observed as relatively low relief, undulating and hummocky terrain in the field (Fig. 2.9). The undulating terrain of the pillow lava country typically exhibits a wavelength of 100 m and is overprinted by shorter-wavelength hummocks that correspond to individual stacks of pillow lavas. Pillow lava outcrops usually appear relatively well-exposed due to sparse scrubby dry (and less commonly green) grass and shrubs. However, on closer inspection, moderate-to-dense (30–75%) lichen cover is typically (and almost exclusively) found on pillow lavas outcrops (see Figs. 2.7b and 2.9).

Lefkara Formation

In the study area, the pillow lavas are directly overlain by the late Cretaceous to early Miocene sedimentary cover of the Lefkara Formation. Consisting of chalks, cherts and marls, the Lefkara Formation is essentially a calcareous unit comprised mostly of calcite and aragonite. It is these carbonate minerals that give the Lefakra Formation rocks their whitish colour (Fig. 2.7c). Specific mineral constituents of the marls in the study area were not identified by Gass (1960). However, illite and chlorite are generally observed in Lefkara Formation rocks in the Troodos ophiolite (Kähler & Stow, 1998). Common clay minerals such as kaolinite and montmorillonite are also likely to comprise the clay component of the marls. Cryptocrystalline cherts — in the form of chalcedony — occur along fractures and as nodules, but are most commonly found as bedded layers. Fractures and joints are also frequently infilled with secondary quartz. Iron oxide is probably responsible for the pink colouration of cherts found near the contact with the underlying pillow lavas.

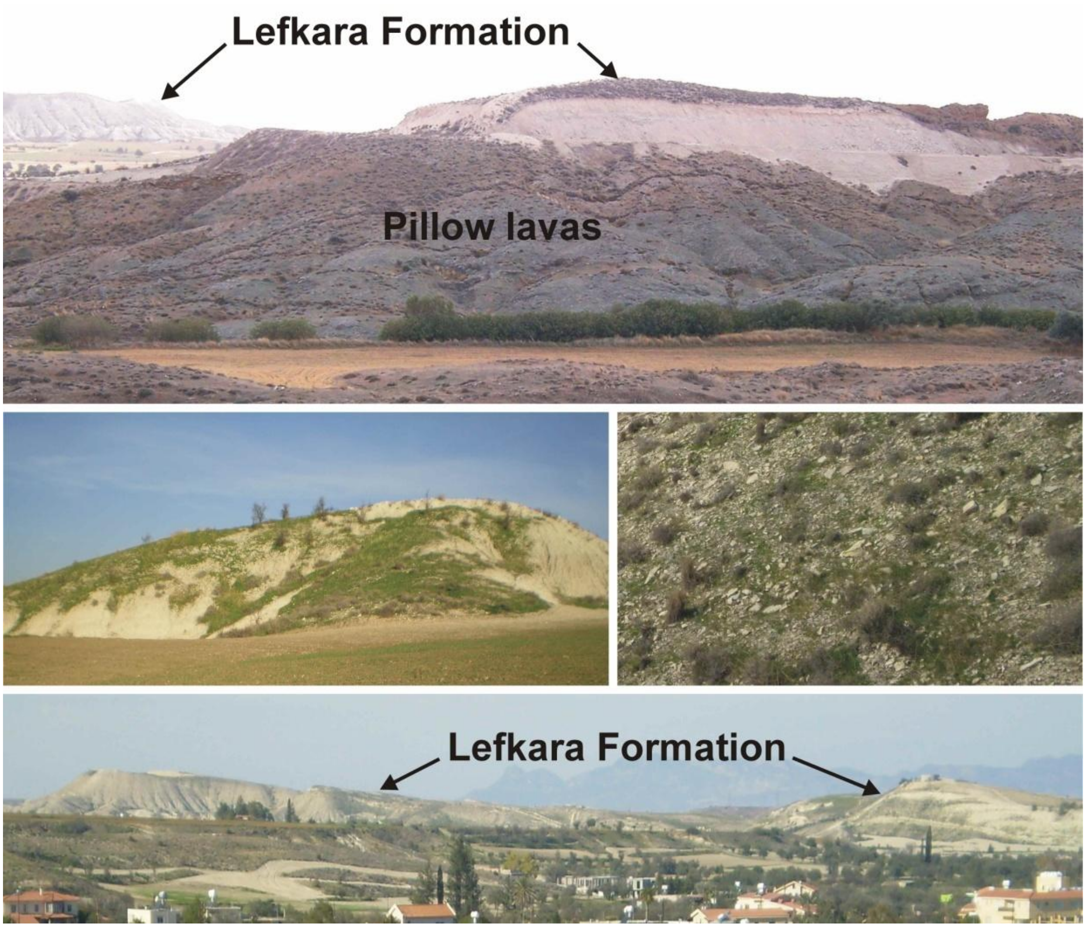

Fig. 2.10. Field photographs showing the physiographical characteristics of the Lefkara Formation in the study area.

The sediments of the Lefkara Formation drape the pillow lavas to form hilly undulating topography which essentially resembles that of subdued pillow lava terrain (Fig. 2.10). In the study area, outcrops are confined to the northeast and northwest. Vegetation cover found growing on the Lefkara Formation rocks could be described as garrigue and somewhat similar to that found growing on rocks of the Basal Group. However, there is a noticeably lack of trees and a somewhat greater abundance of green grass associated with the Lefkara Formation (see Fig. 2.10). Additionally, a relatively small amount of lichen cover is often observed growing on the surfaces of Lefkara Formation rocks. Overall, vegetation surface cover associated with the Lefkara Formation is on the order of 30–75%.

Alluvium–colluvium

In the study area, the alluvium–colluvium unit refers to Quaternary sediments that were deposited fluvially or through local erosion. This unit essentially comprises regoliths and, to a lesser extent, fanglomerates. The fanglomerates are of a continental nature, comprising a heterogeneous mixture of the igneous rocks of the Troodos ophiolite, and are preserved as a flat capping on only a few Lefkara Formation hills following uplift and erosion of the ophiolite. The fanglomerates have been weathered and eroded to produce fragments which vary in size from pebbles to fine grained soils. The most abundant material of the alluvium–colluvium unit is regolith derived from both the pillow lavas and Lefkara Formation. The different types of alluvial–colluvial cover all directly reflect their parental rock type, with fanglomerate forming red-brown coloured material, and the pillow lavas and Lefkara Formation producing grey and white–light grey material, respectively (Fig. 2.7d). Furthermore, the mineralogy of these different cover types should also reflect that of their parent rocks, although weathering processes can result in the formation of additional clay minerals or the removal of carbonate minerals.

Alluvial–colluvial cover is characterised by its distinctive flat and smooth topography, and is regularly found filling depression in the pillow lava terrain throughout the study area (Fig. 2.11). In the northwest, flat caps of fanglomerate-related alluvium–colluvium are locally observed overlying Lefkara Formation outcrops. The alluvial–colluvial cover is frequently exploited for agricultural purposes throughout the study area, although it is largely confined to the northwest. Accordingly, the alluvium–colluvium unit is commonly associated with crops (e.g., cereals, olive groves) as well as both green and dry grasses, which can cover up to 90% of the surface area.

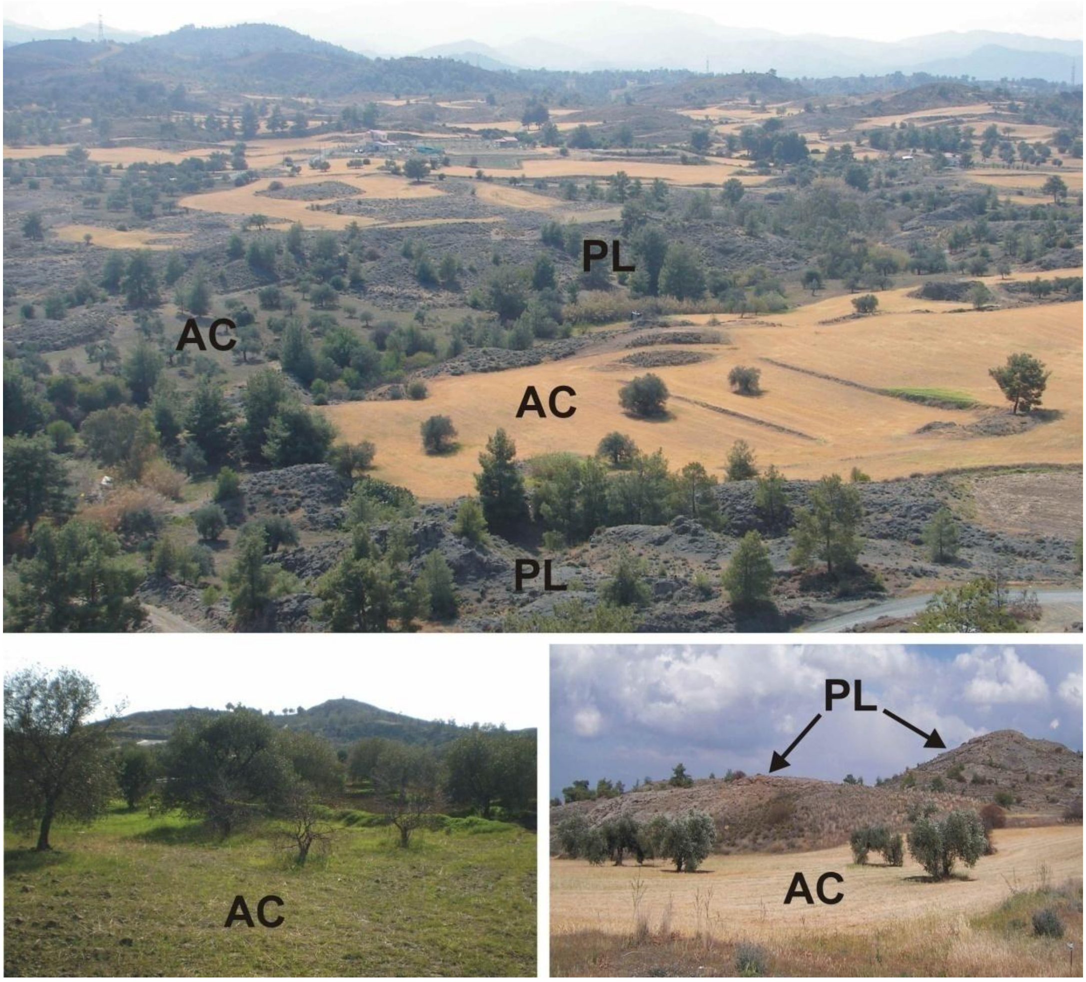

Fig. 2.11. Field photographs showing the physiographical characteristics of alluvium–colluvium in the study area. AC — alluvium–colluvium, PL — pillow lavas.

2.2.2.3 Structural geology

The predominant trend of dykes in the sheeted dyke complex is north–south, indicating that the sea-floor spreading axis associated with the formation of the Troodos ophiolite was also north–south oriented (Allerton & Vine, 1991). Nonetheless, three proposed structural grabens were identified by Varga & Moores (1985) in the northern part of the ophiolite through separation of dykes into domains of consistent strike and dip, and interpreted as fossil axial valleys of an eastward migrating spreading centre. The study area is situated within the most eastward of these — the Larnaca graben (Fig. 2.12). Faulting within the study area is confined to the exposed igneous rocks and is characterised by a dominant northwest–southeast trend and a less significant north–south trend (see Fig. 2.6). The northwest–southeast dominant fault trend is parallel to the interpreted spreading axis of the Larnaca graben and is therefore consistent with the proposed crustal extension in this region. Furthermore, the dominant dyke trend in the study area is parallel to this northwest–southeast faulting trend (Gass, 1960). The minor north–south trend is believed to correspond to a later stage of normal faulting (Gass, 1960; Boyle & Robertson, 1984).

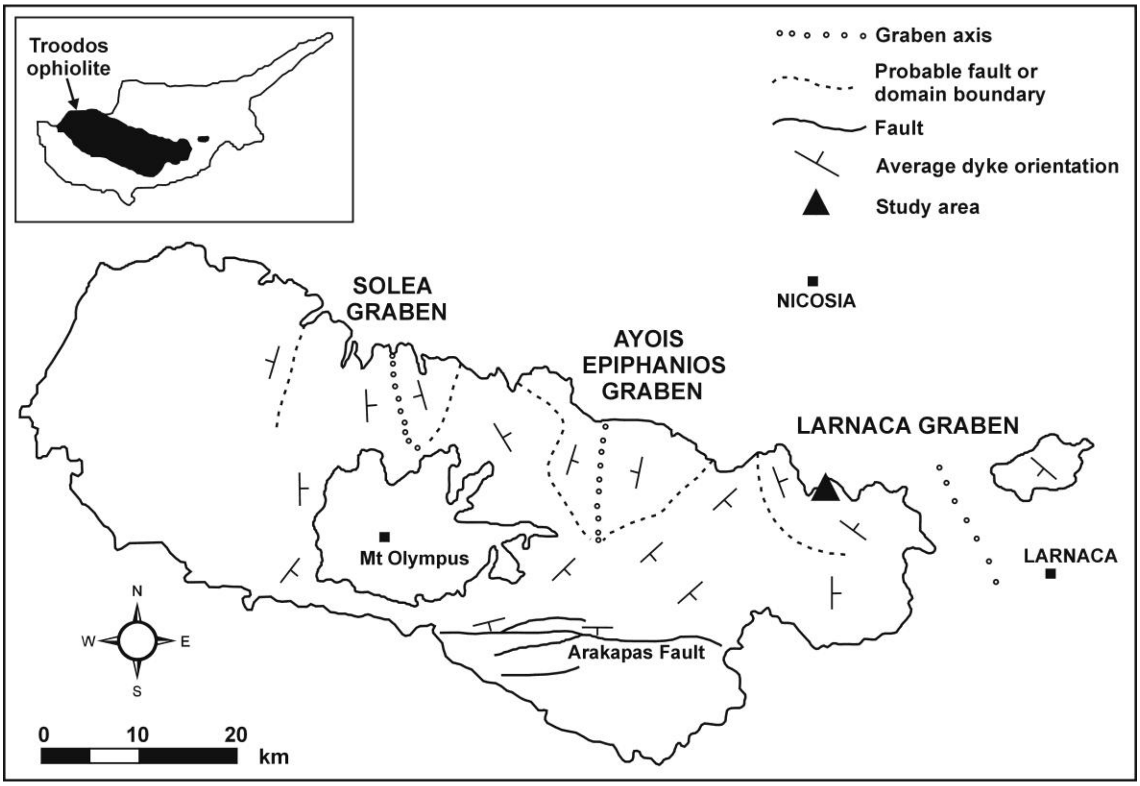

Fig. 2.12. Generalised structural map of the Troodos ophiolite showing the location of the study area within the Larnaca graben. After Varga & Moores (1985).

3. Datasets

This chapter describes the principal datasets — airborne LiDAR topographic data and airborne multispectral imagery in the form of Airborne Thematic Mapper imagery — along with the auxiliary datasets use to assist algorithm development, and interpret and validate the generated map products.

3.1 Airborne Light Detection And Ranging data

3.1.1 Background

Airborne Light Detection And Ranging (LiDAR; also known as airborne laser swath mapping, ALSM or laser scanning) is an emerging active remote sensing technique that can be used to acquire both accurate and high-resolution (ca. 1–4 m) topographic data. The basic concept is relatively simple and involves the emission of laser pulses from an aircraft-mounted LiDAR system towards the ground surface, back and forth along a line typically orthogonal to the flight direction (Flood & Gutelius, 1997; Wehr & Lohr, 1999). This scanning process is achieved by varying the scan angle of the emitted laser pulses using rotating, oscillating or nutating mirrors located inside the LiDAR system (Wehr & Lohr, 1999). For each laser pulse, the precise time interval between its emission and the subsequent detection of surface reflected (backscattered) laser energy is recorded. These round-trip time intervals, t, are then converted to aircraft–ground distances or ranges, R, using:

$$R = c\frac{t}{2} \quad , \tag{3.1}$$

where c is the speed of light. The position of the aircraft and its orientation at the time of the emission of each laser pulse is determined using a differential Global Positioning System (GPS) and an Inertial Navigation System (INS), respectively. Combining this information with the laser ranges and their corresponding scan angles then yields accurate x-y-z coordinates for the origin of every laser reflection (Baltsavias, 1999a; Wehr & Lohr, 1999).

The resulting LiDAR data points have typical absolute vertical accuracies on the order of 15 cm, absolute horizontal accuracies of less than 1 m and relative vertical accuracies on the order of 5 cm (Ahokas et al., 2003; Hsiao et al., 2004; McKean & Roering, 2004; Arnold et al., 2006; Glenn et al., 2006; Webster & Dias, 2006). Amongst many other factors relating to hardware performance and data processing, the absolute accuracy of data points is dependent on acquisition parameters such as the flying height, scan angle and proximity of the differential GPS base stations (Baltsavias, 1999a; Palamara et al., 2007). The relative vertical accuracy, however, is primarily dependent on adequate calibration of the system (Huising & Gomes Pereira, 1998). The density of points on the surface is governed by the point spacing, which is dependent on the scanning frequency and the aircraft flying height and speed (Baltsavias, 1999a; Wehr & Lohr, 1999).

A single laser pulse emitted from a LiDAR system can encounter multiple objects along its travelled path, with each object reflecting a proportion of the emitted laser energy (Mallet & Bretar, 2009). This reflected energy and its associated intensity — defined as the ratio of the strength of reflected energy to that of the emitted energy (Song et al., 2002) — is recorded by LiDAR systems as either multiple discrete reflections (also referred to as returns) or as a full-waveform (Fig. 3.1). Discrete-return LiDAR systems, such as the one used in this study, usually record two returns for each laser pulse — the first and last. Over bare terrain, only a single return from the ground would be expected from each laser pulse (Fig. 3.1a). Over forested terrain, multiple returns from within the canopy would be anticipated, with the first return most likely corresponding to near the canopy top and the last return assumed to originate from the ground (Fig. 3.1b). However, this assumption is not always true, especially in densely vegetated terrain where the last returns can come from within the tree canopy rather than the ground (e.g., Cunningham et al., 2006). Nevertheless, a number of algorithms have been developed to classify and separate the non-ground returns (e.g., returns from tree canopies, buildings) from ground returns (Kraus & Pfeifer, 1998; Axelsson, 2000; Haugerud & Harding, 2001; Sithole, 2001; Zhang et al., 2003). The ability to acquire accurate and high-resolution topographic data through dense forest cover is one of the primary advantages of airborne LiDAR over more conventional topographic data acquisition methods such as photogrammetry (Kraus & Pfeifer, 1998; Baltsavias, 1999b).

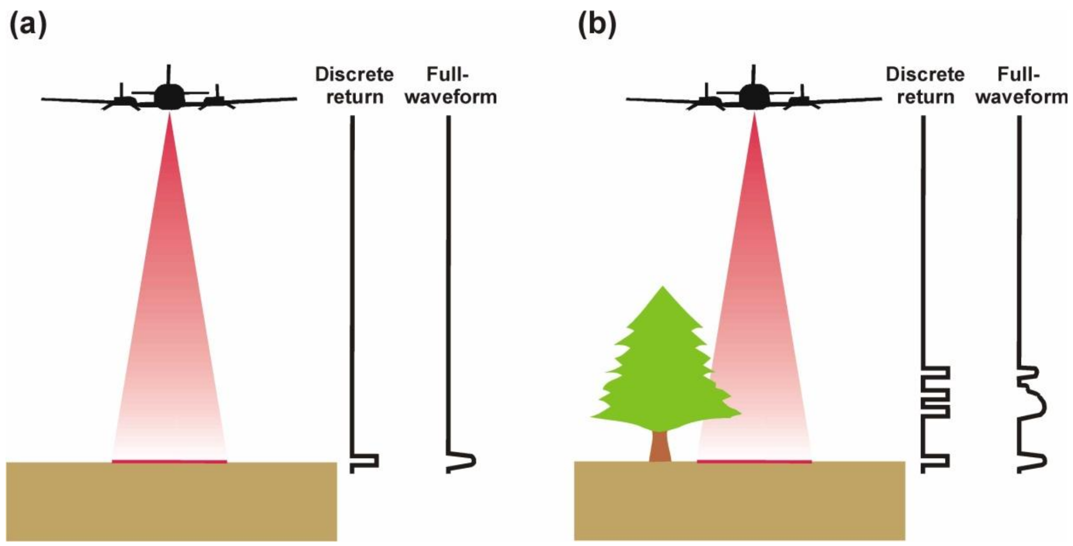

Fig. 3.1. Comparison of discrete return and full-waveform LiDAR over **(a)** bare terrain and **(b)** forested terrain.

Once acquired, the LiDAR data points can be processed to generate a digital elevation model (DEM), by interpolating the x-y-z coordinates of the appropriate returns to a regularly-spaced grid (also known as a raster). A DEM generated from the first returns is generally referred to as a digital surface model (DSM), whereas a DEM generated from only ground returns is known as a 'bare-earth' DEM or digital terrain model (DTM). Although interpolation errors accompany rasterisation, LiDAR topographic data is more efficiently stored in the form of a DEM than in its “raw” vector point form (Chen, 2007). Moreover, there are many algorithms that readily enable qualitative (e.g., generation of shaded relief images; Kennelly, 2008) and quantitative analysis (e.g., derivation of terrain attributes such as slope and curvature; Wood, 1996) of DEMs. For these reasons, high-resolution airborne LiDAR DEMs (both DSMs and DTMs) have been utilised for an array of earth science applications, including fault mapping (Harding & Berghoff, 2000; Haugerud et al., 2003; Prentice et al., 2003; Cunningham et al., 2006), mapping and characterisation of landslide morphology (McKean & Roering, 2004) and the characterisation of alluvial fan morphology (Staley et al., 2006; Frankel & Dolan, 2007).

3.1.2 Data acquisition

Airborne LiDAR data used in this study were acquired on the 14th of May, 2005 by the Natural Environment Research Council Airborne Research and Survey Facility (NERC ARSF). The LiDAR survey was undertaken at an average flying altitude of 2550 m above sea level, using a Dornier aircraft mounted with an Optech ALTM-3033 LiDAR system operating with a laser wavelength of 1.064 μm, a laser pulse repetition rate of 33.3 kHz, a scanning frequency of 19.4 Hz and a scan angle of ± 19° either side of the nadir. Due to topographic relief within the surveyed area, the height of the aircraft above the ground ranged between 1500 and 2300 m. The entire surveyed area comprises nine, northwest-southeast trending, overlapping strips covering approximately 375 km^2 and encompassing the chosen study area (Fig. 3.2). Each strip has a swath width of 1400–1500 m and an overlap of 20–50% between adjacent swaths. Five of these strips contained data for the actual study area.

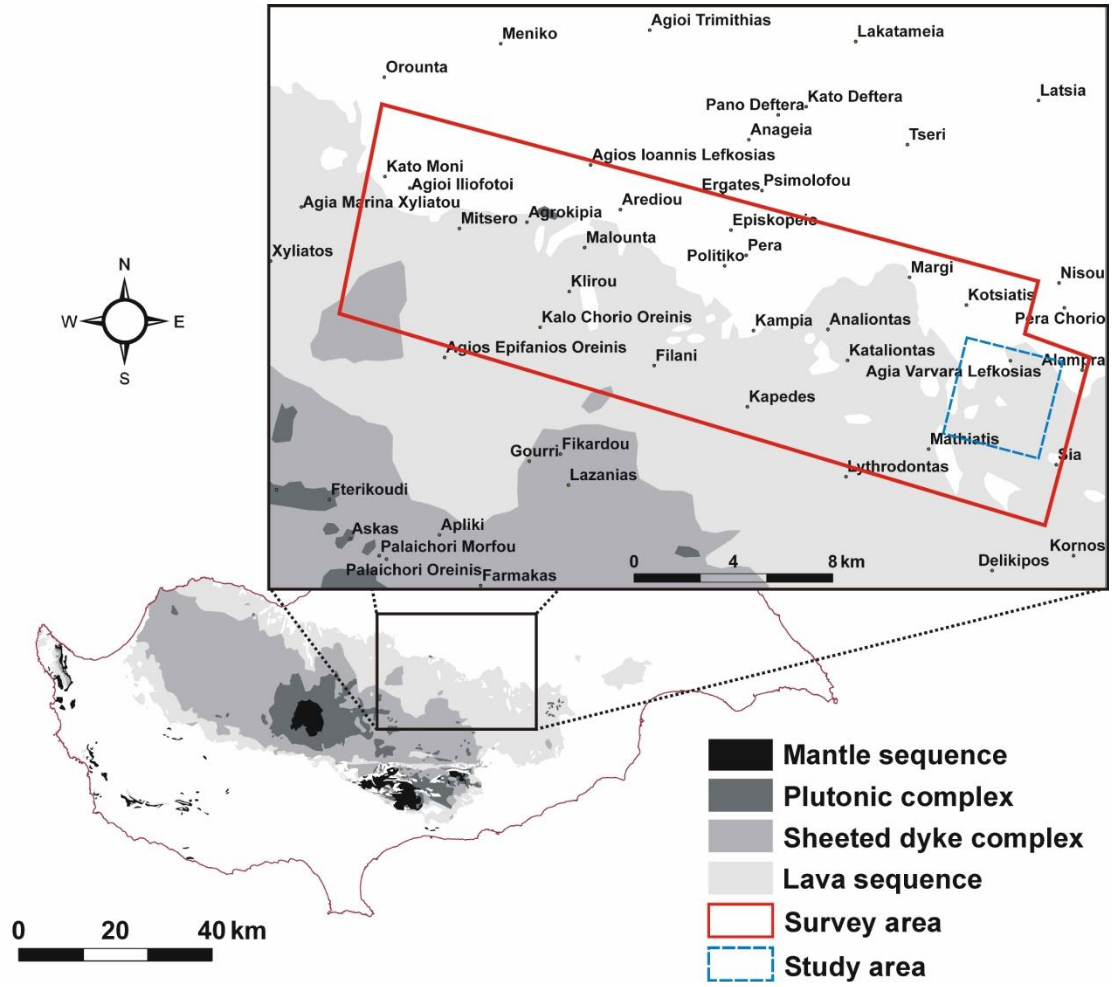

Fig. 3.2. Generalised geological map of Cyprus showing the locations and extents of the airborne survey and study areas.

Initial processing of the instrument data was undertaken by the Unit for Landscape Modelling at the University of Cambridge, UK. This involved combining the ranging data with the aircraft GPS and INS data to determine the 3-dimensional coordinates of all laser returns. The LiDAR point data were delivered as ASCII files containing the x–y–z coordinates and intensity of all first and last returns in the WGS84 Universal Transverse Mercator (UTM) zone 36-North coordinate system. Information regarding the absolute accuracy of the point data was not provided by NERC ARSF, or determined as part of this study. However, airborne LiDAR data acquired using the ALTM-3033 system is widely reported as having an absolute vertical accuracy of ± 15 cm at a height of 1.2 km above the ground, one standard deviation; ± 35 cm at 3 km, one standard deviation; and an absolute horizontal accuracy of better than 1/2000th of the flying height, one standard deviation (Arnold et al., 2006; Mazzarini et al., 2007). Accordingly, given an average flying height of 1900 m above the ground, the absolute vertical and horizontal accuracies of the data are expected to be on the order of 15–35 cm and better than 95 cm, respectively — assuming adequate calibration and ground control. Whereas the absolute accuracy of the data is a crucial consideration for LiDAR applications such as flood-risk modelling (e.g., Webster et al., 2006c), the relative vertical accuracy is arguably of greater significance to this study. Measured as the standard deviation of returns from a flat surface such as that of water (Glenn et al., 2006), the relative vertical accuracy of the data was found to be better than 8 cm. This was calculated using over 6300 returns from the surface of a large dam.

3.1.3 Pre-processing

3.1.3.1 Point data classification

The LiDAR dataset originally contained returns from both ground and non-ground objects. Therefore, in order to generate a DTM it was first necessary to remove all non-ground features from the dataset. Data points were classified as either ground or non-ground returns using a triangulated irregular network (TIN) densification algorithm (Axelsson, 2000), which has been implemented in the TerraScan software (www.terrasolid.fi/en). This algorithm iteratively classifies returns as either ground or non-ground according to angle and distance thresholds applied to TIN facets. Due to the relatively high degree of topographic variability between some of the flight lines, the individual strips of data were classified separately. In each case, the classification parameters and thresholds were determined experimentally. The maximum terrain angle and iteration distance threshold were kept constant throughout the classification process, at 88° and 1.40 m, respectively. The appropriate maximum building size and iteration angle threshold were found to be more scene-dependent. In general, the maximum building size and iteration angle varied from 20 m and 14° for strips dominated by relatively high relief, to 60 m and 6° for strips of data acquired over relatively flat terrain. To verify the results of the classification process, numerous cross-sections were extracted from each strip and inspected to ensure the point data were assigned to the correct return class. Wherever necessary, misclassified points were manually assigned to the correct class. Following classification, non-ground returns were discarded, while points classified as ground returns were retained for the generation of a DTM. Within the study area, a total of approximately 7,600,000 data points were classified as ground returns, corresponding to an average ground point density of 0.48 returns per m^2.

3.1.3.2 Digital terrain model (DTM) generation

The accuracy of gridded LiDAR data products is affected by the choice of interpolation algorithm and raster spatial resolution (Smith et al., 2005; Palamara et al., 2007; Bater & Coops, 2009). It is therefore important to select an appropriate algorithm and spatial resolution in order to avoid errors in the DTM having a significant effect on any subsequent quantitative (e.g., morphometric) analysis. Following a review of the literature, Bater & Coops (2009) concluded that no single interpolation method appears to be universally superior for generating LiDAR DEMs. However, the authors ascribe the accuracy of DEMs to the mathematical design of the interpolator and the raster spatial resolution, in addition to case specific factors such as the LiDAR ground return spacing and complexity of the terrain. Consequently, the optimal algorithm and spatial resolution for generating a DTM of the study area was determined by assessing interpolation errors associated with 1, 2, 3, 4 and 5 m DTMs generated using a range of popular algorithms. The interpolation algorithms evaluated were inverse distance weighted, modified Shepard's, triangulation with linear interpolation, ordinary block kriging, cubic polynomial and nearest neighbour.

The inverse distance weighted (IDW) algorithm calculates unknown elevations as weighted averages of a number of neighbouring elevations which are assigned decreasing weights for increasing distance from the grid node in question (Franke, 1982). The IDW DTMs were generated using the Surfer 8.0 software package (Golden Software, Inc.), with a power parameter of 2 and a search radius of 20 m. Modified Shephard's is an adapted version of IDW that computes unknown elevations as weighted averages of elevations taken from a least squares quadratic surface which is fit to neighbouring points (Franke & Nielson, 1980). Again, the algorithm implemented in Surfer 8.0 (with a smoothing factor of 0 and search radius of 20 m) was used to generate the modified Shepard's DTMs. Triangulation with linear interpolation generates a TIN from known data points using Delaunay triangulation, before linearly interpolating between the coordinates of each Delaunay triangle to calculate elevation values for all enclosed grid nodes (Lee & Schachter, 1980; Guibas & Stolfi, 1985). The triangulation with linear interpolation algorithm in ArcMAP 9.1 (ESRI) was used to generate DTMs as the Surfer 8.0 version was found to be too inefficient in terms of memory and time. Kriging is a complex geostatistical interpolation technique that calculates elevations as a weighted average of neighbouring values, where the weights are determined using a variogram which measures the spatial continuity of the data (Clark, 1979). Unlike point kriging, which can produce large spikes or pits at the data points (Smith et al., 2005), block kriging estimates the average elevation for an area surrounding grid nodes. The block kriging algorithm in Surfer 8.0 was implemented with no drift, a search radius of

20 m and the default linear variogram model. The default variogram model was used because it was inefficient to compute a variogram for the LiDAR data given the large number of data points. Cubic polynomial interpolation determines elevations as weighted averages of elevations extracted from least square polynomial surface that is fit to neighbouring data points. This was performed using Surfer 8.0 with a search radius of 20 m and a power parameter of 2. Nearest neighbour interpolation is the most simplistic algorithm and assigns grid nodes the elevation equal to that of the nearest point. The nearest neighbour DTMs were also generated in Surfer 8.0 using a search radius of 20 m. A search radius of 20 m was selected for all algorithms as a compromise between maximising the number of neighbouring points surrounding each grid node whilst still maintaining a reasonable implementation time.

Interpolation errors associated with each algorithm and spatial resolution were assessed quantitatively using statistics derived through split-sample validation (Smith et al., 2005). This involved the random selection and omission of approximately 9% of the ground return data points, while the remaining 91% were used to generate DTMs. The vertical errors, or residuals, between all omitted data points and their predicted values in the DTM were calculated as:

$$E_i = P_i - A_i \quad , \tag{3.2}$$

where E_i is the vertical error at location i, P_i is the predicted elevation in the DTM at location i, and A_i is the actual elevation of the omitted data point at location i. These vertical errors were then used to derive a set of interpolation error statistics, including the mean error (which indicates the magnitude and direction of any bias) and mean absolute error (Bater & Coops, 2009). The root mean square error conventionally used to assess interpolation errors was not used because it assumes — often invalidly — a mean error of zero (Li, 1998). The DTMs were also visually inspected for interpolation artefacts (e.g., null and spurious elevations) by using shaded relief images with varying illumination directions and vertical exaggeration. Both the visual and quantitative interpolation analyses were undertaken using Surfer 8.0.

Table 3.1. Error statistics derived from split-sample validation (n = 689,902) of DTMs generated using a range of interpolation algorithms and spatial resolutions. Block kriging and modified Shepard's interpolation to 1 m resolution was not performed due to their excessive processing times.

Interpolation algorithm	Resolution (m)	Mean error (m)	Mean |error| (m)	SD |error| (m)	Min error (m)	Max error (m)
IDW	1	-0.11	0.26	0.32	-3.67	5.96
	2	-0.12	0.26	0.31	-3.66	5.85
	3	-0.12	0.26	0.32	-4.27	5.75
	4	-0.12	0.27	0.32	-3.89	5.13
	5	-0.12	0.28	0.33	-4.36	5.64
Nearest neighbour	1	-0.10	0.26	0.34	-5.14	7.49
	2	-0.11	0.25	0.33	-5.07	6.18
	3	-0.11	0.26	0.33	-5.45	6.66
	4	-0.11	0.26	0.33	-4.85	6.00
	5	-0.11	0.27	0.34	-5.23	5.73
Cubic polynomial	1	-0.11	0.23	0.40	-23.08	130.52
	2	-0.11	0.23	1.48	-3.42	1007.83
	3	-0.11	0.23	0.31	-3.43	51.59
	4	-0.11	0.24	0.75	-27.92	472.13
	5	-0.11	0.24	0.50	-7.20	237.67
Block kriging	1	-	-	-	-	-
	2	-0.11	0.22	0.30	-3.73	5.51
	3	-0.11	0.23	0.30	-3.35	5.38
	4	-0.11	0.24	0.30	-3.41	4.91
	5	-0.11	0.25	0.30	-3.59	4.98
Triangulation with linear interpolation	1	0.01	0.23	0.29	-5.61	5.69
	2	0.01	0.29	0.32	-6.54	50.10
	3	0.02	0.35	0.40	-8.25	85.54
	4	0.03	0.42	0.80	-7.46	375.83
	5	0.04	0.49	0.53	-8.58	8.33
Modified Shepard's	1	-	-	-	-	-
	2	-0.11	0.23	0.34	-18.03	15.96
	3	-0.11	0.23	0.34	-33.75	16.30
	4	-0.11	0.24	0.35	-45.96	22.03
	5	-0.10	0.25	0.35	-22.30	19.02

The split-sample validation results (shown in Table 3.1) reveal that the interpolation algorithms tend to underestimate the actual elevation (mean errors ranging from -0.10 m to -0.12 m), with the exception of triangulation with linear interpolation which slightly overestimated elevation (mean errors ranging from 0.01 m to 0.04 m). Mean absolute errors were generally consistent between the interpolation algorithms and spatial resolutions (ranging from 0.23 m to 0.28 m), again with the exception of the triangulation with linear interpolation algorithm. With this algorithm, the mean absolute error increased considerably with spatial resolution, from 0.23 m at 1 m resolution to 0.49 m at 5 m. Standard deviations of the absolute errors were also generally consistent between algorithms and spatial resolution. Large maximum errors observed for the cubic polynomial, triangulation with linear interpolation and modified Shepard's algorithms were found to correspond to spurious elevations occurring at the edges of data voids.

During visual inspection, a "ridge and trough" pattern was observed in all DTMs at the extreme edges of areas where adjacent swaths overlapped. Cross-sectional profiles extracted from the data strips revealed that elevation exhibited an upward concavity error with increasing scan angle towards the edges of swaths (Fig. 3.3). Such phenomenon is often referred to as "smiley face error" (Lohani & Mason, 2005). This parabolic error has been attributed to vertical beam misalignment or systematic range errors (Latypov, 2005). The observed DTM artefact is produced when data acquired from multiple flight lines are merged and measurements acquired at large scan angles from one flight line differ slightly from corresponding measurements made at smaller scan angles from an adjacent flight line (Arrowsmith & Zielke, 2009).

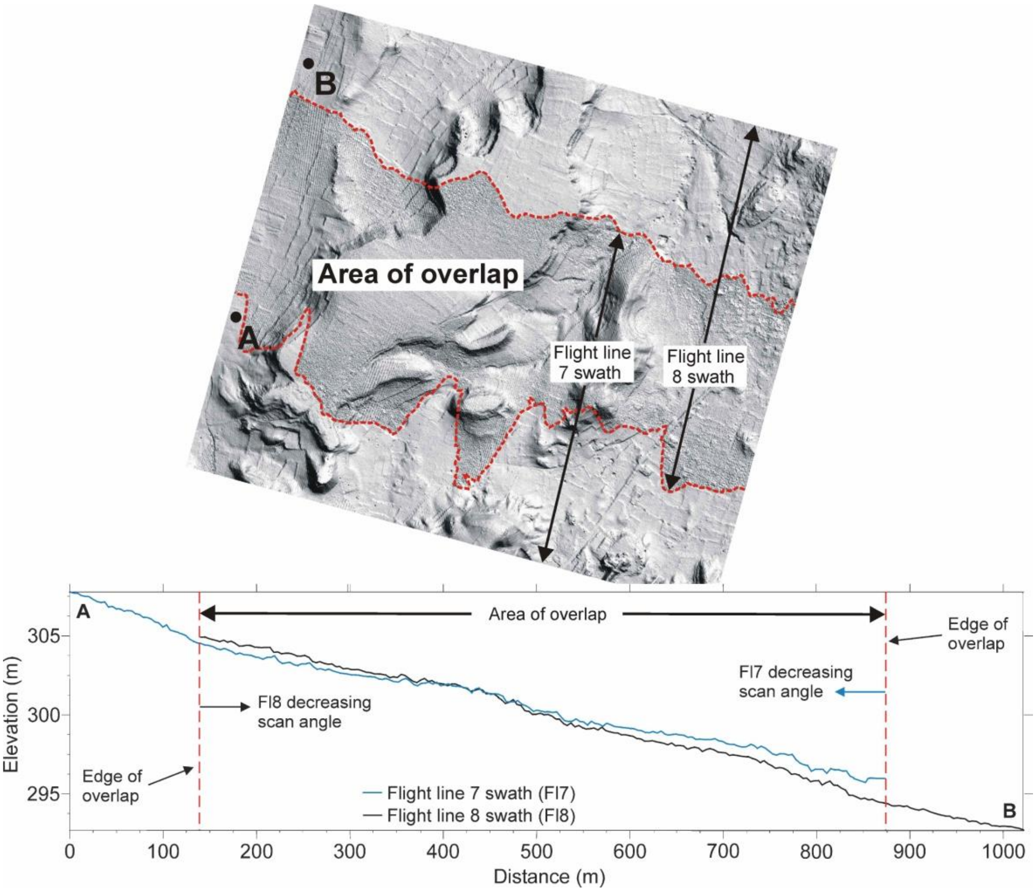

Fig. 3.3. An example of the effects of “smiley error” manifest in a subset of DTM (displayed as a shaded relief image) and cross-sectional profiles of adjacent LiDAR swaths 7 and 8.

The effect of the “ridge and trough” artefact on the quantitative interpolation error analysis was isolated by recalculating the split-sample error statistics using only a subset of residuals located outside the areas of overlap between swaths. As a result, mean errors were reduced to underestimations of between 0.01 m and 0.03 m for all interpolation algorithms except for triangulation with linear interpolation, for which the overestimation increased to between 0.02 m and 0.09 m (Table 3.2). Also, the choice of interpolation algorithm was now found to have a greater effect on mean absolute errors than the spatial resolution, again with the exception of triangulation with linear interpolation. Nevertheless, the mean absolute error showed a significant decrease in all cases when calculated using residuals from outside the areas of overlap. Block kriging, modified Shepard's and cubic polynomial interpolation resulted in the smallest mean absolute errors (ranging from 0.09 m to 0.13 m for all resolutions), followed by the inverse distance weighted and nearest neighbour algorithms (0.15 m to 0.17 m). Triangulation with linear interpolation was the worst performing algorithm, with mean absolute error increasing from 0.12 m at 1 m resolution to 0.43 m at 5 m.

Table. 3.2. Error statistics derived from split-sample validation results for a subset of residuals (n = 153,375) located outside the areas of overlap between swaths.

Interpolation algorithm	Resolution (m)	Mean error (m)	Mean |error| (m)	SD |error| (m)	Min error (m)	Max error (m)
IDW	1	-0.03	0.16	0.19	-2.89	5.96
	2	-0.03	0.15	0.19	-2.87	5.85
	3	-0.03	0.16	0.19	-3.01	5.75
	4	-0.03	0.16	0.20	-3.25	4.61
	5	-0.03	0.17	0.22	-4.01	5.64
Nearest neighbour	1	-0.01	0.15	0.17	-3.05	4.533
	2	-0.01	0.14	0.16	-2.62	3.35
	3	-0.02	0.14	0.16	-2.43	4.14
	4	-0.02	0.15	0.17	-2.99	4.01
	5	-0.02	0.16	0.18	-3.62	4.31
Cubic polynomial	1	-0.02	0.11	0.49	-23.08	130.52
	2	-0.03	0.12	2.58	-2.62	1007.83
	3	-0.02	0.12	0.22	-2.65	51.59
	4	-0.02	0.12	1.22	-27.92	472.13
	5	-0.02	0.13	0.72	-7.20	237.68
Block kriging	1	-	-	-	-	-
	2	-0.02	0.10	0.11	-2.16	3.04
	3	-0.02	0.11	0.12	-2.23	3.14
	4	-0.01	0.12	0.14	-2.57	3.10
	5	-0.01	0.13	0.16	-2.86	3.44
Triangulation with linear interpolation	1	0.02	0.12	0.13	-2.17	4.03
	2	0.03	0.19	0.21	-2.93	5.55
	3	0.05	0.27	0.29	-3.94	6.70
	4	0.07	0.35	0.38	-5.08	9.00
	5	0.09	0.43	0.47	-5.48	8.28
Modified Shepard's	1	-	-	-	-	-
	2	-0.01	0.09	0.15	-18.03	15.96
	3	-0.01	0.09	0.19	-33.75	16.30
	4	-0.01	0.10	0.26	-45.96	22.03
	5	-0.01	0.11	0.23	-22.30	19.02

As the “ridge and trough” pattern was solely confined to the areas of overlap where the point density is greater, it was possible to almost completely eradicate this artefact from the DTMs using a simple point-spacing based filter prior to interpolation. The filter discarded the point with the highest elevation (i.e., the point most affected by “smiley face error”) when multiple ground returns were present within a given radius. The size of the radius was chosen so that the filter only operated on data points within the areas of overlap (in this case a point spacing ≤ 2 m). In addition to removing this artefact, the filter also helps to produce a dataset with a more globally uniform point density by reducing the density of data points in the areas of overlap to match that of the remainder of the study area.

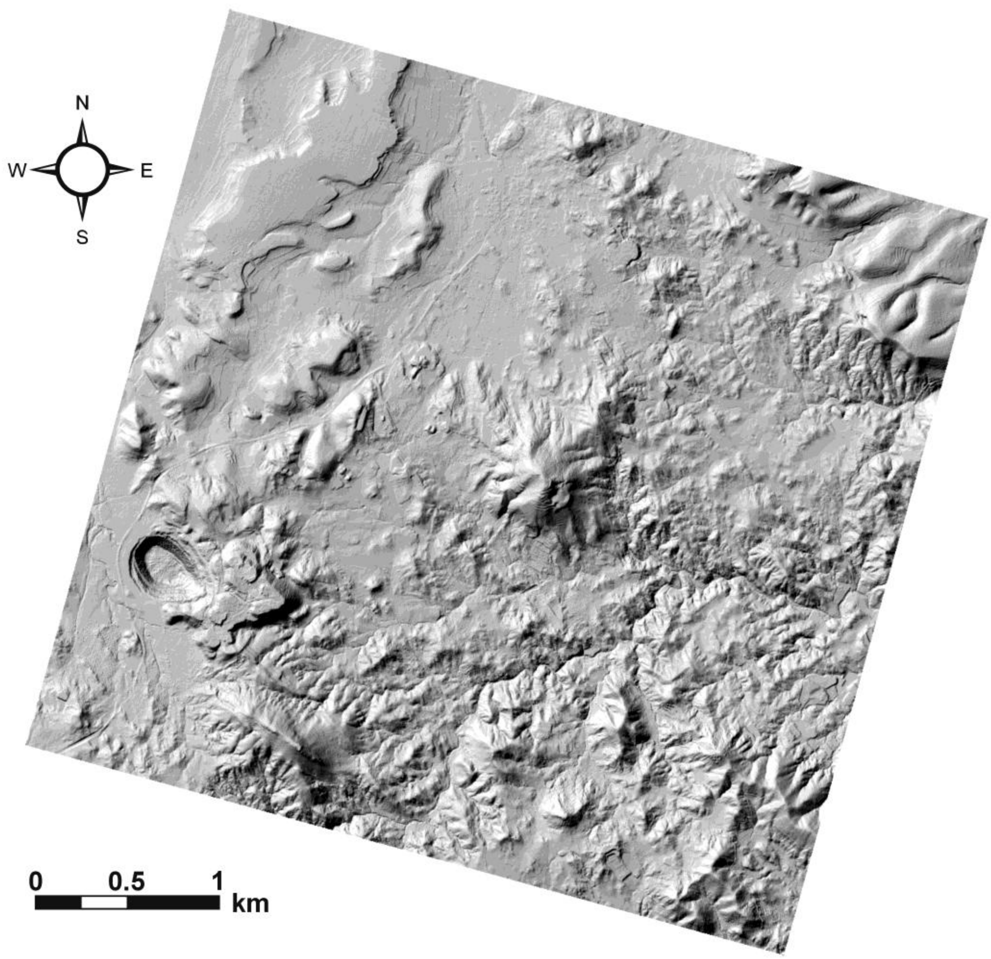

Fig. 3.4. Shaded relief image of the final 4 m DTM of the study area generated using block kriging interpolation with prior application of the point-spacing filter.

The optimal interpolation algorithm and spatial resolution for the final DTM was selected as that which minimised the error statistics and the appearance of interpolation artefacts in the DTM. Consequently, 100% of the ground returns were used to generate the final DTM for the study area at a spatial resolution of 4 m, by applying the point-spacing filter prior to interpolation with the block kriging algorithm (Fig. 3.4).

3.2 Airborne Thematic Mapper imagery

3.2.1 Background

The Daedalus 1268 Airborne Thematic Mapper (ATM) instrument is a passive multispectral scanner that measures electromagnetic radiation in the visible to thermal infrared wavelength region of the spectrum. Specifically, utilising a configuration similar to that of the Landsat TM satellite, the ATM instrument records electromagnetic radiation in 11 fixed-wavelength spectral bands located in the visible near, short-wave and thermal infrared (Table 3.3). Despite the given wavelength range measured by each ATM waveband, scattering within the optical system or inadequate blocking filters may lead to radiation from outside these wavelength ranges being recorded (Clark, 1999). The actual recording response of a waveband as a function of wavelength is known as its bandpass. Knowledge of all bandpasses is crucial when high-spectral resolution data is re-sampled for comparison with data acquired using a different sensor with a lower spectral resolution. A filter function file containing the bandpasses of ATM bands 1–10 was obtained from the NERC Field Spectroscopy Facility (Fig. 3.5).

Table 3.3. Wavelength positions of the 11 ATM spectral bands compared to those of Landsat TM.

ATM waveband	Wavelength (μm)	Spectral region	Equivalent Landsat TM band
1	0.42–0.45	Ultraviolet/blue	
2	0.45–0.52	Blue	1
3	0.52–0.60	Green	2
4	0.60–0.62	Yellow/orange	
5	0.63–0.69	Red	3
6	0.69–0.75	Near-infrared	
7	0.76–0.90	Near-infrared	4
8	0.91–1.05	Near-infrared	
9	1.55–1.75	Short-wave infrared	5
10	2.08–2.35	Short-wave infrared	7
11	8.50–13.00	Thermal infrared	6

The ATM sensor has an instantaneous field of view of 2.5 mrad, a digitised field of view of 90°, and scans a swath width of 938 pixels at scan rates of up to 50 Hz. The instrument measures the detected radiation at a radiometric resolution of 16-bit. As a result, pixels in each of the 11 waveband images are assigned an integer value in the range of 0 to 65,535 according to the intensity of the radiation recorded in that particular waveband. Since the ATM is a scanning sensor, the size of pixels on the ground (i.e., spatial resolution) is governed by the instantaneous field of view, and so varies according to the scan angle, the attitude of the aircraft and its height the above the ground. In summary, the size of pixels on the ground increases with increasing scan angle away from nadir and with increasing aircraft height. The locations of pixels on the ground are dependent on the scan angle, and position and orientation of the aircraft. However, due to a combination of aircraft's forward motion and varying attitude during scanning orthogonal to the flying direction, adjacent pixels in the imagery may not relate to adjacent areas on the ground. As a result, unprocessed ATM imagery often appears distorted. Nevertheless, the imagery can be geocorrected (geometrically rectified and geolocated) to produce a planimetric grid or raster using knowledge of the scan angle, and aircraft position and orientation for all individual pixels. The geographic location of image pixels on the ground can be more precisely determined by also incorporating a DEM into the geocorrection process.

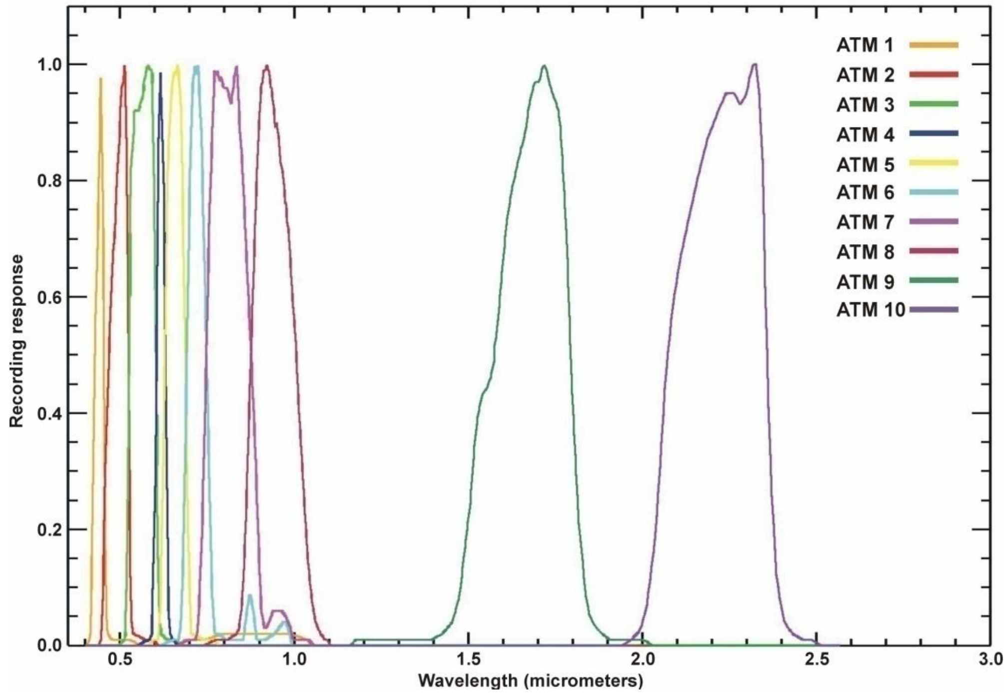

Fig. 3.5. Bandpasses of ATM wavebands 1–10 obtained from the NERC Field Spectroscopy Facility.

3.2.2 Data acquisition

The ATM imagery was acquired by the NERC ARSF in May, 2005, concomitant with the airborne LiDAR data. Seven northwest-southeast trending flight-lines of imagery with an overlap of around 50% between adjacent strips were acquired for the 375 km^2 survey area. For an average flying height of 1900 m above the ground, each strip has a swath width of 3800 m and an average pixel size on the order of 4–5 m. Five of the strips were found to contain data for the chosen study area. The strips of imagery were delivered as Level 1b Hierarchical Data Format (HDF) files, with radiometric calibration algorithms applied and aircraft navigation information appended. Radiometric calibration involved conversion of the raw ATM data to at-sensor radiance units (μW cm^{-2} sr^{-1} nm^{-1}) and then subsequent scaling to 16-bit digital numbers (DNs) to avoid loss of numerical precision. Conversion of the raw data to at-sensor radiance is achieved by applying gains and offsets — determining using a source traceable to a national standard — to the data recorded in each of the wavebands (Hill et al., 2010).

3.2.3 Pre-processing

The ATM imagery was pre-processed using an approach similar to that of Hill et al. (2010). This involved three main steps which are described in the following subsections and illustrated in Fig. 3.6.

3.2.3.1 Geocorrection

On delivery, the Level 1b HDF ATM imagery required geocorrection in order to geometrically rectify and geolocate the imagery to match the WGS84 UTM zone 36-North coordinate system of the airborne LiDAR data (Fig. 3.6a). To achieve this, all image strips were individually geocorrected using the Linux-based AZGCORR software (Azimuth Systems), which was supplied with the data by the NERC ARSF. Utilising the appended aircraft navigation information and a 4 m DSM generated from the LiDAR first returns, the AZGCORR software was used to determine the geographic location of every pixel on the ground and then interpolate these (using the default bi-cubic algorithm) to generate a 4 m raster image (GeoTIFF) for each strip. Since this study is concerned with only reflectance data, the thermal infrared band (Band 11) was discarded at this stage. Band 1 was also omitted as the data are severely affected by atmospheric scattering (Copley & Moore, 1993). Therefore, any subsequent pre-processing steps were only applied to ATM bands 2–10.

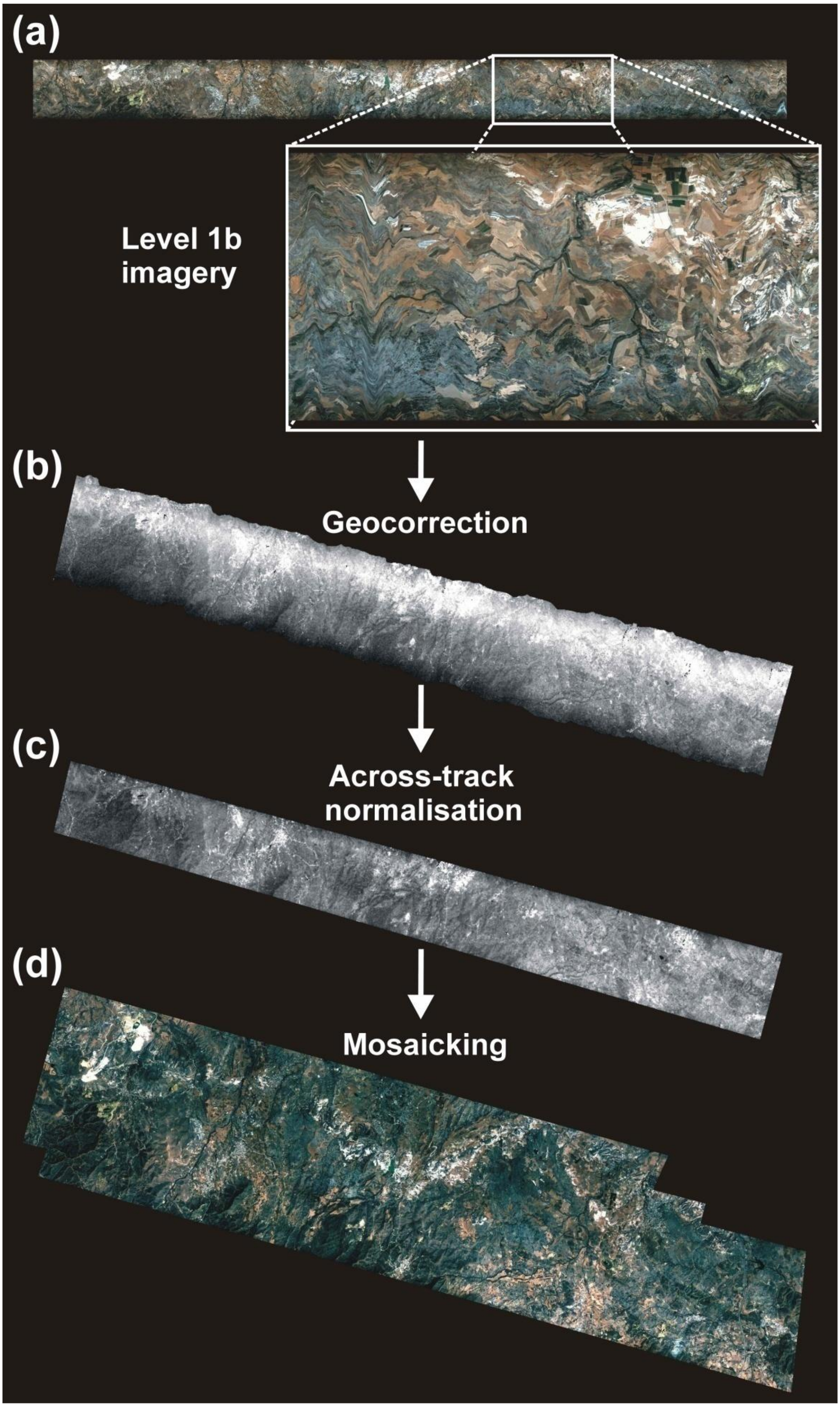

Fig. 3.6. Main pre-processing steps for the ATM imagery. **(a)** Level 1b image strips were **(b)** geocorrected, **(c)** normalised for across-track brightness differences (limb-brightening) and then **(d)** mosaicked to create a single seamless image of the survey area.

3.2.3.2 Across-track brightness normalisation

An across-track (i.e., in the scan direction, orthogonal to the flight direction) brightness effect known as limb-brightening was observed in all geocorrected images (Fig. 3.6b). This limb-brightening effect is manifest as an increase in the at-sensor radiance towards the edge of swaths as a result of increases in path length and variations in the sun–target–sensor angle (Leckie, 1987). Limb-brightening effects are greatest when the flying direction is perpendicular the solar azimuth. In this scenario, the brightening effect is asymmetric across swaths and is generally maximised in the backscatter direction, when the view direction is similar to that of the solar illumination direction (Schiefer et al., 2006). Asymmetric limb-brightening effects were observed in the ATM image strips because the flight lines were flown somewhat perpendicular to the solar azimuth. The effect of limb-brightening in each band of each strip of imagery was minimised using the Cross-track Illumination Correction tool in ENVI 4.3 (ITT Visual Information Solutions). This tool was first used to model the limb-brightening effect in each band by fitting a polynomial function to the average DN of pixels in the across-track direction, and then normalise the brightness effect in the imagery using this polynomial function. A multiplicative second-order polynomial correction was found to be optimal for minimising the limb-brightening effect in all wavebands and in all strips of imagery. Following this correction, pixels at the extreme edges of images were still found to be affected by residual limb-brightening effects. The affected pixels, generally comprising those within 50 pixels of the edges, were therefore cropped from each image strip (Fig. 3.6c).

3.2.3.3 Image mosaicking

Following the correction of limb-brightening effects, image strips were co-registered and then mosaicked to create a single seamless image (Fig. 3.6d); both of these tasks were also performed within ENVI 4.3. Adjacent strips were co-registered through a rubber-sheet transformation (RST) using image-selected tie-points and cubic convolution resampling. Tie-points identified in the areas of overlap between pairs of images comprised targets that could be easily identified and precisely located, such as road intersections and corners of buildings. The image strip most centred on the study area was kept fixed as the reference during co-registration, whilst the two image strips adjacent to this central image were transformed. A systematic approach of designating the strip closest to the central image as reference whilst transforming that which was more distal was implemented to co-register the remaining strips of imagery.

Somewhat minor spectral differences were observed in the areas of overlap between adjacent images prior to mosaicking. This is attributed to differences in the solar illumination and view angle between flight lines (Hill et al., 2010). A Colour Balancing procedure was therefore applied during mosaicking for the purpose of minimising the differences between adjacent strips. This procedure calculates gains and offsets from a fixed (reference) image and then uses these to adjust the DNs of an overlapping image, thus matching the spectral statistics between the two images. Again, all strips were adjusted relative to the image strip most centred on the study area.

3.2.3.4 Additional pre-processing steps

Due to an absence of atmospheric measurements and ground reflectance spectra and at the time of the airborne survey (and also at the time of pre-processing), rigorous model or empirical-based atmospheric corrections could not be reliably applied to the

ATM imagery. Moreover, an inspection of the DNs in the imagery suggested that first-order atmospheric correction for effects such as haze was not necessary and, as a consequence, no atmospheric correction was applied at this stage in the study. As a final pre-processing step, the mosaicked ATM imagery was subsequently co-registered to the 4 m LiDAR DTM using image-selected tie-points (with an estimated root mean square error of 1.6 pixels) and then cropped to the extent of the study area. The final pre-processed spectral data product for the study area was 4 m ATM imagery comprising ATM bands 2–10 (Fig. 3.7). Any further processing steps applied to the ATM imagery are discussed in the relevant chapters.

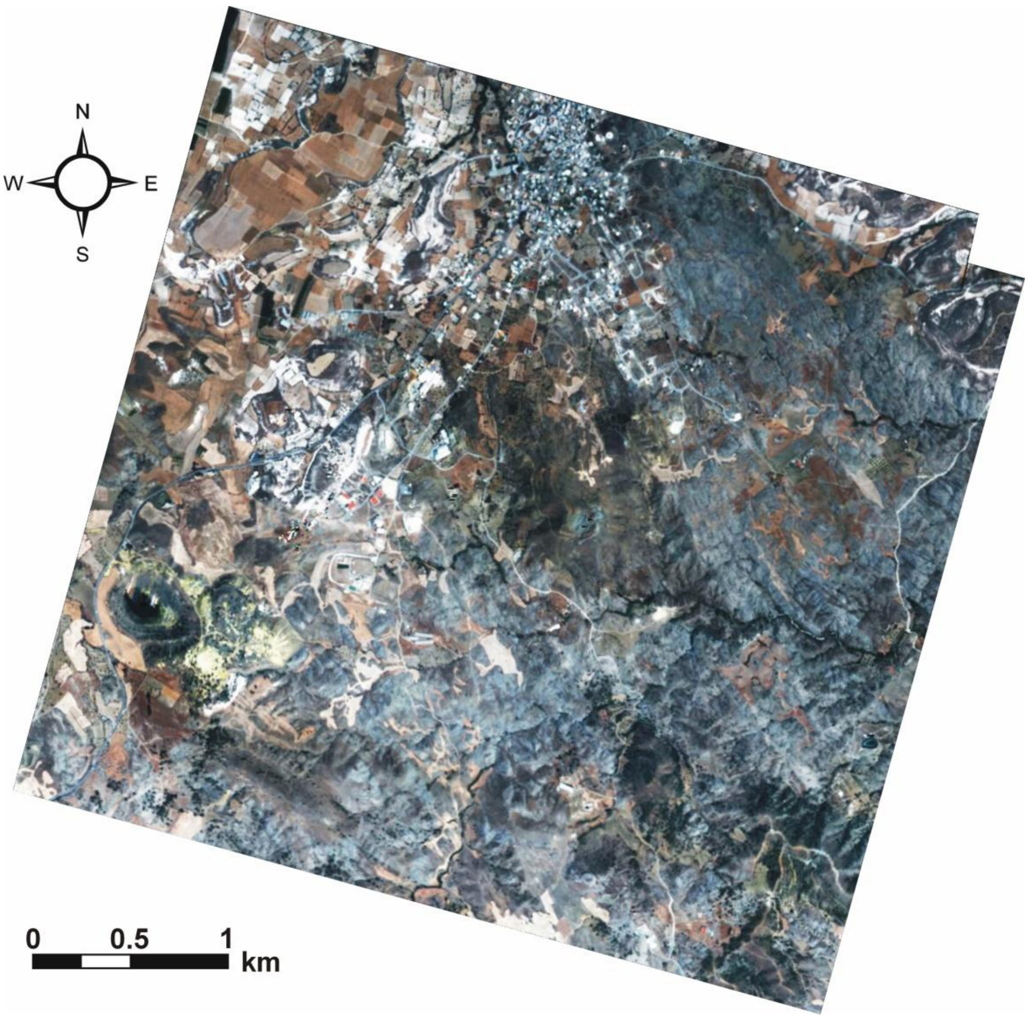

Fig. 3.7. ATM imagery (4 m) for the study area displayed as a true-colour red-green-blue composite (ATM bands 5-3-2). Note that ATM data is missing for a small patch in the north-eastern corner of the study area.

3.3 Auxiliary data

In addition to the airborne LiDAR data and ATM multispectral imagery, a range of auxiliary data was also obtained in order to help augment this study. Specifically, all data helped to provide detailed knowledge of the study area, which was subsequently used to help devise and train the mapping algorithms presented here, and to analyse, interpret and validate their results and outputs. These auxiliary datasets are summarised below.

3.3.1 Metadata

A Geographical Information System (GIS) for Cyprus was obtained from the Cyprus Geological Survey Department (GSD). This GIS initially contained over 35 data layers providing a wealth of useful information, including geological information in the form of the existing lithological and structural maps, the locations of known mineral occurrences and gossans, vegetation information, and geographical information such as place names, roads and rivers, to name but a few. Data layers such as these were not only crucial in helping to train, interpret, analyse and validate the devised mapping algorithms, but also assisted in navigating the study area. Additional spatial data either obtained or derived as part of this study was also integrated in the GIS to readily enable the simultaneous interrogation and comparison of multiple data layers.

3.3.2 QuickBird imagery

QuickBird satellite imagery for the study was also obtained from the GSD. Launched in 2001, QuickBird acquires both high-resolution panchromatic imagery and multispectral imagery (blue, green, red, near-infrared) from an altitude of 480 km. The GSD QuickBird imagery has a spatial resolution of 0.70 m and comprises three bands measuring reflected solar radiation in the blue (430–545 nm), green (466–620 nm) and near-infrared (718–918 nm) regions of the electromagnetic spectrum. These bands can be combined to produce a red-green-blue (RGB) colour composite, which provides an extremely detailed false-colour image of the surface comparable to that of aerial photographs (Fig. 3.8). The QuickBird imagery therefore played an important role in helping to train the mapping algorithms and validate the results.

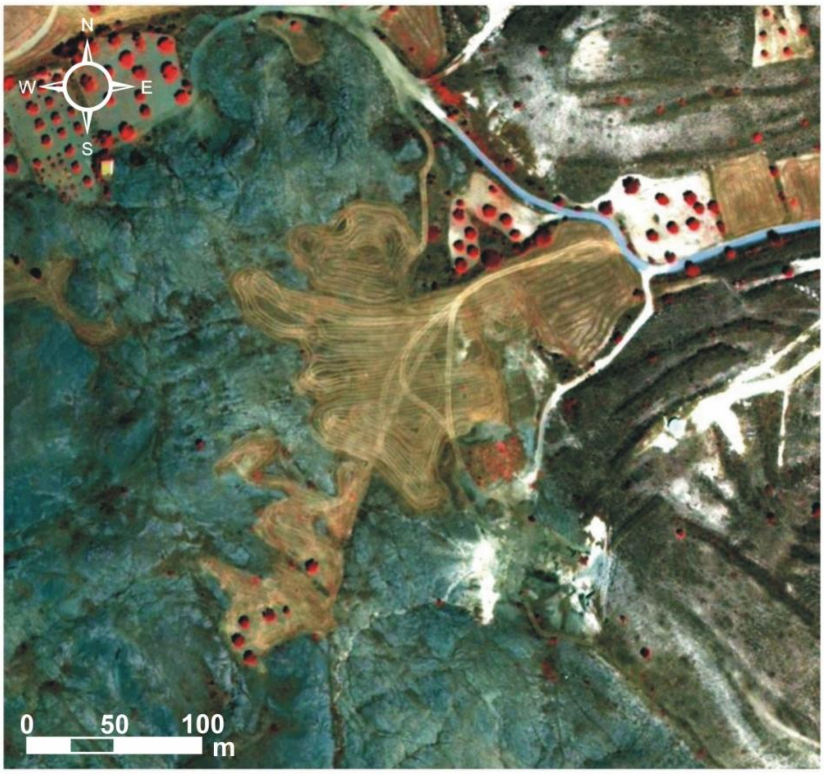

Fig. 3.8. Snapshot of the QuickBird imagery displayed as a RGB (near-infrared, green, blue) false-colour composite. Note that highly photosynthetic vegetation (i.e., trees) appears red because it is highly reflective in the near-infrared region.

3.3.3 Fieldwork

Extensive knowledge of the study area was gained during three fieldtrips. The primary objectives of the first reconnaissance fieldtrip in March and April, 2008 were to provide a geological overview of the Troodos ophiolite and help establish a detailed understanding of the geology and physiographic characteristics of the study area.

Information gained during this first fieldtrip was imperative for devising and training the mapping algorithms devised in this study.

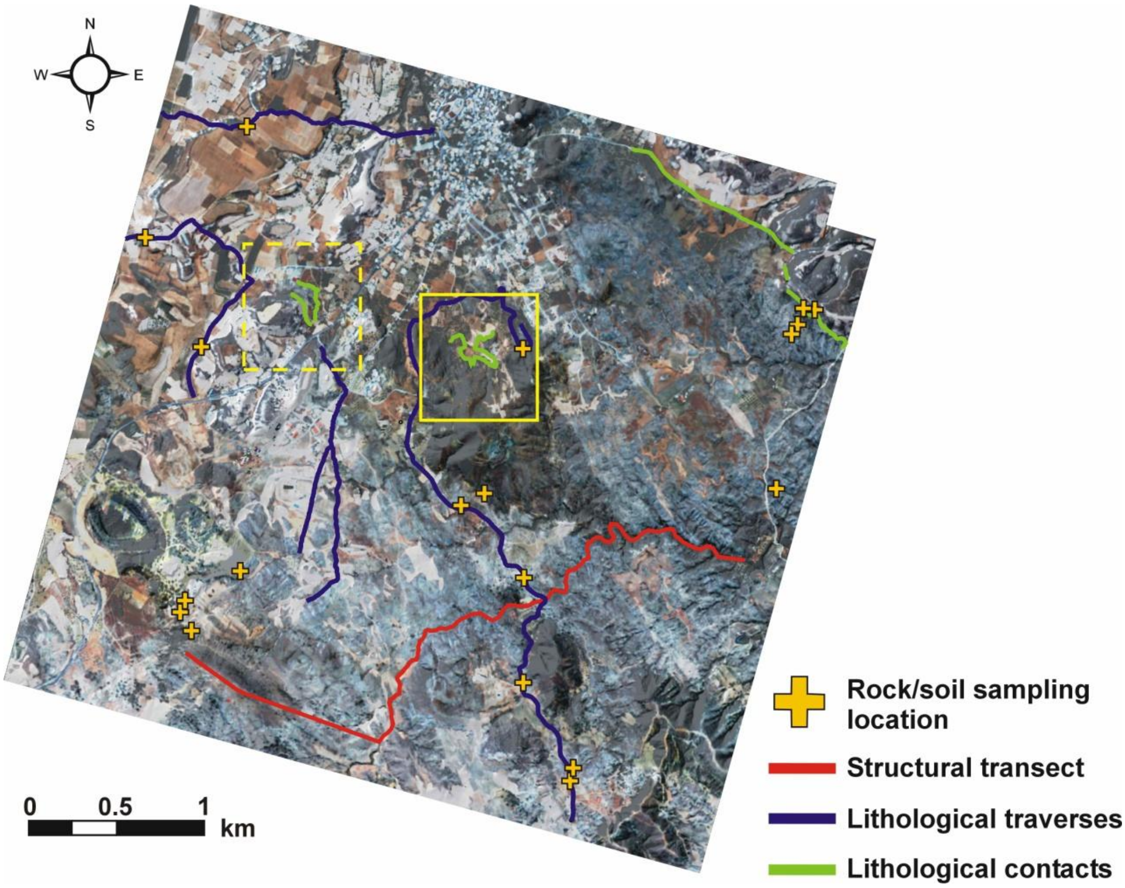

Fig. 3.9. Map showing rock/soil sampling locations and field-based geological mapping undertaken in the study area in order to guide the mapping algorithms, and assist interpretation and validation of the map products. Yellow dashed-line box corresponds to area shown in Fig. 8.1 and yellow solid-line box corresponds to area shown in Fig. 8.2.

Rock and soil samples of the four main lithologies in the study area were collected during the second fieldtrip in November and December, 2009. Numerous samples were collected in order to determine the representative spectral characteristics of each lithological unit prior to use in guiding a conventional remote sensing approach to lithological mapping (see Chapter 4). All sampling locations were recorded using a Garmin eTrex GPS (Fig. 3.9). Geological mapping was also carried out in a number of select locations during this fieldtrip. This involved mapping lithological contacts and traverses for the purpose of acquiring information that could be used to help augment interpretation and validation of the results of the novel lithological mapping algorithms present in this thesis. Lithological contacts were mapped by following the boundary between two different lithologies whilst tracking the path taken with the Garmin GPS. The GPS sampling rate was set so that the location of the contact was mapped in sufficient detail to enable comparison with the generated high-resolution lithological maps. Similarly, the GPS was also used to map lithological contacts along traverses. The mapped traverses and contacts are also shown in Fig. 3.9.

Structural measurement for a section of the study area was acquired during the third fieldtrip in May, 2010 for purpose of obtaining data that could be used to validate the structural mapping results (see Chapter 7). This involved taking strike and dip measurements of faults and dykes exposed along a stream transect running perpendicular to the main structural trend in the study area (Fig. 3.9). A rugged laptop installed with ArcMAP was taken on each fieldtrip to enable information (e.g., existing geological maps, roads) contained in the GIS to be readily accessed, and to facilitate preliminary assessments of the results of both field- and remote sensing-based mapping whilst in the field.

4. Spectral characterisation and mapping of lithologies using reflectance spectroscopy and ATM imagery

Abstract

The reflectance spectra of rocks in the 0.35–2.50 μm wavelength region of the electromagnetic spectrum are unique and provide diagnostic information about their mineralogical and elemental composition. Numerous satellite and airborne sensors are designed to exploit this same wavelength region, therefore providing the means to directly identify rocks types through their spectral characteristics. A conventional direct approach to rapidly mapping lithologies with spectral imagery involves using computer-based algorithms that automatically match image pixel spectra to representative spectra for the lithologies. Adopting this approach, the aim of this study is to assess the utility of Airborne Thematic Mapper (ATM) multispectral imagery for direct spectral discrimination and mapping of the north Troodos study area. Representative spectra for the lithologies were obtained by measuring the spectra of numerous samples in the laboratory using an ASD FieldSpec® Pro. These spectra were then resampled to the ATM bandpasses and used as reference spectra in the Spectral Angle Mapper, Matched Filtering and Mixture-Tuned Matched Filtering algorithms, to generate lithological maps by automatically matching the reference spectra to the calibrated ATM pixel spectra. The resulting maps had very poor overall accuracies (2.4–6.5%) and Kappa coefficients (≈ 0.0) due to large proportions (62–89%) of unclassified image pixels. It was subsequently demonstrated, both qualitatively and quantitatively, that the ubiquitous vegetation cover in the study area was responsible for the poor mapping performance. Spectral mixing analysis revealed that as little as 20% vegetation cover was enough to severely affect the utility of ATM imagery for direct spectral discrimination and mapping of the lithologies. The results of this study therefore reiterate the fact that conventional use of remote sensing for direct spectral mapping of lithologies is effective in only the world’s most barren regions.

4.1 Introduction

Reflectance spectroscopy in the visible/near-infrared (VNIR) to shortwave infrared (SWIR) wavelength region (i.e., 0.35–2.50 μm) provides valuable information on the constituent minerals of rocks (Hunt, 1977). Such diagnostic information is manifest in the occurrence of absorption features at specific wavelengths in the reflectance spectra caused by the absorption of photons of the same wavelengths. The corresponding quantity of energy gained through the absorption of a photon subsequently excites electronic or vibrational processes in specific minerals, thus providing mineralogical information (Rothery, 1987; Fig. 4.1). Electronic processes, including the transition of an electron from a lower energy level to a higher level, normally require more energy than vibrational processes such as the bending and stretching of molecular bonds. Accordingly, absorption features associated with electronic processes are characterised by short wavelengths and occur in the VNIR region of the spectrum, whereas those relating to vibrational processes are observed in the SWIR (Drury, 2001).

The most predominant electronic absorption features observed in mineral spectra are those relating to crystal-field transitions and charge-transfer absorptions. Crystal-field transitions occur when electrons transfer between modified energy levels that transpire when the defined energy levels (or orbitals) of isolated atoms and ions become split when placed in a crystal-field (Burns, 1970). As the splitting of the energy levels varies between minerals according to factors such as the valence state of the atom, its coordination number and the type of ligands formed, specific wavelengths of crystal-field transitions can be useful for mineral identification (Clark, 1999). Charge-transfer (or inter-elemental transition) absorptions occur when absorbed energy causes an electron to transfer between ions, or between ions and ligands (Hunt, 1977).

Absorptions of this type form broad absorption bands, in the ultraviolet to visible region, that are typically hundreds to thousands of times stronger than crystal-field absorptions (Clark, 1999). Electronic absorption features most commonly observed in mineral spectra are due to the presence of iron. For example, electronic transitions in ferrous (Fe^{2+}) ions in iron-bearing minerals are responsible for absorption features in the 1.00 μm region. The precise wavelength of this absorption feature relates to the symmetry, lattice distortion and coordination of Fe^{2+} in specific minerals (Drury, 2001). In general, Fe^{2+} produces an absorption feature near 1.00–1.10 μm when in octahedral coordination (e.g., clinopyroxene, amphibole) or near 0.90–1.10 μm when in six-fold coordination for minerals such as olivine and orthopyroxene (Rothery, 1987). One of the most predominant charge-transfer features is a broad absorption band at wavelengths shorter than 0.55 μm caused by the transfer of electrons from iron to oxygen. This feature is typically associated with weathering products such as hydrated iron oxides (i.e., limonite), and gives rise to the red 'iron-stained' colour associated with these minerals (Rothery, 1987).

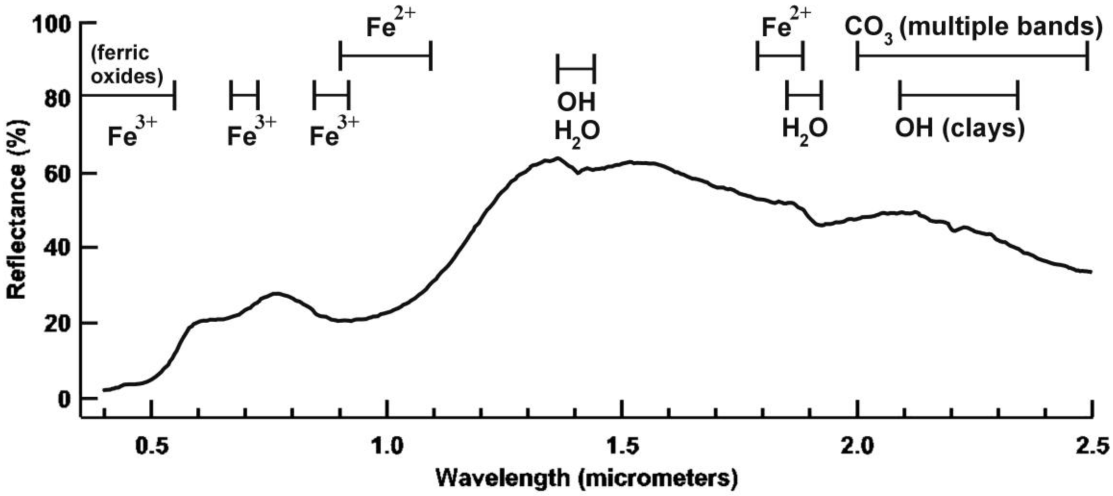

Fig. 4.1. Wavelength positions of common spectral absorption features observed in minerals (after Rothery, 1987).

As previously mentioned, energy absorbed from photons can also cause molecular bonds to vibrate at frequencies which are dependent on the type of bond and the mass of each element in the molecule (Clark, 1999). The number of normal vibrational modes or fundamentals for a molecule with N atoms is given as 3N-6. A water molecule, for example, has three fundamental vibrational modes; the symmetric OH-bond stretch (3.11 μm), the H-O-H bend (6.08 μm) and the asymmetric OH-bond stretch (2.90 μm). Molecular bonds can also excite vibrations at multiples of single fundamental frequencies, producing absorption bands at integer values of the fundamental frequencies (Hunt, 1977). These are known as overtone vibrations. When different fundamental or overtone vibrations combine, additional combination absorption bands occur at the sum of all the individual vibrational frequencies involved. Vibrational absorption features commonly observed in the SWIR region of mineral spectra are associated with molecular water, carbonate (CO_3^{2-}) and hydroxyl (OH^-) ions. Absorption features near 1.40 μm and 1.90 μm, caused by vibration overtones of OH-bond stretches and combinations of H-O-H bending with OH stretches, respectively, are diagnostic of molecular water in minerals. The two most prominent absorption features in the spectra of carbonate minerals occur near 2.35 μm and 2.50 μm due to combination and overtone vibrations of the C-O bond, respectively (Clark et al., 1990). The hydroxyl group — most notably found in clay minerals — has only one fundamental stretching mode that is found near 2.75 μm, although its precise location varies based on what it is bound to (Hunt, 1977). It is most commonly found bound to metals, producing a combination metal-OH bend and stretch absorption feature between 2.20–2.30 μm (Clark, 1999). In general, absorptions near 2.20 μm are attributed to Al-OH vibrations, whereas Mg-OH bonds typically produce absorptions features near 2.30 μm (Hunt, 1997; Drury, 2001).

Since rocks and minerals can be directly identified based on their spectral characteristics, satellite and airborne imaging systems measuring the VNIR–SWIR wavelength region have been extensively exploited for lithological mapping purposes (e.g., Rowan & Mars, 2003; Rowan et al., 2004; Bedini, 2009; Roy et al., 2009; Haselwimmer et al., 2010). Lithological maps are rapidly generated for relatively large areas using automated algorithms that match image pixel spectra to reflectance spectra of lithologies found within the area of interest. In some cases, the representative reflectance spectra for the lithologies are acquired through field or laboratory spectroscopy (e.g., Roy et al., 2009). Of particular relevance to this study is that of van der Meer et al. (1997), who ascertained representative *in situ* SWIR (1.30–2.50 μm) reflectance spectra of the main lithological units of the Troodos ophiolite, Cyprus, using a Portable Infrared Mineral Analyzer (Fig. 4.2). Although it appears that the initial intention of the authors was to try to map the lithologies of their study area by directly comparing these spectra to Landsat TM pixel spectra, this was not possible for two main reasons. Firstly, the *in situ* reflectance measurements were difficult to directly correlate with Landsat TM imagery because the spectra only coincided with two of the Landsat TM bandpasses. Secondly, the inability to successfully calibrate the Landsat TM imagery to ground reflectance also meant that the *in situ* spectra could not be directly linked to the image spectra. As a consequence, mapping was performed by automatically matching image pixel spectra to representative spectra extracted from the Landsat imagery. Building on from the work of van der Meer et al. (1997), the aim of this study is to ascertain representative reflectance spectra for the four main North Troodos lithologies in the VNIR–SWIR region, and to then assess the ability to rapidly and directly map the lithologies of the study area by using these spectra in conjunction with Airborne Thematic Mapper (ATM) imagery. In contrast to the previous study by van der Meer et al. (1997), the reflectance spectra acquired in this study coincide with nine of the ATM bandpasses whilst the 4 m spatial resolution of the ATM imagery potentially enables lithologies to be mapped in much more detail than is possible using 30 m Landsat TM imagery.

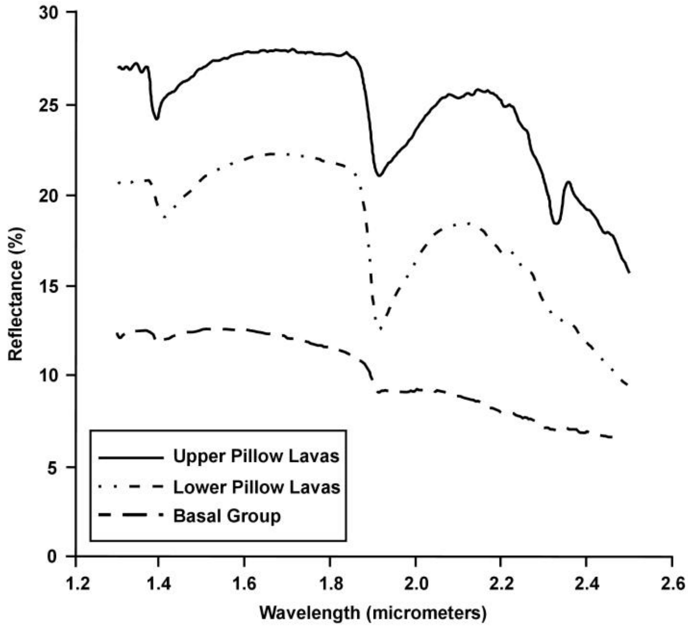

Fig. 4.2. *In situ* SWIR (1.30–2.50 μm) reflectance spectra for rocks of the Troodos ophiolite relevant to this study (after van der Meer et al., 1997).

4.2 Spectral characterisation of the lithological units

Spectral reflectance measurements of rock and soil samples were acquired in the VNIR–SWIR (0.35–2.50 μm) wavelength region to ascertain a set of representative reflectance spectra and interpret the main spectral characteristics of the lithologies found within the study area. Subsequently, this set of representative reflectance spectra may then be utilised in conjunction with the ATM imagery for the direct identification and mapping of the spatial distribution of each of the lithological units. In this section the methodology employed to acquire the spectral reflectance measurements is first presented, followed by a discussion of the spectral characteristics associated with each of the lithological units.

4.2.1 Methods

4.2.1.1 Sample collection

Numerous 'fist-sized' rock and soil samples representative of each lithological unit were collected during fieldwork conducted within the study area in early December, 2009. For each lithology, appropriate sampling locations were identified using both of the existing geological maps a guide, in addition to detailed knowledge of the study area gained during previous fieldwork. A total of twenty sampling locations were selected and the geographic position of each was recorded using a hand-held Garmin eTrex GPS (see Chapter 3, Fig. 3.9). Wherever possible — especially for sampling locations situated well within relatively large areas (> 500 m^2) of homogeneous surface composition — several samples were collected from within a 3 m radius of the recorded positions. This strategy was adopted to take local mineralogical variation into account, and to help establish representative spectra for sample sites located within the homogenous areas for use in calibrating the ATM imagery.

4.2.1.2 Spectral data acquisition

The reflectance spectra of approximately forty rock samples were acquired using an Analytical Spectral Devices (ASD™) FieldSpec® Pro spectroradiometer, which was loaned from the NERC Field Spectroscopy Facility. The ASD FieldSpec® Pro records reflected light within the 0.35–2.50 μm region of the electromagnetic spectrum, and can be used both in the field and in a laboratory. Although *in situ* field spectra were preferable for this study, the ASD FieldSpec® Pro was unavailable during the

December fieldtrip. Instead, the spectra were acquired using a laboratory setup during a loan of the instrument between January and February, 2010.

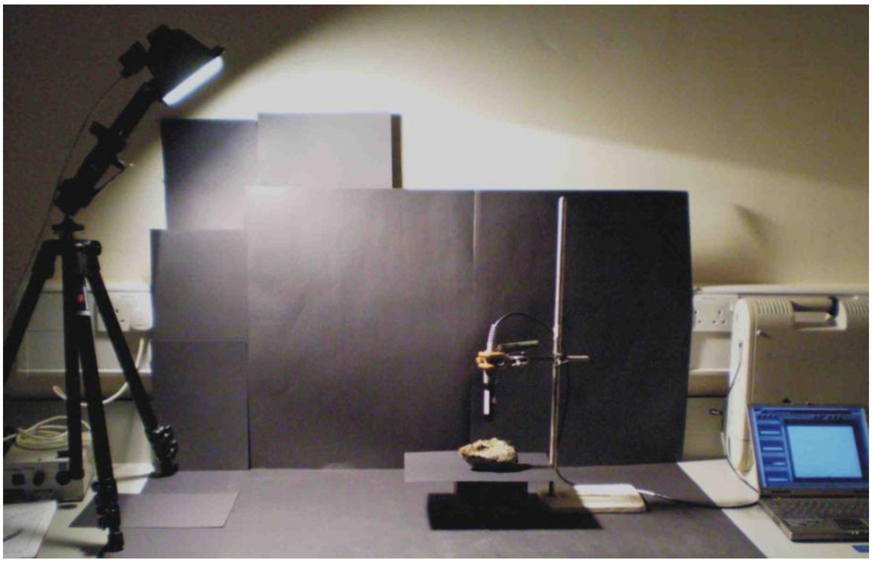

Fig. 4.3. Configuration used to acquire lithological sample spectra in a laboratory with an ASD FieldSpec® Pro.

The laboratory configuration used to acquire the rock spectra is shown in Fig. 4.3. Spectral measurements were acquired using a foreoptic with an 18° Field of View, which was connected to the instrument's fibre optic cable via a pistol grip. A clamp stand was used to hold the pistol grip securely above the sample with the foreoptic directed to nadir. The average distance between each sample and the fibre optic sensor head was 15 cm, resulting in a footprint of approximately 5 cm in diameter and the analysis of a surface area of 18 cm^2 for all spectral measurements. The ASD FieldSpec® Pro unit was connected to a laptop computer and operated using the RS^3 software that is supplied with the instrument. Samples were illuminated with a 500 W tungsten-halogen lamp mounted on an adjustable camera tripod. In order to try to ensure that only light reflected from the samples was detected by the spectroradiometer, black card was used to cover the desk and walls surrounding the setup. The ASD FieldSpec® Pro was left running at least 60 minutes prior to data acquisition to enable the three detector arrays (one covering the VNIR region and two for the SWIR) to reach constant working temperatures. Failure to allow adequate time for the instrument to warm-up can result in significant spectral steps at wavelengths associated with the detector overlap regions at 1.0 μm and 1.8 μm. Similarly, the tungsten-halogen light source was switched on at least 30 minutes prior in order to achieve a stable illumination condition throughout data acquisition. Care was also taken to ensure that the entire Field of View was only occupied by the sample surfaces during data acquisition and that all sample surfaces were free from shadows cast by the foreoptic. With regards to the Field of View, a simple test involved placing a piece of plain white paper at the edges of samples, with no observed change in the reflectance spectrum indicating a Field of View occupied entirely by the sample.

In total, approximately 250 reflectance spectra of fresh and weathered rock surfaces and soil samples were acquired using the laboratory setup. To enable a set of representative spectra to be derived for the lithologies, an average of six spectra were recorded for each individual sample. These spectra were acquired for different configurations of sample orientation and illumination angle (i.e., elevation angles of ~50° and ~65°) in order to help determine a bulk rock spectrum that accounts for spectral variations caused by heterogeneity in both the surface mineralogy and micro-topography. For every 3–5 sample measurements a reference spectrum was acquired using a calibrated Spectralon panel (NERC FSF: SRT#005). Therefore, initially each sample reflectance spectrum is measured relative to the Spectralon panel.

4.2.1.3 Post-processing of spectra

All spectra were first converted from default RS$^{3™}$ file format to ASCII format using the ASD ViewSpec Pro™ software, which is also pre-installed on the laptop.

Next, the relative reflectance spectra of the samples were converted to absolute reflectance using the NERC FSF White Reference Template file in Microsoft Office Excel 2007. Macros within the template are designed to import the absolute reflectance values of the calibrated Spectralon panel in ASCII format and then use this information to convert the sample spectra from relative to absolute reflectance. The output of the conversion process is the absolute reflectance of each sample between 0.35 μm and 2.50 μm at 1 nm resolution.

Following conversion to absolute reflectance, all spectra were first grouped — where appropriate — into fresh and weathered surface spectra for each sample. Next, spectra relating to only completely vegetation-free (i.e., lichen-free) surfaces were selected, while the spectra of surfaces covered by any visible proportion of vegetation were discarded from further analysis during this particular stage of the study. The vegetation-related spectra were excluded to ensure that the observed spectral characteristics were only associated with the elemental and mineralogical composition of the lithological units. A single spectrum representative of each surface type (fresh and weathered) of each lithological unit was then derived by grouping and averaging the corresponding sets of vegetation-free spectra.

4.2.1.4 Interpreting the spectra

In order to interpret the representative spectra in terms of their mineralogy, laboratory spectra of minerals that are important constituents of each lithological unit (Table 4.1) were selected, predominantly from the United States Geological Survey (USGS) mineral spectral library (Clark et al., 1993), for comparison. However, identification of the individual constituent minerals through direct recognition of mutual diagnostic absorption features is somewhat difficult because the rock spectra are products of the combination of all their constituent mineral spectra. In order to identify specific diagnostic features by their wavelength positions and shape, they must be isolated from other effects in the spectrum (Clark et al., 2003). An example of a common effect from which diagnostic features require isolation is that of wavelength-dependent scattering; this becomes significant when the dimensions of scattering centres are on the order of or less than the wavelength of the incident radiation (Morris et al., 1982). The effect of wavelength-dependent scattering is the impartation of a slope to the spectrum, which modifies the appearance of absorption features by causing shifts in the wavelength position of their reflectance minima (Wendlandt & Hecht, 1966; Morris et al., 1982). In addition, weak diagnostic absorption features may become inconspicuous if a significant slope is imparted to the spectrum (Clark & Roush, 1984). The removal of such effects and consequential isolation of diagnostic absorption features can be achieved using a technique called continuum removal (Clark, 1981).

Table 4.1. Important constituent minerals of the lithological units as determined in section 2.2.2.2 based on petrological descriptions by Gass (1960).

Lithological unit	Constituent minerals
Basal Group	Quartz, albite, diopside, epidote, actinolite, chlorite, calcite, goethite (limonite), magnetite, hypersthene, andesine and labradorite
Pillow Lavas	Labradorite, andesine, diopside, magnetite, quartz, opal, calcite, chlorite, celadonite, goethite (limonite), natrolite, olivine, hematite, montmorillonite and analcime
Lefkara Formation	Calcite, aragonite, illite, chlorite, kaolinite, montmorillonite, chalcedony and quartz
Alluvium–colluvium	Mineralogy should reflect that of parent Lefkara Formation, pillow lavas and fanglomerate rock types, with minor variations due to weathering.

Continuum removal (or Hull quotient determination) is based on the concept that a spectrum consists of two components: individual diagnostic features and the "background absorption" or continuum onto which these diagnostic absorption features are superimposed (Clark, 1999). It is this continuum that represents the undesired effects (e.g., wavelength-dependent scattering) that we wish to remove from the reflectance spectrum. Accordingly, by defining and then removing this continuum, diagnostic absorption features can be isolated, thus potentially enabling the identification of individual constituent minerals.

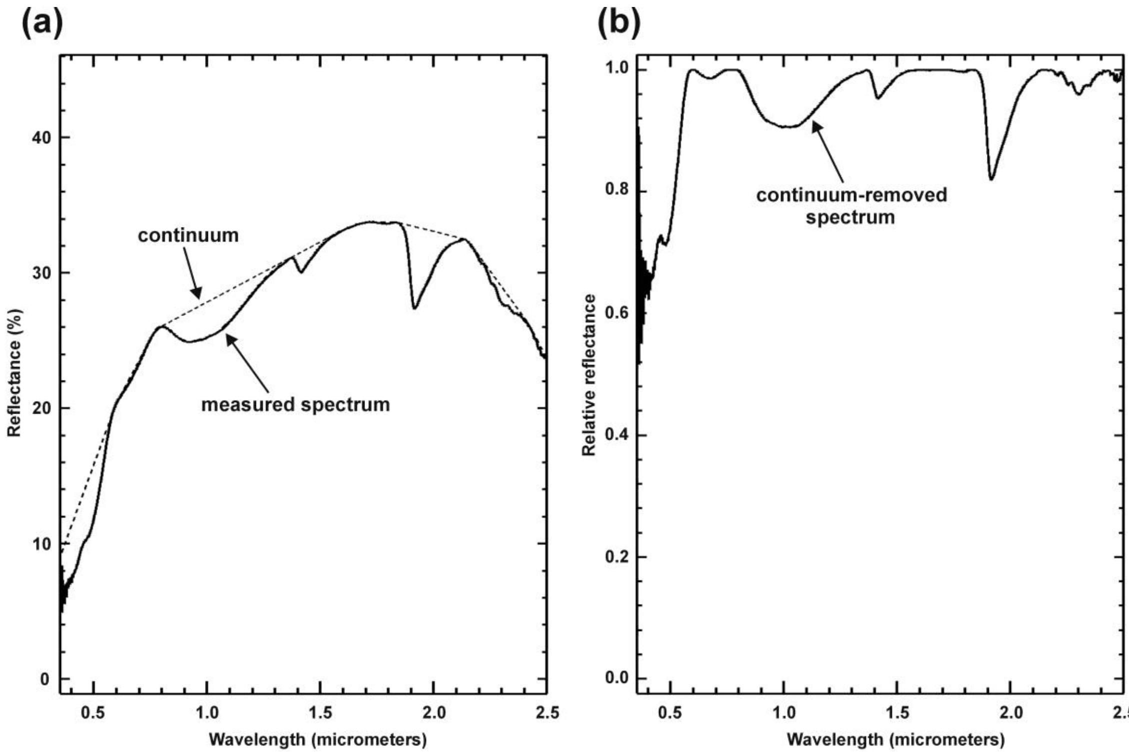

Fig. 4.4. Example of the continuum removal technique applied to a Basal Group reflectance spectrum. **(a)** Definition of the "background absorption" or continuum of the measured spectrum and **(b)** continuum-removed spectrum enhancing weak spectral absorption features.

Continua are defined by fitting a mathematical function — usually straight-line segments — between local reflectance maxima that typically occur on either side of diagnostic absorption features (Fig. 4.4a; Crowley et al., 2003). Since absorption and scattering processes represented by continua have a multiplicative effect on reflectance spectra (Clark & Roush, 1984), the continuum is removed from a reflectance spectrum using (Clark et al., 2003):

$$O_c(\lambda) = \frac{O(\lambda)}{C_o(\lambda)}, \tag{4.1}$$

where $O(\lambda)$ is the observed spectrum as a function of wavelength, λ, $C_o(\lambda)$ is the continuum for the observed spectrum and $O_c(\lambda)$ is the continuum-removed spectrum. In addition to enhancing the appearance of weak diagnostic absorption features (Fig. 4.4b), continuum removal corrects the wavelength position of reflectance minima to the true centre of absorption features with consistent associated bandwidths, and reduces the effects of lighting geometry, as well as variations in grain size and impurity concentration (Clark & Roush, 1984; Clark et al., 2003; Crowley et al., 2003). Application of the continuum removal technique therefore enables spectral features in the representative spectra and mineral library spectra to be reliably compared, subsequently improving the capability to identify individual constituent minerals. The continuum removal technique and comparison with select mineral library spectra were undertaken using ENVI software.

4.2.2 Results and discussion

Representative reflectance spectra for the four main lithologies found within the study area are shown in Fig. 4.5. An initial detailed visual inspection of the igneous rock reflectance spectra reveals that these concur with the equivalent *in situ* SWIR (1.30–2.50 μm) measurements made by van der Meer et al. (1997) — see Fig. 4.2. Specifically, the "Pillow lava A (weathered)" spectrum measured here matches that of the "Upper Pillow Lavas", while the spectra for "Pillow lava B (weathered)" and "Basal Group (weathered)" closely resemble those of the "Lower Pillow Lavas" and "Basal

Group", respectively. In contrast to the work of van der Meer et al. (1997), the main spectral characteristics of these igneous rocks, and additionally the sedimentary units, are described in detail in the following sub-sections for the VNIR to SWIR (0.35–2.50 μm) wavelength region. The continuum-removed spectra of the four lithologies utilised for this purpose are shown in Fig. 4.6, while mineral library laboratory reflectance spectra and continuum-removed spectra of their important constituent minerals are shown in Figs. 4.7–4.10. The wavelength positions of the main spectral absorption features observed in the continuum-removed spectra of the four lithological units are presented in Table 4.2.

Table 4.2. Main spectral absorption features observed in the continuum-removed spectra.

Lithological unit		Wavelengths of spectral absorption features (μm)
Basal Group		$0.47^{F,W}$, $0.55^{F,W}$, $0.65^{F,W}$, 0.92^{W}, 0.99^{F}, 1.10^{W}, $1.41^{F,W}$, $1.92^{F,W}$, 2.20^{F}, 2.25^{F}, $2.30^{F,W}$, $2.35^{F,W}$, 2.40^{F}
Pillow Lavas	A	$0.47^{F,W}$, $0.55^{F,W}$, $0.68^{F,W}$, 0.97^{F}, $1.16^{F,W}$, $1.42^{F,W}$, $1.46^{F,W}$, $1.91^{F,W}$, 1.98^{W}, 2.16^{W}, $2.21^{F,W}$, $2.34^{F,W}$
	B	$0.48^{F,W}$, $0.55^{F,W}$, 0.67^{W}, $1.00^{F,W}$, $1.42^{F,W}$, $1.91^{F,W}$, 2.16^{W}, 2.21^{F}, 2.26^{W}, $2.30^{F,W}$, 2.34^{W}
Lefkara Formation		0.48^{W}, $0.58^{F,W}$, $1.42^{F,W}$, $1.46^{F,W}$, $1.91^{F,W}$, $1.98^{F,W}$, $2.21^{F,W}$, $2.25^{F,W}$, $2.30^{F,W}$, $2.34^{F,W}$, $2.49^{F,W}$
Alluvium–colluvium	A	0.48, 0.58, 0.64, 0.97, 1.16, 1.42, 1.46, 1.91, 1.98, 2.22, 2.25, 2.30
	B	0.48, 0.58, 0.91, 1.42, 1.46, 1.91, 1.98, 2.21, 2.25
	C	0.49, 0.55, 1.01, 1.42, 1.46, 1.91, 2.21, 2.30

^{F} feature observed in the fresh spectrum; ^{W} feature observed in the weathered spectrum.

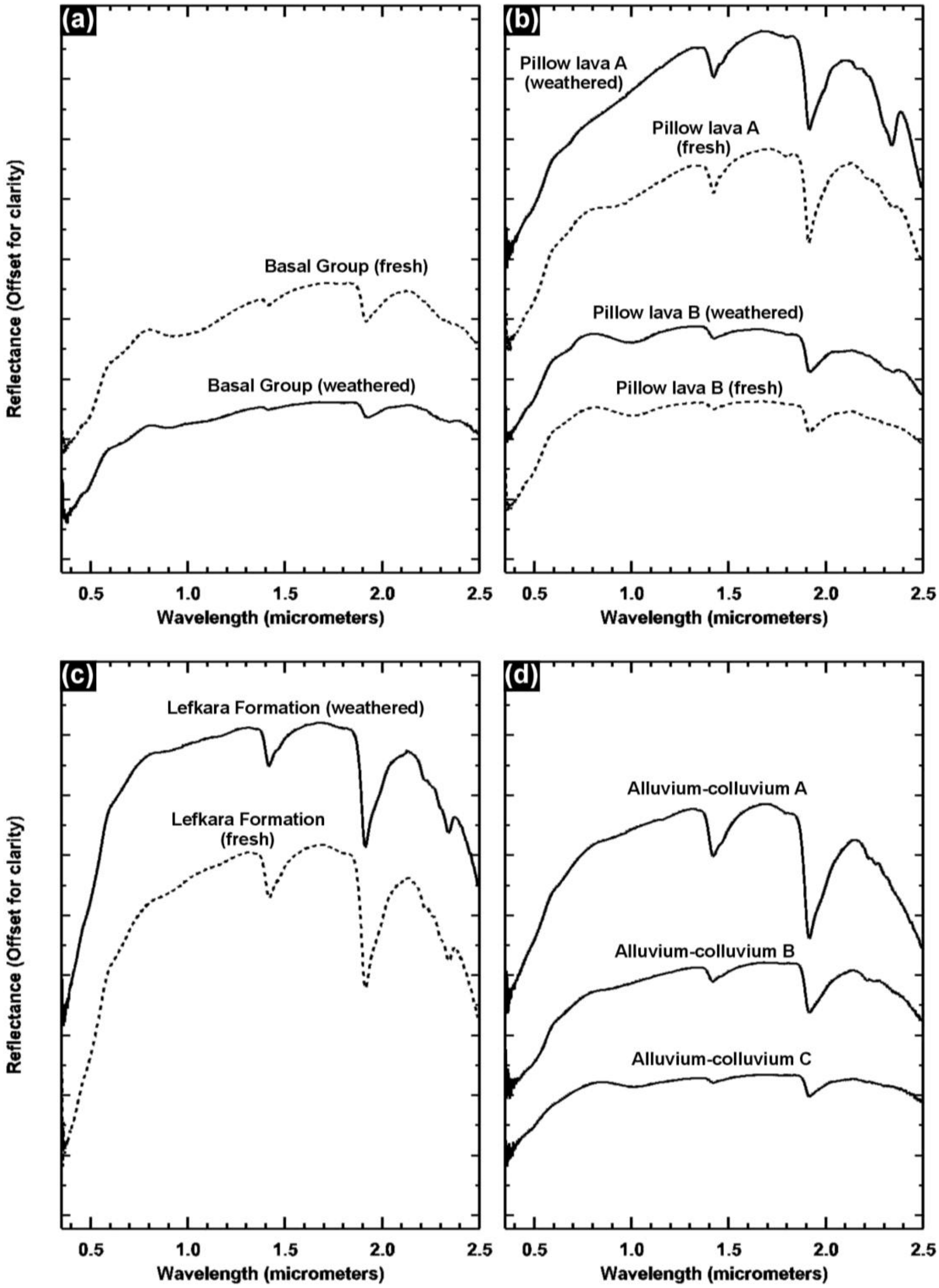

Fig. 4.5. Representative laboratory reflectance spectra of the four main lithologies from within the study area: **(a)** Basal Group, **(b)** pillow lavas, **(c)** Lefkara Formation and **(d)** alluvium–colluvium. Spectra are offset vertically for clarity.

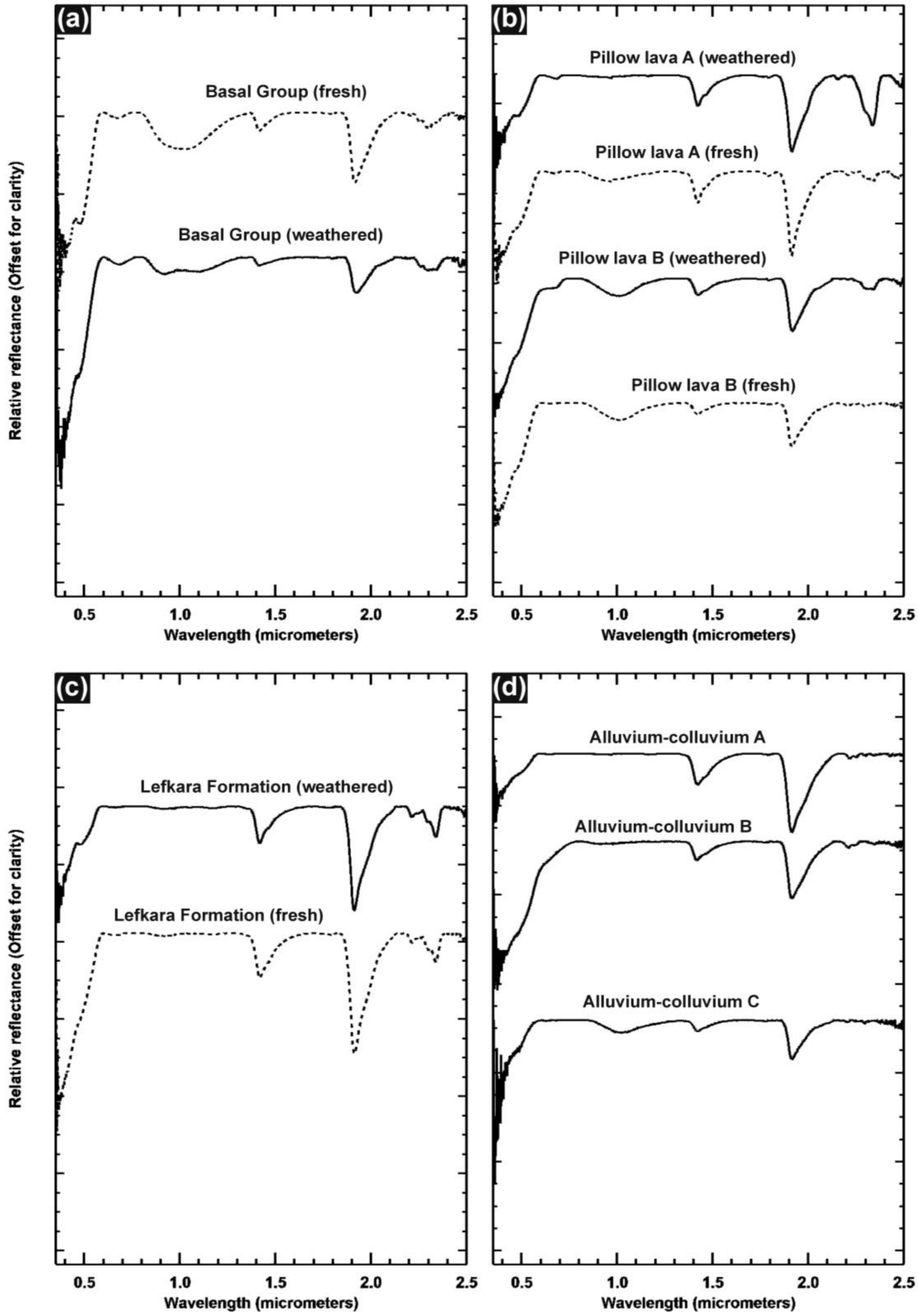

Fig. 4.6. Continuum-removed spectra of the four main lithologies from within the study area: **(a)** Basal Group, **(b)** pillow lavas, **(c)** Lefkara Formation and **(d)** alluvium–colluvium. Spectra are offset vertically for clarity.

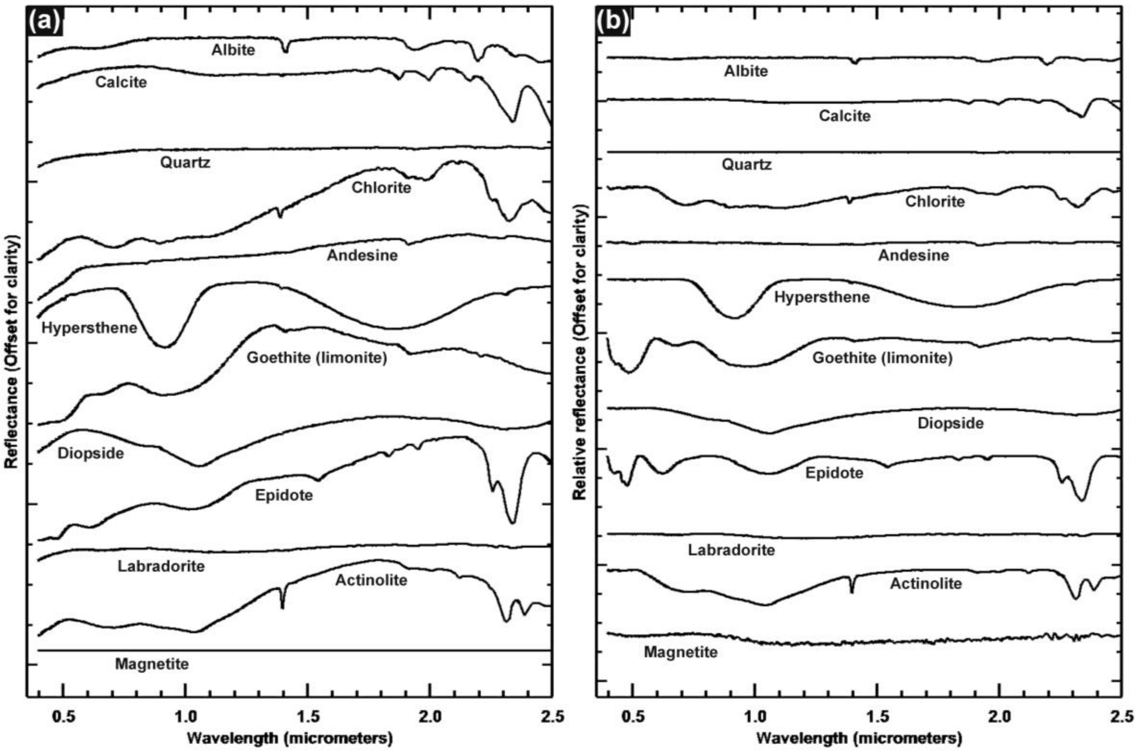

Fig. 4.7. **(a)** Laboratory reflectance spectra and **(b)** continuum-removed spectra of important constituent minerals of Basal Group rocks. All mineral spectra are from Clark et al. (1993). Spectra are vertically offset for clarity.

4.2.2.1 Basal Group

Rocks of the Basal Group typically display low albedo, with fresher surfaces exhibiting a slightly higher albedo than weathered surfaces (Fig. 4.5a). This low albedo is most likely due to the opaque and spectrally featureless minerals such as labradorite and magnetite (Fig. 4.7a), which are commonly observed in Basal Group rocks (Gass, 1960). Numerous spectral absorption features relating to electronic processes are apparent in the VNIR region (Figs. 4.5a and 4.6a). For example, the mutual broad absorption feature at wavelengths less than 0.55 μm — which explains the orange-red colour of the rocks (see Chapter 2, Fig. 2.6) — corresponds to the Fe-O charge-transfer band associated with goethite/limonite (Rothery, 1987). A relatively weak ferric iron (Fe^{3+}) absorption feature at approximately 0.65 μm can also be attributed to goethite/limonite (Fig. 4.7b; Clark et al., 2003). The presence of goethite (limonite) in the Basal Group arises due to the oxidation of fine grained sulphides, such as pyrite (Constantinou, 1972). A weak and narrow absorption feature at 0.47 μm superimposed onto the broader Fe-O charge-transfer band in both the fresh and weathered Basal Group spectra is attributed to a Fe^{3+} crystal-field transition in epidote (Fig. 4.7b; Clark et al., 1990). Broad absorption features are centred near 0.90–1.00 μm in both the weathered and fresh rock reflectance spectra (Fig. 4.5a). However, whilst the fresh continuum-removed spectrum confirms this as a single feature, the weathered spectrum reveals that this actually comprises two separate relatively weak absorption bands, centred near 0.92 μm and 1.10 μm (Fig. 4.6a). Accordingly, these two features in the weathered spectrum may be ascribed to chlorite and its associated ferric (Fe^{3+}) and ferrous iron (Fe^{2+}) absorptions bands, respectively (Fig. 4.7b; King & Clark, 1989). In contrast, the single feature in the fresh spectrum may arise from the mixing of unaltered hypersthene and diopside, whose individual Fe^{2+} absorption features can combine to form a single band near that observed at 0.99 μm (Adams, 1974).

In addition to those features associated with electronic process in the VNIR region, a number of absorption features relating to vibrational processes are also apparent in the SWIR region of the Basal Group spectra (Figs. 4.5a and 4.6a). Of these, the most well-defined are those near 1.41 μm and 1.92 μm, which are due to presence of molecular water. Based on a comparison of the precise wavelength positions of these features to those of common Basal Group rock-forming minerals, it is most likely that this molecular water is associated with the hydration of albite (Fig. 4.7). Furthermore, the presence of albite is corroborated by the appearance of an Al-OH absorption feature near 2.20 μm in the fresh Basal Group spectrum. The prominent absorption band centred on 2.30 μm, and multiple weak absorption features at 2.25 μm, 2.35 μm and 2.40 μm, are probably due to a combination of OH stretching with the Mg-OH bending mode (Hunt, 1977; Rowan et al., 2004). These features indicate the presence of chlorite (Marsh & Mckeon, 1983).

4.2.2.2 Pillow lavas

Two sets of pillow lavas, labelled “Pillow lava A” and “Pillow lava B”, were identified based on a visual comparison of all vegetation-free pillow lava spectra (Fig. 4.5b). Pillow lavas belonging to class “A” exhibit a higher albedo than those of class “B”, with weathered surfaces exhibiting a higher albedo than fresher surfaces in both cases. Nevertheless, both sets of pillow lavas generally have a low albedo again due to an abundance of labradorite and to a lesser extent, magnetite. Numerous spectral absorption features relating to both electronic and vibrational processes are apparent throughout the VNIR–SWIR region (Figs. 4.5b and 4.6b). Features associated with the “Pillow lava A” class will be discussed first, followed by a discussion of those associated with “Pillow lava B” rocks.

In similarity to Basal Group rocks, both fresh and weathered “Pillow lava A” rock surfaces exhibit a broad charge-transfer absorption feature at wavelengths less than 0.55 µm. However, in this case the charge-transfer feature could be associated with Fe-O in hematite (Morris et al., 1985), or a charge-transfer transition in olivine (Fig. 4.8; King & Ridley, 1987, and references therein). Given that it gives rise to the pink colour of the extensive calcite veining (Gass, 1960), hematite is most likely to be responsible for this charge-transfer feature. Hematite is also associated with a Fe^{3+} absorption feature near 0.67 µm (Clark et al., 2003). Superimposed onto the broad charge-transfer feature is a weak absorption near 0.47 µm, which can be ascribed to a ferrous iron (Fe^{2+}) transition in olivine (Burns et al., 1972; King & Ridley, 1987). Concurrent with a broad feature particularly apparent in the fresh “A” spectrum, both montmorillonite and the zeolite analcime exhibit a relatively weak absorption feature centred on 0.97 μm (Fig. 4.8). This feature is attributed to montmorillonite based on its bandwidth, and more specifically, the second overtone of the OH stretch (Clark et al., 1990). A degree of ambiguity also surrounds the origin of absorption features at 1.16 μm and 1.91 μm, as well as a doublet at 1.40–1.48 μm (Fig. 4.6b), which are again typical of both montmorillonite and analcime (Fig. 4.8). Due to their precise wavelength locations, the 1.16 μm absorption and the doublet at 1.40–1.48 μm are most likely to be associated with analcime. The combination of a symmetric OH stretch, an asymmetric OH stretch and an H-O-H bend in bound water is responsible for the 1.16 μm feature (Hunt & Salisbury, 1970; Cloutis et al., 2002), whereas the 1.42 μm and weaker 1.46 μm doublet features are attributed to H_2O stretches plus the first overtone of the H_2O bend in absorbed and bound molecular water, respectively (Bishop et al., 1994; Cloutis et al., 2002). The bandwidth of the absorption feature at 1.91 μm, plus an apparent weak absorption near 1.98 μm in the weathered spectrum, is indicative of combinations of stretching and bending vibrations related to bound and absorbed molecular water in montmorillonite (Bishop et al., 1994). An addition absorption feature at 2.21 μm in both the fresh and weathered spectra is characteristic of a combined Al-OH bend plus OH stretch also in montmorillonite (Hunt, 1977). A weak absorption near 2.16 μm exhibited by weathered surfaces and a stronger broad feature near 2.34 μm, common to both fresh and weathered surfaces, are due to respective combinations and overtones associated with the CO_3^{2-} ion in calcite (Hunt, 1977).

The overall appearance of the “Pillow Lava B” spectra (Figs. 4.5b and 4.6b) closely resemble that of the Basal Group spectra (Figs. 4.5a and 4.6a). This is unsurprising since the spectra are consistent with that of Lower Pillow Lavas in Fig. 4.2 and that the distinction between the Lower Pillow Lavas and Basal Group is largely based on dyke abundances (Bear, 1960). As with the Basal Group rocks, goethite (limonite) is responsible for the broad Fe-O charge-transfer band at wavelengths less than 0.55 μm in the spectra of both fresh and weathered surfaces (Fig. 4.9; Hunt, 1977). A weak crystal-field transition at 0.48 μm and an additional stronger ferric iron (Fe^{3+}) transition at 0.67 μm in the weathered spectrum are also associated with goethite/limonite (Crowley et al., 2003). Both fresh and weathered "Pillow lava B" spectra exhibit a broad feature centred on 1.00 μm. This is likely to be a combination feature of a Fe^{2+} crystal-field transition in clinopyroxene (diopside in this case) and a Fe^{3+} transition in goethite/limonite (Singer, 1981). The molecular water absorption features observed at 1.42 μm and 1.91 μm appear to have a much smaller band depth than those exhibited by the "Pillow lava A" rocks. Since weathering enhances these water absorption bands (van der Meer et al., 1997), "Pillow lava A" rocks probably exhibit a greater band depth because they have generally been exposed to more prolonged weathering due to their higher stratigraphic position. Opal amygdales are the most likely source of water in class "B" pillow lava rocks, since the observed water bands are consistent with those linked to combinations and overtones of isolated water in opal (Goryniuk et al., 2004). A weak absorption feature in the weathered spectrum at 2.16 μm appears to be linked to a combination of overtones of CO_3 fundamentals in calcite (Hunt, 1977). Also only observed in the weathered surface spectrum is an absorption triplet comprised of weak features at 2.26 μm, 2.30 μm and 2.34 μm. Such features are characteristic of celadonite and are attributed to combinations of Al,Fe,Mg-OH absorptions (Bishop et al., 2008). Fresher surfaces, on the other hand, exhibit an absorption feature at 2.21 μm with an associated feature at 2.30 μm. These features may be due to an Al-OH bend and OH stretch combination in dioctahedral phyllosilicates (Hunt & Ashley, 1979), and are possibly attributable to dioctahedral chlorite.

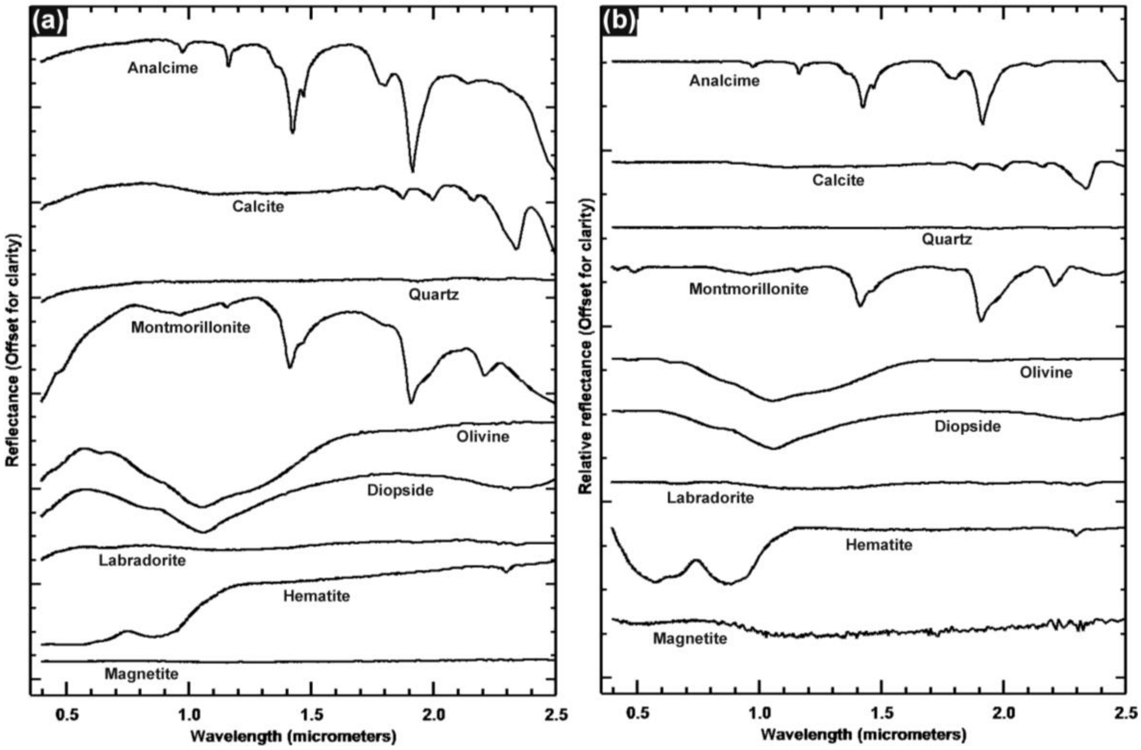

Fig. 4.8. **(a)** Laboratory reflectance spectra and **(b)** continuum-removed spectra of important constituent minerals of "Pillow lava A" rocks. All mineral spectra are from Clark et al. (1993). Spectra are vertically offset for clarity.

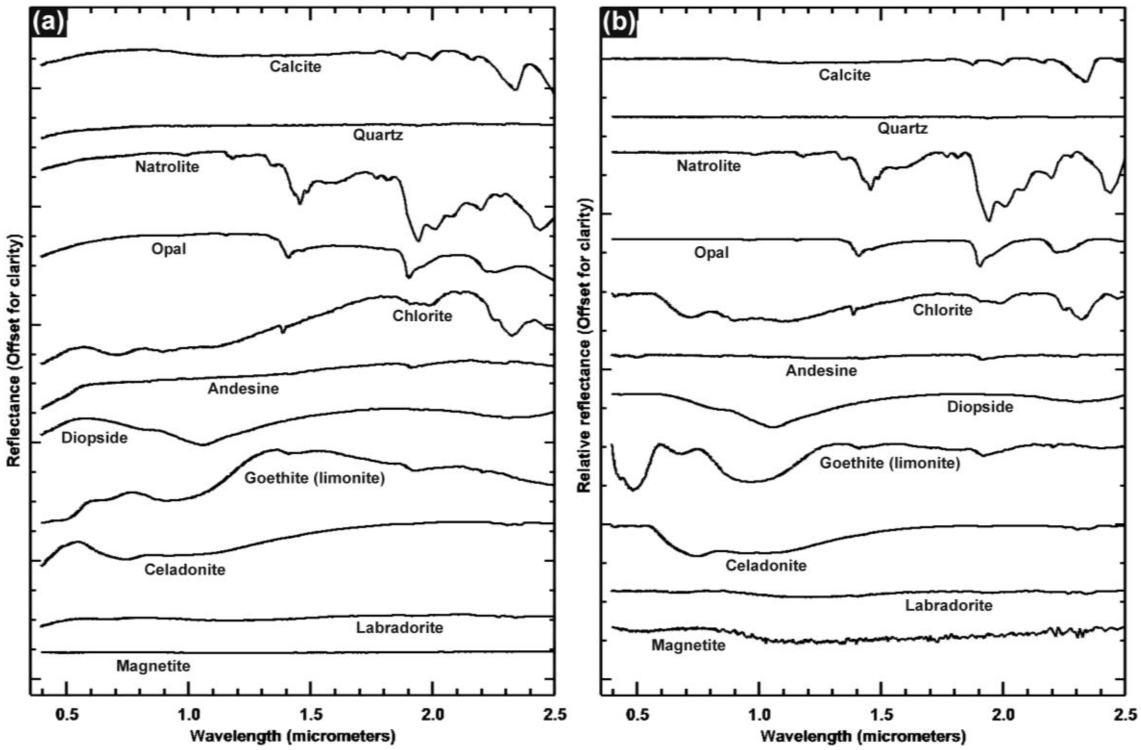

Fig. 4.9. **(a)** Laboratory reflectance spectra and **(b)** continuum-removed spectra of important constituent minerals of "Pillow lava B" rocks. All mineral spectra are from Clark et al. (1993), with the exception of celadonite (Bishop et al., 2008). Spectra are vertically offset for clarity.

4.2.2.3 Lefkara Formation

In contrast to the igneous magnetite-bearing rocks of the Basal Group and pillow lavas, Lefkara Formation rocks exhibit a high albedo with a negligible difference between fresh and weathered surfaces (Fig. 4.5c). The high albedo is due to the predominantly carbonate nature of the rocks, in particular the presence of minerals such as calcite and aragonite (Fig. 4.10a).

As with all preceding lithologies, the Lefkara Formation spectra display a drop-off in reflectance at wavelengths less than 0.58 μm (Fig. 4.5c and 4.6c). A weak absorption feature is also visible at 0.48 μm in the spectra of weathered surfaces, although there is a very subtle hint of a similar feature in the fresh spectrum. As previously discussed, such features usually indicate the presence of iron. Pink cherts commonly observed proximal to the igneous rocks are just one potential source of this iron (Gass, 1960). In this case, these features are probably associated with the weathering of iron to form either an iron oxide or oxyhydroxide as they are more apparent in the spectrum of weathered surfaces. The well-defined water absorption features observed near 1.42 μm (doublet) and 1.92 μm (weak doublet) reflect considerable weathering of the Lefkara unit. Water in the SiO_2 crystal structure (Hunt, 1977) — such as that of chalcedony — could contribute to these features (Fig. 4.10b). However, the presence of doublets near 1.42 μm and 1.92 μm and their precise composite feature wavelength positions suggest that bound and absorbed molecular water in montmorillonite is more attributable (Bishop et al., 1994). Several weaker absorptions are superimposed onto a broad absorption feature observed between 2.19–2.38 μm in both the fresh and weathered spectra. The broad feature, which has a reflectance minimum at 2.34 μm, together with an associated feature near 2.50 μm represent combination and overtone bands of the CO_3 fundamentals (Clark et al., 1990) and are thus attributed to minerals such as aragonite and calcite. The clay component of the marls in the Lefkara Formation is likely to mostly comprise common clay minerals such as kaolinite, illite and montmorillonite. All three of these minerals exhibit a common Al-OH feature at 2.21 μm (Clark et al., 1990; Bishop et al., 2008) and so the corresponding feature in both the fresh and weathered Lefkara Formation spectra is attributed to clay minerals such as these. The moderate absorption features observed at 2.25 μm and 2.30 μm are characteristic of chlorite (Marsh & Mckeon, 1983).

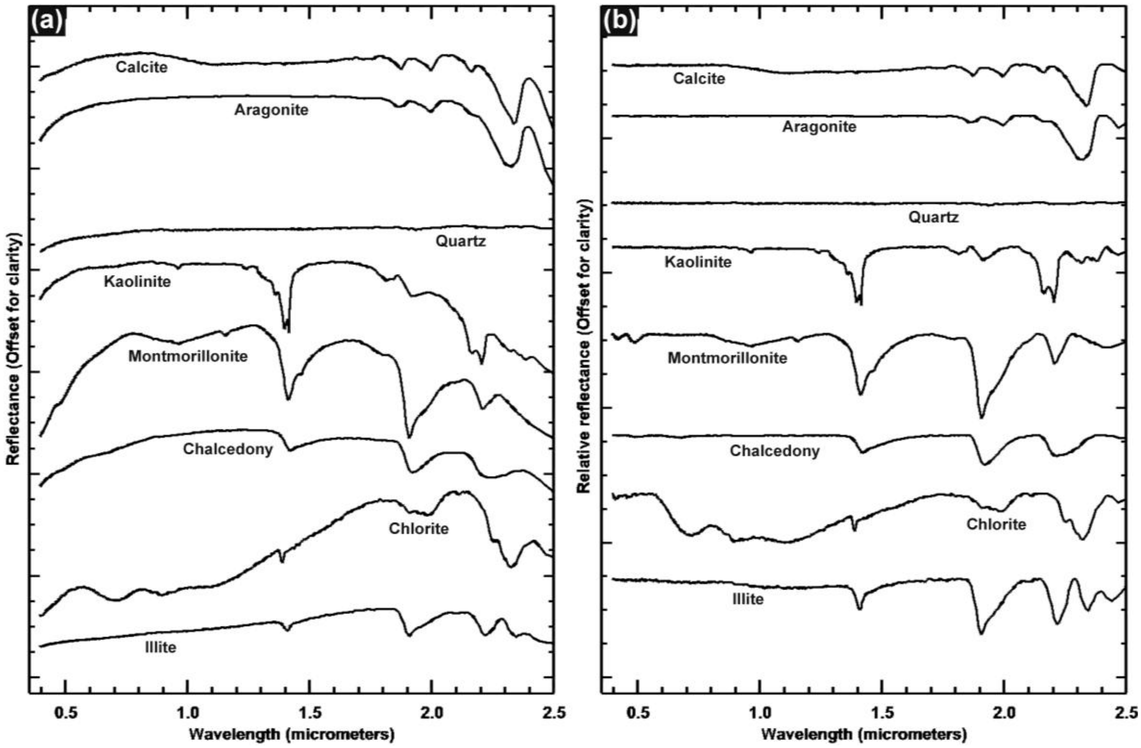

Fig. 4.10. **(a)** Laboratory reflectance spectra and **(b)** continuum-removed spectra of anticipated constituent minerals of Lefkara Formation rocks. All mineral spectra are from Clark et al. (1993), except aragonite which was acquired by Susan J. Gaffey with the NASA RELAB facility at Brown University. Spectra are vertically offset for clarity.

4.2.2.4 Alluvium–colluvium

The three different types of alluvium–colluvium shown in Figs. 4.5d and 4.6d are representative of regolith material derived from the Lefkara Formation (type "A"), fanglomerate (type "B") and pillow lavas (type "C"). Type "A" alluvium–colluvium exhibits a moderate albedo that considerably higher than that of the two other types, while that of type “B” is slightly higher than that of type “C”.

As anticipated, the overall appearance of the spectrum that is representative of Lefkara-derived alluvium–colluvium is generally similar to that of its parental rock type (Figs. 4.5c and 4.6c). However, the most noticeable differences between the two are the significantly lower albedo of the “Alluvium–colluvium A” spectrum in addition to the absence of the broad 2.19–2.38 μm absorption and associated feature at 2.50 μm. These observed spectral differences suggest that weathering processes are responsible for the removal of CO_3 minerals during the formation of this regolith material. Therefore, the spectrum of the derived “Alluvium–colluvium A” regolith only exhibits the Lefkara Formation absorption features previously attributed to the clays and iron. In comparison to the Lefkara Formation, additional absorption features occur at 0.64 μm, 0.97 μm and 1.16 μm. The first of these features is attributed to the presence of iron (Clark et al., 2003), whereas the second and third features are associated with water in clays (Hunt & Salisbury, 1970; Goetz et al., 1991).

Material of the “Alluvium–colluvium B” type are continental fanglomerates that are generally derived from heterogeneous mixtures of the igneous rocks (Gass, 1960). Although this definition suggests a potentially diverse set of constituent minerals for this type of material, its spectrum exhibits several familiar absorption features linked to the presence of iron and clays. An absorption feature near 0.48 μm, superimposed onto a broad charge-transfer band at wavelength less than 0.58 μm, together with an additional absorption at 0.91 μm are typical ferric iron features of goethite (limonite). Bound and absorbed water in clays (e.g., montmorillonite) is probably responsible for absorption doublets observed near 1.42 μm and 1.92 μm. A prominent absorption near

2.21 μm and an addition associated weak feature near 2.25 μm resemble Al-OH absorptions in illite (Clark et al, 1990).

As previously mentioned, the regolith of “Alluvium–colluvium C” is derived from pillow lava rocks, so it is therefore no surprise that there are considerable similarities in their spectra, particularly those of “Alluvium–colluvium C” and “Pillow lava B”. In fact, the main absorption features present in both pillow lava spectra and absent from that of type “C” alluvium–colluvium are those relating to combinations and overtones of CO_3 fundamentals in calcite. The apparent absence of calcite in the regolith is once again likely to be a result of carbonate weathering processes. Consequently, the “Alluvium–colluvium C” spectrum comprises absorption features attributed to ferric iron in goethite/limonite (0.48 μm and 0.55 μm), a mixture of ferric and ferrous iron in diopside and goethite/limonite respectively (1.01 μm), and both molecular water (1.42 μm, 1.46 μm and 1.91 μm) and Al-OH (2.21 μm and 2.30 μm) absorptions in dioctahedral clay minerals.

4.3 Lithological mapping using ATM imagery

The acquisition and subsequent analysis of the representative VNIR–SWIR reflectance spectra in the previous section suggests that the four main lithologies found in the study area should be directly spectrally discernable because of differences in their albedo and absorption features. Accordingly, this section assesses the ability to directly identify and map the spatial distributions of the lithological units in the study area, by using their corresponding representative laboratory reflectance spectra in conjunction with the ATM imagery. To do this, a conventional direct mapping approach is adopted, which involves using the representative laboratory spectra as reference (also referred to as end-member) spectra for input to algorithms that can be used to rapidly generate lithological maps by automatically matching ATM pixel spectra to these reference spectra.

4.3.1 Methods

The methodology employed here to assess the ability to directly identify and map the lithologies of the study area comprises three main steps: 1) data calibration, 2) classification and 3) an accuracy assessment. These steps are discussed in detail below.

4.3.1.1 Data calibration

As mentioned above, the representative laboratory reflectance spectra of the lithologies are to be used as reference spectra for input to automated spectral matching algorithms. However, in order to be able to use the representative laboratory reflectance spectra in conjunction with the ATM imagery for lithological mapping, it is first necessary to ensure the compatibility of these two datasets. A two-stage approach was used for this purpose: 1) resampling the laboratory spectra to match the ATM wavebands and 2) subsequent calibration of the ATM imagery to laboratory measured reflectance.

Spectral resampling was undertaken using the Spectral Library Resampling tool in ENVI. This tool performs multiplication-based convolution of all laboratory spectra to the ATM wavebands (bands 2–10) using a filter function file (obtained from NERC FSF), which contains the sensor response (bandpass) of each ATM waveband. The resulting ATM-bandpass convolved laboratory reflectance spectra for the lithological units are shown in Fig. 4.11. Although many of the spectral features have been lost as a result of resampling, some subtle differences still persist between lithologies, particularly in the VNIR region where the majority of ATM bands are situated.

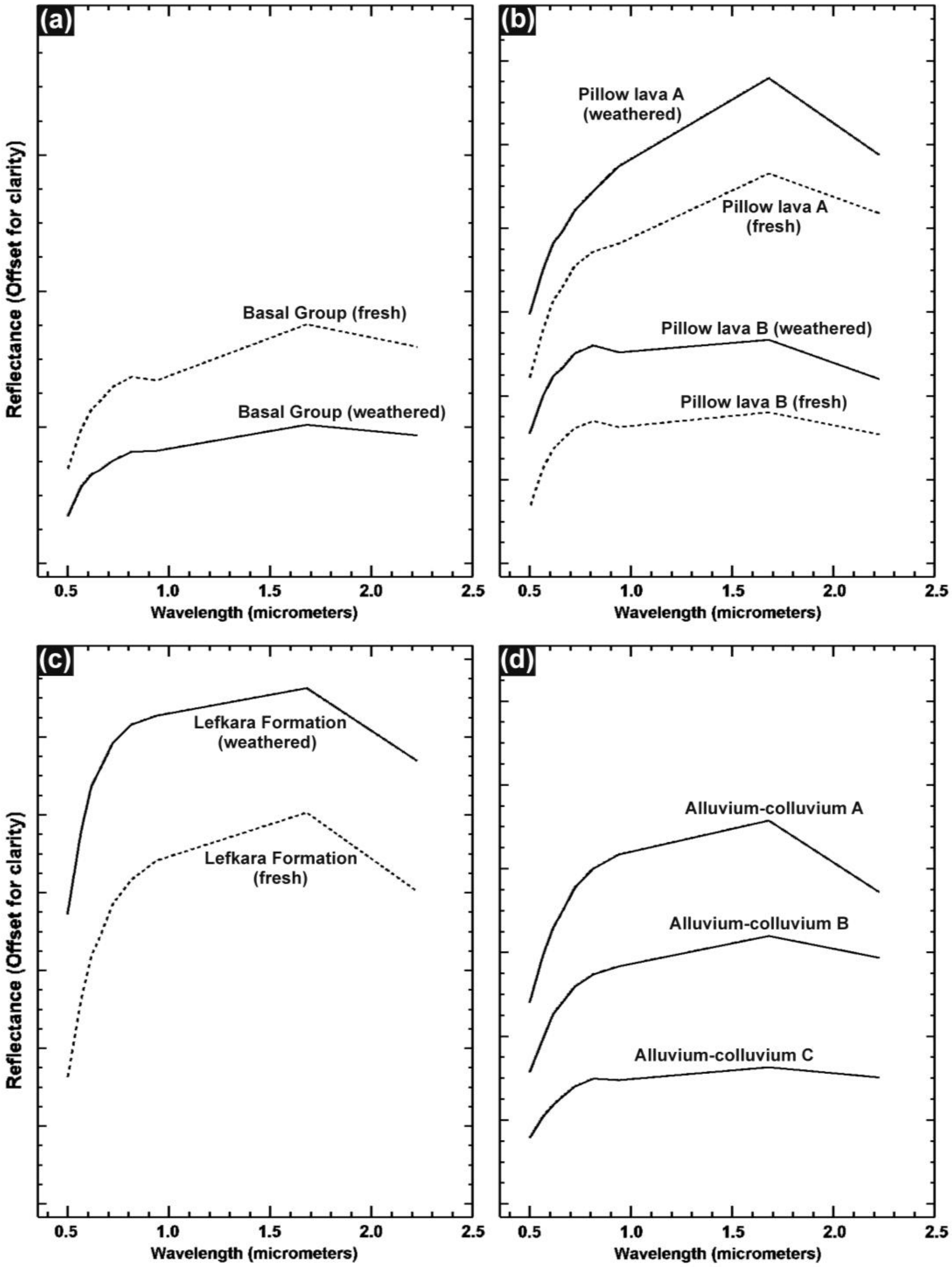

Fig. 4.11. Representative laboratory reflectance spectra of the four lithologies resampled to the ATM bandpasses: **(a)** Basal Group, **(b)** pillow lavas, **(c)** Lefkara Formation and **(d)** alluvium–colluvium. Spectra are offset vertically for clarity.

Calibration of the ATM data to laboratory measured reflectance data is crucial in enabling the ATM-bandpass convolved reflectance spectra (Fig. 4.11) to be used as reference spectra for the lithologies in automated lithological classification routines. Here, this calibration was achieved using the empirical line method (Roberts et al., 1985). The empirical line method performs data calibration by exploiting the linear relationship that exists between digital numbers (DNs) in the imagery and the reflectance of a variety of ground surfaces (Baugh & Groeneveld, 2008). Specifically, the relationship between DNs and reflectance is given as (Ferrier & Wadge, 1996):

$$\mathrm{DN}_b = \rho(\lambda) A_b + B_b \,, \tag{4.2}$$

where DN_b is the DN for a given pixel in band b, $\rho(\lambda)$ is the reflectance of the surface within that pixel at wavelength λ of band b, A_b is the gain term for band b (accounting for multiplicative effects including atmospheric transmittance and instrumental gains) and B_b is the offset term for band b (accounting for effects including atmospheric path radiance and instrumental offsets).

The empirical line calibration method is implemented separately on each ATM band by plotting the measured reflectance of a variety of ground materials against their corresponding DNs, which are extracted from the imagery. For each band, a best-fit line is then fit to these data points using a least squares fitting approach, with the band gain and offset corresponding to the gradient and intercept of this line, respectively (Ferrier & Wadge, 1996). These gains and offsets are then applied to the ATM imagery to calibrate it to laboratory measured reflectance. Although as few as two ground surfaces with contrasting albedos can be used to perform the calibration (e.g., Ferrier, 1995; van der Meer & Bakker, 1997), the relationship between radiance and reflectance is better characterised when more surfaces are used (Smith & Milton, 1999). Nevertheless, several studies have reported accurate calibration results using only 2–4 different surfaces (e.g., Price et al., 1995; Smith & Milton, 1999).

In this study, three calibration sites situated within relatively large areas of homogeneous surface composition were identified during the rock and soil sampling fieldwork. During selection of these sites, care was taken to ensure that the surfaces could reasonably be assumed to have essentially remained unchanged in the time between the ATM data acquisition and measurement of their reflectance (~4 years). The selected sites corresponded to three contrasting surface types: Lefkara Formation, predominantly bare pillow lavas and pillow lavas with well-established and extensive lichen growth. The laboratory reflectance of these sites was established by averaging the spectra of the exposed surfaces of all samples collected within the 3 m radius of their recorded GPS positions. These three surface spectra were subsequently convolved to the ATM bandpasses. Pixels corresponding to these sites were identified by overlaying their GPS locations on top of the ATM imagery. Due to these sites being located well within relatively large homogeneous areas, the single pixel spectra extracted for the precise sampling locations displayed negligible spectral differences to those of their neighbouring pixels. Therefore, since the adjacency effects were insignificant, the ATM pixel spectra were extracted as an average of the pixel spectra within a 2×2 pixel neighbourhood of each sampling location. Extracting the pixel spectra as an average of their neighbouring pixels helps to generate more representative spectra by minimising any minor noise component that may be associated with the ATM sensor (Smith & Milton, 1999). Empirical line calibration of the ATM imagery to laboratory reflectance was implemented in ENVI by pairing the ATM-convolved laboratory reflectance spectra of the three surfaces with their corresponding ATM pixel spectra.

As a robust independent test of the validity of the ATM data calibration, ATM pixel spectra extracted from areas corresponding to green and dry grass were compared with ATM-convolved laboratory reflectance spectra of generic green and dry grass from the USGS spectral library (Fig. 4.12). In both cases there is a remarkable similarity between the ATM pixel spectra and USGS laboratory spectra, signifying that the calibrated ATM imagery is compatible with laboratory reflectance measurements. Thus, the ATM-bandpass convolved laboratory reflectance spectra of the lithological units are now deemed suitable for use as reference spectra for the classification of the calibrated ATM imagery.

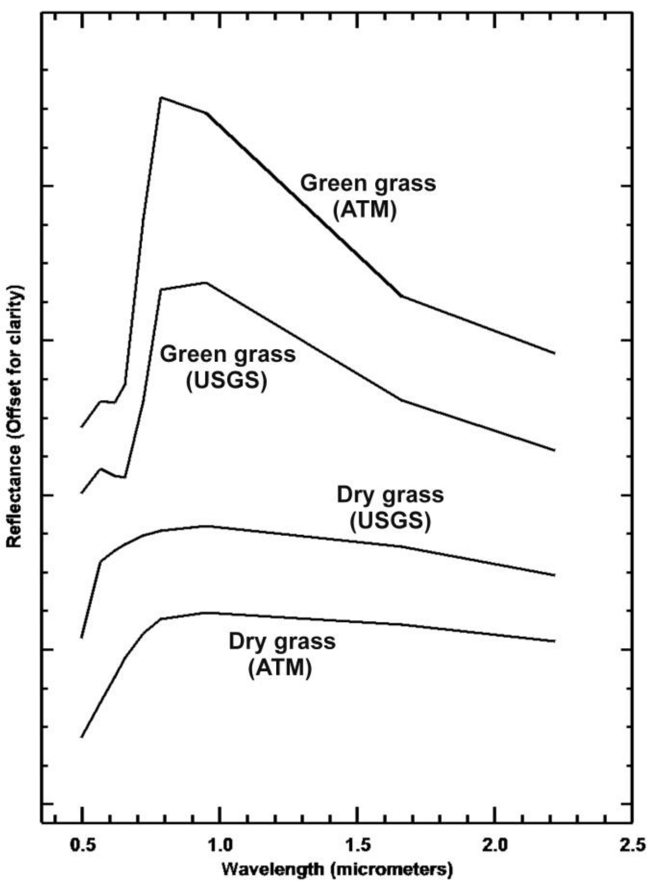

Fig. 4.12. Comparison of empirical line calibrated ATM pixel spectra extracted from areas comprising green and dry grass with ATM-convolved USGS laboratory reflectance spectra of green and dry grass. USGS spectra are from Clark et al. (1993). Spectra are offset vertically for clarity.

4.3.1.2 Spectral classification

Lithological maps were generated through classification of the calibrated ATM imagery according to lithological reference spectra in the form of the ATM-convolved laboratory reflectance spectra (Fig. 4.11). Spectral classification was performed using three spectral matching algorithms that are popular for geological mapping applications and commonly embedded in remote sensing software packages (such as ENVI): Spectral Angle Mapper, Matched Filtering and Mixture-Tuned Matched Filtering.

The Spectral Angle Mapper (SAM) algorithm (Kruse et al., 1993) calculates the spectral similarity between a pixel spectrum and a reference spectrum as the angle between their vectors in a space with dimensionality equal to the number of bands. This 'spectral angle' (α) is calculated as:

$$\alpha = \cos^{-1}\left(\frac{t \cdot r}{\|t\|\|r\|}\right), \tag{4.3}$$

which can also be written as:

$$\alpha = \cos^{-1}\left(\frac{\sum_{i=1}^{nb} t_i r_i}{\left(\sum_{i=1}^{nb} t_i^2\right)^{\frac{1}{2}}\left(\sum_{i=1}^{nb} r_i^2\right)^{\frac{1}{2}}}\right), \tag{4.4}$$

where t is the pixel spectrum, r is the reference spectrum and nb is the number of bands. The SAM algorithm is insensitive to gain factors related to topographic and illumination effects as these only alter the lengths of the vectors and not the angle between them (van der Meer et al., 1997).

For each reference spectrum, the SAM algorithm calculates the spectral angle (in radians) for every image pixel spectrum and assigns this value to the corresponding pixel in a grey-scale SAM output rule image (Kruse et al., 1993). Here, given the number of reference spectra, a total of 11 output rule images were generated with pixels in each image having a spectral angle ranging between 0 and $\pi/2$, signifying a perfect match to that particular reference spectrum and no match, respectively. As in van der Meer et al. (1997), the pixels that most closely matched each reference spectrum were extracted by applying a 0–0.16 rad threshold (i.e., pixels within 10% of a perfect match) to the corresponding output rule image. Pixels extracted from each output rule image were assigned a unique colour and merged to form a single image. If pixels were extracted from multiple output rule images (i.e., within a 10% match of multiple reference spectra), they were assigned to the lithological class for which they had the smallest spectral angle. A lithological map of the four main units was generated by combining classes representing both fresh and weathered surfaces and different types of the same lithological unit (e.g., “Pillow Lava A” and “Pillow Lava B”).

The Matched Filtering (MF) algorithm is an orthogonal subspace projection operator (Harsanyi & Chang, 1994), which is capable of identifying subpixel abundances of end-members through partial unmixing of image pixel spectra (Harris et al., 2005). The algorithm — which utilises the Minimum Noise Fraction (MNF) Transformation (Green et al., 1988) — first simultaneously maximises the spectral response of the target end-member in each image pixel whilst suppressing that of the interfering background materials, and then calculates an MF score by comparing the enhanced spectra to that of the end-member reference spectrum (Rowan et al., 2004). Specifically, MF scores are determined for each pixel by projecting a matched filter vector (reference spectrum in MNF space) onto the inverse covariance of the MNF-transformed image data, and then normalising it to the magnitude of the reference spectrum so that the length of the matched filter vector corresponds to an estimate of the end-member abundance, ranging from 0–100% (Mundt et al., 2007). The resulting MF scores are normally distributed around a mean of 0, with scores of 0 or less corresponding to the background materials and scores near to 1 representing a close match to the reference spectrum (Mundt et al., 2007; Mitchell & Glenn, 2009).

The output of the MF algorithm is the generation of grey-scale MF score images for each of the 11 reference spectra. Pixels representing close matches to each reference spectrum were again extracted by applying a threshold to the relevant MF score images. In keeping with the SAM classification, the threshold for each MF score image was set to extract pixels representing a ≥ 90% match to each of the reference spectra, with pixels extracted from multiple MF score images again assigned to that for which it has the highest MF score. A lithological map was created by merging the colour-coded pixels and then combining the relevant classes as described above.

Mixture-Tuned Matched Filtering (MTMF) is a pixel classifier that captures the synergism of the linear spectral mixing model and MF algorithm (Boardman, 1998). In addition to generating MF score images for each reference spectrum, the MTMF algorithm also generates infeasibility images for each of the MF score images. Values in the infeasibility images indicate the plausibility of the corresponding MF scores, and thus pixels with a high MF score and a low infeasibility value are most likely to be correctly classified (Harris et al., 2006). Feasible close-matching pixels were extracted for each lithological end-member spectrum by thresholding based on the ratio of the MF score to infeasibility value (e.g., Mitchell & Glenn, 2009). Appropriate minimum ratio threshold values were determined for each lithological end-member by generating a scatter plot of MF score vs. infeasibility value and then identifying typically MF scores and infeasibility values for a small subset of points known to correspond to that particular lithology. Only pixels equal to or greater than the specified ratio threshold value for each lithological end-member were extracted. Thresholding according to such a ratio enables pixels with MF scores (or end-member abundances) lower than those used as thresholds in the MF algorithm to be extracted, provided that they also have low infeasibility values. A lithological map was generated from the threshold images using the same method as described for the two previous classification routines.

The MNF transformation, utilised by both the MF and MTMF algorithms, is a spectral enhancement and data compression technique (Green et al., 1988). The transformation is used to determine the inherent dimensionality of the data and segregate image noise using two PCA transformations (Boardman & Kruse, 1994). The result is a set of images comprising coherent eigenimages (or MNF bands) associated with large eigenvalues (i.e., signal-to-noise ratios) and noise-dominated eigenimages with small eigenvalues. Spectral enhancement and image noise segregation is effectively achieved by discarding the bands with small eigenvalues and selecting only bands with large eigenvalues. When applied to the 9 bands of the calibrated ATM imagery using a shift-difference noise estimate for the entire scene, 91.6% of the cumulative eigenvalues for the entire dataset was explained by the first 6 (out of 9) MNF bands. Consequently, only the first 6 MNF bands were selected during the implementation of the MF and MTMF algorithms.

4.3.1.3 Accuracy assessment

The accuracy of the derived lithological maps was determined by comparing the true class identities of a sample of validation pixels to those assigned through classification. To enable this, a random stratified sampling protocol was used to select a sample of validation pixels from a number of regions of interest (ROIs) of unambiguous lithological identity. Several ROIs were carefully selected for each lithology throughout the entire study area using extensive field-based knowledge and the Quickbird imagery in combination with the existing geological maps. A random stratified sampling protocol was adopted to ensure that each class was represented proportionately and to avoid spatial autocorrelation within the validation dataset (Chini et al., 2008; Pacifici et al., 2009). The numbers of validation pixels selected for each lithological class are shown in Table 4.3. For a discussion of the individual class validation sample sizes and total validation sample size see Chapter 6 (section 6.4.1).

Table 4.3. Number of validation pixels, the equivalent area and the approximate proportion of the study area (PS) selected to represent each lithological class in the accuracy assessment.

Lithological class	Pixels	Area (m^2)	PS (%)
Alluvium–colluvium	4087	65,392	0.40
Basal Group	3200	51,200	0.32
Lefkara Formation	2451	39,216	0.24
Pillow lavas	3208	51,328	0.32

Calculated using the validation pixels, the classification accuracy for each lithological map was assessed by way of the overall, user's and producer's accuracies and the Kappa coefficient (K) derived from a confusion matrix (Congalton, 1991). The overall accuracy is the percentage of all validation pixels correctly classified, whereas the user's and producer's accuracies provide information regarding the commission and omission errors associated with the individual classes, respectively. Unlike the overall accuracy, K takes into account the possibility of agreements occurring by chance through a random classification (Brown et al., 1998). For example, a $K = 0$ indicates the obtained overall accuracy could be achieved through a random classification, whereas $K < 0$ and $K > 0$ indicate the obtained overall accuracy is less than and greater than chance agreement, respectively (Rosenfield & Fitzpatrick-Lins, 1986).

4.3.2 Results and discussion

4.3.2.1 Lithological mapping and accuracy assessment

The three lithological maps generated using the SAM, MF and MTMF classification algorithms described above are shown in Figs. 4.13a, b and c, respectively. The corresponding overall and individual lithological class accuracies associated with these maps are summarised in the confusion matrices shown in Tables 4.4, 4.5 and 4.6.

According to the accuracy assessment, all three algorithms generated inaccurate maps, with the SAM algorithm achieving the highest overall accuracy (6.5%), followed by MTMF (2.8%) and MF (2.4%). However, values of $K \approx 0$ for all three algorithms indicate that these results could easily be achieved through random classifications. Thus, the higher overall accuracy achieved using SAM is just an artefact that arises due to the greater number of pixels classified using this approach, rather than a demonstration of its superiority over MF and MTMF. The cause of the poor overall classification accuracies is manifest in the individual lithological class accuracies, shown in the confusion matrices. Whilst partially attributable to confusion primarily between inherently similar lithologies, the low user's and producer's accuracies ultimately arise as a consequence of the vast numbers of unclassified validation pixels. The proportion of validation pixels left unclassified in each of the three classifications was found to vary between 75–95%. This is mirrored throughout the entire study area, with all three maps displaying large areas of unclassified pixels — particularly the MF- and MTMF-derived maps. The proportion of all study area pixels left unclassified through each of the three classifications algorithms varied between 62–89%. Only a negligible proportion of these unclassified pixels can be attributed to the occurrence of non-lithological surface materials (e.g., gossan, mine spoil, roads and buildings).

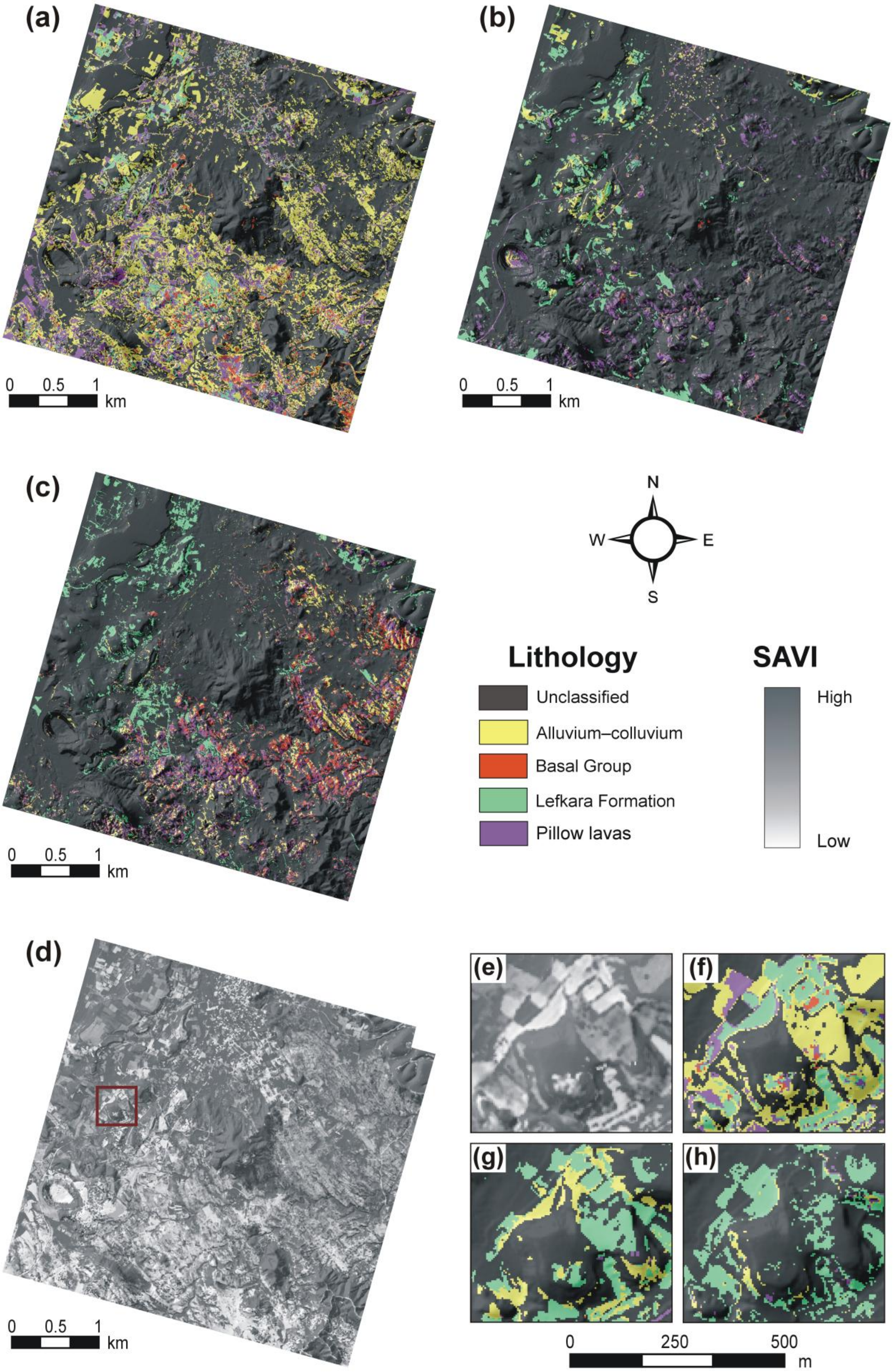

Fig. 4.13. **(a)** SAM-, **(b)** MF- and **(c)** MTMF-derived lithological maps, **(d)** Soil-Adjusted Vegetation Index (SAVI) map, and detailed views of the **(e)** SAVI, **(f)** SAM, **(g)** MF and **(h)** MTMF maps for the area (red box) indicated in **(d)**. High and low SAVI values correspond to high and low fractional vegetation cover, respectively.

Table 4.4. Confusion matrix for SAM classification using the calibrated ATM imagery in conjunction with the ATM-convolved laboratory reflectance spectra.

Mapped as	Validation data				Row total	User's accuracy (%)
	Alluvium–colluvium	Basal Group	Lefkara Formation	Pillow lavas		
Unclassified	3299	2544	1969	1875	9687	–
Alluvium–colluvium	589	542	393	1046	2570	22.9
Basal Group	1	61	12	93	167	36.5
Lefkara Formation	34	2	50	52	138	36.2
Pillow lavas	164	51	27	142	384	37.0
Column total	4087	3200	2451	3208		
Producer's accuracy (%)	14.4	1.9	2.0	4.4		
Overall accuracy = 6.5% K = -0.01						

Table 4.5. Confusion matrix for MF classification using the calibrated ATM imagery in conjunction with the ATM-convolved laboratory reflectance spectra.

Mapped as	Validation data				Row total	User's accuracy (%)
	Alluvium–colluvium	Basal Group	Lefkara Formation	Pillow lavas		
Unclassified	4006	3052	2315	2960	12333	–
Alluvium–colluvium	31	0	65	21	117	26.5
Basal Group	0	0	0	17	17	0.0
Lefkara Formation	50	84	67	0	201	33.3
Pillow lavas	0	64	4	210	278	75.5
Column total	4087	3200	2451	3208		
Producer's accuracy (%)	0.8	0.0	2.7	6.5		
Overall accuracy = 2.4% K = 0.01						

Table 4.6. Confusion matrix for MTMF classification using the calibrated ATM imagery in conjunction with the ATM-convolved laboratory reflectance spectra.

Mapped as	Validation data				Row total	User's accuracy (%)
	Alluvium–colluvium	Basal Group	Lefkara Formation	Pillow lavas		
Unclassified	3846	3055	2223	2104	11228	–
Alluvium–colluvium	9	18	98	420	545	1.6
Basal Group	4	9	8	381	402	2.2
Lefkara Formation	216	79	51	3	349	14.6
Pillow lavas	12	39	71	300	422	71.1
Column total	4087	3200	2451	3208		
Producer's accuracy (%)	0.2	0.3	2.1	9.3		

Overall accuracy = 2.8%
K = -0.01

The proportion of unclassified pixels in each map can be reduced by significantly adjusting the thresholds to enable much weaker matching pixels to be assigned to lithological classes. However, as a consequence, this will undoubtedly lead to an increase in the confusion between classes and hence a further reduction in the overall mapping accuracy. Consequently, an attempt to identify the true cause of the vast numbers of unclassified pixels was instigated. Given that the study area is characterised by widespread vegetation cover and the potential effects of vegetation on spectral discrimination of lithologies (e.g., Siegal & Goetz, 1977; Ager & Milton, 1987; Fraser & Green, 1987; Murphy & Wadge, 1994), a link between unclassified pixels and vegetation cover was investigated. For this purpose, a Soil-Adjusted Vegetation Index (SAVI) Map was first derived using (Huete, 1988):

$$\mathrm{SAVI} = (1+L)\frac{B_7 - B_5}{B_7 + B_5 + L} \tag{4.5}$$

where B_5 and B_7 is the reflectance in the calibrated ATM bands 5 and 7, respectively, and L = 1.0, 0.5 or 0.25 for increasing vegetation densities. An intermediate value of L = 0.5 was selected here to represent the overall vegetation density observed in the study area. The SAVI — which minimises the influence of background materials such as soil — was chosen as it is directly proportional to fractional vegetation cover (Leprieur et al., 1994) and is recommended for general-purpose vegetation studies (Rondeaux et al., 1996).

The derived grey-scale SAVI map (Fig. 4.13d) varies from low values (i.e., close to 0), indicating a low percentage of fractional vegetation cover, to high values (i.e., close to 1), corresponding to a high percentage of fractional vegetation cover. Visually, a spatial correlation clearly exists between the occurrence of higher fractional vegetation cover and unclassified pixels (Figs. 4.13e, f, g and h). This relationship is also confirmed quantitatively for all classifiers, with both unclassified validation pixels (Table 4.7) and all unclassified study area pixels (Table 4.8) typically exhibiting higher and significantly different SAVI values than those of classified pixels (irrespective of whether they are correctly classified). From this, it is evident that the ability to directly identify the lithological units in the ATM imagery is controlled by the abundance of vegetation cover within each pixel.

Table 4.7. SAVI statistics and statistical difference in SAVI between classified and unclassified validation pixels as determine using the unequal variance *t*-test.

Classifier	Classified			Unclassified			p-value
	n	mean	SD	n	mean	SD	
SAM	3259	0.25	0.03	9687	0.36	0.07	<0.0001
MF	613	0.23	0.04	12,333	0.33	0.08	<0.0001
MTMF	1718	0.26	0.03	11,228	0.34	0.08	<0.0001

n, number of pixels; SD, standard deviation.

Table 4.8. SAVI statistics and statistical difference in SAVI between all classified and unclassified study area pixels as determine using the unequal variance *t*-test.

Classifier	Classified			Unclassified			p-value
	n	mean	SD	n	mean	SD	
SAM	378,484	0.23	0.04	629,052	0.35	0.10	<0.0001
MF	105,721	0.21	0.06	901,815	0.32	0.10	<0.0001
MTMF	174,647	0.25	0.03	832,889	0.32	0.11	<0.0001

n, number of pixels; SD, standard deviation.

4.3.2.2 The effects of vegetation on the spectral identification of lithologies

The effects of vegetation cover on the inability to directly identify and subsequently map lithologies using the ATM imagery can be elucidated by the phenomenon of spectral mixing. Spectral mixing is the mixing of materials having discrete spectral properties (e.g., bare rock and vegetation) within an individual pixel to form a composite reflectance spectrum (Kruse et al., 1993). A simple spectral mixing model considers the composite pixel spectrum to be a linear combination of the spectra of the different materials (Singer & McCord, 1979). For the example involving two surface cover end-members, lithological unit L and vegetation type V, this model can be written as:

$$R_{obs}(\lambda_{ATM}) = X_L R_L(\lambda_{ATM}) + X_V R_V(\lambda_{ATM}) \tag{4.6}$$

and

$$X_L + X_V = 1 \ , \tag{4.7}$$

where $R_{obs}(\lambda_{ATM})$ is the observed ATM pixel reflectance spectrum, X_L is the relative proportion of that pixel comprising surface cover type L, $R_L(\lambda_{ATM})$ is the ATM-convolved reflectance spectrum of lithology L, X_V is the relative proportion of that pixel comprising surface cover type V and $R_V(\lambda_{ATM})$ is the ATM-convolved reflectance spectrum of vegetation type V.

The linear spectral mixing model above can be adapted to include numerous end-members and, provided that the pure ATM-convolved reflectance spectra of all surface cover end-members are known, all ATM pixel spectra can be “unmixed” to determine the relative pixel abundances of each end-member (e.g., Adams et al., 1989; van der Meer, 1996; Chabrillat et al., 2000). However, since the ASD FieldSpec® Pro instrument was unavailable during the sampling fieldtrip, spectra of most vegetation types found growing in the Troodos study area were not acquired. Instead, a semi-qualitative and quantitative insight into the effects of vegetation on direct spectral identification of the lithologies in the ATM imagery was obtained by generating synthetic spectral mixtures (Siegal & Goetz, 1977; Ager & Milton, 1987; Murphy & Wadge, 1994). Synthetic composite spectra were generated by mixing — using the two end-member spectral mixing model described in Eqs. 4.6 and 4.7 — the ATM-convolved spectrum of each lithology with increasing amounts (in 10% gradations) of a generic ATM-convolved spectrum that is representative of vegetation commonly found growing on that rock or soil type. The representative vegetation spectra include those of lichen (acquired in this study), green grass and dry grass (both from the USGS spectral library) — three of most abundant vegetation types within the study area. Combinations of lithology and vegetation type that were analysed are summarised in Table 4.9.

Table 4.9. Combinations of lithology and vegetation type synthetically mixed in order to elucidate the effects of vegetation cover on spectral identification of lithologies in the ATM imagery.

Lithological class	Associated vegetation types
Basal Group (weathered)	Green grass*, dry grass
Pillow lavas (A and B weathered)	Lichen, green grass*, dry grass
Lefkara Formation (weathered)	Lichen*, green grass, dry grass
Alluvium–colluvium (A, B and C)	Green grass, dry grass

* less frequently observed growing on this unit.

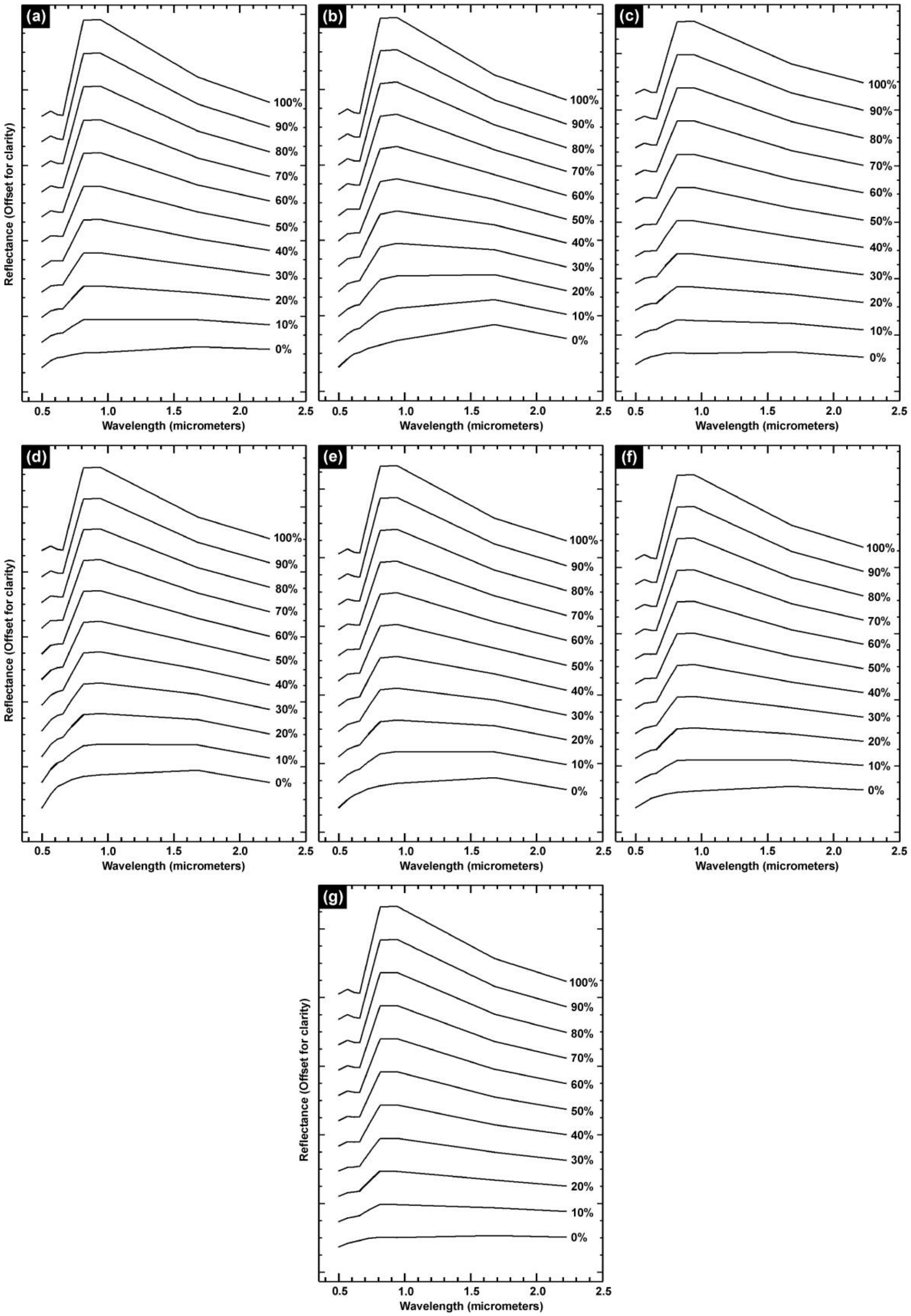

Fig. 4.14. Effect of increasing amounts of fractional green grass cover on the ATM-convolved spectra of the **(a)** Basal Group, **(b)** Pillow lava A, **(c)** Pillow lava B, **(d)** Lefkara Formation and Alluvium–colluvium **(e)** A, **(f)** B and **(g)** C. Spectra are offset vertically for clarity.

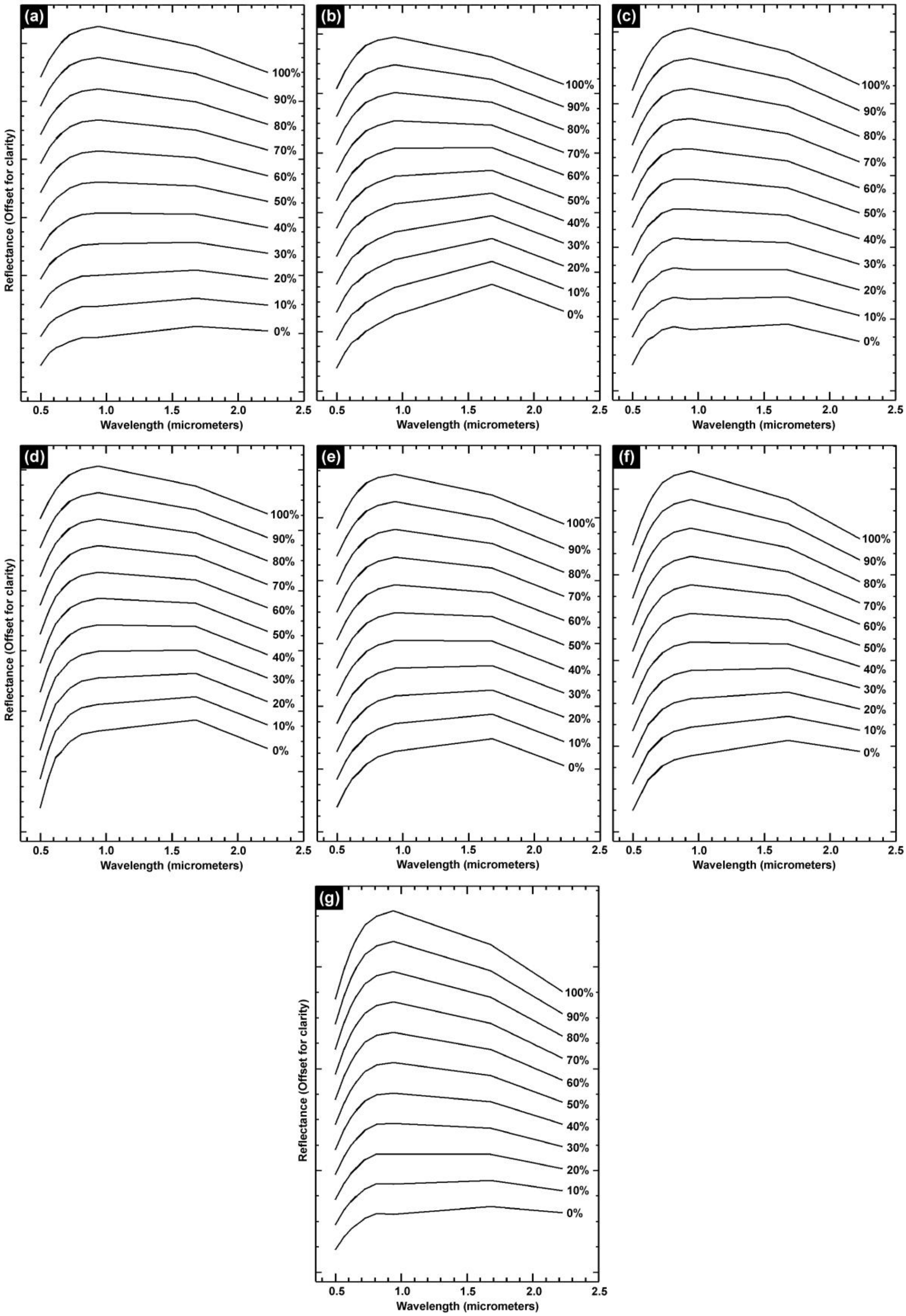

Fig. 4.15. Effect of increasing amounts of fractional dry grass cover on the ATM-convolved spectra of the **(a)** Basal Group, **(b)** Pillow lava A, **(c)** Pillow lava B, **(d)** Lefkara Formation and Alluvium–colluvium **(e)** A, **(f)** B and **(g)** C. Spectra are offset vertically for clarity.

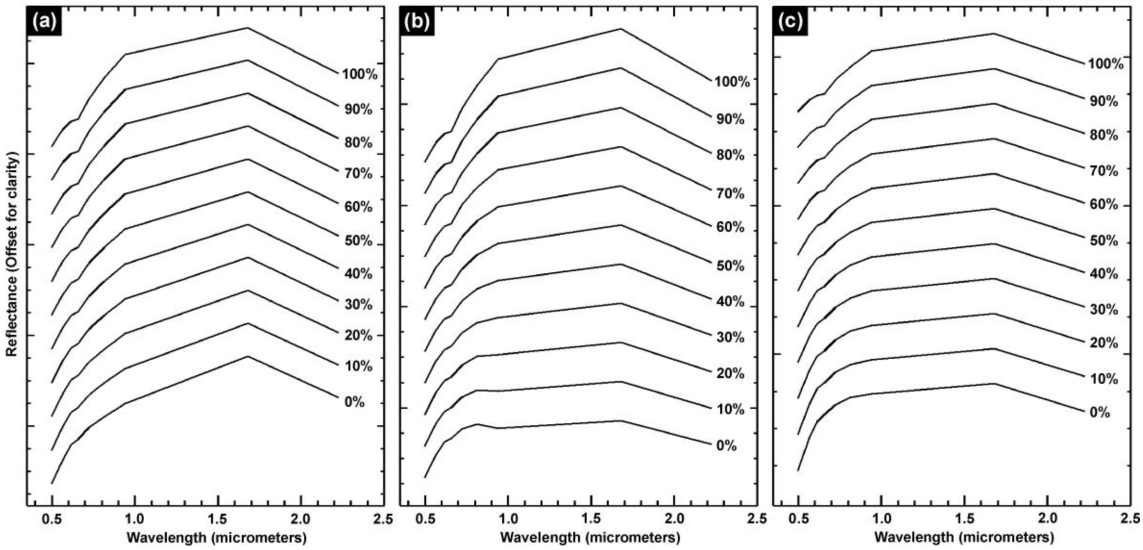

Fig. 4.16. Effect of increasing amounts of fractional lichen cover on the ATM-convolved spectra of **(a)** Pillow lava A, **(b)** Pillow lava B and the **(c)** Lefkara Formation. Spectra are offset vertically for clarity.

The synthetic linearly-mixed ATM-convolved composite spectra illustrating the effects of increasing amounts of fractional vegetation cover on the spectra of the different lithological classes are shown in Figs. 4.14–4.16. The effects of green grass cover on the spectra are pronounced for all lithologies (Fig. 4.14). With only 10% surface coverage, the spectral characteristics of all lithologies become obscured by the impartation of a characteristic green grass absorption feature at 0.62–0.66 μm (ATM bands 4 and 5). Thus, it is likely to be somewhat difficult to identify the underlying lithology through comparison with the representative bare-rock spectra for ATM image pixels containing as little as 10% relative green grass surface coverage. The spectra of low albedo lithologies, such as the Basal Group, Pillow lavas and Alluvium–colluvium B and C, are unrecognisably obscured by fractional green grass cover in excess of 20% due to a combination of the 0.62–0.66 μm absorption feature and a significant increase in reflectance at 0.80–0.95 μm (ATM bands 7 and 8). For 40–50% cover, the composite spectra of the low albedo lithologies are completely dominated by the spectrum of green grass. Although the higher albedo spectra of the Lefkara Formation and Alluvium–

colluvium A are still obscured beyond recognition with fractional cover in excess of 20%, their spectral characteristics are not completely masked until the green grass coverage exceeds approximately 70%.

Dry grass generally has a less pronounced effect on the ability to spectrally identify the lithologies than green grass (Fig. 4.15). Most lithologies are still identifiable through their spectra with fractional dry grass cover up to 30–40%, with the exception of the lowest albedo lithological classes — Basal Group, Pillow lava B and Alluvium–colluvium C. These lithologies become difficult to identify when the fractional cover exceeds 20% because a mutual characteristic absorption feature in their spectra near 0.95 μm (ATM band 8) becomes severely obscured. For fractional cover in excess of 70%, the spectral characteristics of all lithologies are completely masked by those of dry grass. At this abundance, an increase in reflectance between 0.95–1.65 μm (ATM band 8–9) observed in the spectra of all lithologies is replaced by a decrease in reflectance, which is a distinctive feature of dry grass.

Lichen cover appears to have adverse effects on the spectral recognition of the associated lithologies (Fig. 4.16). With just 20% cover, a subtle absorption feature characteristic of lichen becomes imparted to the Lefkara Formation and Pillow lava A and B spectra near 0.65 μm (ATM band 5). For increasing fractional lichen cover, this feature becomes progressively more well-defined in the composite spectra of all lithologies, as does an increasingly steeper slope that is imparted to the spectra between 0.65–0.95 μm (ATM bands 5–8). An additional effect of increasing lichen cover on the spectrum of the Lefkara Formation is a significant reduction in albedo. When fractional cover exceeds 50–60%, the composite spectra for all three lithological classes are completely dominated by lichen.

To summarise, the insight into the effects of vegetation obtained through use of a spectral mixing model reveals that as little as 20% fractional vegetation cover can severely obscure the spectra of all lithologies, whilst only 50% cover can completely mask the spectra of the underlying lithological substrates. When these effects are considered together with the fact that widespread vegetation in the study area covers between 30–90% of the surface area, the difficulty in directly identifying and mapping the lithological units through their reflectance spectra is comprehensible. This is particularly the case for straightforward spectral matching algorithms such as SAM. With regards to the partial unmixing based algorithms of MF and MTMF, the difficulty in identifying the lithologies is likely to be due to the inability to adequately separate the spectral responses of the lithological end-members from that of the background. Considering that vegetation is both abundant and ubiquitous, this is probably due to vegetation spectra dominating the vast majority of ATM pixel spectra, thus severely obscuring or completely masking the spectral signature of the underlying lithologies.

4.4 Conclusion

In this study, a set of representative reflectance spectra for the four main lithologies found within the Troodos study area was acquired by taking laboratory reflectance measurements of numerous samples in the 0.35–2.50 μm wavelength region using an ASD FieldSpec® Pro. A total of eleven representative spectra were obtained from the rock and soil samples collected in the field. These include the spectra of both fresh and weathered surfaces for each rock type, as well as those for spectrally distinct types of the same lithology (i.e., pillow lavas and alluvium–colluvium). With the aid of the continuum removal technique, the spectral characteristics associated with each lithological unit were then interpreted in terms of their mineralogy, by comparing the precise wavelengths of electronic and vibrational absorption features to those exhibited by known constituent minerals. Absorption features exhibited by the lithologies were found to be consistent with those exhibited by their constituent minerals.

Subsequently, the ability to directly identify and map the lithologies by using their representative reflectance spectra in conjunction with the ATM imagery was then evaluated. To achieve this, the ATM imagery was first calibrated to laboratory reflectance using the empirical line method and then the ATM-bandpass convolved laboratory reflectance spectra were used as end-members in three spectral matching classification algorithms — SAM, MF and MTMF. The resulting lithological maps all had very low overall accuracies of $\geq 7\%$ and $K \approx 0$, with between 62–89% of all study area pixels remaining unclassified. A correlation between unclassified pixels and higher SAVI values was confirmed both qualitatively and quantitatively, indicating that the inability to directly map the lithologies could be ascribed to the obscuring effects of the vegetation cover. The effects of a selection of vegetation cover types on spectral identification of the lithologies were therefore elucidated using a linear spectral mixing model. The results revealed that as little as 20% lichen, green or dry grass cover could severely obscure the spectra of all lithologies in the ATM imagery, whilst the spectra of the underlying lithological substrates can be completely masked by 50% vegetation cover. As vegetation cover in the study area frequently exceeds such proportions, the majority of ATM pixels undoubtedly exhibit the spectral characteristics of the vegetation, which makes the observed difficulty in performing direct spectral mapping of rock types comprehensible.

In summary, the results of this study demonstrate that just small amounts of vegetation cover can critically affect the direct spectral identification and mapping of lithologies in a typical Mediterranean region, such as Cyprus. Consequently, the utility of this conventional mapping approach is apparently limited to only regions essentially barren of vegetation, i.e., deserts, alpine areas and cold regions. Although the obscuring and masking effects of vegetation on hyperspectral imagery may or may not be as significant as those observed here for multispectral imagery, any expansion in the utility of remote sensing data to a broader array of environmental settings would undoubtedly be based on the deployment of indirect mapping approaches. For example, this could involve exploiting geobotanical relationships or perhaps a correlation between topography and lithology.

5. Lithological mapping using airborne LiDAR topographic data

This chapter is derived from:

Grebby, S., Cunningham, D., Naden, J., & Tansey, K. (2010). Lithological mapping of the Troodos ophiolite, Cyprus, using airborne LiDAR topographic data. *Remote Sensing of Environment*, *114*, 713–724.

Abstract

Traditional field-based lithological mapping can be a time-consuming, costly and challenging endeavour when large areas need to be investigated, where terrain is remote and difficult to access and where the geology is highly variable over short distances. Consequently, rock units are often mapped at coarse-scales, resulting in lithological maps that have generalised contacts which in many cases are inaccurately located. Remote sensing data, such as aerial photographs and satellite imagery are commonly incorporated into geological mapping programmes to obtain geological information that is best revealed by overhead perspectives. However, spatial and spectral limitations of the imagery and dense vegetation cover can limit the utility of traditional remote sensing products. The advent of Airborne Light Detection And Ranging (LiDAR) as a remote sensing tool offers the potential to provide a novel solution to these problems because accurate and high-resolution topographic data can be acquired in either forested or non-forested terrain, allowing discrimination of individual rock types that typically have distinct topographic characteristics. This study assesses the efficacy of airborne LiDAR as a tool for detailed lithological mapping in the upper section of the Troodos ophiolite, Cyprus. Morphometric variables (including slope, curvature and surface roughness) were derived from a 4 m digital terrain model in order to quantify the topographic characteristics of four principal lithologies found in the area. An artificial neural network (the Kohonen Self-Organizing Map) was then employed to classify the lithological units based upon these variables. The algorithm presented here was used to generate a detailed lithological map which defines lithological contacts much more accurately than the best existing geological map. In addition, a separate map of classification uncertainty highlights potential follow-up targets for ground-based verification. The results of this study demonstrate the significant potential of airborne

LiDAR for lithological discrimination and rapid generation of detailed lithological maps, as a contribution to conventional geological mapping programmes.

5.1 Introduction

Geological mapping is traditionally carried out by employing field strategies that are best suited to a specific area, including following azimuthal traverses, cross-strike transects, stream sections, ridgetops, bedrock contacts, or moving between individual isolated outcrops (Barnes & Lisle, 2004). However, field mapping in complex and poorly accessible terrain can be challenging, time-consuming and costly (Gad & Kusky, 2007; Grunsky et al., 2009; Rogge et al., 2009). As a consequence, lithologies are often mapped coarsely at reconnaissance (e.g., 1:250,000) or more local scales (e.g., 1:50,000), potentially resulting in geological simplifications and inaccuracies (Roy et al., 2009).

Remote sensing data including aerial photographs, and multi- and hyperspectral imagery are also used for lithological mapping (e.g., Drury, 1987; Rothery, 1987; Van der Meer et al., 1997; Rowan & Mars, 2003; Bedini, 2009; Roy et al., 2009). One of the primary benefits of using remote sensing data for lithological mapping is the ability to map areas that are poorly accessible in the field. Although high-resolution aerial photographs can be manually interpreted to help produce detailed lithological maps, the visual discrimination and mapping of surface materials can be subjective, difficult and time-consuming (Crouvi et al., 2006). Multi- and hyperspectral imagery can be automatically classified to rapidly generate lithological maps over large areas, but spatial and spectral limitations of the data may affect the ability to resolve small outcrops or discriminate units with similar spectral properties (Rowan & Mars, 2003; Dong & Leblon, 2004). Dense vegetation cover, such as forests, can also be a hindrance to both field and remote sensing mapping techniques. Whilst making field mapping logistically difficult, dense vegetation also obscures the ground surface and conceals some of the terrain attributes required for photogeological mapping. Additionally, dense vegetation may also obstruct or completely mask the spectral signature of the underlying substrate (Carranza & Hale, 2002).

Airborne Light Detection And Ranging (LiDAR) is an emerging active remote sensing technique. It offers a potential solution for overcoming the obscuring effects that dense vegetation has on discrimination of ground materials, as it has the capability of acquiring accurate and high-resolution (ca. 1–4 m) topographic data, even through forest cover (Kraus & Pfeifer, 1998). This is important because individual rock and soil types respond differently to surface processes, such as weathering and erosion, based on their combined mineralogical, petrological and textural characteristics, and thus they typically have distinct topographic characteristics (Kühni & Pfiffner, 2001; Belt & Paxton, 2005). Laser reflections (or returns) from the ground can be separated from vegetation returns to virtually deforest the terrain, enabling the generation of digital terrain models (DTMs; Haugerud & Harding, 2001). The ability to identify subtle topographic features in high-resolution DTMs makes LiDAR an important tool for geosciences research in both vegetated and non-vegetated terrain. Previous geological applications of airborne LiDAR include fault mapping (Harding & Berghoff, 2000; Haugerud et al., 2003; Prentice et al., 2003; Cunningham et al., 2006), mapping and characterisation of landslide morphology (McKean & Roering, 2004; Glenn et al., 2006) and the characterisation of alluvial fan morphology (Staley et al., 2006; Frankel & Dolan, 2007).

Lithological mapping using topographic data is highly dependent upon the recognition of differences in the topographic characteristics between lithologies. Despite its potential for detecting subtle topographic features in vegetated terrain, few studies have assessed the use of airborne LiDAR for lithological mapping. Webster et al. (2006a, 2006b) visually identified subtle topographic differences in a LiDAR-derived DTM and used these to help map three basalt flow units in Nova Scotia, Canada. In comparison to other sources of topographic data, only the LiDAR DTM had the resolution required to identify the subtle contacts between the units. Wallace (2005) quantitatively discriminated three distinct lithological units in the Sudbury Basin, Ontario, Canada, using elevation and morphometric variables of slope and plan, profile, minimum and maximum curvatures derived from a LiDAR DTM. Several lithological maps were also generated through the classification of elevation and slope using a number of conventional classifiers, including the Maximum Likelihood Classification algorithm. In the same study area, Wallace et al. (2006) used fractal dimension analysis to discriminate three lithological units according to differences in topographic roughness. These studies demonstrate the potential of airborne LiDAR for both qualitative and quantitative lithological discrimination and mapping in areas with relatively simple lithological distributions. The use of airborne LiDAR for mapping in more geologically complex terrain, where the spatial distribution of lithologies is more heterogeneous and distinction of different rock units is potentially problematic in itself, has not been demonstrated.

The aim of this study is to assess the efficacy of airborne LiDAR for the detailed lithological mapping of a section of the Troodos ophiolite, Cyprus. Given the lithological heterogeneity of the study area, the intention was to develop a semi-automated algorithm to increase the speed and objectivity of the mapping process in comparison to traditional field surveys and visual image interpretation. The algorithm is based on the identification and classification of an optimal set of morphometric variables that were chosen for their ability to discriminate four principal lithological units within the study area. The mapping performance of this algorithm is assessed using conventional classification accuracy statistics and is spatially revealed by mapping the classification uncertainty.

5.2 Study area

The Troodos ophiolite has long been recognised as an uplifted slice of oceanic crust and mantle that was created through sea-floor spreading (Gass, 1968; Moores & Vine, 1971). Forming the central region of the eastern Mediterranean island of Cyprus, the ophiolite displays a dome-like structure centred on Mt Olympus (1,952 m; Fig. 5.1). The ophiolite stratigraphy includes a mantle sequence consisting of harzburgites, dunites and a serpentinite diapir exposed at the highest elevations. Along the north slope of the range, the mantle sequence is stratigraphically overlain by a largely gabbroic plutonic complex, a sheeted dyke complex, extrusive lavas and oceanic sediments (Varga & Moores, 1985).

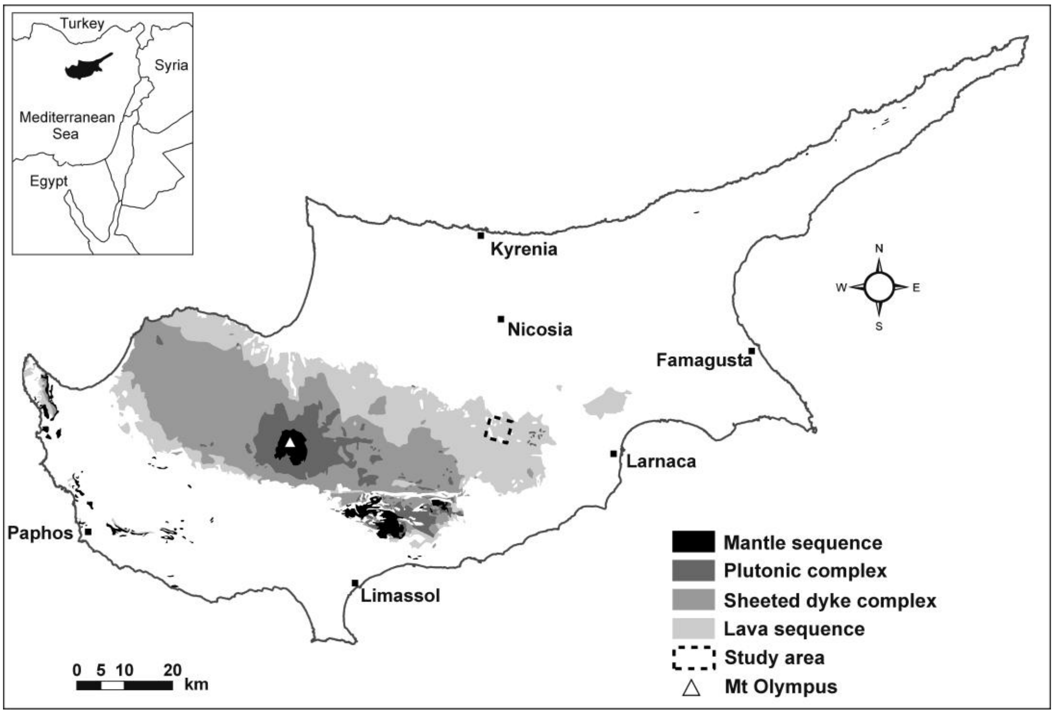

Fig. 5.1. Location of the study area (dashed box) and simplified geology of the Troodos ophiolite. Digital geology was provided by the Geological Survey Department of Cyprus.

The study area is located on the northern flank of the Troodos ophiolite (Fig. 5.1) and comprises a 16 km^2 area with topographic relief on the order of 200 m. The area has a complex landscape in terms of geology and both natural and anthropogenic influences on topography. The area consists of four main lithological units — the Basal Group lavas and dykes, pillow lavas (Upper and Lower), Lefkara Formation chalky marls and alluvium–colluvium. Conventional field and photogeological mapping, together with some ambiguity in defining the units, is apparently responsible for some considerable differences between the two existing geological maps of this study area (Fig. 5.2). Despite having a coarser scale, the 1:250,000-scale map is the most recent version and considered to be the most geologically accurate.

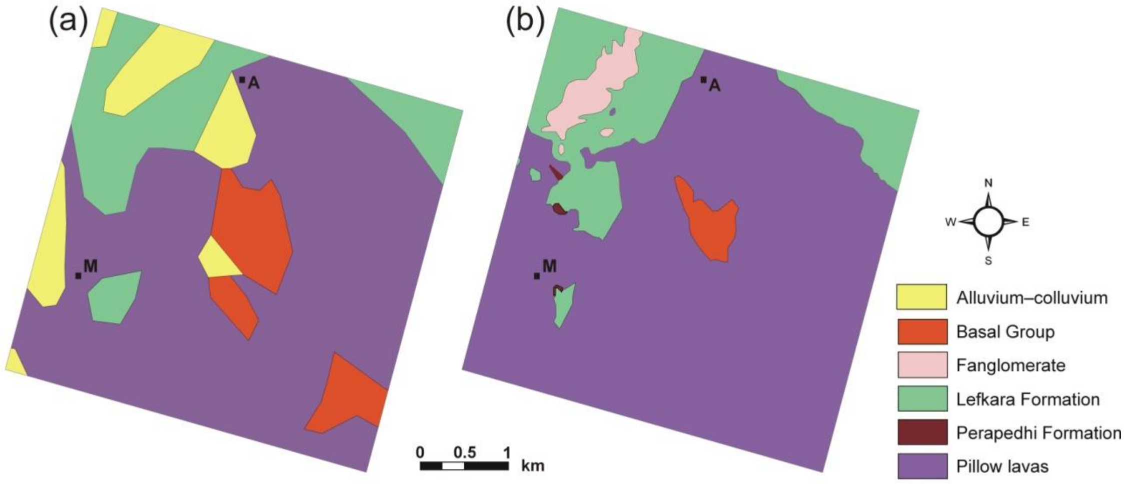

Fig. 5.2. Existing geological maps of the study area shown in Fig. 5.1. **(a)** 1:250,000 and **(b)** 1:31,680-scale maps adapted from the digital geology provided by Geological Survey Department of Cyprus. M–Mathiati mine and A–Agia Varvara Lefkosias.

Stratigraphically, the Basal Group is the lowest unit in the study area. This unit represents a transition from the underlying sheeted dyke complex (100% dykes) to the overlying pillow lavas. Consisted of both dykes and screens of pillow lavas, the definition of the Basal Group is somewhat subjective. In general it contains at least 50% dykes, but more commonly has a dyke abundance of 80–90% dykes (Bear, 1960).

Typical Basal Group outcrops can usually be identified in the field according to their relatively high topography and steep relief (Fig. 5.3a).

The pillow lavas are divided into the Upper Pillow Lavas and the Lower Pillow Lavas according to mineralogy, colour and dyke abundance (Wilson 1959; Gass, 1960). However, this division is difficult to apply in the field (Govett & Pantazis, 1971) and an unconformable or transitional boundary between the two lava units has led to uncertainty over this division (Boyle & Robertson, 1984). Due to this ambiguity, the pillow lavas are treated as one unit in this study. In the field, pillow lava terrain is characterised by undulating, hummocky topography (Fig. 5.3b). Accurate mapping of this unit is crucial to volcanogenic massive sulphide (VMS) mineral exploration on Cyprus, as the Troodos VMS deposits are predominantly confined to the pillow lavas (Constantinou, 1980).

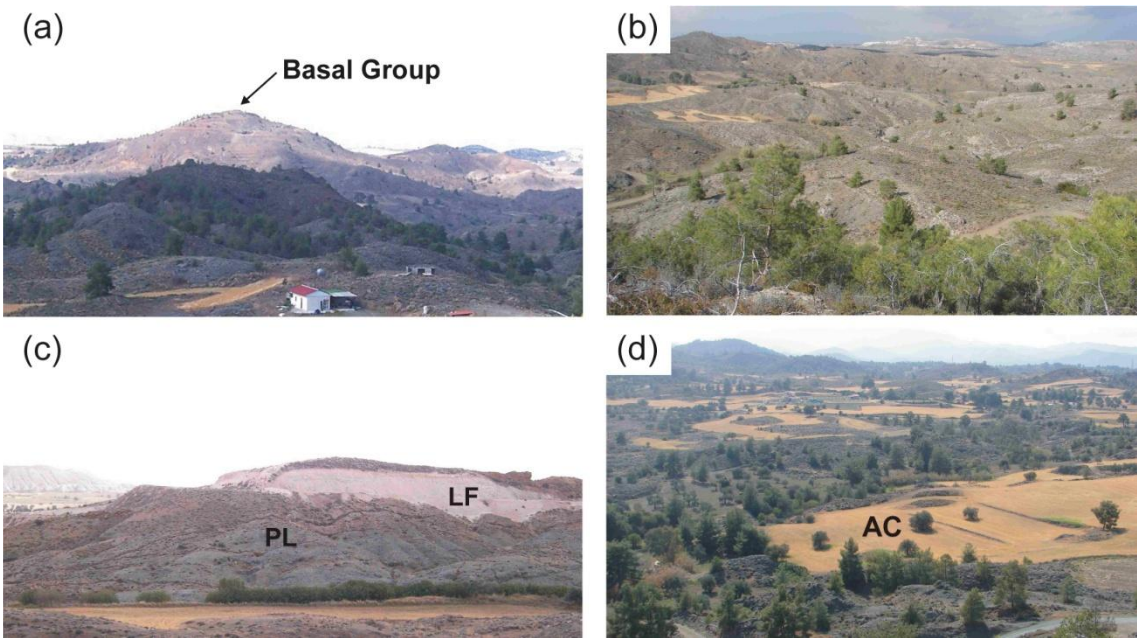

Fig. 5.3. Field photographs showing the four main lithological units: **(a)** Basal Group, **(b)** pillow lavas, **(c)** quarry exposure of the Lefkara Formation overlying pillow lavas (LF and PL, respectively) and **(d)** alluvium–colluvium (AC).

Two types of sedimentary cover are present within the study area: the Lefkara Formation and alluvium–colluvium. The Lefkara Formation represents part of the early oceanic sedimentation that was deposited during the late Cretaceous to early Miocene (Kähler & Stow, 1998). This formation, which comprises marls, chalks and cherts, directly overlays pillow lavas to form gently rolling hills (Fig. 5.3c). Alluvium–colluvium refers to Quaternary sediments, such as sand, silts, soils and gravels that were deposited fluvially or through erosion. Alluvial–colluvial cover is characterised by its relatively flat and smooth topography (Fig. 5.3d), which regularly fills depressions in pillow lava terrain. Alluvial–colluvial cover is frequently exploited for agricultural purposes throughout the study area.

Major anthropogenic features are quite scarce and include the Mathiati VMS mine with spoil tips and the village of Agia Varvara Lefkosias in the north. Land disturbances due to agricultural activity are confined to alluvial–colluvial areas and although these occur throughout the study area, they are most commonly found in the north-west. The study area has a semi-arid environment and vegetation cover is relatively dense and widespread, resulting in only small areas of completely exposed rock outcrops. Vegetation cover consists of crops, patchy forests, shrubbery, grasses and lichen. The combination of variable geology, vegetation cover and land-use makes this a particularly complex area for evaluating the application of airborne LiDAR to lithological mapping.

5.3 Airborne LiDAR data and pre-processing

5.3.1 Data acquisition

Airborne LiDAR data were acquired on the 14th May, 2005 by the Natural Environment Research Council Airborne Research and Survey Facility (NERC ARSF).

The survey was undertaken at an average flying altitude of 2550 m above sea level, using a Dornier aircraft mounted with an Optech ALTM-3033 system. The aircraft–ground distance ranged between 2100–2300 m due to topographic relief within the study area. Operating with a laser pulse repetition rate of 33 kHz and half-scan angle of ±19.4° either side of nadir, approximately 7,600,000 points were acquired for the study area with an average point density of 0.48 m^{-2}. The dataset contains point data from five overlapping flight lines, each with a swath width of 1400–1500 m and an overlap of 20%–50% between adjacent swaths.

Initial data processing was undertaken by the Unit for Landscape Modelling at the University of Cambridge, UK. This involved combining Global Positioning System (GPS) data with the aircraft orientation — recorded using an Inertial Navigation System (INS) — to determine the 3-dimensional coordinates of each laser return (Wehr & Lohr, 1999). The LiDAR point data were delivered as ASCII files containing the x-y-z coordinates and intensity values of all first and last returns in the WGS84 Universal Transverse Mercator (UTM) zone 36-North coordinate system. Information regarding the absolute accuracy of the processed point data was not provided, however the relative vertical accuracy was found to be less than 8 cm as determined from the standard deviation of returns from a flat water surface (Glenn et al., 2006).

5.3.2 Digital terrain model (DTM) generation

The LiDAR dataset originally contained returns from both ground and non-ground objects, such as trees and buildings. In order to generate a DTM it is necessary to remove all non-ground features from the dataset. Point data were classified as either ground or non-ground returns using a triangulated irregular network (TIN) densification algorithm (Axelsson, 2000), implemented in the TerraScan software (www.terrasolid.fi/en). This algorithm iteratively classifies returns as either ground or non-ground according to angle and distance thresholds applied to TIN facets. Due to the relatively high degree of topographic variability within the study area, the data in individual flight lines were classified separately. In each case the classification parameters and threshold were determined experimentally. The maximum terrain angle and iteration distance threshold were kept constant throughout, at 88° and 1.40 m, respectively. The appropriate maximum building size and iteration angle threshold were found to be more scene-dependent. In general, the maximum building size and iteration angle varied from 20 m and 14° for flight lines dominated by relatively high relief, to 60 m and 6° for flight lines acquired over relatively flat terrain. To verify the results of the classification process, several cross-sections were extracted from each flight line and inspected to ensure the point data were assigned to the correct return class. Wherever necessary, misclassified points were manually re-assigned to the correct class. Following classification, non-ground returns were discarded, while points classified as ground returns were used in the generation of the DTM.

The accuracy of gridded LiDAR data products is affected by the choice of interpolation algorithm and spatial resolution (Smith et al., 2005; Palamara et al., 2007; Bater & Coops, 2009). It is therefore important to select an appropriate algorithm and resolution in order to avoid errors in the DTM having a significant effect on subsequent morphometric analysis. To determine the most appropriate algorithm and resolution, DTMs were generated at 1, 2, 3, 4 and 5 m resolutions using a range of popular interpolation algorithms. The interpolation algorithms evaluated were inverse distance weighted, block kriging, nearest neighbour, cubic polynomial, modified Shepard's and triangulation with linear interpolation. Interpolation errors associated with each algorithm and resolution were assessed quantitatively using statistics generated through split-sample validation (Smith et al., 2005). This involved the random selection and omission of approximately 9% of the ground returns, while the remaining 91% were used to generate DTMs. The residuals between all omitted data points and their predicted values in the DTM were calculated and used to generate interpolation error statistics, such as the mean error (indicating the magnitude and direction of any bias) and mean absolute error (Bater & Coops, 2009). The DTMs were also visually inspected for interpolation artefacts (e.g., null and spurious elevations) using shaded relief images with varying illumination directions and vertical exaggeration. The DTM generation, along with both visual and quantitative interpolation analysis were all undertaken using Surfer 8.0 (Golden Software, Inc.).

The split-sample validation results showed that all of the interpolation algorithms tended to underestimate the actual elevation (mean errors ranging from -0.10 m to -0.12 m), with the exception of the triangulation with linear interpolation which slightly overestimated elevation (mean errors ranging from 0.01 m to 0.04 m). Mean absolute errors were generally consistent between the interpolation algorithms and spatial resolutions (ranging from 0.23 m to 0.28 m), except for the triangulation with linear interpolation algorithm for which mean absolute error increased significantly with increasing spatial resolution (from 0.23 m at 1 m resolution to 0.49 m at 5 m).

During visual inspection, a “ridge and trough” pattern was observed in all DTMs at the extreme edges of areas where adjacent flight lines overlap. Cross-sectional profiles extracted from the flight lines revealed that elevation exhibited an upward concavity error with increasing scan angle towards the edges of swaths — a phenomenon often referred to as “smiley face error” (Lohani & Mason, 2005). Such parabolic vertical error has been attributed to vertical beam misalignment or systematic range errors (Latypov, 2005). The observed DTM artefact is generated when data from multiple flight lines are merged and measurements from large scan angles do not coincide with corresponding measurements from smaller scan angles. The effect of “ridge and trough” artefact on the quantitative analysis was isolated by recalculating the split-sample error statistics using only a subset of residuals selected from outside the areas of overlap (corresponding to ~3% of the total ground returns). As a result, mean errors were reduced to underestimations of between 0.01 m and 0.03 m for all interpolation algorithms except triangulation with linear interpolation, for which the overestimation increased to between 0.02 m and 0.09 m. Also, the choice of interpolation algorithm was found to have a greater effect on mean absolute errors than the spatial resolution, again with the exception of triangulation with linear interpolation. Nevertheless, the mean absolute error showed a significant decrease in all cases when calculated using residuals from outside the areas of overlap. Kriging, modified Shepard’s and cubic polynomial interpolation resulted in the smallest mean absolute errors (ranging from 0.09 m to 0.13 m for all resolutions), followed by the inverse distance weighted and nearest neighbour algorithms (0.15 m to 0.17 m). Triangulation with linear interpolation was the worst performing algorithm, with mean absolute error increasing from 0.12 m at 1 m resolution to 0.43 m at 5 m.

As the “ridge and trough” pattern was solely confined to the areas of overlap where the point density is greater, it was possible to almost completely eradicate this artefact from the DTMs using a simple point spacing based filter prior to interpolation. The filter discarded the point with the highest elevation (i.e., the point most affected by “smiley face error”) when multiple ground returns were present within a given radius. The size of the radius was chosen so that the filter only operated on data points within the areas of overlap (in this case a point spacing ≤ 2 m). In addition to removing this artefact, the filter also generates a dataset with a globally uniform point density. The most appropriate interpolation algorithm and spatial resolution for the final DTM was selected as that which minimised the mean and mean absolute errors, and the appearance of interpolation artefacts in the DTM. Consequently, 100% of the ground returns were used to generate the final DTM at a spatial resolution of 4 m, by applying the point-spacing filter prior to interpolation with the kriging algorithm.

5.4 Methods

The efficacy of airborne LiDAR topographic data for detailed lithological mapping is assessed using the methodological approach presented in Fig. 5.4. Following the generation of the DTM, the method consists of five major steps, which are discussed in the following section.

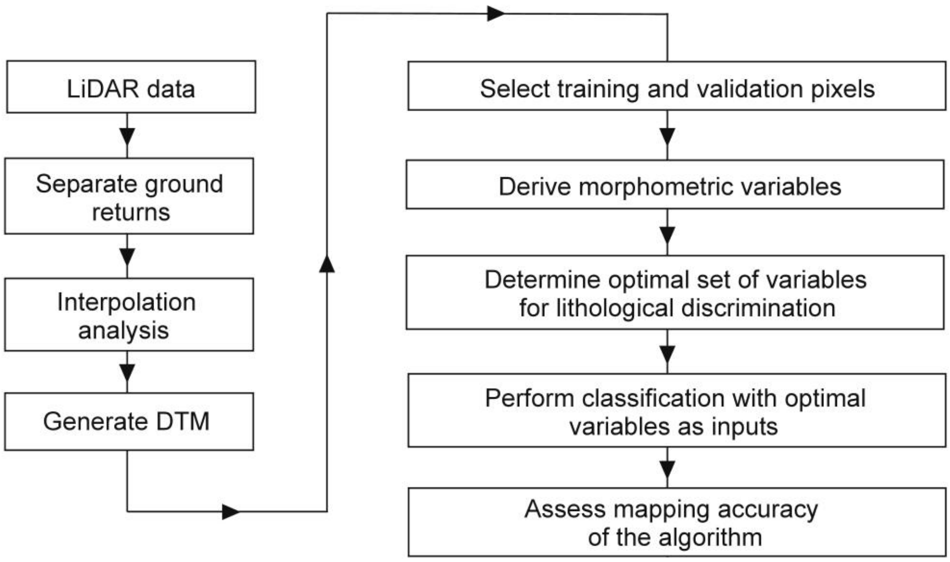

Fig. 5.4. Flow diagram presenting the methodological approach implemented to assess the efficacy of airborne LiDAR for detailed lithological mapping.

5.4.1 Training and validation data

Two independent sets of pixels were selected for the purpose of training and validating the results of the algorithm developed herein. Using knowledge of the study area, QuickBird imagery (0.70 m resolution) and the existing geological maps, four training areas (i.e., regions of interest; ROIs) were carefully selected in ENVI 4.3 (Research Systems, Inc.) to represent the four lithological classes. All pixels located within these four training areas were included in the training dataset. The validation pixels were selected using a random stratified sampling protocol to ensure that each class was represented proportionately and to avoid spatial autocorrelation within the dataset (Chini et al., 2008; Pacifici et al., 2009). To do this, several ROIs were identified for each lithological class in the same way as that used to identify the training areas. Validation pixels were then randomly sampled from these according to the total area of the ROIs associated with each lithological class. Table 5.1 shows the number of pixels, the equivalent area and the proportion of the study area selected for each lithological class for use in training and validation. In order to determine their effect on the mapping performance, it was decided not to mask-out or treat anthropogenic features as a separate class.

Table 5.1. Number of pixels, the equivalent area and the proportion of the study area (PS) selected for each lithological class for training and validation purposes.

Lithological class	Training			Validation		
	Pixels	Area (m^2)	PS (%)	Pixels	Area (m^2)	PS (%)
Alluvium–colluvium	1712	27,392	0.17	4087	65,392	0.40
Basal Group	1780	28,480	0.18	3200	51,200	0.32
Lefkara Formation	2769	44,304	0.27	2451	39,216	0.24
Pillow lavas	3095	49,520	0.31	3208	51,328	0.32

5.4.2 Morphometric variables

The correlation between lithology and topography that is apparent in the field is also clearly evident in the 4 m DTM of the study area (Fig. 5.5). In order to automatically classify and map lithology using LiDAR data, it is first necessary to numerically quantify the topographic characteristics of the lithologies using variables that enable adequate discrimination. After considering the observed topographic characteristics, seven candidate morphometric variables were derived from the DTM for this purpose (Table 5.2).

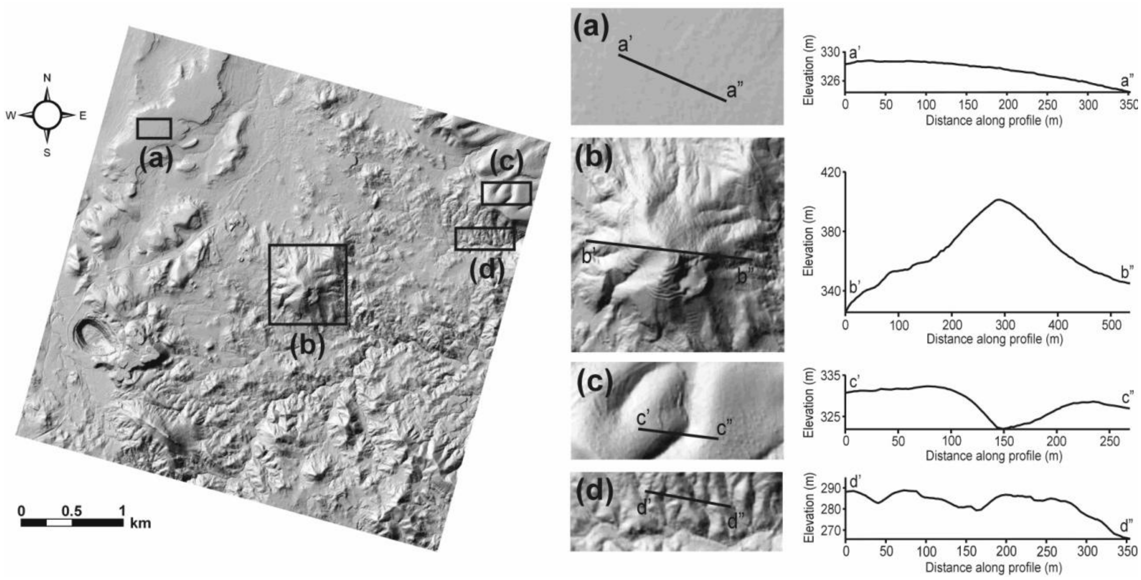

Fig. 5.5. Shaded relief DTM of the study area displaying the distinct topographic characteristics of: **(a)** alluvium–colluvium, **(b)** Basal Group, **(c)** Lefkara Formation and **(d)** pillow lavas.

Morphometric variables like slope, plan and profile curvature are typical examples of basic first and second order derivatives of elevation. These three variables were derived using a standard routine in ENVI 4.3, which calculates the derivatives from a quadratic surface fitted to elevations within a moving window (or kernel) that is passed over the DTM (Wood, 1996). Absolute values of plan and profile curvature were used to avoid an alternating pattern of convexity and concavity in highly undulating such as that of the pillow lavas. Morphometric variables such as these are scale-dependent; therefore, in order to identify the most suitable scales for maximum lithological discrimination, each variable was derived using fifteen different moving window sizes ranging from 3 × 3 pixels (12 m × 12 m) to 31 × 31 pixels (124 m × 124 m). Moving window sizes were limited to 31 × 31 pixels as larger windows were found to reflect more regional-scale topographic information, rather than the local-scale information which is more relevant to detailed lithological discrimination.

Table 5.2. Candidate morphometric variables for lithological discrimination.

Morphometric variable	Description	Optimal moving window size (pixels)
Slope (°)	Magnitude of the steepest gradient	15 × 15
Relief (m)	Elevation range within a given area	3 × 3
|Profile curvature| (1/m)	Absolute value of vertical curvature component in aspect direction	21 × 21
|Plan curvature| (1/m)	Absolute value of horizontal curvature component in aspect direction	31 × 31
Slope roughness (°)	Standard deviation of slope	31 × 31
Residual roughness (m)	Standard deviation of residual topography	3 × 3
Hypsometric integral	Elevation distribution within a given area	11 × 11

Relief, hypsometric integral and the two LiDAR-derived measures of surface roughness were derived in Surfer 8.0. Hypsometry describes the elevation distribution within a given area (Strahler, 1952) and can be estimated using the hypsometric integral (Pike & Wilson, 1971). The hypsometric integral (HI) is calculated as:

$$\mathrm{HI} = \frac{h_{\mathrm{mean}} - h_{\mathrm{min}}}{h_{\mathrm{max}} - h_{\mathrm{min}}} \tag{5.1}$$

where h_{mean}, h_{min} and h_{max} are the average, minimum and maximum elevations within a moving window, respectively. This hypsometric integral variable was also derived at multiple scales using the same set of fifteen moving window sizes detailed above.

Surface roughness can be measured using the standard deviation of slope within a moving window (Frankel & Dolan, 2007). This variable — referred to here as slope roughness —was derived at multiple scales by first determining slope within a 3 × 3 pixel window (i.e., 12 m × 12 m) and then calculating the standard deviation of slope within each of the fifteen moving windows. The second measure of surface roughness (known here as residual roughness) is defined as the standard deviation of residual topography (Cavalli et al., 2008). First, a 100 m mean DTM was created by smoothing the 4 m DTM using a 25 × 25 pixel moving average filter. A residual topographic surface was then calculated by subtracting the 100 m mean DTM from the 4 m DTM. Finally, the standard deviation of this residual topographic surface was calculated within each of the fifteen different sized moving windows.

In general, good discrimination and classification performance relies upon homogeneity within classes and dissimilarity between classes (Li et al., 2009). The morphometric homogeneity of the lithologies can be maximised by identifying the optimal scale for each candidate variable. The optimal scales can be determined statistically by identifying the moving windows size which minimises the spread of morphometric data within the training areas (Prima et al., 2006). Here, using the standard deviation of each training area as a measure of its spread, the most suitable moving window size for each candidate variable was defined as that which minimised the average data spread within the training areas. More specifically, for each of the fifteen moving window sizes, the standard deviations within each of the four training areas were calculated and then averaged. The moving window size resulting in the smallest average was deemed to represent the most suitable scale for that variable. This procedure was applied separately to each candidate variable, thus enabling multi-scale topographic information to be utilised. The optimal moving window size for each candidate variable is shown in Table 5.2.

5.4.3 Variable selection

Classification using all available variables might not necessarily produce the highest mapping accuracy. Some of these variables may be highly correlated, noisy, redundant or irrelevant (Pacifici et al., 2009). Better classification results may be achieved when such input variables are discarded and classification is performed using a smaller set of informative variables (Kavzoglu & Mather, 2002; Verikas & Bacauskiene, 2002). An optimal set of variables can be determined independently of the classification algorithm, based on statistical criteria such as class separability (the filter approach), or in conjunction with the chosen classifier (the wrapper approach). Despite using a non-parametric classifier, a filter approach was adopted as this enabled an exhaustive evaluation of all possible variable combinations to be conducted more efficiently than with a wrapper approach.

The number of candidate variables was initially reduced by identifying and discarding linearly correlated and therefore redundant variables through the calculation of Pearson's Product Moment Correlation Coefficients. The optimal set of variables for lithological discrimination was then determined from the remaining candidates through class separability analysis (Dong & Leblon, 2004). To do this, the morphometric separability between pairs of lithological classes (i.e., training areas) was calculated for every combination of two or more variables using the Jeffries-Matusita (JM) distance (Richards, 1994). For four lithologies, there are six possible pairs of classes and therefore six JM distances for each combination of variables. The JM distance ranges from 0–2, with pairs classes being inseparable for JM distances of 0 but completely separable for distances close to 2. The combination of variables resulting in both the largest minimum and largest average JM distances is selected as the optimum for lithological discrimination.

5.4.4 Classification

A lithological map was generated using the optimal set of morphometric variables as inputs to a topologically preserving artificial neural network classifier; the Kohonen Self-Organizing Map (SOM) (Kohonen, 1982, 2001). Artificial neural networks possess many advantages over conventional statistical classifiers, since they are non-parametric, robust in handling noisy data and can learn complex patterns (Ji, 2000). Applications of the SOM to remote sensing data include land-use classification (Ji, 2000; Bagan et al., 2005; Jianwen & Bagan, 2005), lithological mapping (Mather et al., 1998; Bedini, 2009) and geomorphometric feature analysis (Ehsani & Quiel, 2008a, 2008b).

The SOM network consists of an input layer and an output layer. The input layer contains one neuron for each of the input variables, whereas the output layer is a two-dimensional array of neurons. Neurons in the output layer are connected to those in the input layer via synaptic weights. Random synaptic weights, ranging from 0 to 1, are initially assigned to the output neurons. These weights are then adjusted during learning to best describe patterns in the input data (Mather et al., 1998). Network learning is an iterative process and involves two stages: unsupervised coarse tuning and supervised fine tuning. The SOM algorithm in IDRISI Andes was used in this study (Li & Eastman, 2006).

An input vector (a pixel in morphometric space) is represented by the vector $\mathbf{x} = \{x_1, x_2 ..., x_n\}$, where n is the number of input variables (and input neurons) used in the classification. During coarse tuning, input vectors are presented to the network and in each case the output neuron with the minimum Euclidean distance between its weight vector and the input vector is selected as the winner:

$$\text{winner} = arg\min_j \left(\sqrt{\sum_{i=1}^{n} (x_i(t) - w_{ji}(t))^2} \right) \tag{5.2}$$

where $x_i(t)$ is the input to neuron i at iteration t and $w_{ji}(t)$ is the synaptic weight connecting output neuron j to the input neuron i at iteration t. The weight vector of the winner and output neurons within a neighbourhood of radius γ of the winner are then adjusted in the direction of the input vector:

$$w_{ji}(t+1) = w_{ji}(t) + \alpha(t)[x_i(t) - w_{ji}(t)] \tag{5.3}$$

where $w_{ji}(t+1)$ is the adjusted weight vector and $\alpha(t)$ is the learning rate at iteration t. The weights of neurons outside the neighbourhood remain unadjusted. The learning rate decreases gradually during the coarse tuning stage from an initial learning rate ($\alpha_{\max}$) to a final learning rate ($\alpha_{\min}$) , after the total number of iterations ($t_{\max}$):

$$\alpha(t) = \alpha_{\max} \left(\frac{\alpha_{\min}}{\alpha_{\max}} \right)^{\frac{t}{t_{\max}}} \tag{5.4}$$

Similarly, the radius of the neighbourhood also decreases steadily during the coarse tuning stage:

$$\gamma(t) = \gamma_{\max} \left(\frac{\gamma_{\min}}{\gamma_{\max}} \right)^{\frac{t}{t_{\max}}} \tag{5.5}$$

A large initial neighbourhood is usually chosen, resulting in widespread adjustments to the weight vectors of neurons in the output layer. As learning progresses, γ decreases until the weight of only the winning neuron is adjusted.

The SOM network parameters used in this study are based on experimentation guided using the existing literature (e.g., Ji, 2000; Jianwen & Bagan, 2005; Bedini, 2009). An output layer consisting of 10 × 10 neurons was chosen, with $\alpha_{\max} = 0.05$, $\alpha_{\min}$

= 0.01 and γ_{max} = 12. Coarse tuning was performed using all input vectors, therefore t_{max} was equal to the number of pixels in each input variable image (i.e., 1,012,841 iterations). Prior to learning, the input variables were normalised to the range 0–1 using a logistic (softmax) function. This function performs a nearly linear transformation on most of the data whilst also acting to reduce the influence of any outliers in each variable (Priddy & Keller, 2005). Normalisation increases the learning efficiency and also ensures that the input variable with the largest range does not dominate the calculation of the Euclidean distances and the organisation of the output layer (Ehsani & Quiel, 2008a).

Before fine tuning commences, neurons in the output layer must be preliminarily labelled using input vectors with known class identities. To achieve this, pixels from the training areas were presented to the coarsely tuned network and in each case the output neuron with the closest matching weights was triggered. Output neurons were labelled according to the training pixel class they were triggered by most frequently — a procedure known as majority voting.

Fine tuning was performed using the type-one Learning Vector Quantization (LVQ1) algorithm (Kohonen, 1990). The aim of fine tuning is to improve the classification accuracy by defining the class boundaries in the output layer more precisely. Pixels within the training areas were again presented to the SOM and the output neuron with the minimum Euclidean distance between a training pixel and its weight vector was selected as the Best Matching Unit (BMU). The weights of the BMU were adjusted accordingly:

$$w_c(t+1) = w_c(t) + \delta(t)[x_i(t) - w_c(\mathrm{t})], \quad \text{if } \mathbf{x} \text{ is correctly labelled} \tag{5.6}$$

$$w_c(t+1) = w_c(t) - \delta(t)[x_i(t) - w_c(\mathrm{t})], \quad \text{if } \mathbf{x} \text{ is incorrectly labelled} \tag{5.7}$$

$$w_i(t+1) = w_i(t), \qquad \text{if } i \neq c \tag{5.8}$$

where w_c is the weight vector of the BMU, $w_c(t + 1)$ is the adjusted BMU weight vector and $\delta(t)$ is a scalar gain term, which decreases with each iteration like the learning rate during coarse tuning. Consequently, if the class identity of a training pixel matches the label of its BMU, the weight vector of the BMU is adjusted in the direction of the training vector, but is moved away if not. Fine tuning was performed using $\delta_{\max} = 0.005$, which decreases to $\delta_{\min} = 0.001$ after 200 iterations. Output neurons were re-labelled following fine tuning. In order to classify lithology, all input vectors were presented again to the trained network and assigned the class identity of their corresponding BMU.

5.4.5 Accuracy assessment

The classification accuracy was assessed by determining the overall (OA), user's (UA) and producer's (PA) accuracies and the Kappa coefficient (K) from a confusion matrix (Congalton, 1991). The OA is the percentage of validation data correctly classified, whereas the UA and PA detail the commission and omission errors, respectively. The K is considered a more reliable measure of classification accuracy because, unlike the OA, it takes into account the possibility of agreements occurring by chance in a random classification (Brown et al., 1998; Pignatti, 2009).

In addition to the lithological map, a second map was generated to analyse the spatial context of classification uncertainties. To do this, the degree of commitment that each pixel has to its assigned lithological class was determined using the SOM Commitment (SOM-C) (Li & Eastman, in press). Calculated from the triggering proportion of classes on output neurons during labelling, SOM-C essentially provides an indication of classification uncertainty. Values range from 0 to 1, with SOM-C values close to 1 indicating little uncertainty in the class identity of a pixel, whereas values close to 0 indicate high classification uncertainty.

5.6 Results and discussion

5.6.1 Variable selection for lithological discrimination

The Pearson's Product Moment Correlation Coefficients revealed that the relief variable was highly linearly correlated (r > 0.80) with both the slope and the residual roughness variables. Also, slope roughness showed moderate-to-high positive correlation (r > 0.54) with almost all candidate variables. Consequently, the relief and slope roughness variables were deemed to be redundant and discarded, reducing the number of candidate variables from seven to five.

Minimum and average JM distances for pairs of lithological classes were computed for all twenty-six combinations of two or more of the five remaining candidate variables (Fig. 5.6). The minimum and average JM distances are generally smallest when separability is calculated using only pairs of variables and increases when additional variables are included. The slope variable appears to have the greatest influence on the separability, since its exclusion results in at least a 20% and 50% decrease in the minimum and average JM distances, respectively. In terms of the pair-wise class separability, the Lefkara Formation and pillow lavas were consistently the least separable lithological units and were responsible for the minimum JM distance for almost all variable combinations. The lack of morphometric separabilty between these two units can be attributed to their stratigraphic relationship, where the Lefkara Formation has been deposited directly on top of the pillow lavas. This results in the Lefkara Formation displaying some topographic characteristics of the subdued pillow lava terrain that it drapes. Conversely, the Basal Group and alluvium–colluvium were consistently the most separable units with JM distances typically exceeding 1.90. Such separability is expected due to their contrasting topographic characteristics. Large JM distances were also usually observed between alluvium–colluvium and both the pillow lavas and Lefkara Formation.

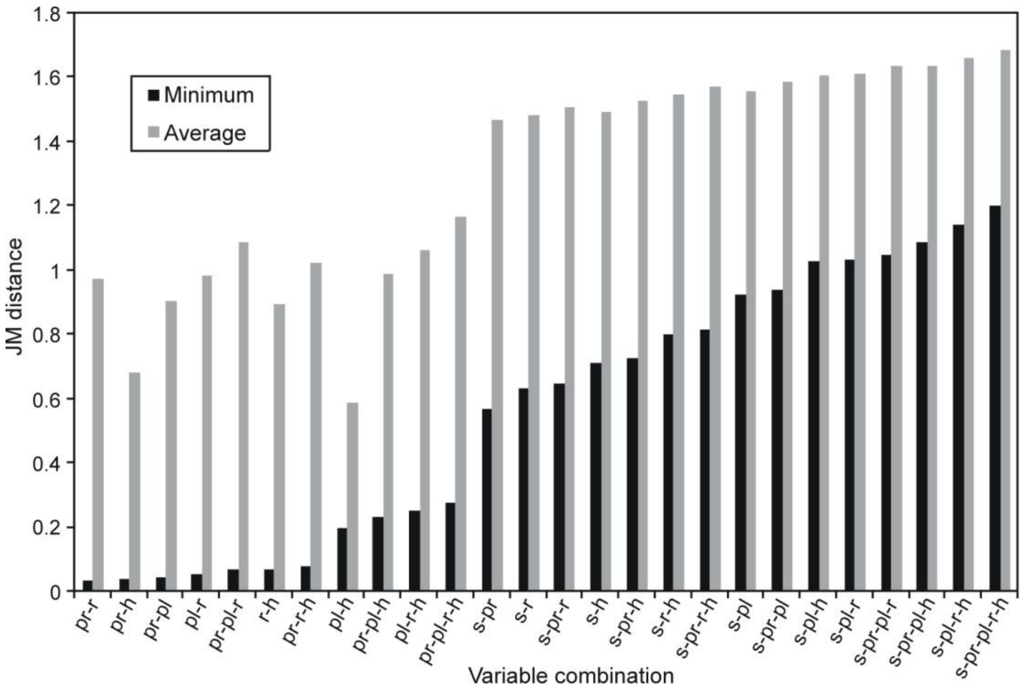

Fig. 5.6. Minimum and average separability (JM distance) for combinations of the slope (s), absolute profile curvature (pr), absolute plan curvature (pl), residual roughness (r) and hypsometric integral (h) variables.

The combination which includes all five remaining candidate variables is the optimum for lithological discrimination, as this combination resulted in both the largest minimum and largest average JM distances (1.20 and 1.69, respectively). Furthermore, this combination of variables results in the largest JM distances for all six pairs of classes. For this optimal combination, the Lefkara Formation and pillow lavas were the least separable lithologies, followed successively by the Lefkara Formation and Basal Group (JM distance of 1.22), pillow lavas and Basal Group (1.70) and alluvium–

colluvium versus all other units (all with JM distances of 2.00). The relative importance of each variable to the separability of lithologies was evaluated by examining the decrease in the JM distances after each variable was removed (Table 5.3). Removing the slope variable produced the largest decrease in the JM distances for all six pairs of lithological classes and the minimum and mean JM distances. This suggests that slope contributes most to the separability of the lithologies in the study area. Apparently, absolute plan curvature is also an important variable; particularly for separating the morphometric characteristics of the Lefkara Formation, Basal Group and pillow lavas. The absolute profile curvature variable is arguably the least important as its removal resulted in the smallest decrease in the minimum, mean and the majority of pair-wise JM distances. Removing the residual roughness and hypsometric integral variables produced a similar decrease in all JM distances, suggesting these are of equal importance. This optimal set of morphometric variables — slope, absolute profile curvature, absolute plan curvature, residual roughness and the hypsometric integral (Fig. 5.7) — was subsequently used in the classification stage.

Table 5.3. The relative importance of variables to the separability of lithologies, determined by individually removing each variable from the pair-wise JM distance calculations.

Variable removed	JM distance							
	LF vs. PL	LF vs. BG	PL vs. BG	LF vs. AC	PL vs. AC	BG vs. AC	Min.	Mean
None	1.20	1.22	1.70	2.00	2.00	2.00	1.20	1.69
Slope	0.27	0.50	0.41	1.92	1.95	1.94	0.27	1.17
|Profile curvature|	1.17	1.14	1.67	2.00	1.99	2.00	1.14	1.66
|Plan curvature|	0.81	1.02	1.59	2.00	1.99	2.00	0.81	1.57
Residual roughness	1.09	1.10	1.67	2.00	1.97	2.00	1.09	1.64
Hypsometric integral	1.05	1.13	1.65	2.00	1.99	2.00	1.05	1.64

LF, Lefkara Formation; PL, pillow lavas; BG, Basal Group; AC, alluvium–colluvium.

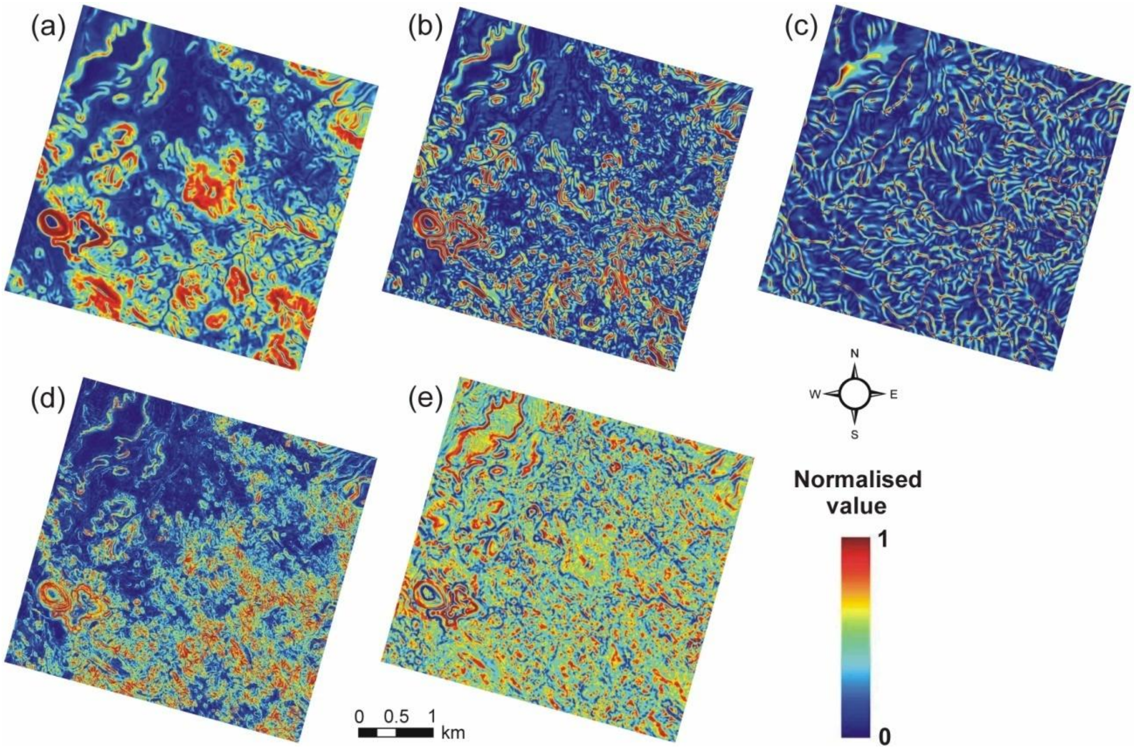

Fig. 5.7. Optimal set of (normalised) morphometric variables selected as inputs to the SOM classification: **(a)** slope, **(b)** absolute profile curvature, **(c)** absolute plan curvature, **(d)** residual roughness and **(e)** hypsometric integral.

5.6.2 Lithological mapping and accuracy assessment

A lithological map displaying the four principal units and a SOM-C map, indicating the classification uncertainty, were generated using the LiDAR-derived topographic data (Fig. 5.8). Following classification, a small amount of noise in the classified image was reduced using a 3 × 3 mode filter.

The accuracy of the lithological map was assessed using the validation pixels and the results were summarised using a confusion matrix (Table 5.4). The lithological map has an overall accuracy of 65.4% and a K of 0.53. Alluvium–colluvium is the best mapped unit with a producer's accuracy of 87.9% and a user's accuracy of 98.8%, while the Lefkara Formation was mapped with the least accuracy. A good producer's classification accuracy was achieved for the pillow lavas (66.8%), however more than

50% of all validation pixels mapped as pillow lavas actually belong to other classes. Only 50.4% of Basal Group validation pixels were mapped correctly, but with a commission error of just 29.7%. The most classification confusion occurs between the Lefkara Formation, pillow lavas and Basal Group, which corroborates the results of the separability analysis. Although the majority of this confusion can be explained by their stratigraphic relationships or natural deviations from the typical topographic characteristics of each unit, anthropogenic activity is also responsible for a significant component. An obvious example of this can be found proximal to Mathiati mine and spoil tips where the natural topographic characteristics have been destroyed, leading to misclassification (Fig. 5.8).

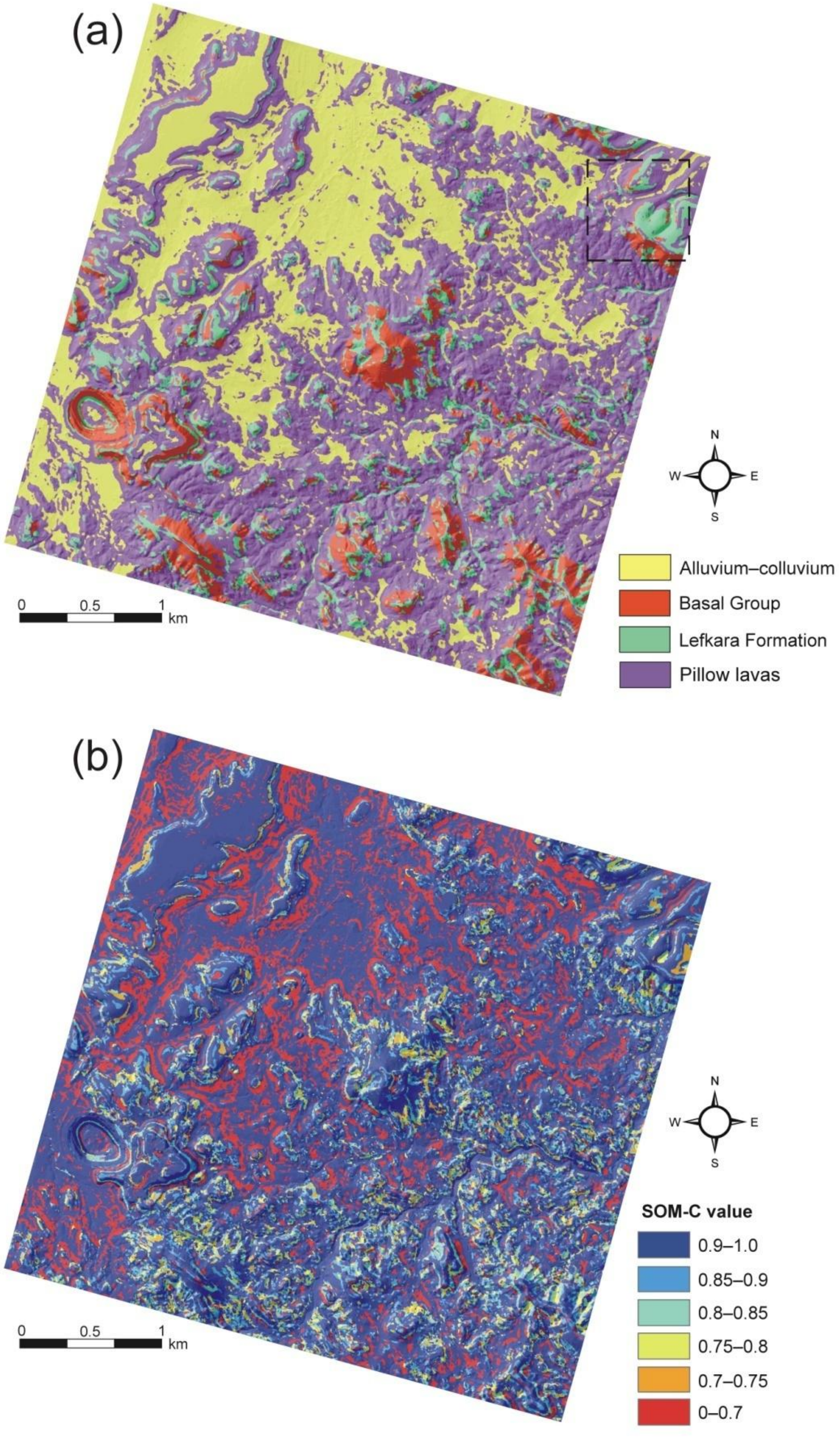

Fig. 5.8. **(a)** Lithological map of the study area generated using LiDAR-derived topographic data. The dashed black box indicates the spatial extent of Fig. 5.9. **(b)** SOM-C map depicting classification uncertainty.

Table 5.4. Confusion matrix for SOM classification using the optimal set of morphometric variables.

Mapped as	Validation data				Row total	User's accuracy (%)
	Alluvium–colluvium	Basal Group	Lefkara Formation	Pillow lavas		
Alluvium–colluvium	3594	1	30	11	3636	98.8
Basal Group	0	1614	299	383	2296	70.3
Lefkara Formation	2	816	1114	672	2604	42.8
Pillow lavas	491	769	1008	2142	4410	48.6
Column total	4087	3200	2451	3208		
Producer's accuracy (%)	87.9	50.4	45.4	66.8		
Overall accuracy = 65.4% K = 0.53						

Through comparison with the QuickBird imagery, it is clear that the algorithm is capable of defining lithological contacts more accurately than the best existing geological map (Fig. 5.9). Furthermore, the algorithm can be used to generate a more detailed lithological map by identifying lithologies in areas that have not been mapped previously. The SOM-C map is useful for highlighting areas of uncertainty in the lithological map. In general, SOM-C values less than 0.75 correspond to areas with a high degree of classification uncertainty, as clearly illustrated by the portion of Lefkara Formation incorrectly classified as pillow lavas (Fig. 5.9). In this particular case, the confusion is related to the difficulty in detecting the ground beneath some types of low-lying vegetation using airborne LiDAR. The class containing SOM-C values of 0–0.7 consists solely of SOM-C values of 0. These values are due to unlabelled neurons in the output layer which were not triggered by any of the training pixels (Li & Eastman, in press). For the purpose of classification, unlabelled neurons were assigned class labels using a minimum distance auxiliary labelling algorithm (Li & Eastman, 2006), resulting in no unclassified pixels in the lithological map. Pixels in the lithological map with corresponding SOM-C values of 0 do not necessarily possess a higher degree of uncertainty than pixels associated with larger SOM-C values. The uncertainty of pixels classified using the auxiliary labelling algorithm is case specific. Examples where such SOM-C values correspond to both correct and incorrect classification are evident throughout the study area and therefore each case should be considered individually. Frequent misclassifications occurring at the contacts between agricultural alluvium–colluvium and upstanding Lefkara Formation outcrops are highlighted by SOM-C values of 0. Ploughing proximal to the contacts is responsible for pixels with atypical topographic characteristics, which results in them being incorrectly classified as pillow lavas through the auxiliary labelling algorithm.

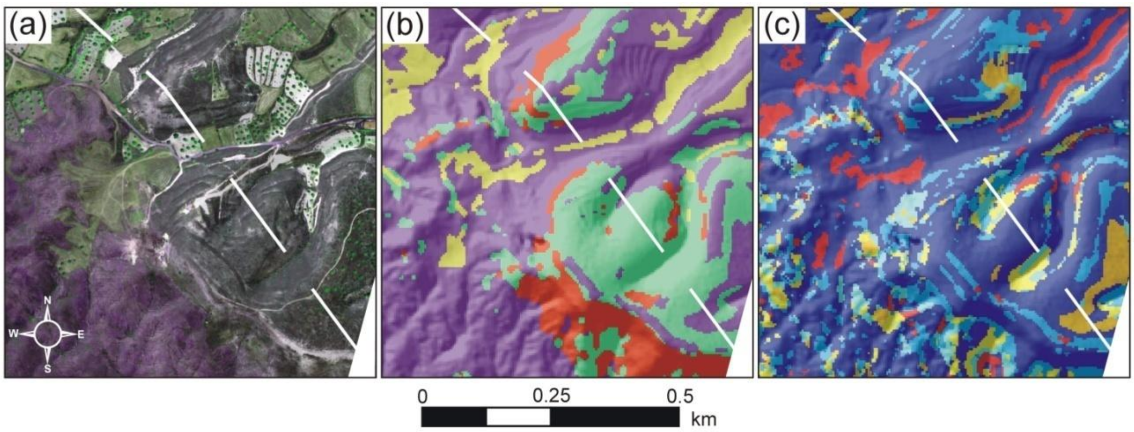

Fig. 5.9. Detailed view of the mapping performance for the area shown in Fig. 5.8. **(a)** QuickBird image, **(b)** lithological map generated using LiDAR-derived topographic data and **(c)** SOM-C map. The white dashed line represents the pillow lava–Lefkara Formation contact from the 1:250,000-scale geological map in Fig. 5.2a.

The accuracy of the lithological map produced in this study is higher than the accuracies reported by Wallace (2005) who investigated an area with a simpler lithological outcrop pattern. In contrast to Wallace’s (2005) study, our analysis involves a larger number of morphometric variables and a more complex classification algorithm. In addition, the distribution of the pillow lavas, Basal Group and overlying sediments is more complex because they are separated by low-angle contacts and are differentially eroded. Therefore, there is no simple strike-belt pattern. Given the geological complexity and anthropogenic factors affecting the topography in this study area, we consider the results of our algorithm to be good. Additionally, the algorithm was implemented using minimal *a priori* knowledge of the spatial distribution of each lithological unit. However, higher mapping accuracies can be achieved using more a priori knowledge. Doubling the total number of training pixels (to approximately 2% of the total number of pixels within the study area) increases the overall accuracy to 67.3% and Κ to 0.56 when the same SOM network parameters are used. The ability to produce good mapping results given limited knowledge regarding the spatial distribution of units makes this algorithm particularly relevant to mapping relatively unexplored terrain.

5.7 Conclusions

This study assesses the efficacy of airborne LiDAR topographic data for detailed lithological mapping of a geologically complex area of the Troodos ophiolite, Cyprus. Typical topographic characteristics associated with each of the lithologies were recognised in a 4 m LiDAR DTM and quantified using a morphometric approach. An optimal set of morphometric variables for lithological discrimination were identified and used in conjunction with a SOM classifier to produce a lithological map. The resulting map achieved an overall accuracy of 65.4% and a Κ of 0.53, which is considered good given the complexity of the study area and the lack of a priori knowledge. The lithological map is more detailed than the best existing geological map and the lithological contacts are more accurately defined. The results of this study demonstrate the significant potential of airborne LiDAR as a tool for generating detailed lithological maps over large areas of either forested or non-forested terrain, where conventional methods are of limited use. Furthermore, the SOM-C map highlights areas with high classification uncertainty, therefore providing information regarding follow-up targets for efficient ground-based verification.

Further studies are required to assess whether improvements in the lithological mapping accuracy can be made through the integration of airborne LiDAR data with high-resolution multispectral imagery. It is anticipated that the multispectral imagery will help to reduce misclassification in non-vegetated areas where the natural topographic characteristics of the various rock types have been destroyed by anthropogenic activity.

The detailed lithological map generated in this study represents a valuable aid to VMS mineral exploration in the Troodos ophiolite because the mapped distribution of potential host rocks is now much better resolved than on previous maps. In addition, the efficacy of this algorithm extends to other geological settings where lithology and topography are positively correlated, with exciting implications beyond mineral exploration. In particular, the relative ease with which basement rocks and sedimentary cover can be discriminated at high-resolution could be useful in all terrains from open ground to densely forested landscapes for: 1) identifying local areas for groundwater extraction, 2) locating areas with enhanced agricultural potential, and 3) for general infrastructure planning where it is important to know construction site substrates. Thus the methods presented here may have widespread utility for a range of applications, especially in areas of mixed basement and sedimentary cover exposure.

6. Integrating ATM imagery and airborne LiDAR data for enhanced lithological mapping

This chapter is derived from:

Grebby, S., Naden, J., Cunningham, D., & Tansey, K. (2011). Integrating airborne multispectral imagery and airborne LiDAR data for enhanced lithological mapping in vegetated terrain. *Remote Sensing of Environment, 115*, 214–226.

Abstract

Practical and financial constraints associated with traditional field-based lithological mapping are often responsible for the generation of maps with insufficient detail and inaccurately located contacts. In arid areas with well exposed rocks and soils, high-resolution multi- and hyperspectral imagery is a valuable mapping aid as lithological units can be readily discriminated and mapped by automatically matching image pixel spectra to a set of reference spectra. However, the use of spectral imagery in all but the most barren terrain is problematic because just small amounts of vegetation cover can obscure or mask the spectra of underlying geological substrates. The use of ancillary information may help to improve lithological discrimination, especially where geobotanical relationships are absent or where distinct lithologies exhibit inherent spectral similarity. This study assesses the efficacy of airborne multispectral imagery for detailed lithological mapping in a vegetated section of the Troodos ophiolite (Cyprus), and investigates whether the mapping performance can be enhanced through the integration of LiDAR-derived topographic data. In each case, a number of algorithms involving different combinations of input variables and classification routine were employed to maximise the mapping performance. Despite the potential problems posed by vegetation cover, geobotanical associations aided the generation of a lithological map — with a satisfactory overall accuracy of 65.5% and Kappa of 0.54 — using only spectral information. Moreover, owing to the correlation between topography and lithology in the study area, the integration of LiDAR-derived topographic variables led to significant improvements of up to 22.5% in the overall mapping accuracy compared to spectral-only approaches. The improvements were found to be considerably greater for algorithms involving classification with an artificial neural network (the Kohonen Self-Organizing Map) than the parametric Maximum

Likelihood Classifier. The results of this study demonstrate the enhanced capability of data integration for detailed lithological mapping in areas where spectral discrimination is complicated by the presence of vegetation or inherent spectral similarities.

6.1 Introduction

Over large areas and where the terrain is geologically complex or poorly accessible, field-based lithological mapping can be time-consuming, costly and challenging (Gad & Kusky, 2007; Grunsky et al., 2009; Rogge et al., 2009). For these reasons lithological maps are typically generated using limited numbers of field and outcrop observations which may, as a consequence, result in some concern regarding the accuracy of the lithological contacts (Philip et al., 2003). Remote sensing data, such as aerial photographs and multi- and hyperspectral imagery, offers solutions to many of the restrictions associated with field-based surveys. For instance, remotely sensed data can provide more continuous and detailed information for large areas, thus enabling even the most inaccessible terrain to be mapped for only a fraction of the time and cost required for an equivalent field survey.

The application of multi- and hyperspectral imagery to lithological mapping is well established for arid and semi-arid areas which are essentially devoid of vegetation. Due to the good exposure of rocks and soils, lithology can be mapped directly by matching image pixel spectra with the reference reflectance spectra of individual rock units using automated classification routines (e.g., Rowan & Mars, 2003; Harris et al., 2005; Roy et al., 2009). However, spectral discrimination and mapping in all but the most barren terrain can be problematic, because just small amounts ($\geq$ 10%) of vegetation cover (e.g., trees, shrubs and lichen) can obscure or completely mask the spectra of underlying lithologies (Siegal & Goetz, 1977; Ager & Milton, 1987; Murphy & Wadge, 1994).

Where the effects of vegetation prevail, image processing techniques such as principal component analysis (Fraser & Green, 1987; Loughlin, 1991) and spectral unmixing (Bierwirth, 1990; Chabrillat et al., 2000; Zhang et al., 2005) have been employed to try and separate the spectral responses of vegetation and substrate, and to detect rock exposures at sub-pixel resolutions. Alternatively, indirect lithological discrimination is possible if geobotanical relationships with the underlying substrates are realised (Paradella et al., 1997; Leverington, 2010). For example, Rowan et al. (2004) utilised subtle spectral features relating to variations in vegetation cover to map specific lithological units in the Mordor Complex, Australia, while Harris et al. (2005) used a vegetation spectral end-member as a proxy for mapping metagabbroic rocks in southern Baffin Island, Canada. However, if lithology and vegetation are unrelated, or if distinct lithologies exhibit an inherent spectral similarity regardless of vegetation cover, spectral data alone are often insufficient for successful discrimination (Schetselaar et al., 2000; Dong & Leblon, 2004). In such circumstances it may be beneficial to consider ancillary information for the differentiation and mapping of lithological units.

Numerous studies have assessed the ability to augment the lithological mapping results of spectral-only classifications by incorporating ancillary data such as topographic information (Hutchinson, 1982; Ricchetti, 2000), spectral-derived texture (Chica-Olmo & Abarca-Hernández, 2000; Li et al., 2001) and radar-derived texture (Mather et al., 1998; Dong & Leblon, 2004). These data are potentially useful because they provide information about the surface morphology, which is often found to be correlated with lithology through differences in the weathering and erosion characteristics of individual units (Mather et al., 1998; Kühni & Pfiffner, 2001; Belt & Paxton, 2005). Although previous studies have demonstrated the capability to improve lithological classification accuracies through data integration, they have been confined to using data with only moderate-to-coarse spatial resolutions (i.e., 12.5–30 m). The potential to delineate lithological contacts in finer detail and with better accuracy is further enhanced by the availability of high-resolution remote sensing data (Philip et al., 2003).

Aircraft-mounted sensors provide remotely sensed data with a spatial resolution of up to an order of magnitude greater than the classic spaceborne sensors such as Landsat TM and ASTER. Furthermore, airborne surveys are commonly exploited for the concomitant acquisition of multisource data; in particular both multi- or hyperspectral imagery and Light Detection And Ranging (LiDAR) data. In contrast to passive spectral sensors, airborne LiDAR is an active remote sensing technique that has the capability of acquiring accurate and high-resolution (ca. 1–4 m) topographic data, even through forest cover (Kraus & Pfeifer, 1998). It offers a solution for overcoming the obscuring effects that dense vegetation has on lithological discrimination because laser reflections (or returns) from the ground can be separated from vegetation returns to virtually deforest the terrain, enabling the generation of digital terrain models (DTMs; Haugerud & Harding, 2001). The resulting high-resolution DTMs can then be used both qualitatively (Webster et al., 2006a 2006b) and quantitatively (Wallace, 2005; Wallace et al., 2006; Grebby et al., 2010) to reveal subtle topographic differences that reflect changes in lithology. Topographic data from sources other than airborne LiDAR can lack the spatial resolution required for delineating subtle contacts between lithological units (Webster et al., 2006a). Accordingly, the integration of airborne LiDAR topographic data with airborne multi- or hyperspectral imagery may provide a significant improvement of the classification results, especially in cases where there are no geobotanical relationships. However, the true efficacy of this approach has not yet been demonstrated.

This study concerns the detailed lithological mapping of a vegetated section of the Troodos ophiolite, Cyprus. In a previous study for the same area, Grebby et al.

(2010) demonstrated the ability to discriminate and map the main lithological units to a respectable accuracy solely using LiDAR-derived topographic information. Despite this, natural and anthropogenically induced deviations from the typical topographic characteristics were the cause of some classification confusion between specific units. In an effort to identify a more optimal approach, the aims of the current study are to: (i) assess the efficacy of airborne multispectral imagery for detailed lithological mapping and (ii) utilise the results of the previous study to investigate whether the integration of airborne LiDAR-derived topographic data can further enhance the mapping capabilities. For both aims, a number of different algorithms were investigated in an attempt to maximise the mapping accuracy. The mapping results of the algorithms were first assessed individually using conventional classification accuracy statistics, before pair-wise comparisons were made in order to establish the algorithm capable of generating the most accurate lithological map.

6.2 Study Area

The study area is located in the foothills on the northern flank of the Troodos ophiolite, Cyprus (Fig. 6.1). The Troodos ophiolite is an uplifted slice of oceanic crust and lithospheric mantle that was created through sea-floor spreading (Gass, 1968; Moores & Vine, 1971). Exhibiting a dome-like structure centred on Mt. Olympus (1,952 m), the ophiolite stratigraphy includes a mantle sequence comprising harzburgites, dunites and a serpentinite diapir exposed at the highest elevations. This mantle sequence is stratigraphically overlain by a largely gabbroic plutonic complex, a sheeted dyke complex, extrusive lavas and oceanic sediments at decreasing elevations along the northern slope of the range (Varga & Moores, 1985).

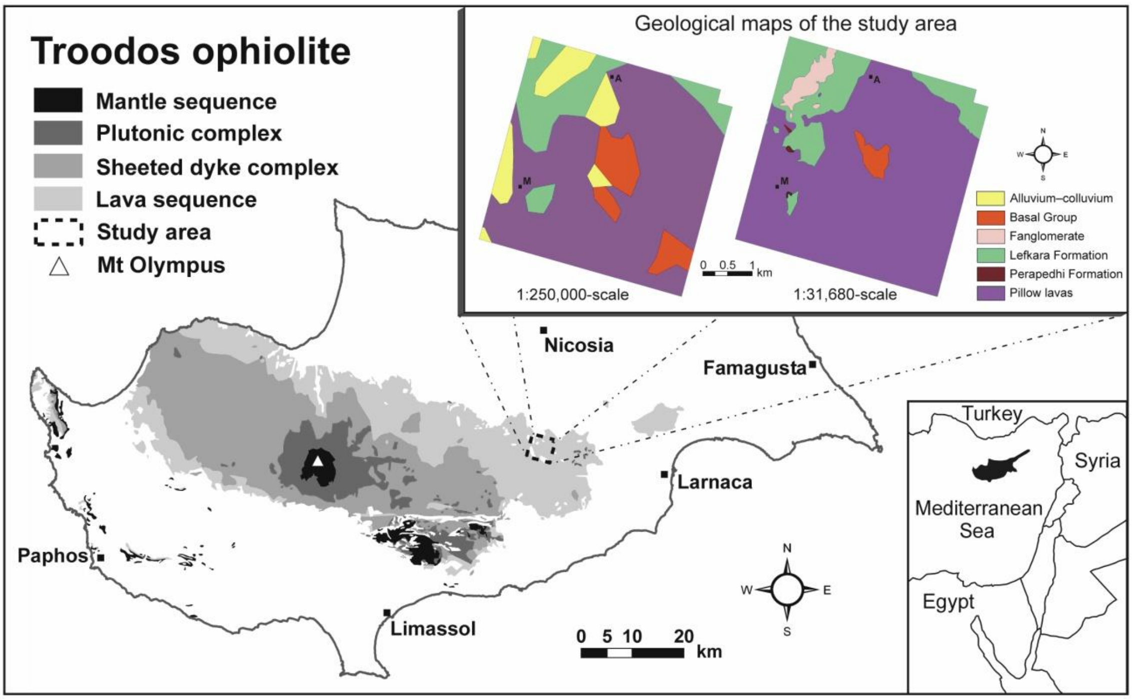

Fig. 6.1. Simplified geology of the Troodos ophiolite and existing geological maps of the study area (inset; M – Mathiati mine and A – Agia Varvara Lefkosias). Digital geology provided by the Geological Survey Department of Cyprus.

The study area covers approximately 16 km^2 of the upper section of the ophiolite, and comprises four main lithological units — the Basal Group lavas and dykes, pillow lavas (Upper and Lower), Lefkara Formation chalky marls and alluvium–colluvium. Two published geological maps of the island cover this area at both regional and local mapping scales (see Fig. 6.1). The 1:31,680-scale map is the product of a mapping campaign undertaken in the late 1950’s and early 1960’s, whereas the 1:250,000-scale map is the more recent version, revised in 1995. Regardless of scale, the two maps exhibit some obvious geological differences. This can be ultimately attributed to the limited area covered during fieldwork, the subjectivity of the employed mapping techniques and some degree of ambiguity in defining a number of the lithological units.

Stratigraphically, the Basal Group is the lowest unit in the study area. Consisting of both dykes and screens of pillow lavas, this unit represents a transition from the underlying sheeted dyke complex (100% dykes) to the overlying pillow lavas. An exact definition of the Basal Group is somewhat lacking, although it generally contains at least 50% dykes but with a more common dyke abundance of 80–90% (Bear, 1960). The pillow lavas have traditionally been divided into the Upper Pillow Lavas and the Lower Pillow Lavas according to mineralogy, colour and dyke abundance (Wilson 1959; Gass, 1960). However, this division is difficult to apply in the field (Govett & Pantazis, 1971) and an unconformable or transitional boundary between the two lava units has led to some uncertainty about this division (Boyle & Robertson, 1984). For this reason, the pillow lavas are treated as a single unit in the current study. The pillow lavas are stratigraphically overlain by the chalks, marls and cherts of the Lefkara Formation. This unit represents late Cretaceous to early Miocene marine sedimentation (Kähler & Stow, 1998). The alluvium–colluvium unit refers to Quaternary sediments, such as sand, silts, soils and gravels, that were deposited fluvially or through hill-slope processes. The alluvium–colluvium is commonly found filling depressions within the hummocky pillow lava terrain.

The study area contains a complex landscape due to the variable geology, both natural and anthropogenic influences on the topography, and vegetation cover. Prominent anthropogenic features include the disused Mathiati mine with spoil tips, Agia Varvara Lefkosias village (see Fig. 6.1) and a significant proportion of agricultural land which is confined to areas underlain by alluvial–colluvial materials. Vegetation is widespread throughout, covering between 30–90% of the surface area, therefore resulting in a heterogeneous surface mixture of vegetation and rock/soil (Fig. 6.2a). Correlation between some species of vegetation and particular lithological units is also apparent within this area. For example, green grasses plus a variety of crops (including olive groves) are predominantly associated with alluvium–colluvium (Fig. 6.2b), whereas in addition to some low scrubby vegetation, moderate-to-dense lichen cover is almost exclusively found growing on pillow lava outcrops (Fig. 6.2c). Conversely, some similarities in the types of low and medium-growth vegetation commonly found growing on the Lefkara Formation and Basal Group terrain are also apparent. Other types of mostly sporadic vegetation cover occurring throughout the study area include trees — ranging from isolated trees (e.g., pines and oaks) to dense thickets and copses — and areas covered by tall, dry grasses and other scrubland.

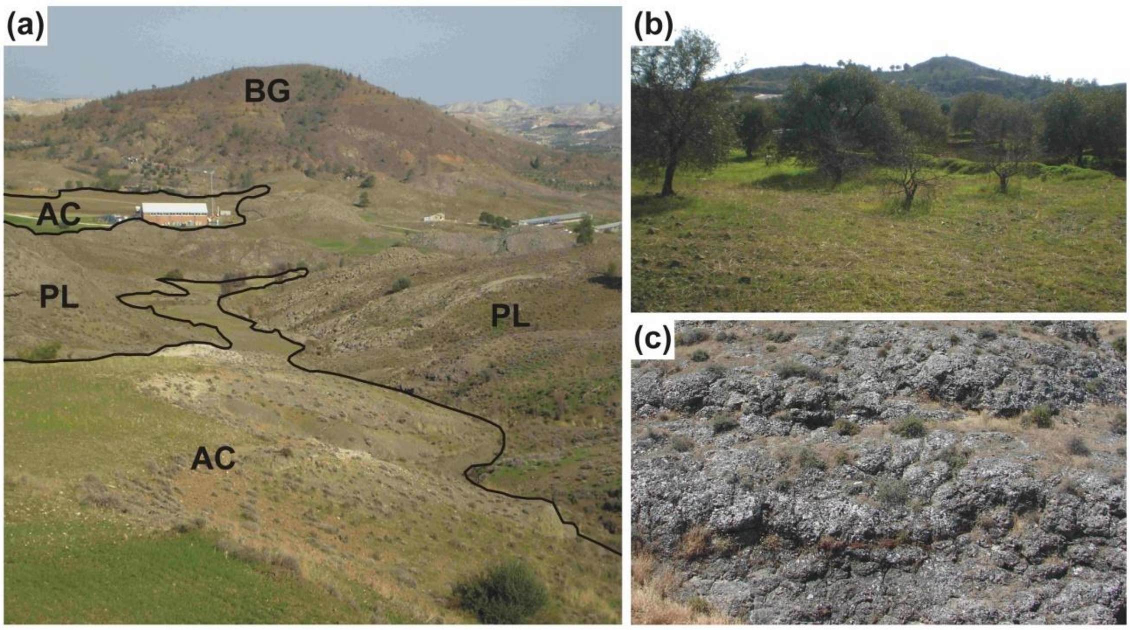

Fig. 6.2. Field photographs of the study area showing: **(a)** the heterogeneous vegetation cover and typical vegetation types associated with **(b)** alluvium–colluvium and **(c)** the pillow lavas.

6.3 Data and pre-processing

6.3.1 Airborne multispectral imagery

Airborne Thematic Mapper (ATM) multispectral imagery was acquired by the Natural Environment Research Council (NERC) Airborne Research and Survey Facility (ARSF) in May, 2005. The ATM imagery comprises 11 spectral bands in the visible/near-infrared (VNIR; Bands 1–8), short-wave infrared (SWIR; Bands 9–10) and thermal infrared (TIR; Band 11). Since this study is concerned with only reflectance data, the TIR band (Band 11) was discarded. Band 1 was also omitted as the data are significantly affected by atmospheric scattering (Copley & Moore, 1993). Five northwest-southeast trending flight-lines of imagery were acquired over the study area and delivered as Level 1b Hierarchical Data Format (HDF) files, with radiometric calibration algorithms applied and aircraft navigation information appended. Radiometric calibration involved conversion of the raw ATM data to at-sensor radiance units and then subsequent scaling to 16-bit digital numbers (DNs). All image strips were individually geocorrected and re-sampled to a spatial resolution of 4 m using the AZGCORR software (Azimuth Systems) in conjunction with a 4 m LiDAR digital elevation model.

Across-track (i.e., perpendicular to the flight direction) brightness differences observed in all geocorrected images were minimised through a multiplicative second-order polynomial correction, which was applied using the Cross-track Illumination Correction tool in ENVI 4.3 (ITT Visual Information Solutions, 2006). Following this correction, image strips were co-registered with the aid of tie-points identified in pairs of overlapping images, and then mosaicked to create a single seamless image; both tasks were performed within ENVI 4.3. Colour Balancing was applied during mosaicking to minimise the spectral differences between overlapping images. This procedure calculates gains and offsets from a fixed image and then uses these to adjust the spectral values of an overlapping image, thus matching the spectral statistics between the images. Due to an absence of ground reflectance spectra and atmospheric measurements at the time of the airborne survey, rigorous model or empirical-based atmospheric corrections could not be reliably applied. Moreover, an inspection of the spectral values in the pre-processed imagery suggested that first-order atmospheric correction for effects such as haze was not necessary and, as a consequence, no atmospheric correction was applied to the ATM imagery.

6.3.2 Airborne LiDAR data

At the same time as the ATM data acquisition an airborne LiDAR survey was also undertaken using an Optech ALTM-3033 system. It was undertaken at an average flying altitude of 2550 m above sea level, resulting in an aircraft–ground distance ranging between 2100–2300 m due to topographic relief on the order of 200 m. The ALTM-3033 system was operated with a laser pulse repetition rate of 33 kHz and half-scan angle of ±19.4° either side of the nadir, resulting in the collection of approximately 7,600,000 points for the study area with an average density of 0.48 points per m^2. The dataset contains point data from five overlapping flight-lines, each with a swath width of 1400–1500 m and an overlap of 20%–50% between adjacent swaths. Following pre-processing by the Unit for Landscape Modelling (ULM) at the University of Cambridge, UK, the LiDAR point data were delivered as ASCII files containing the x-y-z coordinates of all first and last returns in the WGS84 Universal Transverse Mercator (UTM) zone 36-North coordinate system. Following delivery, the point data were classified as either ground or non-ground returns using a triangulated irregular network (TIN) densification algorithm (Axelsson, 2000). This algorithm, which is implemented in the TerraScan software (Terrasolid Ltd.), first establishes a set of low (ground) points and then iteratively classifies the remaining points as either ground or non-ground returns according to angle and distance thresholds applied to TIN facets. For further information regarding the classification process, such as the parameters and thresholds used and verification of the results, the reader is referred to Grebby et al. (2010). Following classification, non-ground returns were discarded, while those classified as ground were then used to generate a DTM. As the choice of interpolation algorithm and spatial resolution can affect the accuracy of DTMs, an experiment was conducted in order to determine the most appropriate combination (Grebby et al., 2010). Consequently, a 4 m DTM was generated in Surfer 8.0 (Golden Software, Inc.) using a block kriging algorithm, since this combination resulted in the smallest interpolation errors. As a final step, the ATM imagery was subsequently co-registered to the 4 m DTM in ENVI 4.3, using an RST method with image-selected tie-points and cubic convolution resampling.

6.4 Methods

The methodology employed here to assess the efficacy of ATM imagery for detailed lithological mapping in vegetated terrain, and to evaluate whether improvements can be made through the integration of LiDAR-derived topographic data, is outlined in Fig. 6.3. In summary, the mapping methodology consists of four main steps: 1) the selection of training and validation pixels, 2) derivation of the input variables, 3) classification, and 4) an accuracy assessment.

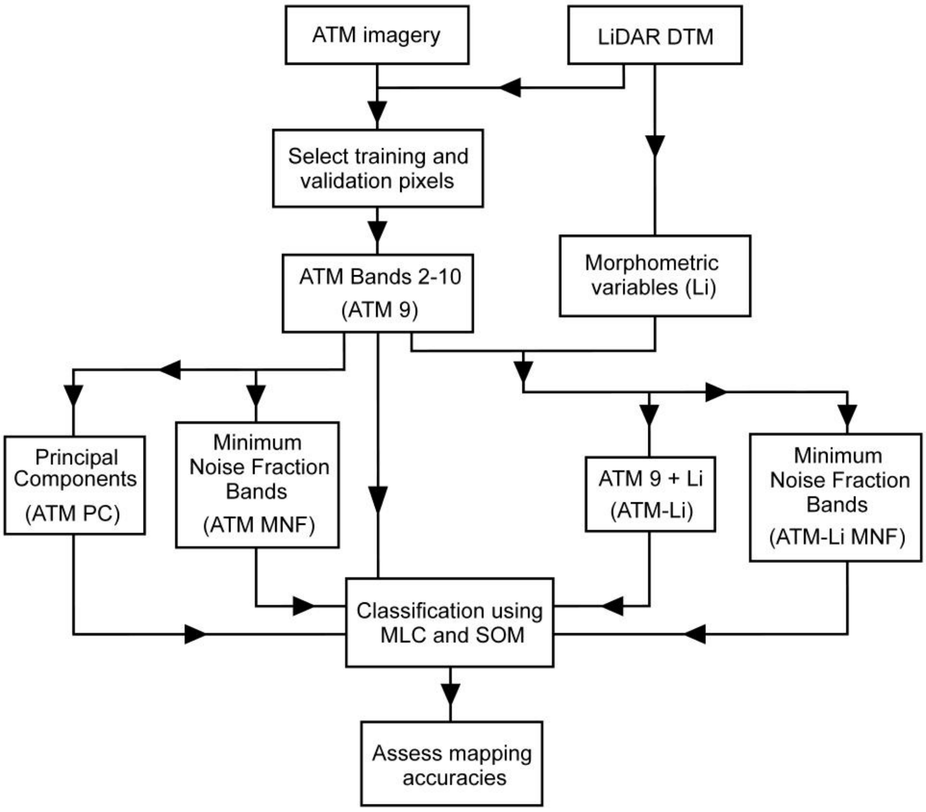

Fig. 6.3. Overview of methodological approach used to assess the efficacy of ATM imagery and the integration of LiDAR-derived topographic data for detailed lithological mapping. Bracketed acronyms (see section 6.4.2 for explanation) denote names of sets of input variables used in conjunction with the Maximum Likelihood Classifier (MLC) and the Kohonen Self-Organizing Map (SOM).

6.4.1 Training and validation pixels

Two independent samples of pixels with known class identities were identified for training and validating the algorithms. The set of training pixels was used to assist all classifications of the full scene by helping to spectrally and topographically characterise the four lithological units. This set comprised pixels located within four representative areas (i.e., regions of interest; ROIs) with unambiguous class identities, which were carefully defined in the imagery using information gathered from detailed field surveys and 0.7 m QuickBird satellite imagery. Due to the inconsistencies between the existing geological maps, their use was limited at this stage to providing only a general lithological overview of the study area. The number of training pixels representing each unit was deliberately kept to a minimum to investigate how the algorithms perform using only minimal *a priori* information about the spatial distribution of the lithologies. In total, the training dataset comprises less than 1% of the total number of pixels within the study area (Table 6.1).

Table 6.1. Number of pixels, the equivalent area and the proportion of the study area (PS) selected to represent each lithological class during training and validation.

Lithological class	Training			Validation		
	Pixels	Area (m^2)	PS (%)	Pixels	Area (m^2)	PS (%)
Alluvium–colluvium	1712	27,392	0.17	4087	65,392	0.40
Basal Group	1780	28,480	0.18	3200	51,200	0.32
Lefkara Formation	2769	44,304	0.27	2451	39,216	0.24
Pillow lavas	3095	49,520	0.31	3208	51,328	0.32

The accuracy of a thematic map is customarily determined by comparing the true class identities of a sample of validation pixels to those assigned through classification. In order to obtain a statistically valid accuracy estimate for an entire mapped area from only a sample of validation pixels, an appropriate sample size is required (Foody, 2009). The required sample size can be determined using statistical sampling theory such as the normal approximation of the binomial distribution (Fitzpatrick-Lins, 1981):

$$n = \frac{\mathrm{Z}^2 pq}{E^2}, \tag{6.1}$$

where n is the sample size, Z is the critical value of the normal distribution for the two-tailed significance level, p is the expected accuracy, q = 100–p, and E is the allowable error (or level of precision). If the value of p is unknown, then a "worst case" (large) estimate of n can be found by maximising the term pq using p = 50.

Although the sample size determined using the above method is suitable for estimating the overall accuracy of a thematic map — where pixels are either correctly or incorrectly classified — it does not account for the confusion that may occur between multiple classes (Congalton, 1991). To ensure that each class is adequately represented in a confusion matrix, Congalton (1991) suggests using a minimum of 50 to 100 validation pixels per class. Alternatively, the minimum number of samples for each class can be determined from the multinomial distribution (Tortora, 1978; Congalton & Green, 1999). For a specified confidence level (α) and absolute precision (b_i), the required number of samples, $n_{i,}$, for class i can be calculated as:

$$\boldsymbol{n}_i = \frac{B\Pi_i\left(1-\Pi_i\right)}{\boldsymbol{b}_i^{\,2}} \tag{6.2}$$

where Π_i is the proportion of the scene covered by class i, B is the upper $(\alpha/k) \times 100^{th}$ percentile of the χ^2 distribution with one degree of freedom, and k is the number of exhaustive and mutually exclusive classes. A total of k calculations are needed to determine the sample sizes for all classes, with the largest n typically chosen as the required sample size for all individual classes. Again, if Π_i is unknown, then a large estimate of n_i can be found by assuming Π_i = 0.5.

To achieve statistically valid estimates of both the overall accuracy and individual class accuracies for the whole map, the validation sample must satisfy both the total and individual class size criteria. Therefore, in order to derive estimates of the overall accuracy of a map to say a precision of ±1% (E = 1) and the individual class accuracies to a precision of ±3% (b_i = 0.03) at the 95% confidence level (α = 0.05; also assuming p = 50; Π_i = 0.5), a validation sample of at least 9,604 pixels is required, with a minimum of 1,734 pixels in each class. To achieve this, several ROIs with unambiguous class identities were defined throughout the imagery to represent each lithological class — again with the aid of field knowledge and QuickBird imagery. Validation pixels were then sampled from these ROIs using a random stratified sampling protocol to ensure classes were represented proportionally, and to help reduce bias caused by spatial autocorrelation (Chini et al., 2008; Pacifici et al., 2009). Consequently, a total of 12,946 validation pixels were sampled, with a minimum class size of 2,451 pixels. Details regarding the areal extent and the number of pixels selected to represent each lithological class during validation can also be found in Table 6.1.

6.4.2 Derivation of variables

6.4.2.1 Spectral variables

The efficacy of ATM imagery for lithological mapping in the vegetated Troodos study area was assessed by deriving three sets of spectral variables for use as inputs for classification. The first set of input variables (ATM 9) comprised the nine ATM Bands 2–10. However, an examination of the spectral signatures for the lithologies reveals low separability for some units (Fig. 6.4). A combination of inherent or vegetation-induced spectral similarities and the considerable intra-class variability due to heterogeneous vegetation cover are ultimately responsible for this lack of distinction.

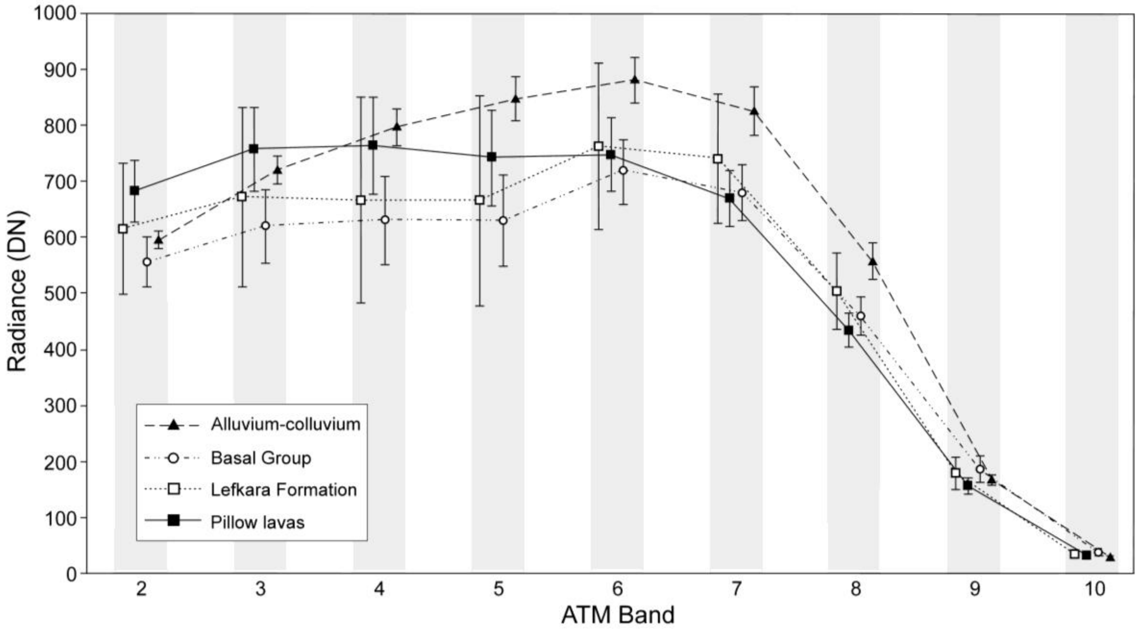

Fig. 6.4. Mean spectral signatures (±1 standard deviation) derived from training pixels for ATM Bands 2–10. Radiometrically calibrated radiance values are expressed as 16-bit digital numbers (DNs). Spectra are horizontally offset within ATM bands for clarity.

In order to try and improve lithological discrimination, two image enhancement techniques were employed: principal component analysis (PCA) and the Minimum Noise Fraction (MNF) transformation. Variables derived from the application of PCA and the MNF transformation are frequently used as inputs to classifiers to try to enhance the spectral separability of classes present within the original imagery (Li & Moon, 2004; Belluco et al., 2006; Liberti et al., 2009). A second set of spectral variables was therefore derived through the application of PCA to the nine ATM bands. The PCA technique can enhance spectral information by decorrelating the data, segregating noise and reducing the data dimensionality (Jensen, 2005). The outcome of PCA is a new set of uncorrelated variables called Principal Components (PCs), which are linear combinations of the original nine ATM bands. These PCs are ordered decreasingly in terms of the proportion of the total data variance they contain, with the higher-order PCs containing most of the total variance. The small proportion of the total variance contained within the lower-order PCs is mostly regarded as the noise within the original ATM bands, and so discarding these PCs effectively segregates this noise. Following the PCA transformation, examination of the eigenvalues revealed that the first three PCs accounted for 97.5% of the total image variance (Table 6.2), while the remaining six PCs were deemed to contain mostly noise. Consequently, in an attempt to enhance lithological discrimination, only the first three PCs were selected to form the second set of inputs variables for classification (ATM PC). Eigenvector loadings in Table 6.2 show that the first PC (PC1) receives equal positive contributions from all nine ATM bands and therefore represents albedo information. The high positive eigenvector loadings for ATM Bands 7 and 8 indicate that PC2 describes the presence of vegetation, which is highly reflective in the near-infrared (0.76–1.05 μm). The third PC primarily describes the contrast between the VNIR and SWIR regions of the electromagnetic spectrum.

Table 6.2. Eigenvalues and eigenvector loadings for the first three PCs derived from the application of PCA to ATM Bands 2–10. Eigenvector loadings measure the contribution of the original ATM bands to each PC.

Eigenvectors	PC1	PC2	PC3
ATM 2	0.33	-0.40	-0.19
ATM 3	0.35	-0.32	-0.20
ATM 4	0.35	-0.26	-0.16
ATM 5	0.36	-0.17	-0.14
ATM 6	0.36	0.19	-0.19
ATM 7	0.33	0.47	-0.19
ATM 8	0.30	0.57	-0.05
ATM 9	0.32	0.17	0.50
ATM 10	0.29	-0.19	0.74
Eigenvalues	7.25	1.00	0.53
Variance (%)	80.56	11.10	5.84
Cumulative variance (%)	80.56	91.66	97.50

Spectral enhancement and data compression was also performed using the Minimum Noise Fraction (MNF) transformation (Green et al., 1988). The MNF transformation determines the inherent dimensionality of the data and segregates noise using two PCA transformations (Boardman & Kruse, 1994). The first transformation — based on an estimated noise covariance matrix — decorrelates and rescales the data noise, while the second step comprises a PCA transformation of the noise-whitened data. As a result, the MNF transformation produces a set of coherent eigenimages (MNF bands) with correspondingly large eigenvalues (i.e., signal-to-noise ratios), and an accompanying set of noise-dominated images characterised by small eigenvalues. Accordingly, image noise can be segregated by selecting only the coherent MNF Bands.

The MNF transformation implemented in ENVI 4.3 was applied to ATM Bands 2–10. An estimate of the noise statistics was generated from a lithologically homogeneous area of alluvium–colluvium that was overlain with variable vegetation cover. As the spectral response of the underlying lithological substrate was considered to be constant in this area, it was expected that the noise would primarily relate to the spectral variability caused by the heterogeneous rock/vegetation surface mixture. Although the noise estimate considers only one lithological unit, an MNF transformation based on these statistics was still anticipated to produce an overall reduction in vegetation-related spectral variability throughout, and a consequential increase in lithological discrimination. Of the resulting nine MNF bands, the first four accounted for approximately 99% of the cumulative eigenvalues for the data (Table 6.3). These four MNF bands were subsequently selected to comprise the third set of spectral variables (ATM MNF), while the remaining five noise-dominated MNF bands were discarded. According to the eigenvector loadings shown in Table 6.3, the four selected MNF bands receive their highest loadings from the ATM bands situated in the visible part of the spectrum (i.e., Bands 2–5). In addition, the relatively minor contributions of ATM Bands 7 and 8 to all four MNF bands are noteworthy.

Table 6.3. Eigenvalues and eigenvector loadings for the first four MNF bands derived from the MNF transformation of ATM Bands 2–10. Eigenvector loadings measure the contribution of the original ATM bands to each MNF band.

Eigenvectors	MNF1	MNF2	MNF3	MNF4
ATM 2	0.94	0.13	0.08	0.27
ATM 3	0.04	-0.88	0.38	0.09
ATM 4	0.14	0.13	0.28	-0.84
ATM 5	-0.18	0.36	0.72	0.21
ATM 6	0.10	-0.05	-0.13	-0.21
ATM 7	0.11	-0.04	-0.25	-0.23
ATM 8	-0.01	0.03	0.15	-0.06
ATM 9	-0.09	0.20	0.17	0.16
ATM 10	0.18	-0.08	0.35	-0.22
Eigenvalues	2660.43	218.50	76.66	52.54
Proportion (%)	87.28	7.17	2.51	1.72
Cumulative proportion (%)	87.28	94.45	96.96	98.68

6.4.2.2 Integrated spectral and topographic variables

As the occurrence of vegetation is likely to affect the spectral discrimination and mapping of lithologies, ancillary topographic information was also considered. Within the Troodos study area, a correlation between topography and the four lithological units is clearly evident in the field. Grebby et al. (2010) showed it was possible to exploit this relationship to discriminate and map these lithologies solely using topographic information derived from a 4 m LiDAR DTM. Derived at their appropriate scales, the five morphometric variables of slope, absolute profile curvature, absolute plan curvature, residual roughness and the hypsometric integral were found to be optimal for separating the topographic characteristics of the four lithological units.

In an attempt to improve the mapping results of the spectral-only classifications, these five morphometric variables were integrated with the ATM spectral imagery through two different approaches. The simplest approach to integrating ancillary data is to increase the number of variables used as inputs to the classification — a technique known as the “logical channel” approach (Strahler et al., 1978). Accordingly, the five morphometric variables were merged with the nine ATM bands to form a first integrated set of fourteen input variables (ATM-Li). Multisource data can also be integrated using both PCA and the MNF transformation. A comparison of the two approaches by Mutlu et al. (2008) robustly demonstrates the superior classification results that are achievable using the MNF approach to multisource integration. Therefore, in order to try and enhance the spectral-topographic discrimination of lithologies while simultaneously reducing data redundancy, the MNF transformation was applied to the merged set of fourteen spectral and morphometric variables. As a result, the first five MNF bands accounted for approximately 98% of the cumulative eigenvalues (Table 6.4) and were subsequently selected to form the second set of integrated variables for classification (ATM-Li MNF). The first of these five integrated MNF bands (MNF1) receives its highest loading from ATM Band 2, with sizeable contributions also from ATM Band 5, and the absolute profile curvature and residual roughness variables. Both absolute profile curvature and ATM Band 5 contribute the most information to the second MNF band, while also contributing significantly, along with residual roughness, to MNF3. The fourth MNF band largely describes the contrast between absolute plan curvature and the hypsometric integral, whereas MNF5 receives high positive loadings from both of these morphometric variables.

Table 6.4. Eigenvalues and eigenvector loadings for the first five MNF bands derived from the MNF transformation of the fourteen spectral and morphometric variables. Eigenvector loadings measure the contribution of the original bands to each MNF band.

Eigenvectors	MNF1	MNF2	MNF3	MNF4	MNF5
ATM 2	0.70	0.12	-0.20	-0.21	0.10
ATM 3	0.02	-0.12	0.00	0.25	-0.01
ATM 4	0.15	0.40	0.14	0.14	-0.36
ATM 5	-0.36	-0.51	-0.47	-0.02	-0.15
ATM 6	-0.07	0.02	-0.08	0.02	-0.05
ATM 7	-0.01	-0.11	0.05	0.06	0.09
ATM 8	0.02	0.02	0.03	-0.04	0.03
ATM 9	-0.03	-0.17	-0.06	-0.05	0.22
ATM 10	0.09	-0.12	0.10	-0.08	0.01
Slope	-0.06	0.10	-0.06	-0.01	-0.09
|Profile curvature|	0.36	-0.65	0.56	0.15	-0.04
|Plan curvature|	0.11	0.08	-0.23	0.64	0.65
Residual roughness	-0.41	0.21	0.52	0.24	0.09
Hypsometric integral	-0.16	0.04	0.21	-0.60	0.58
Eigenvalues	7942.20	2422.13	1300.35	247.91	201.14
Proportion (%)	64.47	19.66	10.55	2.01	1.63
Cumulative proportion (%)	64.47	84.13	94.68	96.69	98.32

6.4.3 Classification

The three sets of spectral variables and two sets of integrated spectral-topographic variables derived above were used in conjunction with classification routines to generate lithological maps. With the aid of the training pixels, supervised classification was performed using two classifiers with contrasting properties; the statistical Maximum Likelihood Classifier (MLC) and a non-parametric artificial neural network, called the Kohonen Self-Organizing Map (SOM; Kohonen, 1982, 2001).

The MLC is a popular image classifier that assumes the class probability density functions are multivariate normal (Mather et al., 1998). Individual class probability density functions are first computed using the mean vectors and covariance matrices of the classes, which are antecedently determined from the training pixels. Using this information, the probabilities of an image pixel belonging to each of the classes is estimated and the pixel is accordingly assigned to the class for which the probability is highest. Where prior knowledge of the study area is available, the MLC classification can also be refined using prior probabilities (Mather et al., 1998). However, since it was the intention to restrict the *a priori* knowledge to only a small number of training pixels in this study, the MLC was used with equal prior probabilities for each lithological class.

In many cases, the utility of statistical classifiers, such as the MLC, are often compromised by the prevalence of complex lithological class probability density functions, which arise due to spatial variability in vegetation cover (Leverington, 2010). Furthermore, the simple multivariate normal assumption regarding class probability density functions is also often invalid for ancillary data (Hutchinson, 1982). Following this, it is apparent that artificial neural networks (NNs) are better suited to lithological classification because they are non-parametric, robust in handling noisy data and can learn complex input patterns (Ji, 2000). These advantages over conventional classifiers are responsible for the increasing interest in NNs, the most popular of which is the Multilayer Perceptron (MLP). Alternative NNs, particularly the SOM, have not been investigated as thoroughly as the MLP. Nevertheless, the SOM is becoming increasingly popular as a classifier, by demonstrating its ability to achieve promising results for many remote sensing applications, including land-use classification (Ji, 2000; Bagan et al., 2005; Jianwen & Bagan, 2005), and lithological mapping (Mather et al., 1998; Bedini, 2009). Considering this, all input variables were additionally classified using the SOM algorithm implemented in IDRISI Andes (Li & Eastman, 2006), which is summarised below.

A SOM network consists of two layers; an input layer containing one neuron for each of the input variables, and an output layer made up of a two-dimensional array of neurons. Neurons in the output layer are connected to those in the input layer via synaptic weights. Random synaptic weights, ranging 0–1, are initially assigned and these are then adjusted during learning to best describe patterns in the input data (Mather et al., 1998). Network learning is an iterative process and involves two stages: unsupervised coarse tuning and supervised fine tuning. During coarse tuning, normalised input vectors (i.e., pixels in spectral or combined spectral-morphometric space) are presented to the network to determine the output neuron with the best-matching weight vector. The weight vectors of this best-matching neuron and output neurons within a given neighbourhood of the winner are subsequently adjusted in the direction of the input vector according to the learning rate. Both the radius of the neighbourhood and the learning rate decrease with each iteration. Prior to fine tuning, input vectors with known class identities (i.e., training pixels) are used to preliminarily label the output neurons through a process known as majority voting. Fine tuning with the type-one Learning Vector Quantization (LVQ1) algorithm (Kohonen, 1990) was then used to define the class boundaries in the output layer more precisely. To do this, training pixels are again presented to the SOM and the weight vector of the best-matching neuron is adjusted in the direction of the training vector if its label matches the class identity of the pixel, but moved away if not. Once trained, output neurons are re-labelled and then all image pixels are presented to the network and assigned the class identity of their best-matching output neuron.

For classification using the SOM, parameters such as the number of output neurons, initial neighbourhood radius and minimum and maximum learning rates must be defined. Using the existing literature as a guide (e.g., Ji, 2000; Jianwen & Bagan, 2005; Bedini, 2009), numerous tests were conducted to determine appropriate sets of parameters for all SOM classifications. In each case, the appropriate parameters were chosen to try and minimise the average quantisation error (average of Euclidean distances between input vectors and best-matching neurons) and maximise the labelling accuracy of training pixels. The chosen parameters for each classification are shown in Table 6.5. In all cases, coarse tuning was performed using all available input vectors (i.e., all 1,008,596 pixels), with a maximum learning rate of 0.05 and a minimum learning rate of 0.01. Fine tuning was performed with LVQ1 using a maximum gain term of 0.005 and a minimum of 0.001.

Table 6.5. SOM network parameters.

Input variables	Neurons in output layer	Initial neighbourhood radius	Fine tuning iterations
ATM 9	20 × 20	15.14	300
ATM PC	15 × 15	8.07	200
ATM MNF	25 × 25	30.00	100
ATM-Li	25 × 25	18.00	200
ATM-Li MNF	35 × 35	40.00	200

After classification using both the MLC and SOM, a 3 × 3 pixel majority filter was applied to every map. The purpose of the majority filter was to remove pixels that are isolated in terms of their lithological class because, as lithological units tend to form homogeneous areas, it is somewhat unlikely that the relatively small areal extent represented by these isolated pixels truly represents a different lithological unit in an otherwise homogeneous area (Ricchetti, 2000).

6.4.4 Accuracy assessment

For each set of input variables, the classification accuracy for the entire mapped area was assessed using the overall (OA), user's (UA) and producer's (PA) accuracies and the Kappa coefficient (K) derived from a confusion matrix (Congalton, 1991). The

OA is the percentage of all validation pixels correctly classified, whereas the UA and PA provide information regarding the commission and omission errors associated with the individual classes, respectively. Unlike the OA, K takes into account the possibility of agreements occurring by chance in a random classification (Brown et al., 1998).

In order to compare the two classifiers and to evaluate whether the integration of topographic data can improve on the spectral-only mapping results, tests for statistically significant differences were computed. Although this commonly involves performing a Z-test using the K statistics derived from two classification results (e.g., South et al., 2004; Liberti et al., 2009), this method is inappropriate for the current study as the same validation pixels are used to assess the accuracies of all classifications involved in pair-wise comparisons (Foody, 2004). For cases where the validation data are related, the McNemar test is more appropriate for testing the significance of any differences in classification accuracies (Foody, 2004; De Leeuw et al., 2006). Based upon a Chi-squared (χ^2) distribution, the McNemar test involves a cross-tabulation of the number of validation pixels correctly and incorrectly classified through two algorithms. The test is computed as:

$$\chi^2 = \frac{(f_{12} - f_{21})^2}{f_{12} + f_{21}} \quad , \tag{6.3}$$

where f_{12} is the number of validation pixels correctly classified in classification 1 but incorrectly classified in classification 2, and f_{21} is the number of pixels classified correctly in classification 2, but incorrectly classified in classification 1. The statistical significance of the difference is then determined from the resulting χ^2 value and expressed as a p-value (p).

6.5 Results and discussion

6.5.1 Spectral classification

A total of six lithological maps were generated using spectral information. Following initial classification, use of the majority filter helped to remove isolated pixels in the classified images by refining, on average, the classes of 1.5% of the total number of pixels in each image. As a consequence, the OA of all maps was increased by an average of 1.3%. All subsequent discussion concerns the lithological maps produced following majority filtering. A summary of the spectral-only lithological mapping results is shown in Table 6.6.

Table 6.6. Results for spectral-only classification algorithms and statistical significance of differences between corresponding MLC and SOM classifications (p-value).

	MLC		SOM		
Input variables	OA (%)	K	OA (%)	K	p-value
ATM 9	61.6	0.50	60.3	0.48	0.0010
ATM PC	51.4	0.37	50.2	0.35	0.0007
ATM MNF	59.3	0.46	65.5	0.54	<0.0001

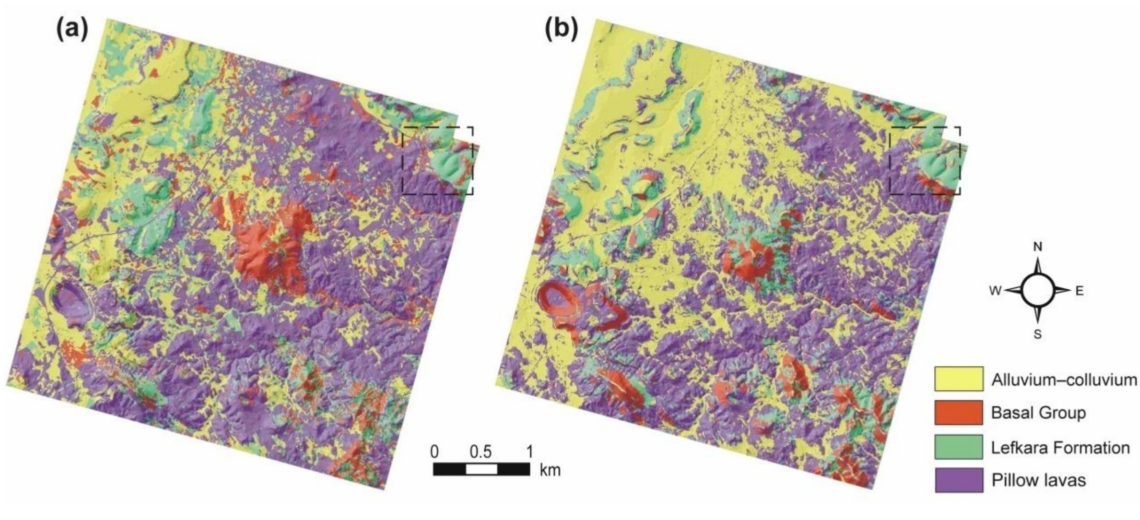

Fig. 6.5. Lithological maps generated using: **(a)** the best spectral-only algorithm (ATM MNF SOM) and **(b)** the best integrated spectral–topographic algorithm (ATM-Li MNF SOM). Dashed black box indicates the spatial extent of Fig. 6.7.

The best spectral-only result was obtained through SOM classification of the MNF-transformed variables (ATM MNF), which resulted in an OA of 65.5% and a K of 0.54 (Fig. 6.5a). The result of this algorithm is comparable to the OA (65.4%) obtained for the same area using only LiDAR-derived topographic information (Grebby et al., 2010). Considering the complexity of the landscape and the adverse effects that vegetation cover can have on the spectral discrimination of lithologies, this is deemed to be a good result. The worst performing algorithm was the SOM classification used in conjunction with the PC variables (ATM PC; OA = 50.2%, K = 0.35), resulting in decreases of 15% in the OA and 35% in K when compared to the ATM MNF approach. A similar finding was also observed for the MLC; decreases in the OA of 8% and 20% in K were obtained when classification was performed on the ATM PC variables in contrast to the ATM MNF variables. Such concomitant differences imply that the MNF transformation is more effective than PCA in enhancing discrimination through suppression of the intra-class spectral variability ascribed to the heterogeneous vegetation/rock surface mixtures (i.e., the predominant source noise in this case). The ascendancy of the MNF transformation is doubtlessly due to the ability to target the desired noise component in the noise estimation and then order the MNF bands in terms of their signal-to-noise ratio, thus enabling this noise to be reliably segregated prior to classification. In fact, the poor performance of both ATM PC classifications in comparison to the non-transformed ATM 9 results (i.e., decreases of 10% in the OA and ~26% in K) suggests that PCA actually accentuates, rather than suppresses the vegetation-induced intra-class spectral variability. This is due to the inability of PCA to reliably identify and separate the contributions of the signal and noise-related variances to the total data variance contained within the higher-order PCs (Chen et al., 2003); the first three of which are included in the ATM PC variable set. Based on a comparison of the eigenvector loadings for the PC and MNF input variables, it appears that PC2 is responsible for accentuating the intra-class spectral variability because it maximises the contrast between pixels dominated by vegetation and those dominated by the exposed substrate. The exclusion of PC2 should therefore help to reduce the intra-class spectral variability and improve the overall classification results of the PCA approach.

With regards to classifier performance, the MLC outperforms the SOM in classifying two out of the three sets of spectral input variables. Although the observed differences in the OA between the MLC and SOM in both cases are only small (~1%), these are statistically significant nonetheless ($p \leq 0.001$). Given the noisy spectral signatures associated with the ATM 9 variables, the success of the MLC over the SOM is somewhat surprising as NNs are commonly touted as being more robust in handling noisy data than parametric classifiers (e.g., Ji, 2000). This result may therefore indicate selection of sub-optimal SOM network parameters for classifications based upon these two sets of variables. For the lone case in which the SOM outperforms the MLC (i.e., the ATM MNF variables) a more significant difference of ~6% is obtained ($p<0.0001$). The considerable superiority of the non-parametric SOM in this case could be attributable to a deviation from the multivariate class normality assumption made by the parametric MLC.

Table 6.7. Individual class accuracies for spectral-only algorithms: Producer's (PA) and User's (UA) accuracies for alluvium–colluvium (AC), Basal Group (BG), Lefkara Formation (LF) and pillow lavas (PL).

	PA (%)				UA (%)			
Algorithm	AC	BG	LF	PL	AC	BG	LF	PL
MLC								
ATM 9	46.5	46.0	84.3	79.0	99.6	55.4	41.8	73.7
ATM PC	29.9	41.4	60.2	82.1	97.6	41.9	32.3	66.5
ATM MNF	51.5	40.0	64.5	84.5	99.8	40.1	47.4	62.9
SOM								
ATM 9	48.4	30.1	87.6	84.7	83.8	58.2	46.8	63.6
ATM PC	21.5	35.6	75.5	81.8	95.7	43.6	34.7	64.2
ATM MNF	66.0	39.1	71.1	86.8	93.5	49.6	51.8	66.8

Of the individual lithological classes, the pillow lavas were the most accurately mapped unit with a PA and UA frequently exceeding 80% and 60% respectively, regardless of the algorithm used (Table 6.7). The Lefkara Formation is also mapped with relatively good accuracy for all sets of input variables, but especially when classification is performed using the SOM (PA > 71%). Despite this, the Lefkara Formation is associated with considerable commission errors, ranging from 48–68% for all combinations of input variables and classification routine. An inspection of the error matrices (Appendix I) revealed that confusion with the Basal Group is largely responsible for the high commission errors associated with the Lefkara Formation unit. Since these two units are geologically very distinct, this confusion must be ascribed to their associations with similar vegetation types. Both the Basal Group and alluvium–colluvium are poorly classified using both the MLC and SOM. The omission error for the Basal Group is consistently greater than 54%, while the commission error varies from 40–60% for all algorithms. Despite its close geological relationship to the pillow lava unit, a greater proportion of Basal Group validation pixels are incorrectly assigned to the Lefkara Formation; again reiterating that the spectral similarity between these distinct units must be related to their association with similar types of vegetation. Conversely, the occurrence of dissimilar vegetation types (i.e., shrubs vs. lichen) is arguably responsible for the lack of spectral confusion between the Basal Group and pillow lavas. With the exception of classifications based upon the ATM MNF variables, the PA for alluvium–colluvium never exceeds 50%, with the unit most frequently confused with the Lefkara Formation and the other units to a lesser extent. Some degree of confusion with the other units can be expected because alluvium-colluvium is a generic unit which includes all Quaternary sediments regardless of their parental rock type. Contrary to its poor PA, the alluvium–colluvium unit exhibits the highest UA for all algorithms, with a maximum of 99.8% for the MLC classification of the ATM MNF variables and a minimum of 83.8% when using the ATM 9 variables in conjunction with the SOM.

6.5.2 Classification based on integrated spectral and topographic variables

The use of ancillary data for enhancing the discrimination and mapping of lithologies was evaluated through incorporating LiDAR-derived topographic data using two approaches; resulting in the generation of four lithological maps. Again, all analysis concerns lithological maps produced following the application of a majority filter. In this case, the majority filter helped refine (on average) the classes of 0.9% of the total number of pixels in each image, leading to increases in the OA of all maps by an average of 1.4%. A summary of the integrated mapping results is shown in Table 6.8 and Table 6.9, while the statistical significance of differences between spectral and integrated classification accuracies can be found in Table 6.10.

Table 6.8. Results for integrated spectral–topographic classification algorithms and statistical significance of differences between corresponding MLC and SOM classifications (p-value).

	MLC		SOM		
Input variables	OA (%)	K	OA (%)	K	p-value
ATM-Li	61.9	0.50	70.2	0.60	<0.0001
ATM-Li MNF	60.8	0.49	72.7	0.63	<0.0001

Table 6.9. Individual class accuracies for integrated spectral–topographic algorithms: Producer's (PA) and User's (UA) accuracies for alluvium–colluvium (AC), Basal Group (BG), Lefkara Formation (LF) and pillow lavas (PL).

	PA (%)				UA (%)			
Algorithm	AC	BG	LF	PL	AC	BG	LF	PL
MLC								
ATM-Li	41.6	40.4	96.2	83.2	100	87.3	40.6	67.4
ATM-Li MNF	27.5	56.3	88.8	86.2	100	77.9	52.3	51.7
SOM								
ATM-Li	75.9	44.3	78.2	82.4	93.0	76.5	58.1	59.3
ATM-Li MNF	92.5	45.2	63.4	81.9	86.5	75.7	53.7	69.8

Table 6.10. Statistical significance of differences (expressed as p-values) between spectral-only and integrated spectral–topographic classification algorithms.

		Spectral–topographic variables	
Classifier	Spectral variables	ATM-Li	ATM-Li MNF
MLC	ATM 9	0.1875	0.0579
	ATM PC	<0.0001	<0.0001
	ATM MNF	<0.0001	0.0018
SOM	ATM 9	<0.0001	<0.0001
	ATM PC	<0.0001	<0.0001
	ATM MNF	<0.0001	<0.0001

Overall, the results show that the incorporation of topographic information leads to general improvements in the overall lithological mapping accuracy when compared to classifications based solely on spectral data. However, the level of improvement attainable is somewhat classifier dependent. Once again the highest OA was obtained using the SOM classifier in conjunction with MNF transformed variables (ATM-Li

MNF; OA = 72.7%, K = 0.63; Fig. 6.5b). This results in an OA at least 7% higher than — and significantly different ($p < 0.0001$) from — all spectral-only SOM classifications, with a maximum improvement of 22.5% over the ATM PC result. Highly significant statistical differences ($p<0.0001$) were also observed between the SOM ATM-Li and all spectral-only SOM classifications; reflecting increases in the OA and K of at least 4.7% and 10%, respectively, when topographic information is incorporated. Improvements attainable using the MLC are somewhat varied. Compared to the best spectral-only MLC result (ATM 9), MLC classification with the ATM-Li variables produced an increase in the OA of only 0.3%, which was subsequently found not to be a statistically significant difference (61.6% vs. 61.9%; $p = 0.1875$). However, significant differences ($p < 0.0001$) were obtained in comparison to the ATM PC and ATM MNF MLC-based classifications, reflecting improvements of $\geq 2.6\%$ in the OA. Classification performed using the MLC and ATM-Li MNF variables was less successful as this produced the worst classification accuracy of all the integrated approaches (OA = 60.8%, K = 0.49). In actual fact, this algorithm performs worse than the best MLC spectral approach (ATM 9). Nevertheless, the OA obtained using this algorithm is higher and the result is statistically different ($p<0.002$) from those achieved through the two other spectral-only MLC approaches. Ultimately, the SOM is far superior for classification of the multisource data as it outperforms the MLC considerably for both sets of integrated variables (ATM-Li: 70.2% vs. 61.9%, $p<0.0001$; ATM-Li MNF: 72.7% vs. 60.8%, $p< 0.0001$). The dominancy of the NN over the parametric classifier for multisource data classification observed here is consistent with other published results (e.g., Arora & Mathur, 2001). Additionally, the SOM consistently achieves considerable improvements in the overall lithological mapping accuracy in comparison to sole use of spectral information.

With regards to the individual classes, the pillow lava unit remains the most accurately mapped, with a PA in excess of ~82% for all algorithms. Good classification accuracies are achieved for the Lefkara Formation (PA > 63.4%), especially when classified using the MLC (PA > 88%). Despite this, the UA for the Lefkara Formation unit is relatively low, leading to commission errors ranging from 41.3–59.4%. The alluvium–colluvium unit is accurately mapped with algorithms based on the SOM (PA> 75%), while excellent UA's (> 86%) are achieved for all algorithms. Although the omission errors for the Basal Group are high for all algorithms (43.7–59.6%), only small commission errors (<25%) are attached to the unit.

A summary of the effects of topographic integration on the individual class accuracies for the SOM algorithms is provided by Fig. 6.6. From this, it is evident that improvements in the lithological mapping performance that result from the addition of topographic information are primarily linked to substantial increases in both the PA associated with alluvium–colluvium and the UA of the Basal Group unit; reflecting decreases in the omission and commission errors of the units, respectively. Spectral-only classifications typically produce considerable alluvium–colluvium omission errors because the alluvium–colluvium unit is frequently confused with the parental rock types from which the sedimentary unit is derived. The integration of topographic information help reduces this confusion and the ensuing omission errors because, unlike its spectral signature which is inherently similar to the parental rocks from which the unit is derived, the topographic characteristics associated with alluvium–colluvium are distinctive (Grebby et al., 2010). Likewise, the typical topography associated with the Basal Group is relatively disparate from the other lithological units — particularly in terms of slope — and so the inclusion of such information provides the additional discriminating power that is required to reduce the confusion largely caused by vegetation-related spectral similarity with other units. Examples illustrating the functional benefits described above can be seen in Fig. 6.7. Although the overall mapping improvements obtained through incorporating topographic information are indisputable, ambiguous classifications occasionally occur in areas where the lithological units exhibit atypical topographic characteristics — mostly due to anthropogenic activity such as agriculture. This is also illustrated in Fig. 6.7 by the apparent increase in the number of Basal Group pixels proximal to the mapped Lefkara Formation–pillow lava contact. In this particular case the source of the atypically steep topography is unclear, but it is likely to be linked to underlying structures (e.g., a fault or dykes).

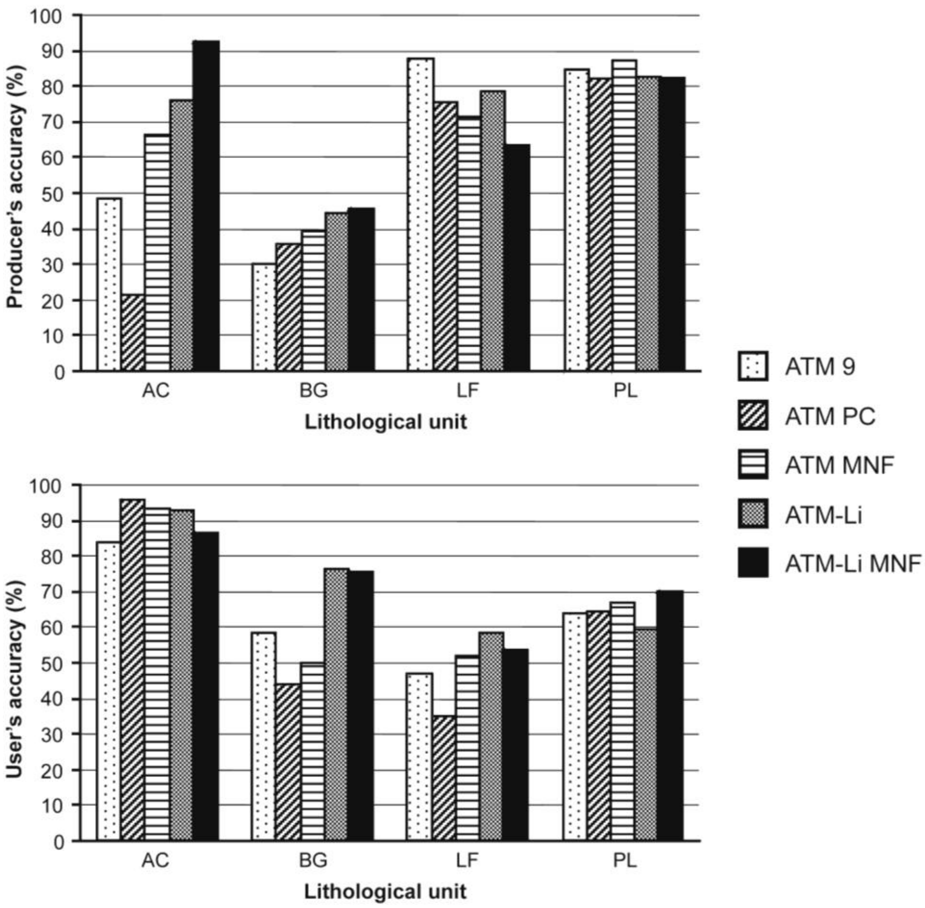

Fig. 6.6. Effect of topographic integration on the Producer's and User's accuracies of individual units for all SOM algorithms. Alluvium–colluvium (AC), Basal Group (BG), Lefkara Formation (LF) and pillow lavas (PL).

It is also clearly evident that — despite the complexity of the landscape — both spectral-only and integrated SOM approaches possess the capability to define lithological contacts more accurately and map the units in more detail than what is shown on existing geological maps (Fig. 6.7). Although the best spectral-only approach (ATM MNF SOM) and LiDAR-derived topographic approach (Grebby et al., 2010) can be used to generate accurate lithological maps, the potential of data integration for detailed lithological mapping in this type of vegetated environment is clearly demonstrated through the significant improvements attainable over the sole use of either dataset.

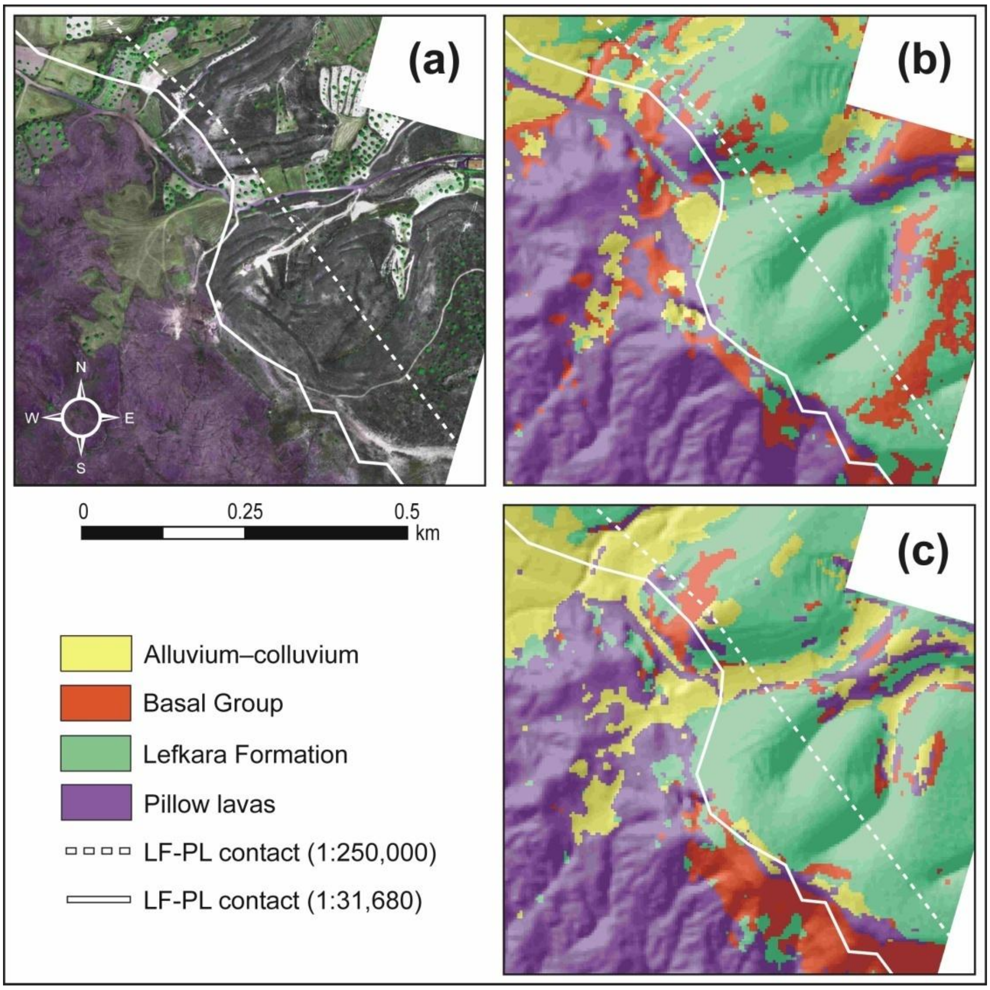

Fig. 6.7. Detailed illustration of the mapping performance for area shown in Fig. 6.5. **(a)** QuickBird image, and lithological maps generated using **(b)** the best spectral-only algorithm (ATM MNF SOM) and **(c)** the best integrated spectral–topographic algorithm (ATM-Li MNF SOM).

6.6 Conclusions

The application of spectral remote sensing to lithological mapping can be hindered by the presence of just small amounts of vegetation cover, and so its use has been predominantly restricted to essentially barren environments. Although lithological mapping using geobotanical relationships and the integration of spectral and ancillary data are not new concepts, their use has been limited to data with only moderate-to-coarse spatial resolutions and areas with a relative lack of ubiquitous vegetation cover. This study takes advantage of increasingly available high-resolution remote sensing data to evaluate the efficacy of airborne multispectral imagery for detailed lithological mapping in a complex and vegetated area of the Troodos ophiolite, Cyprus. Furthermore, this study also investigates whether spectral and LiDAR-derived topographic data can be integrated to increase lithological discrimination and enhance the overall mapping performance.

Lithological mapping using only spectral imagery was somewhat hindered by a combination of the intra-class spectral variability caused by the heterogeneous vegetation cover, and by both vegetation-induced and inherent spectral similarities between some of the lithological units. Despite these hindrances, a lithological map with a satisfactory OA of 65.5% and K of 0.54 was generated through the SOM classification of a set of MNF-transformed spectral variables. The MNF transformation was effective in suppressing the intra-class spectral variability (or “noise”) caused by the variable vegetation cover, and thus generally resulted in enhanced lithological discrimination in comparison to PCA and non-transformed spectral variables. In fact, PCA accentuated the contrast between pixels dominated by the spectral response of vegetation and those dominated by the rock type, resulting in an adverse effect on discrimination. Nevertheless, regardless of the algorithm employed, distinct geobotanical associations (i.e., lichen vs. shrubs) apparently aided the differentiation of the pillow lavas and the closely related Basal Group unit. With regards to the classifier performances, the MLC outperformed the SOM in two of the three sets of spectral variables, possibly owing to sub-optimal SOM network selections.

Incorporating high-resolution topographic information generally resulted in improvements to the overall lithological mapping accuracy when compared to the spectral-only approaches. However, the attainable improvements are considerably greater for the SOM than for the MLC. This result demonstrates the SOM's superiority for multisource data classification. The most accurate lithological map is obtained using the SOM classifier in conjunction with the MNF-transformed spectral and topographic variables (OA = 72.7% and K = 0.63). This represents a minimum and maximum increase in the OA of 7% and 22.5%, respectively, when compared to the corresponding spectral-only approaches. The improvements generated by the addition of topographic information are primarily linked to substantial decreases in both the omission error associated with alluvium–colluvium and the commission error of the Basal Group unit. Both of these lithological units have particularly distinct topographic characteristics, which provide the additional discriminatory power required to separate the lithologies following inherent or vegetation-induced spectral similarities. Occasional lithological misclassifications are observed in areas where the units display atypical topographic characteristics due to either anthropogenic influences or natural deviations.

The optimum spectral-only and integrated SOM approaches presented here are capable of producing lithological maps with more detail and more accurately defined contacts than the existing geological maps of the study area. Furthermore, this capability is demonstrated using minimal *a priori* knowledge regarding the spatial distribution of each lithological unit, which offers great promise for lithological mapping in relatively unexplored terrain. Nevertheless, the efficacy of these algorithms can potentially be extended to any geological setting where direct spectral discrimination is difficult due to the presence of vegetation or inherent spectral similarities, and where lithology and topography are linked. It is also anticipated that the algorithms can be successfully applied to areas with heavier vegetation cover, provided that geobotanical and/or litho-topographic relationships can be recognised. In particularly dense vegetation cover such as forests, it may be necessary to acquire the LiDAR data at a high point density in order to ensure an adequate DTM can be generated, thus maximising the capability to identify potential litho-topographic relationships.

Irrespective of the mapping capabilities of any remote sensing approach, the final lithological map product will always require additional refinement. This usually involves a laborious combination of manual computer-based image refinement and fieldwork to eradicate spurious classifications from the map. Further work is required to investigate whether this process can be automated to some extent, possibly using a rule-based procedure which refines the class of spurious pixels according to established stratigraphic relationships. This could ultimately help to further increase the veracity of the derived map and the efficiency of follow-up fieldwork.

7. Structural mapping using airborne LiDAR data and ATM imagery

Abstract

Besides lithological information, geological structure comprises another essential component of geological maps. Structural maps are traditionally produced by mapping features such as faults, folds, fabrics, fractures and joints in the field. However, large map areas and the limited ground perspective of the field geologist leads to the inevitability that some important geological features will not be identified. The ability to recognise and map both local and regional structural features using high-resolution remote sensing data provides an opportunity to complement field-based mapping, enabling the generation of more comprehensive structural maps. Nonetheless, as with lithological mapping, vegetation cover can adversely affect the extraction of structural information from remotely sensed data because it is capable of masking the appearance of subtle spectral and geomorphological features that correspond to geological structures. The objective of this study is to investigate the utility of airborne LiDAR data and ATM imagery for detailed structural mapping of the vegetated ophiolitic rocks and sedimentary cover of Troodos study area. Visual enhancement techniques were applied to the 4 m airborne LiDAR DTM and 4 m ATM imagery to assist the manual generation of lineament maps. The visual enhancement techniques included the generation of shaded relief images, in addition to the application of edge enhancement convolution filtering and morphological transformations. Despite widespread vegetation cover, a preliminary analysis showed that faults and dykes were recognisable in the airborne LiDAR DTM and ATM imagery as lineaments defined by edges. The predominant strike trends of lineaments in all resulting maps were found to be in agreement with field-based structural data, thus demonstrating the efficacy of airborne LiDAR data and ATM imagery for extracting detailed and accurate structural information to help complement field-based mapping.

7.1 Introduction

In addition to identifying the variety of rock types and their distributions within a given area, an important objective of geological mapping is to also document the structural geology (Barnes & Lisle, 2004). Structural information is valuable for understanding the crustal architecture, studies of seismic and landslide hazards, engineering and the exploration of groundwater, petroleum and mineral resources (Moore & Waltz, 1983; Kresic, 1995; Karnieli et al., 1996; Wladis, 1999; Harris et al., 2001; Peña & Abdelsalam, 2006; Corgne et al., 2010).

Structural maps are traditionally produced by mapping features such as faults, folds, fabrics, fractures and joints in the field. Although arguably the most reliable and accurate maps are those produced using field mapping techniques, large map areas and the limited ground perspective of the field geologist leads to the inevitability that important geological features, including local and regional structures, will not be identified (Süzen & Toprak, 1998). However, the ability to recognise and map structural features for large areas using remote sensing data provides complementary information and also an opportunity to generate more comprehensive structural maps.

Important structural features may be expressed as lineaments on remotely sensed imagery and DEMs (Masoud & Koike, 2006). The term lineament is defined by O'Leary et al. (1976) as "a mappable, simple or composite linear feature of a surface, whose parts are aligned in a rectilinear or slightly curvilinear relationship and which differs distinctly from the patterns of adjacent features and presumably reflects a subsurface phenomenon". In spectral imagery, lineaments are typically recognised as edges defined by a series of adjacent pixels at the boundary of brightness changes (Koike et al., 1998). Such spectral features may correspond to variations in surface composition or shadowing. With regards to the topographic domain, geological lineaments are typically associated with geomorphological features such as linear valleys, ridgelines, escarpments and slope breaks (Jordan & Schott, 2005). These features are also expressed as edges in DEMs, defined either by an abrupt change in elevation (slope break) or by an increase or decrease in elevation for a short lateral distance (valleys and ridgelines).

Typically, geological lineaments are mapped manually through the visual interpretation and tracing of linear features that are expressed in remotely sensed imagery. However, this technique can be time-consuming and tedious at regional mapping scales, and also highly subjective and therefore irreproducible (Masoud & Koike, 2006). A variety of image enhancement techniques are commonly used to try to make the visual interpretation and mapping process more efficient and less subjective. Principal Component Analysis (PCA), decorrelation stretching and false-colour composite (FCC) images are useful techniques for exaggerating subtle colour differences in spectral imagery to accentuate the appearance of lineaments (Qari, 1991; Mountrakis et al., 1998). Shaded relief models generated from DEMs are a powerful tool for enhancing the appearance of lineaments in topographic data. This is because the illumination azimuth and inclination can be varied to help identify lineaments in all orientations by recognising the shadowing effects (i.e., boundaries between light and dark tones) caused by abrupt changes in elevation (Jordan & Schott, 2005). Other common visual edge enhancement techniques include the application of convolution filters, such as Sobel, Prewitt and Laplacian filters (Moore & Waltz, 1983; Süzen & Toprak, 1998; Wladis, 1999), and application of morphological operations, such as erosion, dilation, opening and closing (Tripathi et al., 2000; Ricchetti & Palombella, 2005) to spectral imagery and DEMs.

Algorithms for the automated mapping of geological lineaments have also received considerable attention (Argialas & Mavrantza, 2004). Common examples include algorithms based on Canny edge detection (Corgne et al., 2010), the Hough transform (Karnieli et al., 1996; Fitton & Cox, 1998), line-tracing (Koike et al., 1995) and morphometric feature parameterisation (Wallace, 2005; Wallace et al., 2006). Although automated algorithms further increase the reproducibility, efficiency and objectivity of lineament mapping, there are concerns regarding their suitability for geological lineament detection (Parsons & Yearley, 1986). The most obvious issue associated with automated algorithms is the inability to differentiate lineaments of a geological origin from non-geological lineaments, such as roads and field boundaries. For reasonably sized areas, this task is arguably best performed when based on human perception.

As with lithological mapping, vegetation cover can adversely affect the extraction of structural information from remotely sensed data. This is because vegetation, especially tall dense vegetation (i.e., forests), is capable of masking the appearance of subtle spectral and geomorphological lineaments that correspond to structural features. In addition, the utility of moderate spatial resolution data acquired from classic spaceborne instruments (e.g., Landsat TM imagery and Shuttle Radar Topographic Mission DEMs) is restricted to only regional structural mapping. The efficacy of remote sensing for structural mapping may be enhanced through use of airborne LiDAR topographic data and airborne spectral imagery because they are acquired at a considerably higher spatial resolution and therefore permit more detailed mapping of geological structure. Furthermore, airborne LiDAR has the capability to acquire accurate and high-resolution topographic data even in forested terrain, thus giving it the potential to be a powerful structural mapping tool. Nevertheless, the application of airborne LiDAR to structural mapping has been primarily limited to mapping the surface traces of regionally-significant faults in vegetated and non-vegetated terrain through visual interpretation of shaded relief models (e.g., Harding & Berghoff, 2000; Haugerud et al., 2003; Prentice et al., 2003; Cunningham et al., 2006).

The objective of this study is to investigate the utility of airborne LiDAR data and ATM imagery for detailed structural mapping of the vegetated ophiolitic rocks and sedimentary cover of Troodos study area. Owing primarily to the reliability concerns associated with automated algorithms, the efficacy of airborne LiDAR data and ATM imagery for structural mapping is evaluated by applying several visual enhancement techniques to the datasets to assist the manual generation of lineament maps. These visual enhancement techniques include the generation of shaded relief images, in addition to the application of edge enhancement convolution filtering and morphological transformations.

7.2 Data

Data used in this study comprises both the 4 m airborne LiDAR-derived DTM and 4 m ATM imagery (comprising bands 2–10), which were processed as per Chapter 3. Preliminary analysis was first undertaken to determine whether the main structural features present in the study area could be identified using the datasets. The two main types of structural features in the study area are faults and dykes (Fig 7.1). Typical examples of a fault and a dyke were identified during fieldwork and their locations were recorded using GPS (Fig. 7.2). At each location, cross-sectional profiles were extracted from both the LiDAR DTM and ATM imagery and subsequently inspected for evidence that the faults and dykes can be recognised as lineaments.

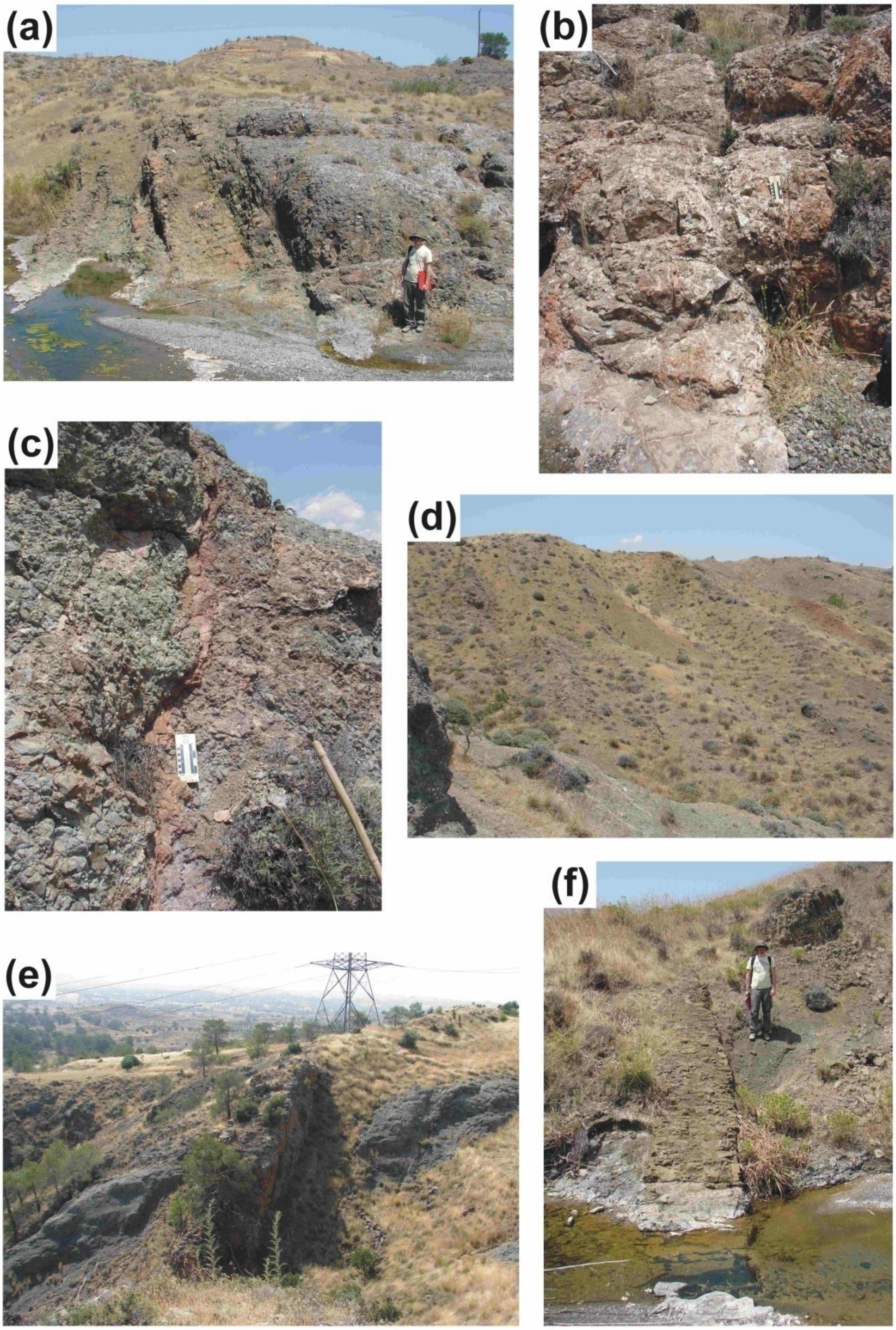

Fig. 7.1. Field photographs showing typical examples of structural features observed within the study area. **(a)** Set of NW-SE striking dykes intruding pillow lavas, **(b)** and **(c)** brittle fault zones in pillow lavas, **(d)** NW-SE dykes expressed in landscape, **(e)** and **(f)** upstanding dykes intruding pillow lavas.

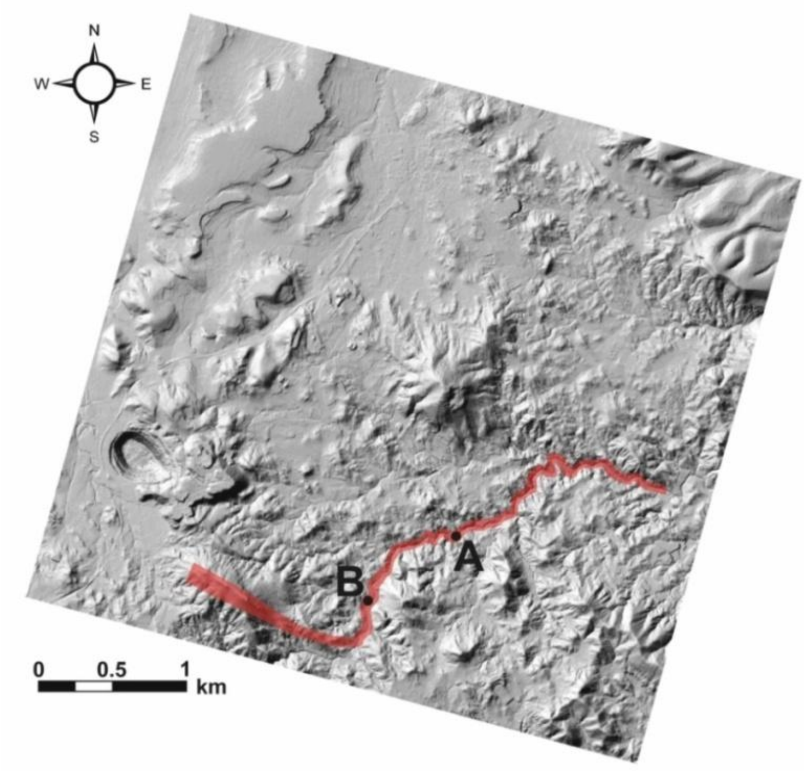

Fig. 7.2. Shaded relief of the study area showing the locations of typical examples of a fault (labelled A; see Fig. 7.3) and a dyke (B; see Fig. 7.4). Red shading depicts route of transect walked during field validation.

The fault example is of a major fault located along a stream transect (see Fig. 7.2), which forms a cleft that cuts both sides of a canyon that contains the stream (Fig. 7.3a). Cross-sectional profiles extracted from the DTM and ATM imagery in the locality of this fault are shown in Fig. 7.3b and 7.3c, respectively. The fault can be clearly recognised in the DTM profile as a drop in elevation of approximately 0.5 m over a relatively short lateral distance of 7 m; forming a linear trough. The fault is also visible in the ATM imagery, albeit as a subtle decrease in brightness (or radiance) with edges defined by relatively abrupt differences in the brightness gradient at both boundaries.

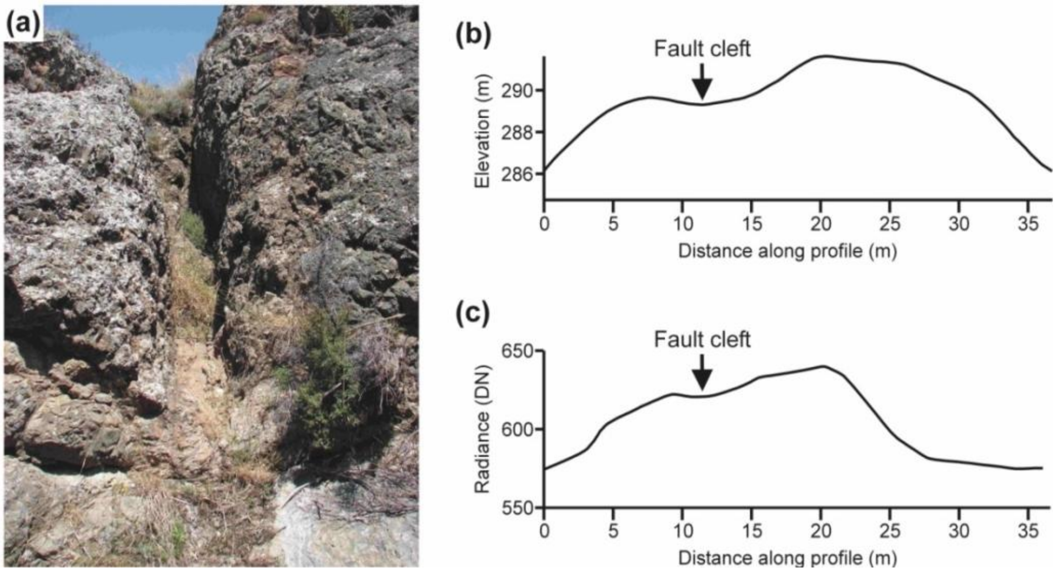

Fig. 7.3. **(a)** Field photograph of the fault at location 'A' in Fig. 7.2, and cross-sectional profiles showing the expression of this fault in **(b)** the LiDAR DTM and **(c)** ATM Band 2.

The dyke example is located upstream (southwest) from the fault example (see Fig. 7.2). The dyke (or potentially a set of dykes) can be seen cutting across the stream to form an upstanding linear ridge feature in pillow lavas on the western bank of the stream (Fig. 7.4a). Cross-sectional profiles extracted from the DTM and ATM imagery in the locality of this dyke are shown in Fig. 7.4b and 7.4c, respectively. The dyke is clearly recognised as a 3 m wide ridgeline in the DTM profile, bounded by abrupt decreases in elevation at both edges. The dyke can be also identified in the ATM profile, although its expression is more inconspicuous because of the narrower (~1 m) width of the feature. Nevertheless, the dyke is defined by boundaries caused by abrupt changes in the brightness gradient. Illumination conditions during ATM acquisition or smoothing effects during pre-processing of the imagery could be responsible for the narrowed appearance of the dyke in this example.

The results of the preliminary analysis show that both datasets are adequate for identifying the main structural lineaments. Following this, both the LiDAR DTM and ATM imagery were subjected to visual enhancement techniques to help generate structural maps for the study area. However, in order to reduce the number of ATM bands without significant loss of the spectral information contained within the entire dataset, PCA was applied to the 9 ATM bands. Since an examination of the eigenvalues calculated during PCA revealed that the first three PCs accounted for 97.5% of the total data variance (Table 6.2), these three bands were selected to represent the ATM imagery for further analysis.

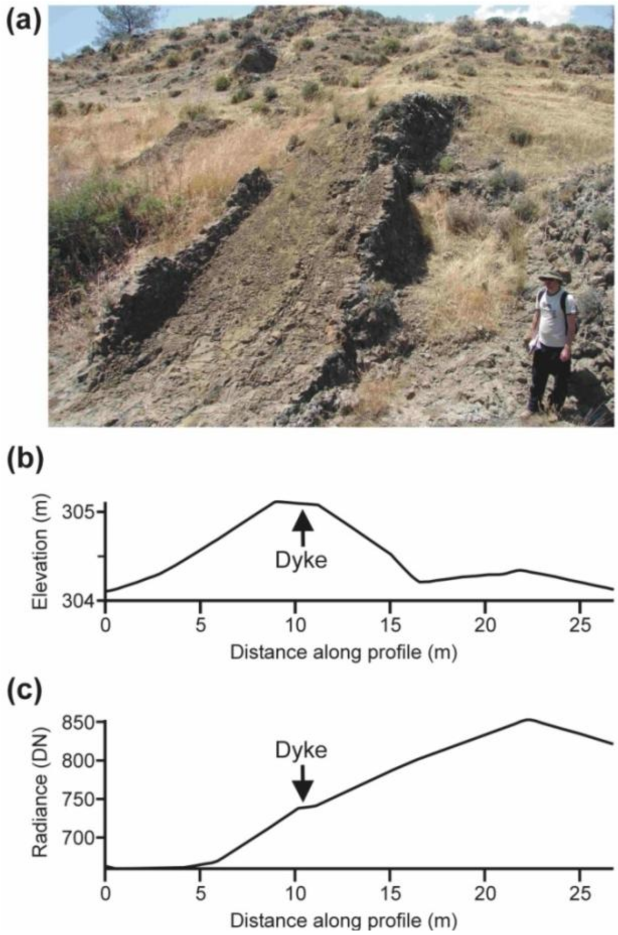

Fig. 7.4. **(a)** Field photograph of dyke at location 'B' in Fig. 7.2, and cross-sectional profiles showing the expression of this dyke in **(b)** the LiDAR DTM and **(c)** ATM Band 5.

7.3 Methods

The methodology employed in this study comprises three main steps: lineament enhancement, mapping and analysis. These steps are discussed in detail in the following sections.

7.3.1 Lineament enhancement

7.3.1.1 Shaded relief models

Shaded relief models (such as that in Fig. 7.2) are shaded topographic images generated from DEMs by simulating the reflection of artificial light that is incident upon the surface from a specified inclination and azimuth. An image is generated by assigning shades of grey to pixels to represent reflectance values, which are commonly determined from a Lambertian reflection model based on the angle at which the light is incident upon the terrain (Masoud & Koike, 2006). The aforementioned ability to vary the illumination inclination and azimuth to alter the shadowing effects makes shaded relief models an excellent tool for indentifying lineaments in all orientations. Consequently, a lineament map was generated by visually interpreting a series of shaded relief models generated from the LiDAR DTM and illuminated at azimuth intervals of 45° (i.e., N, NE, E, SE, etc). At each azimuth interval, the inclination angle and vertical exaggeration were also systematically varied to try to ensure all potential lineaments were visible.

7.3.1.2 False-colour composite

In order to help identify lineaments using the ATM imagery, a false-colour composite image was created by assigning the ATM PC bands 1, 2 and 3 to the red, green and blue channels of the monitor, respectively. Subtle variations in the spectral properties of the surface materials are typically enhanced in the false-colour composite by their representation as contrasting colours. As a consequence, lineaments are readily identifiable in the FCC as linear edges defined by sharp colour differences. Accordingly, the ATM PC FCC was visually interpreted in ENVI 4.3 to generate a lineament map.

7.3.1.3 Laplacian filtering

Laplacian filters are a type of convolution filter commonly applied to remote sensing data for lineament mapping applications (Saha et al., 2002; Ali & Pirasteh, 2004; Ricchetti & Palombella, 2005). It is a second derivative edge enhancement filter that operates without regard to edge orientation (i.e., it is non-directional). A Laplacian filter was applied to both the LiDAR DTM and each of the three ATM PC bands using a 3 × 3 kernel with a weighting structure such as that shown in Fig. 7.5. In each case, the filtered image was added to the original image at a ratio of 9:1 in order to improve the image interpretability. Two lineament maps were subsequently generated by visually interpreting the greyscale edge-enhanced DTM and a FCC created from the three filtered ATM PC bands.

0	-1	0
-1	4	-1
0	-1	0

Fig. 7.5. Kernel weighting used in Laplacian filtering.

7.3.1.4 Morphological transformation

As previously mentioned, mathematical morphological operations such as dilation, erosion, opening and closing have also been applied to enhance lineaments in grey-scale remotely sensed imagery. One of the most popular morphological techniques for edge detection is top hat transformation (e.g., Tripathi et al., 2000; Ricchetti & Palombella, 2005). This technique involves closing or opening operations followed by subtraction with the original image:

$$\text{Top hat}(f) = f^{B} - f \qquad (7.1)$$

$$\text{Top hat}(f) = f - f_{B} \qquad (7.2)$$

where f is the original image, f^{B} is the image obtained following the closing operation and f_{B} is the image obtained after the opening operation. The top hat transformation involving the closing operation (Eq. 7.1) is considered to yield better results for the extraction of structural features such as faults and fractures (Tripathi et al., 2000). Therefore, the transformation in Eq. 7.1 was applied to the DTM and each of the ATM PC bands using a kernel with a weighting of 1 assigned to all elements — to avoid introducing directional bias. Two lineament maps were again generated through visual interpretation of the transformed DTM and FCC created from the three top hat transformed ATM PC bands.

7.3.2 Lineament mapping

A standard approach was adopted to try to minimise the subjectivity associated with visual lineament mapping. This involved the generation of all lineament maps within the ENVI 4.3 software using the following protocol. All enhanced products were displayed in two image windows; one providing a regional perspective (1× zoom) and a second window providing more detailed view (2× zoom). In each case, the image was divided into sections so that each could be examined separately to help ensure that the entire study area was subjected to a near-uniform examination (Parsons & Yearley, 1986). A systematic approach was then used to examine each section of the image for potential lineaments. Potential lineaments were inspected in order to establish their origin, and those interpreted to be of a geological nature were traced onscreen as line vectors using the overlay tool in ENVI 4.3. The same criteria were used to determine the length and origin of all lineaments within a single image, and wherever else applicable. This consistency should help to further reduce the effects of subjectivity on the mapping results. Following interpretation, line vectors for each enhancement technique were exported as shapefiles for subsequent interrogation.

7.3.3 Lineament analysis

Lineament maps generated using the above procedure were analysed to compare and evaluate the utility of the LiDAR DTM and ATM imagery for structural mapping. To do this, the lineament orientations and lengths were extracted from each map by interrogating the shapefiles in ArcMap (ArcGIS 9.2). Orientation information was plotted as rose diagrams, using StereoWin software, to help reveal the dominant structural trends exhibited within the edge-enhanced data products. In addition, various statistics relating to the numbers and lengths of lineament were also computed. Lineament density maps were also derived from the lineament maps using the Spatial Analyst Line Density tool in the ArcMap Arc Toolbox, with a search radius of 250 m.

Additionally, a field survey was undertaken to collect structural measurements for the purpose of providing some degree of validation of the LiDAR and ATM-derived lineament maps. The survey was conducted by measuring the strike and dip of faults and dykes encountered along the stream transect highlighted in Fig. 7.2. The stream transect provides excellent exposure and runs perpendicular to an apparent NW-SE structural trend visible in both the DTM and ATM imagery. Structural information within this transect was therefore deemed to reflect the dominant regional structural trends, thus removing the need to undertake extensive mapping of the entire study area for validation purposes. During the field survey, only faults extending beyond the local drainage were measured since minor faults were not anticipated to be detectable in the imagery. Field-based structural measurements were plotted on stereonets and rose diagrams (again using StereoWin) to enable comparison with imagery-derived lineament data.

7.4 Results and discussion

7.4.1 Field-based structural data

Field-based measurements of the strike and dip of faults and dykes exposed along the 4 km transect enabled the most prominant structural trends within the study area to be determined. In the field, individual dykes and less abundant sets of dykes were predominantly observed striking NW-SE and dipping steeply towards the NE (Fig. 7.6a). This is in agreement with other observations concerning the attitude of dykes which were made during mapping of the same locality (Gass, 1960). The average strike orientation for the 64 dykes was computed as 318° with relatively little deviation, although minor secondary N-S and E-W trends are apparent. The dip angle was found to vary between 42° and 90°, with an average dip of approximately 70°. On the other hand, brittle faults measured in the field do not appear to exhibit a clear dominant trend (Fig. 7.6b). However, the majority of faults observed strike between E-W and NW-SE. Dip angles for the measured faults coincide with those of dykes; varying between 40–90° with an average in the region of 70°. The dip direction associated with the faults is also variable, although the majority dip NE. Orientation data for the dykes and faults were combined to reveal a dominant NW-SE structural trend within the study area (Fig. 7.6c). This dominant trend concurs with the initial observation made during identification of a suitable field transect, and is primarily dictated by the abundance of NW-SE striking dykes. Minor trends striking E-W, NE-SW and approximately N-S are also apparent in the combined field-based structural data.

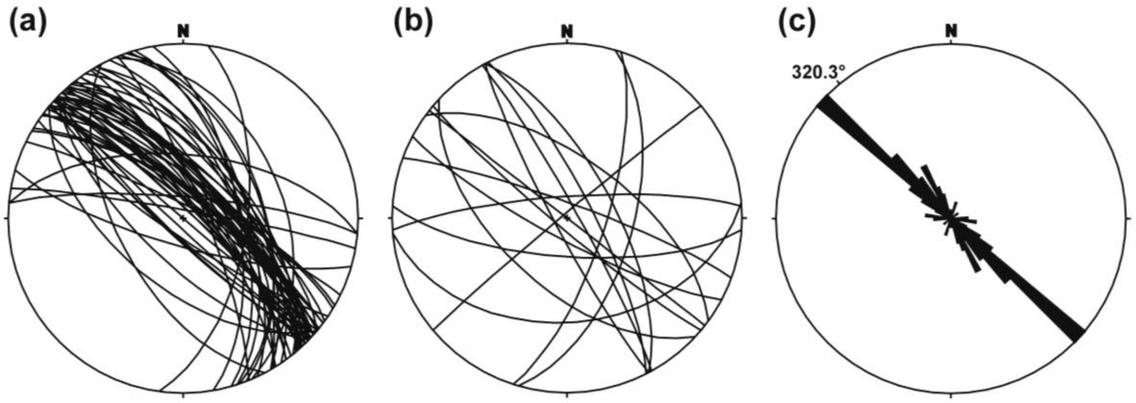

Fig. 7.6. Structural data obtain through field-based mapping. Stereonet plots for **(a)** dykes (n=64), **(b)** faults (n=16) and **(c)** rose diagram of dyke and fault data combined (n=80, outer circle=26%), with the average orientation indicated.

7.4.2 LiDAR- and ATM-based lineament mapping

The six lineament maps that result from the visual interpretation of the edge-enhanced LiDAR DTM and ATM products are shown in Fig. 7.7. An initial inspection reveals that the dominant NW-SE structural trend that is observable in the field is also apparent in all six lineament maps. Moreover, the overall spatial extent of the lineaments is similar for all six maps. The vast majority of lineaments are dykes, and are confined to the SE sector of the study area. Lineaments were not identified in the NW and the extreme NE corner of the study area. The confinement of lineaments to the SE is expected since this area coincides with the extent of the pillow lava and Basal Group units in which dykes commonly occur. Predominant alluvial–colluvial cover in the NW and the outcrop of Lefkara cherts, chalks and marls in the NE corner explain the lack of lineaments in those areas.

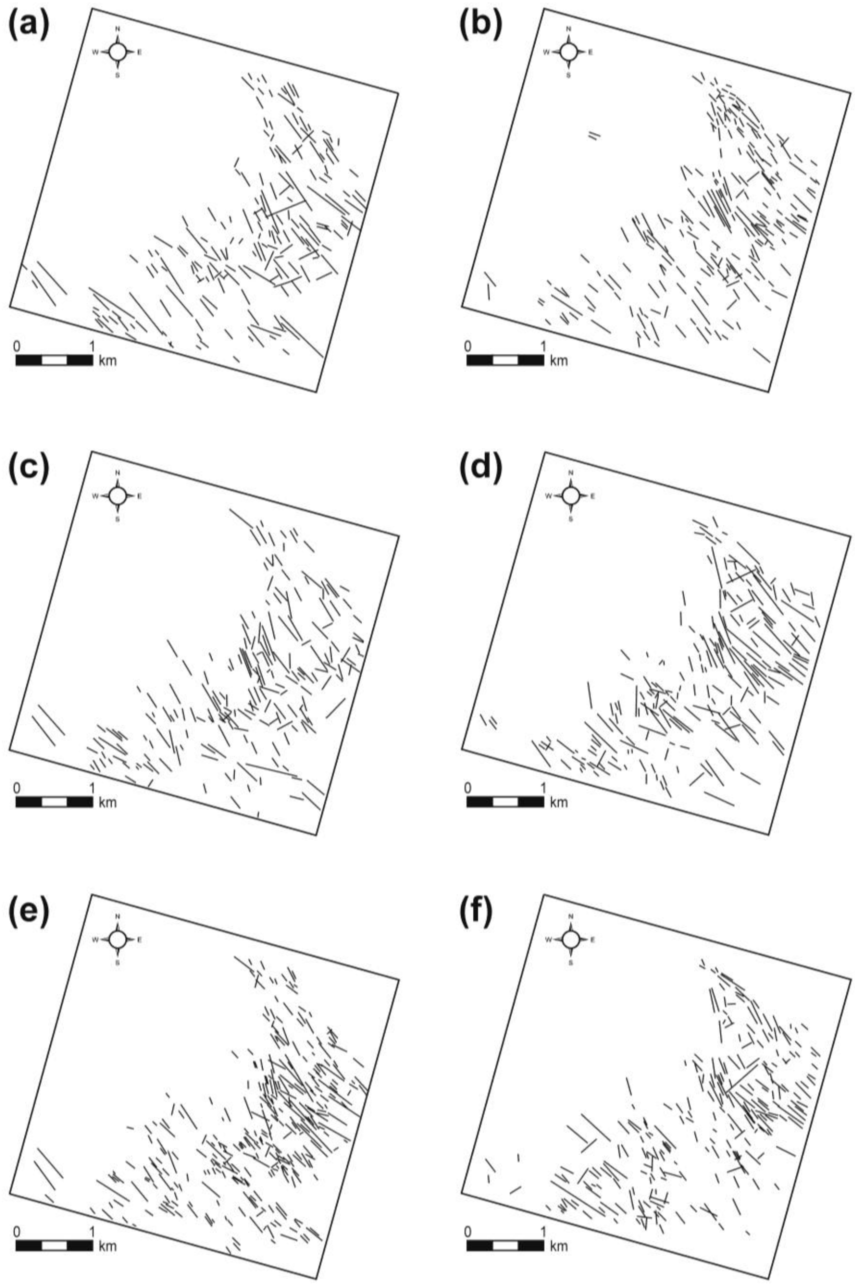

Fig. 7.7. Lineament maps generated through visual interpretation of **(a)** shaded relief DTM, **(b)** ATM PC FCC, **(c)** top hat transformed DTM, **(d)** top hat transformed ATM PC FCC, **(e)** Laplacian filtered DTM and **(f)** Laplacian filtered ATM PC FCC.

Rose diagrams produced for all six lineament maps confirm a dominant NW-SE trend for the study area (Fig. 7.8). This result is corroborated by the structural measurements collected in the field. Furthermore, the minor secondary NE-SW trend seen in all rose diagrams is also in agreement with the field data. A number of additional secondary trends are indentified using the top hat transformed DTM (Fig.

7.8c). Of these, the N-S and E-W trends are substantiated by the field measurements. Resultant average lineament orientations are fairly consistent for all maps, ranging from approximately 313° for the shaded relief (Fig. 7.8a) to nearly 318° for the top hat transformed DTM (Fig. 7.8c). These average orientations are also comparable to that obtained from the field-based data. Therefore, based upon comparison of the rose diagrams, it is evident that both the LiDAR and ATM products are useful tools for revealing the dominant structural trends within the study area.

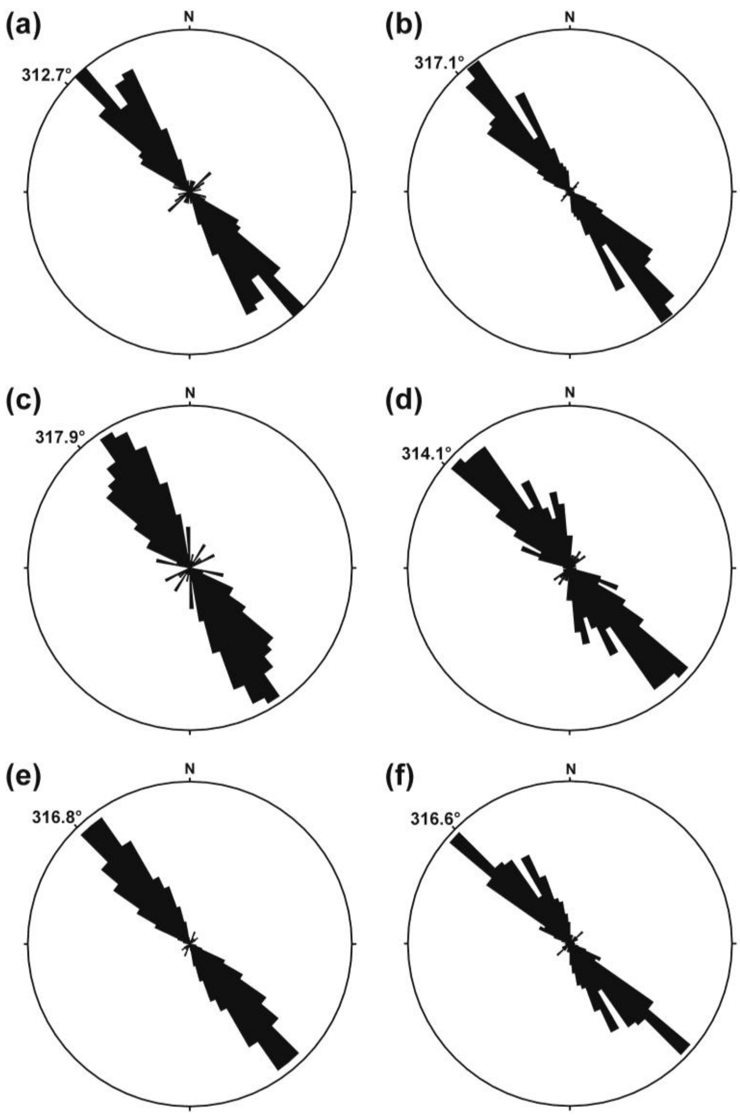

Fig. 7.8. Rose diagrams for lineament maps generated using **(a)** shaded relief DTM (15%), **(b)** ATM PC FCC (17%), **(c)** top hat transformed DTM (12%), **(d)** top hat transformed ATM PC FCC (12%), **(e)** Laplacian filtered DTM (16%) and **(f)** Laplacian filtered ATM PC FCC (16%). Average orientations are indicated. Percentages denote proportion of lineaments represented by outer circles in corresponding rose diagrams (see Table 7.1).

Despite only minor differences in the orientation information for the various enhancement techniques, further interrogation of the lineament maps reveals some notable differences relating to the number and lengths of lineaments (Table 7.1). In terms of the number of lineaments, a maximum of 316 were identified using the Laplacian filtered DTM, compared to an average of 213 for the five other techniques. With regards to the individual datasets, ATM-based enhancement techniques generally result in the identification of 15% more lineaments on average than LiDAR DTM-based techniques (with the exception of the Laplacian filtered DTM). One possible explanation for the higher number of lineaments with ATM-based techniques is that lineaments are typically more conspicuous in colour images than in greyscale representations of LiDAR elevation (DTM) products. However, this does not appear to be the case for the Laplacian filtered DTM, possibly due to a higher greyscale contrast associated with edges.

Table 7.1. Statistics relating to the number and lengths of lineaments identified using the various enhancement techniques.

Enhancement technique	No. of lineaments	Minimum length (m)	Maximum length (m)	Average length (m)	Total length (m)
Shaded relief DTM	192	51.1	801.0	207.4	39817.5
ATM PC FCC	227	38.2	714.7	167.5	38021.0
Top hat DTM	199	55.2	709.2	199.5	39707.1
Top hat ATM PC FCC	210	52.5	665.4	217.0	45563.1
Laplacian DTM	316	37.7	735.1	158.4	50059.3
Laplacian ATM PC FCC	239	53.5	868.3	174.9	41791.4

Frequency distributions of lineament lengths for each enhancement technique are shown in Fig. 7.9. The distributions for all enhancement techniques appear unimodal, and positively skewed due to a wide range of lengths with a profusion of lineaments with lengths between 50–400 m. In the enhanced products, The Laplacian filtered DTM has the greatest abundance of shorter lineaments and is responsible for both the shortest mapped lineament (~38 m) and the shortest average lineament length (158.4 m). This, together with the high number of lineaments associated with this technique, could suggest that larger lineaments appear segmented in the Laplacian filtered DTM, therefore resulting in shorter, but more numerous lineaments. However, evidence of lineament segmentation is not apparent in the Laplacian filtered DTM and the total lineament length is at least 10% longer than for any other technique, indicating that the additional lineaments do not simply arise through the division of lineaments that appear longer in other enhanced products.

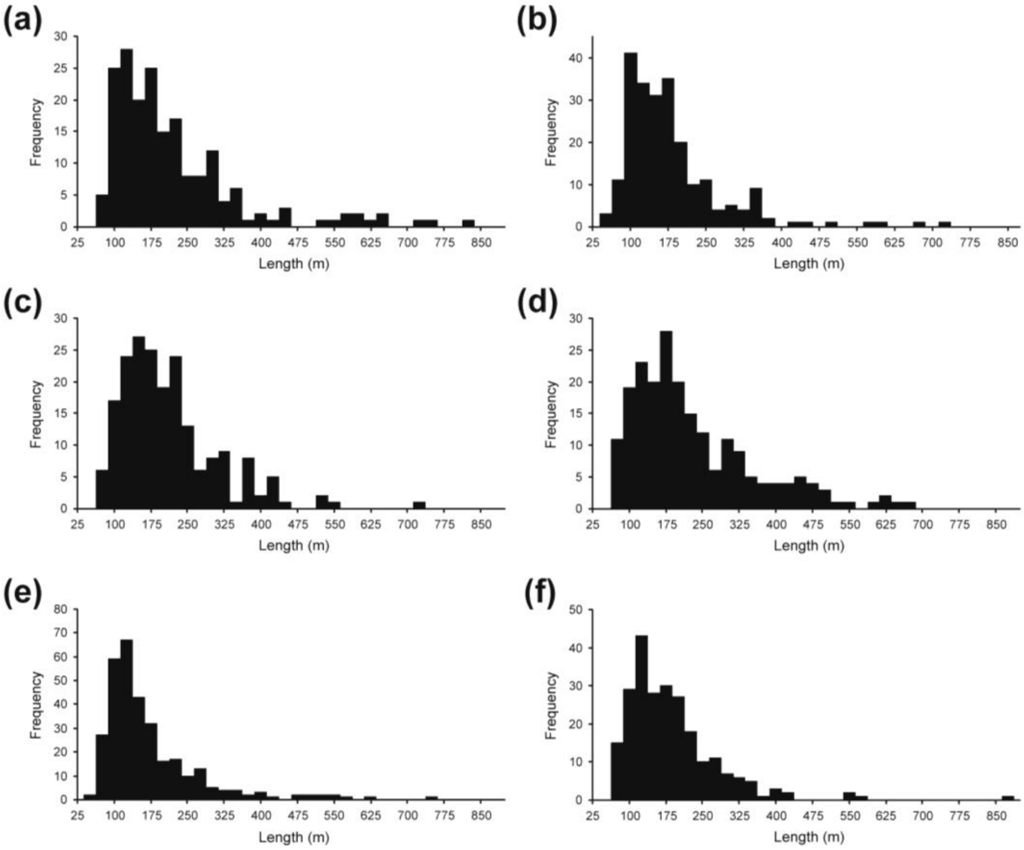

Fig. 7.9. Frequency distribution of lineament lengths mapped using the various enhancement techniques. **(a)** Shaded relief DTM, **(b)** ATM PC FCC, **(c)** top hat transformed DTM, **(d)** top hat transformed ATM PC FCC, **(e)** Laplacian filtered DTM and **(f)** Laplacian filtered ATM PC FCC.

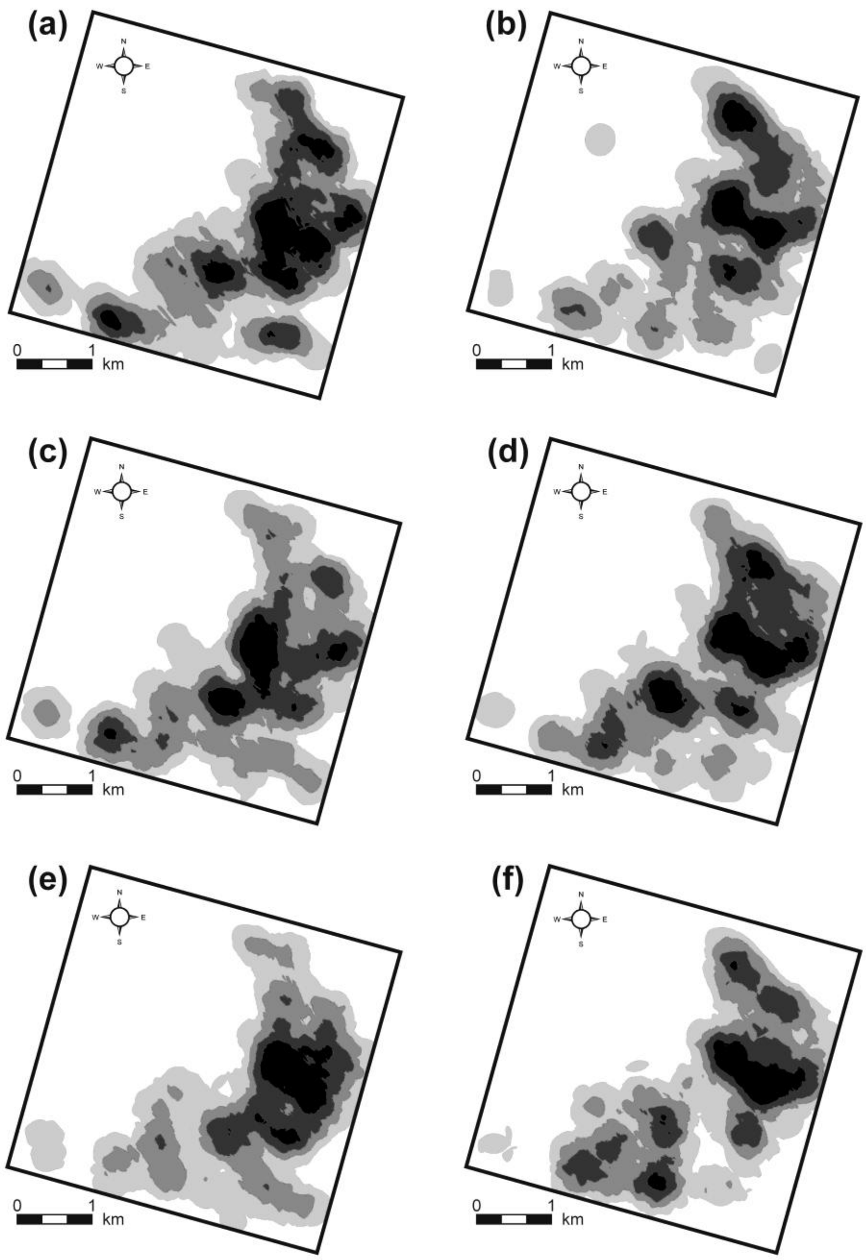

Fig. 7.10. Lineament density maps derived from the lineament maps for **(a)** Shaded relief DTM, **(b)** ATM PC FCC, **(c)** top hat transformed DTM, **(d)** top hat transformed ATM PC FCC, **(e)** Laplacian filtered DTM and **(f)** Laplacian filtered ATM PC FCC. Shading represents low (white) to high lineament density (black).

The lineament density maps shown in Fig. 7.10 reveal the spatial distribution of lineaments mapped using each of the enhancement techniques. As might be expected due partly to the similarities in the spatial extent of lineaments in all six maps, the ensuing lineament density maps are also visibly similar. The highest densities commonly occur in the east of the study area, in pillow lavas. In a number of maps, smaller regions of high density can also be seen towards the NE and due S of the centre, again coinciding with the pillow lavas. Considering that the field data shows the vast majority of lineaments in the study area are dykes, and given the definitions of the Basal Group and pillow lava units (e.g., Bear, 1960), one might expect the highest lineament densities to be associated with the Basal Group. According to the above results, this is clearly not the case. A likely explanation for this could relate to the ability to distinguish dykes from their host rocks. For example, in the topographic domain the relative lack of lineaments (in the form of dykes) in the Basal Group could be due to uniform weathering and erosion of outcrops, which then leads to difficulty discerning individual or sets of dykes at the surface. On the other hand, the contrast in hardness between dykes and host pillow lava rocks results in differential erosion and weathering, thus giving dykes an obvious positive topographic surface expression. Spectrally, it is also difficult to identify dykes in the Basal Group because of a lack of spectral contrast between individual dykes and the dyke-dominated rocks, whereas dykes in pillow lavas are more readily recognisable due to better spectral contrast linked to subtle compositional differences and different jointing characteristics. Similarly, lineaments that occur as faults are also easier to trace in the pillow lavas than in the Basal Group (Gass, 1960).

Lineament density maps can also be used help to determine whether lineament maps with a greater number of lineaments actually contain more information than those with less. If there is significant correlation between any two maps with differing numbers of lineaments then they can essentially be regarded as equivalent, whereas weak correlation suggests that the two maps contain different information (Parsons & Yearly, 1986). The results of the correlation analysis show strong correlations between all maps (Table 7.2). The Laplacian filtered ATM PC FCC and top hat transformed DTM maps are the most weakly correlated, while the Laplacian filtered ATM PC FCC and the top hat transformed ATM maps are the most correlated. Correlations between the map associated with the greatest number of lineaments (Laplacian filtered DTM) and all other maps do not fall below 0.81. This result suggests that all lineament maps essentially contain the same information regardless of the numbers of lineaments. Also, if the additional lineaments in the Laplacian filtered DTM map are related to the segmentation of longer lineaments then higher densities in these areas would likely result in low correlations between all other maps.

Table 7.2. Correlation matrix of lineament density maps.

	Shaded relief DTM	ATM PC FCC	Top hat DTM	Top hat ATM PC FCC	Laplacian DTM	Laplacian ATM PC FCC
Shaded relief DTM	–					
ATM PC FCC	0.82	–				
Top hat DTM	0.89	0.79	–			
Top hat ATM PC FCC	0.87	0.87	0.83	–		
Laplacian DTM	0.88	0.81	0.84	0.85	–	
Laplacian ATM PC FCC	0.81	0.87	0.76	0.90	0.81	–

7.4.3 Significance of structural trends and implications

Following the separation of the northern part of the ophiolite into domains of uniform dyke strike and dip, three structural grabens have been indentified and interpreted as fossil axial valleys of an eastward jumping spreading centre (Varga & Moores, 1985). From west to east, these are the Solea graben, Ayios Epiphanios (or Mitsero) and the Larnaca graben. The area selected in this study is situated in the

Larnaca graben (see Fig. 2.12). Field-based measurements show that dykes in this area are dipping NE, which is concurrent with the location of the study area on the western flank of the Larnaca graben proposed by Varga & Moores (1985). The injection of dykes parallel to the NW-SE trending spreading axis in an extensional setting explains the prevailing NW-SE trend revealed by both the field measurements and results of lineament mapping. An additional contribution to this dominant trend may also originate from normal faulting during graben development and dyke injection (Gass, 1960). Whilst there is a slight indication of dyke-parallel faulting in the field-based data, the rather variable orientations of the faults recorded in the field are likely to reflect local deformation and possibly younger faulting subsequent to formation of the ophiolitic crust. The secondary N-S trend apparent in both the field data and certain lineament maps is consistent with a later stage of faulting previously reported in the vicinity of the study area (Gass, 1960; Boyle & Robertson, 1984).

7.5 Conclusions

This study investigates the efficacy of airborne LiDAR topographic data and ATM imagery for assisting structural mapping of the Troodos study area. Despite widespread vegetation cover, a preliminary analysis showed that the main structural features — faults and dykes — were recognisable in both the 4 m LiDAR-derived DTM and ATM imagery as lineaments defined by edges. Accordingly, several different edge enhancement techniques were applied to the LiDAR DTM and ATM imagery to aid the visual identification and mapping of lineaments. The predominant strike trends of lineaments in all resulting maps were found to be in agreement with field-based structural data acquired along a stream transect, in addition to observations made by other workers in the vicinity. The dominant trend in the study area is orientated NW-SE and corresponds to the injection of dykes and concordant faulting parallel to the spreading axis of the proposed Larnaca graben. To the best of the author's knowledge, this appears to be the first application of airborne LiDAR to detailed structural mapping of ophiolitic rocks.

Whilst the results of this study have direct implications for mapping ophiolite structure, it is anticipated that both high-resolution airborne LiDAR data and airborne spectral imagery can be easily be applied in similar Mediterranean regions in order to complement field-based structural mapping. With the capability of acquiring high-resolution topographic data even in densely forested terrain, airborne LiDAR has the potential to be a valuable tool for structural mapping in any geological setting, irrespective of vegetation cover, provided that an adequate DTM can be generated. However, airborne spectral imagery is likely to be of limited use in areas where geological features are subtly expressed in the terrain beneath tall dense vegetation cover.

8. Synthesis and conclusions

8.1 Introduction

The aim of this thesis is to explore the novel application of airborne LiDAR data and airborne multispectral imagery for high-resolution geological mapping of vegetated ophiolitic rocks and sedimentary cover in the Troodos Range, Cyprus. A direct spectral approach to lithological mapping — which utilises the airborne multispectral (i.e., ATM) imagery — is deployed in Chapter 4 for the purpose of assessing the capability of a conventional remote sensing approach, and for subsequently revealing any adverse effects that vegetation cover may have on its performance. Novel lithological mapping methods utilising ATM imagery and airborne LiDAR data are explored in Chapters 5 and 6 for use in areas where vegetation cover thwarts the deployment of conventional spectral mapping approaches. Additionally, the utility of airborne LiDAR data and ATM imagery for detailed structural mapping is investigated in Chapter 7. This chapter provides a synthesis of the main findings of each chapter and uses this information to evaluate the efficacy of ATM imagery and airborne LiDAR data for rapid, high-resolution geological mapping of the vegetated ophiolitic rocks and sedimentary cover in the Troodos Range. Furthermore, the wider impact regarding the use of these datasets and the devised mapping algorithms will also be discussed.

8.1.1 Conventional lithological mapping using airborne multispectral imagery

Airborne multi- or hyperspectral imagery has been recognised as a valuable tool for performing rapid, high-resolution lithological discrimination and mapping (e.g., Rowan et al., 2004; Harris et al., 2005; Roy et al., 2009). Conventionally, mapping is performed by matching image pixel spectra to distinct spectral signatures exhibited by lithologies. This approach was employed, by using representative reflectance spectra acquired in the laboratory in conjunction with three different spectral matching algorithms (SAM, MF and MTMF), to directly map the four main lithological units in the Troodos study area (Chapter 4). The maps derived through this approach had very poor overall accuracies (2.4–6.5%) and Kappa coefficients (≈ 0.0), and it was demonstrated, both qualitatively and quantitatively, that ubiquitous vegetation cover in the study area was responsible for compromising lithological classification of large proportions (62–89%) of the total scene (or image) pixels. Subsequent spectral mixing analysis revealed that as little as 20% vegetation cover was enough to severely affect the utility of ATM imagery for direct spectral discrimination and mapping of the vegetated rocks of the Troodos study area. This figure is consistent with previous studies of different rock types (Siegal & Goetz, 1977; Ager & Milton, 1987; Murphy & Wadge, 1994) and therefore reiterates the fact that conventional use of spectral imagery is effective in only the world's most barren regions (e.g., deserts, alpine areas, cold regions). Although it is widely accepted that vegetation cover can obscure or mask the spectra of the underlying lithologies, the work presented in Chapter 4 appears to be the first attempt to quantitatively and qualitatively demonstrate the obscuring effects of vegetation at both the image-level and pixel-level.

8.1.2 Novel lithological mapping using airborne multispectral and LiDAR data

A time- and cost-effective programme enabling the production of accurate and high-resolution geological maps of any part of the Earth's surface would be a desirable product for geological surveys, government agencies and resource exploration companies. Inevitably, such a programme would rely heavily on the exploitation of remote sensing data through largely automated algorithms that can rapidly map the spatial distribution of lithologies accurately and in great detail, thus reducing the overall cost of fieldwork. This concept appears to be some way off considering that conventional spectral remote sensing approaches are critically limited by just small amounts of vegetation cover, together with the fact that the majority of the Earth's land surface is covered by a least some proportion of vegetation. Thus, the development of novel and alternative remote sensing-based mapping techniques that are impervious to the adverse effects of vegetation is both timely and essential.

Novel algorithms were developed in Chapters 5 and 6 for the purpose of exploring the use of high-resolution ATM imagery and airborne LiDAR data for overcoming the obscuring effect vegetation has on conventional lithological discrimination and mapping. These algorithms involve quantification of a characteristic that is distinct for each lithological unit, automated image classification based upon this characteristic, and an accuracy assessment of the generated maps. The characteristics exploited by these novel algorithms for indirect discrimination and mapping are the geobotanical spectral characteristics and topographic characteristics of the lithologies. Geobotanical spectral characteristics of the lithologies were extractable from the ATM imagery because the pixel spectra were generally dominated by the spectra of vegetation. The topographic characteristics of the four lithologies were obtainable from the airborne LiDAR topographic data. The accuracy statistics for maps generated using the novel indirect spectral (geobotanical) and topographic discrimination and mapping algorithms are summarised in Table 8.1.

Table 8.1. Lithological mapping accuracies obtained using novel algorithms in this thesis.

Discrimination approach	Input variables	MLC		SOM		p-value
		OA (%)	K	OA (%)	K	
Geobotanical	ATM 9	61.6	0.50	60.3	0.48	0.0010
	ATM PC	51.4	0.37	50.2	0.35	0.0007
	ATM MNF	59.3	0.46	65.5	0.54	<0.0001
Topographical	s, pr, pl, r and h	54.4*	0.40*	65.4	0.53	<0.0001
Geobotanical–topographical	ATM-Li	61.9	0.50	70.2	0.60	<0.0001
	ATM-Li MNF	60.8	0.49	72.7	0.63	<0.0001

* generated as an addendum to Chapter 5 (see Appendix II).

The exploitation of geobotanical associations for indirect lithological discrimination is not a new concept; several studies have utilised vegetation types as proxies for specific rock units during lithological mapping using airborne hyperspectral imagery (e.g., Rowan et al., 2004; Harris et al., 2005). In contrast to these studies, vegetation cover in the Troodos study area is mostly ubiquitous and so any successful lithological mapping attempt here must be almost fully reliant upon characterising the geobotanical associations. The results obtained using the devised algorithms presented in Chapter 6 demonstrate the ability to exploit geobotanical associations in order to generate high-resolution lithological maps of satisfactory accuracy for the relatively complex Troodos landscape. In fact, it was revealed that the algorithms based on geobotanical discrimination were capable of generating lithological maps that provide more detail and have more accurately defined contacts than the existing 1:250,000- and 1:31,680-scale geological maps of the study area. However, in some areas a combination of spectral similarity between lithologies (predominantly the Basal Group and Lefkara Formation) arising largely from an overlap in some types of vegetation, and intra-class variability — due to the heterogeneous vegetation cover (i.e., vegetation/rock mixtures) — appeared to hinder lithological discrimination somewhat. The algorithm which utilises the MNF transformation in conjunction with the SOM artificial neural network classifier was found to be effective in suppressing the intra-class spectral variability to help improve lithological discrimination and the mapping accuracy. It is likely that hyperspectral imagery, with its far superior spectral resolution, could provide the potential for improved geobotanical characterisation of the lithologies to further enhance the mapping results. This may be achievable with the aid of image-derived vegetation indices that reveal subtle intra-species variation which is related to the type of underlying geological substrate.

The ability to acquire accurate and high-resolution topographic data even in densely forested terrain is a key feature of airborne LiDAR. This feature provides the opportunity to detect subtle, but distinct topographic characteristics which reflect the different responses of individual lithologies to weathering and erosion. The results of the algorithm presented in Chapter 5 show that LiDAR-derived topographic data — specifically the morphometric variables of slope, absolute plan and profile curvatures, residual roughness and hypsometric integral — can be used to characterise lithology-specific topographic characteristics to facilitate the generation of a map that is also capable of providing more detail and more accurately defined contacts than the existing geological maps of the study area. However, both natural and anthropogenic-induced deviations from the typical topographic characteristics were found to be responsible for some confusion between lithologies in the resulting map. This approach is therefore perhaps best applied in virgin or wilderness terrain which is devoid of anthropogenic impacts. On the other hand, improved characterisation using additional or alternative morphometric variables (e.g., fractal dimension) might help to reduce the confusion, especially that relating to natural topographic deviations. The presence of low-to-medium height vegetation in the airborne LiDAR DTM was occasionally problematic because it forms artificial topography, which can subsequently result in misclassification of the corresponding area. The inability to remove vegetation of this type from the LiDAR DTM is likely to be attributable to either the vertical resolution of the LiDAR system (i.e., the ability to resolve multiple returns over short vertical distances) or misclassification of the associated LiDAR returns prior to DTM generation. This issue should be surmountable using either a more modern LiDAR system with improved vertical resolution, full-waveform airborne LiDAR, or by incorporating LiDAR intensity data into the point return classification process to aid separation of ground and low lying non-ground returns prior to DTM generation (Hui et al., 2008). Despite these relatively minor drawbacks, the estimated overall lithological mapping accuracy achievable with the airborne LiDAR algorithm is comparable to that attainable through indirect spectral discrimination using the ATM imagery. Moreover, the application of airborne LiDAR to lithological mapping has implications that extend beyond the study area, because correlations between lithology and topography have been recognised in other parts of the world (e.g., Kühni & Pfiffner, 2001; Belt & Paxton, 2005).

Integrating airborne LiDAR data and ATM imagery to simultaneously exploit the correlations between vegetation and lithology, and topography and lithology, was generally found to significantly improve the overall lithological mapping accuracy (by up to 22% in terms of the OA) in comparison to the individual use of either dataset. The result suggest that this arises because airborne LiDAR–ATM data integration is synergistic in the Troodos study area, with topographic information providing the additional discriminatory power required to separate spectrally similar lithologies (e.g., Basal Group and Lefkara Formation) and *vice versa*. Nevertheless, some classification ambiguity still persisted, particularly in areas where the lithological units exhibit both spectral similarity and atypical topographic characteristics due to either natural or anthropogenic deviation. Again, the use of hyperspectral imagery or alternative morphometric variables could enhance the separability between lithologies, therefore increasing the overall lithological mapping accuracy.

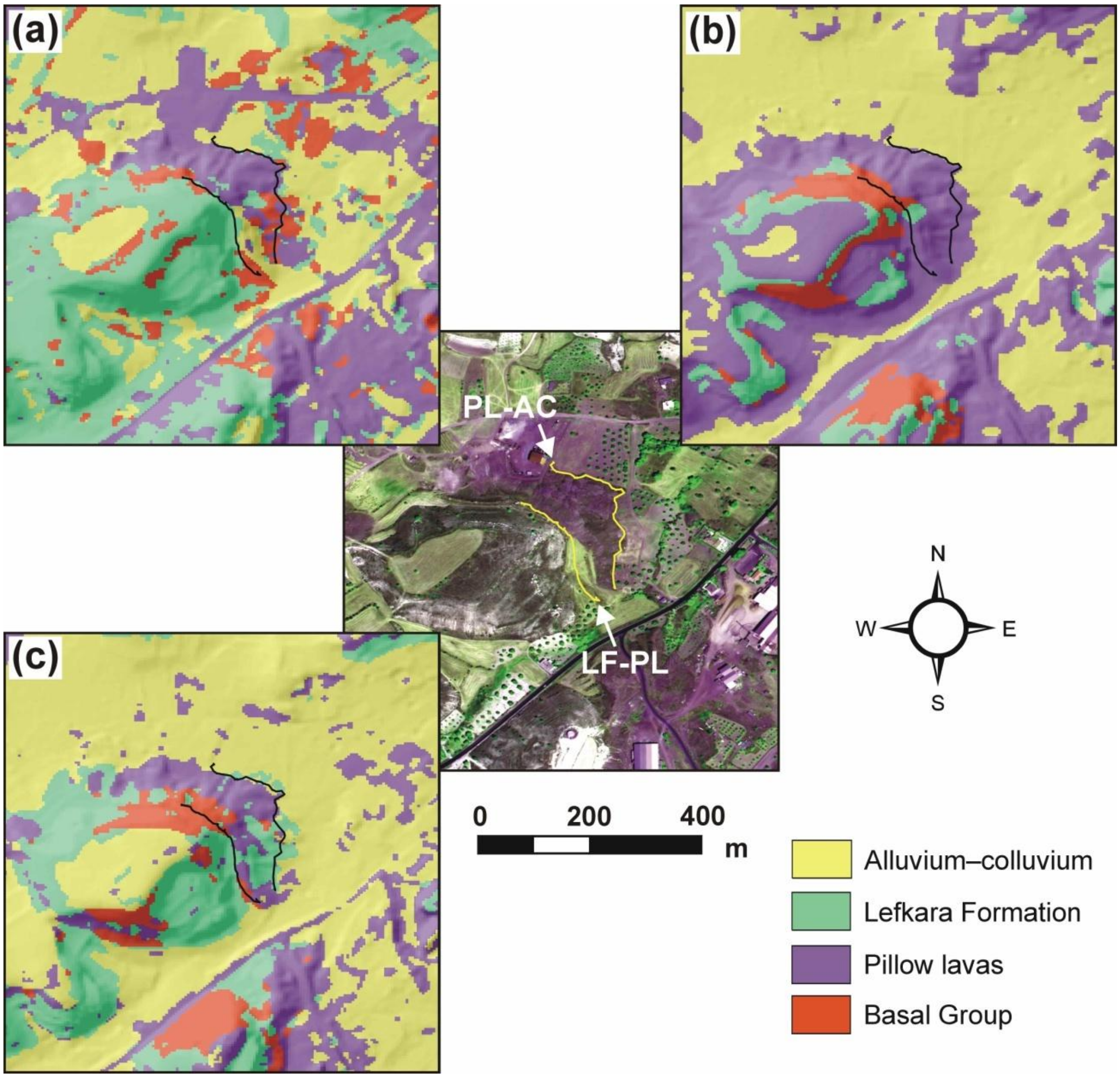

Fig. 8.1. Field-mapped Lefkara Formation–pillow lavas (LF-PL) and pillow lavas–alluvium-colluvium (PL-AC) contacts overlain on top of QuickBird image (centre) and the **(a)** ATM MNF SOM, **(b)** LiDAR SOM and **(c)** Li-ATM MNF SOM maps for the area shown in Fig. 3.9. Accuracy of the field-mapped contacts is estimated at ± 10 m due to a combination of GPS accuracy and some difficulty in discerning the contacts in places.

The optimal algorithms for each of the three discrimination approaches (geobotanical, topographical and geobotanical–topographical discrimination) are the ATM MNF SOM, LiDAR SOM and ATM-Li MNF SOM. According to the guidelines provided by Landis & Koch (1977) for interpreting K, these algorithms can discriminate lithologies and map their overall spatial distributions to quite a substantial degree of accuracy. As previously discussed, these algorithms are capable of generating lithological maps that are more detailed and have more accurately defined contacts than the two existing geological maps of the study area. Additional comparison with field data allows better appreciation of the mapping capabilities. As seen in Figs. 8.1 and 8.2, all three algorithms have the capacity to map lithological contacts with an accuracy similar to that which is attainable through field-based mapping. The ATM MNF SOM algorithm is most effective at mapping Lefkara Formation–pillow lavas contacts, whereas the LiDAR SOM algorithm can readily delineate pillow lavas–alluvium-colluvium contacts. The Li-ATM MNF SOM algorithm seems to be able to map both of these contacts accurately. Importantly, the intricate contacts between basement rocks and cover material, especially the pillow lavas or Basal Group–alluvium-colluvium contacts, are very accurately resolved. This is often a difficult boundary for field geologists to map in accurately. Overall, following a comparison with all field data, it evident that the three algorithms have the ability to perform high-resolution lithological mapping that is accurate to a scale of 1:5000.

In contrast to the conventional direct mapping approach deployed in Chapter 4, the novel algorithms devised in Chapter 5 and 6 are able to perform accurate, high-resolution lithological mapping of the Troodos study area, despite widespread vegetation cover. This is significant outcome because it provides evidence contrary to the general view that the utility of remote sensing for lithological mapping is restricted to only the most barren terrain. It is anticipated that these algorithms can be used to map barren terrain, and that their utility can easily be extended to similar vegetated Mediterranean-type regions and even areas with significantly denser, ubiquitous vegetation cover (e.g., temperate and possibly tropical forests), provided that geobotanical associations exists and/or lithology and topography are linked. Also, these algorithms require very limited (or even no) prior knowledge regarding the spatial distributions of lithologies, which makes them particularly relevant to mapping relatively unexplored terrain.

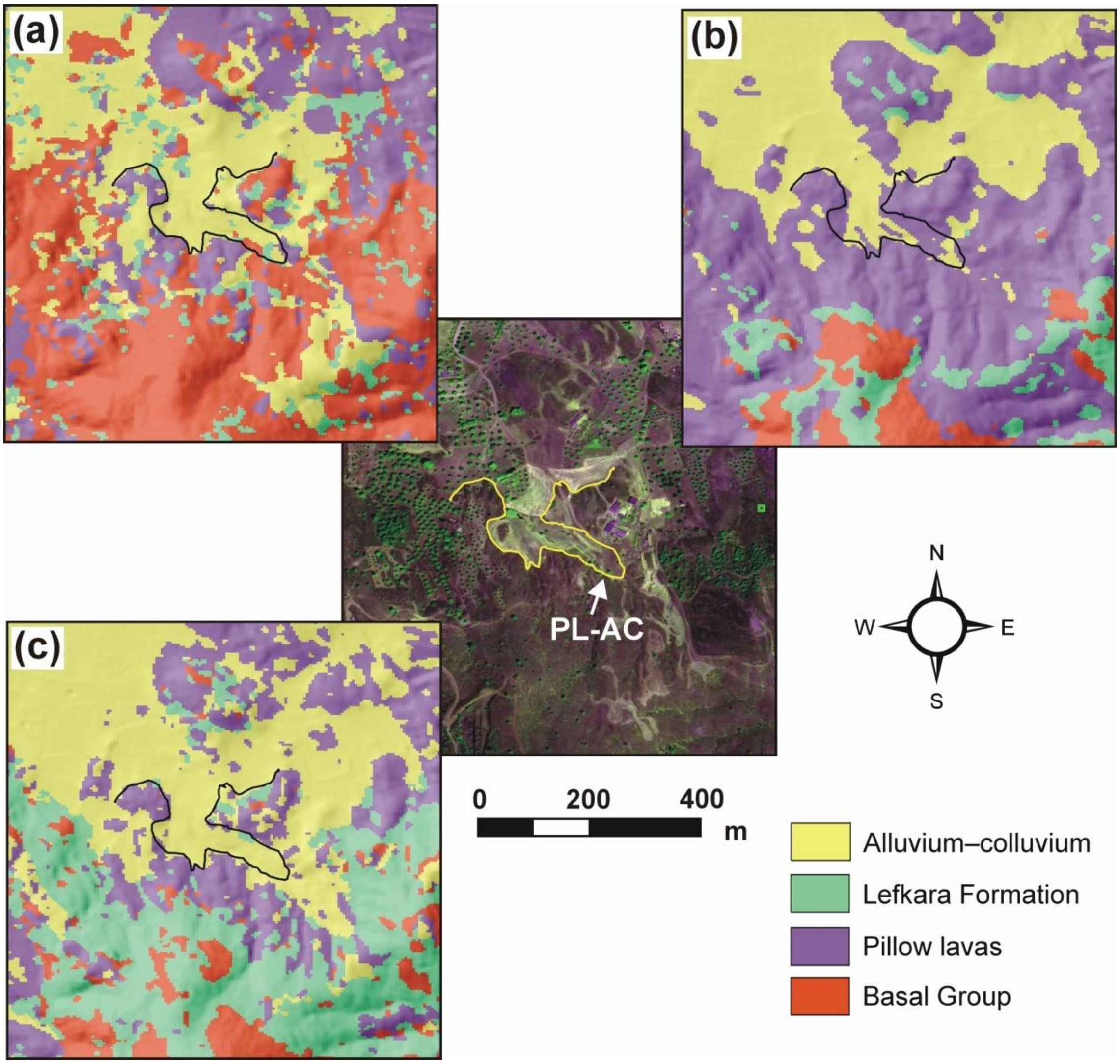

Fig. 8.2. Field-mapped pillow lavas–alluvium-colluvium (PL-AC) contact overlain on top of QuickBird image (centre) and the **(a)** ATM MNF SOM, **(b)** LiDAR SOM and **(c)** Li-ATM MNF SOM maps for the area shown in Fig. 3.9. Accuracy of the field-mapped contact is estimated at ± 5 m due to a combination of GPS accuracy and some difficulty in discerning the contact in places.

8.1.3 Structural mapping using airborne multispectral and LiDAR data

Similarly to lithological mapping, the application of remote sensing to structural mapping is also restricted by vegetation cover and spatial limitations of the data. In comparison to that of classic spaceborne instruments, data acquired from airborne platforms can have a considerably higher spatial resolution which presents opportunities to resolve much more detailed structural information. Moreover, airborne LiDAR has already been established as a major tool for mapping surface traces of faults in both vegetated and non-vegetated terrain. However, with the exception of a recent study which applies airborne LiDAR to resolve bedrock structure in areas of poor exposure (Pavlis & Bruhn, 2011), the broader structural utility of airborne LiDAR has not been appreciated. The efficacy of airborne LiDAR data and ATM imagery for assisting structural mapping of the Troodos study area was investigated in Chapter 7 — mapping the structure of ophiolitic rocks appears to be a novel application of airborne LiDAR. The results demonstrated that airborne LiDAR data and ATM imagery can be utilised to extract detailed and accurate structural information that is consistent with field-based data. Although these results are directly relevant to structural mapping in other ophiolites, it is anticipated that utility of both datasets can easily be extended to diverse geological settings with similar vegetative cover. However, airborne LiDAR data is likely to be more effective than airborne spectral imagery in areas with denser vegetation, such as forest, provided that an adequate DTM can be generated. To achieve this, it may be necessary to use high laser point density in order to increase the canopy penetration rate and thus the number of ground returns. Although accurate and detailed structural mapping using a manual approach was not time-consuming in the Troodos study area, for larger map areas automated lineament extraction algorithms would be more efficient. In this context, further research is required to help differentiate between lineaments of a geological origin from artificial lineaments. As established with lithological mapping, an integrated spectral–topographic approach could provide the added discriminatory power for reducing the confusion between geological and artificial lineaments.

8.2 Recommendations and future work

Remote sensing-based algorithms, such as those described in this thesis, will never completely eradicate the need for field-based geological mapping. Instead, it is clear that the most time- and cost-effective method of producing accurate and detailed geological maps is through a combination of fieldwork and remote sensing — this is especially true for large map areas. An ideal geological mapping programme is one that involves an iterative process of fieldwork and use of remote sensing-based algorithms. This might involve an initial fieldtrip to obtain knowledge of the study area (although not essential as some algorithms, such as the SOM-based ones, can be deployed unsupervised, i.e., without any training data), application of remote sensing mapping algorithms to generate what is essentially a detailed and accurate reconnaissance map, follow-up field validation and necessary refinement of the geological map product. Depending on the efficacy of the remote sensing algorithms, the geological map-making process can ultimately be made more efficient by significantly reducing the effort and cost of fieldwork.

Irrespective of their significant potential, the algorithms devised here most importantly provide evidence towards the proof-of-concept that airborne LiDAR data and airborne spectral imagery can be individually and simultaneously utilised to aid accurate and high-resolution geological mapping, regardless of vegetative cover. The veracity of the generated lithological map products could potentially be improved through refinement of these novel algorithms. An obvious starting point would be to simply replace the airborne multispectral imagery with hyperspectral imagery. This will undoubtedly be useful for improving the geobotanical spectral characterisation and separability. Instead of relying primarily on differences in vegetation species for indirect lithological discrimination, properties which may be more unique to each of the lithologies could be derived from hyperspectral imagery in the form of vegetation indices.

The classification stage of the novel lithological mapping algorithms in this study is performed on a per-pixel basis. For all three discrimination approaches (geobotanical, topographical and integrated geobotanical–topographical) the maximum mapping accuracy was achieved using the SOM classifier. This demonstrates the superiority of artificial neural networks over conventional classifiers such as the MLC in using minimal *a priori* knowledge to classify noisy and complex data — as is often the case with high-resolution data (Aplin, 2006; Pacifici et al., 2009). Another important feature of the SOM is the accompanying SOM-C map, which was shown to highlight areas with high classification uncertainty, therefore providing information on follow-up targets to allow more efficient field-based verification. Further work is required to assess whether the overall mapping accuracy can be improved by using the SOM artificial neural network to perform object-based lithological classification. Object-based classification, which classifies homogenous groups of pixels as opposed to individual pixels, is often regarded as being more suitable for classifying high-resolution data than per-pixel methods (Kressler et al., 2001). Although segmentation of imagery into objects usually depends on subjective trial-and-error methods, recent attention has focussed on making segmentation less problematic, more automated and more objective (Drăguț et al., 2010). Thus, an investigation into a combined object-based artificial neural network classification approach to lithological mapping now seems more timely and appealing.

Additional aspects that are also worthy of further investigation include evaluating the use of LiDAR intensity data for lithological discrimination, the application of these or refined mapping algorithms to other geologically diverse parts of the world, and the utility of the developed algorithms when applied to current (e.g., ASTER) and future datasets (e.g., EnMAP, TanDEM-X/TerraSAR-X). Ambitious it may be, but the ultimate objective is to try to develop a software toolkit which comprises a set of algorithms which can utilise airborne LiDAR data and hyperspectral imagery to perform rapid and accurate high-resolution geological mapping in any terrain, irrespective of vegetation cover. This toolkit should include algorithms for performing other important aspects of geological mapping, such as alteration mapping and improved geological hazard detection and mapping (e.g., faults and volcanic landforms).

8.3 Conclusions

This thesis explores novel applications of airborne LiDAR data and airborne multispectral imagery for high-resolution geological mapping of vegetated ophiolitic rocks and sedimentary cover in the Troodos Range, Cyprus. Overall, it has been demonstrated that both airborne spectral imagery and airborne LiDAR data can be utilised to overcome the effects of vegetation cover that critically limit the conventional use of remote sensing to essentially barren areas. To summarise, the main conclusions are:

- Lithologies can be discriminated and mapped through geobotanical associations and their distinct topographic characteristics;

- Integration of airborne multispectral imagery and airborne LiDAR data can be synergistic for lithological mapping;
- Algorithms presented here are capable of producing lithological maps with more detail and more accurately defined contacts than the existing geological maps of the study area using minimal *a priori* knowledge;
- Algorithms can potentially be applied to any geological setting where direct spectral discrimination is difficult, provided that geobotanical associations exists and/or lithology and topographic are linked;
- Airborne spectral imagery and airborne LiDAR data can be used to map detailed and accurate structural information that is consistent with field-based data;
- Overall, the novel application of airborne spectral imagery and airborne LiDAR data have significant potential to aid rapid high-resolution geological mapping campaigns over large areas of vegetated or non-vegetated terrain.

Appendix I

Table I.1. Confusion matrix for ATM 9 MLC.

Mapped as	Validation data				Row total	User's accuracy (%)
	Alluvium–colluvium	Basal Group	Lefkara Formation	Pillow lavas		
Alluvium–colluvium	3594	1	30	11	3636	98.8
Basal Group	0	1614	299	383	2296	70.3
Lefkara Formation	2	816	1114	672	2604	42.8
Pillow lavas	491	769	1008	2142	4410	48.6
Column total	4087	3200	2451	3208		
Producer's accuracy (%)	87.9	50.4	45.4	66.8		
Overall accuracy = 61.6% K = 0.50						

Table I.2. Confusion matrix for ATM 9 SOM.

Mapped as	Validation data				Row total	User's accuracy (%)
	Alluvium–colluvium	Basal Group	Lefkara Formation	Pillow lavas		
Alluvium–colluvium	1979	284	59	39	2361	83.8
Basal Group	522	964	98	71	1655	58.2
Lefkara Formation	861	1268	2146	382	4657	46.8
Pillow lavas	725	684	148	2716	4273	63.6
Column total	4087	3200	2451	3208		
Producer's accuracy (%)	48.4	30.1	87.6	84.7		
Overall accuracy = 60.3% K = 0.48						

Table I.3. Confusion matrix for ATM PC MLC.

Mapped as	Validation data				Row total	User's accuracy (%)
	Alluvium–colluvium	Basal Group	Lefkara Formation	Pillow lavas		
Alluvium–colluvium	1224	0	29	1	1254	97.6
Basal Group	747	1324	844	247	3162	41.9
Lefkara Formation	1510	1258	1476	326	4570	32.3
Pillow lavas	606	618	102	2634	3960	66.5
Column total	4087	3200	2451	3208		
Producer's accuracy (%)	29.9	41.4	60.2	82.1		
Overall accuracy = 51.4% K = 0.37						

Table I.4. Confusion matrix for ATM PC SOM.

Mapped as	Validation data				Row total	User's accuracy (%)
	Alluvium–colluvium	Basal Group	Lefkara Formation	Pillow lavas		
Alluvium–colluvium	879	24	15	0	918	95.7
Basal Group	693	1140	475	305	2613	43.6
Lefkara Formation	1745	1456	1850	278	5329	34.7
Pillow lavas	770	580	111	2625	4086	64.2
Column total	4087	3200	2451	3208		
Producer's accuracy (%)	21.5	35.6	75.5	81.8		
Overall accuracy = 50.2% K = 0.35						

Table I.5. Confusion matrix for ATM MNF MLC.

Mapped as	Validation data				Row total	User's accuracy (%)
	Alluvium–colluvium	Basal Group	Lefkara Formation	Pillow lavas		
Alluvium–colluvium	2103	0	4	0	2107	99.8
Basal Group	888	1280	770	255	3193	40.1
Lefkara Formation	290	1222	1582	241	3335	47.4
Pillow lavas	806	698	95	2712	4311	62.9
Column total	4087	3200	2451	3208		
Producer's accuracy (%)	51.5	40.0	64.5	84.5		

Overall accuracy = 59.3%
K = 0.46

Table I.6. Confusion matrix for ATM MNF SOM.

Mapped as	Validation data				Row total	User's accuracy (%)
	Alluvium–colluvium	Basal Group	Lefkara Formation	Pillow lavas		
Alluvium–colluvium	2699	155	31	0	2885	93.5
Basal Group	638	1252	455	181	2526	49.6
Lefkara Formation	288	1093	1744	243	3368	51.8
Pillow lavas	462	700	221	2784	4167	66.8
Column total	4087	3200	2451	3208		
Producer's accuracy (%)	66.0	39.1	71.1	86.8		

Overall accuracy = 65.5%
K = 0.54

Table I.7. Confusion matrix for ATM-Li MLC.

Mapped as	Validation data				Row total	User's accuracy (%)
	Alluvium–colluvium	Basal Group	Lefkara Formation	Pillow lavas		
Alluvium–colluvium	1699	0	0	0	1699	100.0
Basal Group	95	1294	31	63	1483	87.3
Lefkara Formation	1775	1195	2357	477	5804	40.6
Pillow lavas	518	711	63	2668	3960	67.4
Column total	4087	3200	2451	3208		
Producer's accuracy (%)	41.6	40.4	96.2	83.2		
Overall accuracy = 61.9% K = 0.50						

Table I.8. Confusion matrix for ATM-Li SOM.

Mapped as	Validation data				Row total	User's accuracy (%)
	Alluvium–colluvium	Basal Group	Lefkara Formation	Pillow lavas		
Alluvium–colluvium	3103	110	93	31	3337	93.0
Basal Group	27	1419	184	224	1854	76.5
Lefkara Formation	46	1025	1916	308	3295	58.1
Pillow lavas	911	646	258	2645	4460	59.3
Column total	4087	3200	2451	3208		
Producer's accuracy (%)	75.9	44.3	78.2	82.4		
Overall accuracy = 70.2% K = 0.60						

Table I.9. Confusion matrix for ATM-Li MNF MLC.

Mapped as	Validation data				Row total	User's accuracy (%)
	Alluvium–colluvium	Basal Group	Lefkara Formation	Pillow lavas		
Alluvium–colluvium	1124	0	0	0	1124	100.0
Basal Group	129	1801	222	159	2311	77.9
Lefkara Formation	893	807	2177	285	4162	52.3
Pillow lavas	1941	592	52	2764	5349	51.7
Column total	4087	3200	2451	3208		
Producer's accuracy (%)	27.5	56.3	88.8	86.2		
Overall accuracy = 60.8% K = 0.49						

Table I.10. Confusion matrix for ATM-Li MNF SOM.

Mapped as	Validation data				Row total	User's accuracy (%)
	Alluvium–colluvium	Basal Group	Lefkara Formation	Pillow lavas		
Alluvium–colluvium	3780	169	357	66	4372	86.5
Basal Group	0	1446	301	163	1910	75.7
Lefkara Formation	0	991	1555	351	2897	53.7
Pillow lavas	307	594	238	2628	3767	69.8
Column total	4087	3200	2451	3208		
Producer's accuracy (%)	92.5	45.2	63.4	81.9		
Overall accuracy = 72.7% K = 0.63						

Appendix II

Table II.1. Confusion matrix for LiDAR MLC.

Mapped as	Validation data				Row total	User's accuracy (%)
	Alluvium–colluvium	Basal Group	Lefkara Formation	Pillow lavas		
Alluvium–colluvium	1959	0	0	0	1959	100
Basal Group	0	1613	243	315	2171	74.3
Lefkara Formation	73	820	1350	774	3017	44.7
Pillow lavas	2055	767	858	2119	5799	36.5
Column total	4087	3200	2451	3208		
Producer's accuracy (%)	47.9	50.4	55.1	66.0		
Overall accuracy = 54.4% K = 0.40						

References

Adamides, N. (1984). Cyprus volcanogenic sulphide deposits in relation to their environment of formation. PhD thesis, University of Leicester, Leicester.

Adams, J.B. (1974). Visible and near-Infrared Diffuse Reflectance Spectra of Pyroxenes as Applied to Remote-Sensing of Solid Objects in Solar-System. *Journal of Geophysical Research, 79*, 4829-4836.

Adams, J.B., Smith, M. O., & Gillespie, A. R. (1989). Simple models for complex natural surfaces: a strategy for the hyperspectral era of remote sensing. In, *IEEE Proceedings of IGARSS'89: 12th Canadian Symposium on Remote Sensing* (pp. 16-21).

Ager, C.M., & Milton, N.M. (1987). Spectral reflectance of lichens and their effects on the reflectance of rock substrates. *Geophysics, 52*, 898-906.

Ahokas, E., Kaartinen, H., & Hyyppä, J. (2003). A quality assessment of airborne laser scanner data. *International Archives of Photogrammetry, Remote Sensing and Spatial Information Sciences, 34*, 1-7.

Ali, S.A., & Pirasteh, S. (2004). Geological applications of Landsat Enhanced Thematic Mapper (ETM) data and Geographic Information System (GIS): mapping and structural interpretation in south-west Iran, Zagros Structural Belt. *International Journal of Remote Sensing, 25*, 4715-4727.

Allerton, S., & Vine, F.J. (1991). Spreading Evolution of the Troodos Ophiolite, Cyprus. *Geology, 19*, 637-640.

Amer, R., Kusky, T., & Ghulam, A. (2010). Lithological mapping in the Central Eastern Desert of Egypt using ASTER data. *Journal of African Earth Sciences, 56*, 75-82.

Aplin, P. (2006). On scales and dynamics in observing the environment. *International Journal of Remote Sensing, 27*, 2123-2140.

Argialas, D.P., & Mavrantza, O. D. (2004). Comparison of edge detection and Hough transform techniques for the extraction of geologic features. *International Archives of Photogrammetry, Remote Sensing and Spatial Information Sciences, 34*, 790-795.

Arnold, N.S., Rees, W.G., Devereux, B.J., & Amable, G.S. (2006). Evaluating the potential of high-resolution airborne LiDAR data in glaciology. *International Journal of Remote Sensing, 27,* 1233-1251.

Arora, M.K., & Mathur, S. (2001). Multi-source classification using artificial neural network in a rugged terrain. *Geocarto International, 16*, 37-44.

Arrowsmith, J.R., & Zielke, O. (2009). Tectonic geomorphology of the San Andreas Fault zone from high resolution topography: An example from the Cholame segment. *Geomorphology, 113*, 70-81.

Axelsson, P. (2000). DEM Generation from Laser Scanner Data Using Adaptive TIN Models. *International Archives of Photogrammetry and Remote Sensing, XXXIII-B4/1*, 110-117.

Bagan, H., Wang, Q.X., Watanabe, M., Yang, Y.H., & Jianwen, M. (2005). Land cover classification from MODIS EVI times-series data using SOM neural network. *International Journal of Remote Sensing, 26*, 4999-5012.

Bailey, W.R., Holdsworth, R. E., & Swarbrick, R. E. (2000). Kinematic history of a reactivated oceanic suture: the Mamonia Complex Suture Zone, SW Cyprus. *Journal of the Geological Society, London*, *157*, 1107-1126.

Baltsavias, E.P. (1999a). Airborne laser scanning: basic relations and formulas. *ISPRS Journal of Photogrammetry and Remote Sensing*, *54*, 199-214.

Baltsavias, E.P. (1999b). A comparison between photogrammetry and laser scanning. *ISPRS Journal of Photogrammetry & Remote Sensing, 54,* 83-94.

Barnes, J.W., & Lisle, R. J. (2004). *Basic Geological Mapping, Fourth edition.* Chichester: John Wiley & Sons.

Bater, C.W., & Coops, N.C. (2009). Evaluating error associated with lidar-derived DEM interpolation. *Computers & Geosciences, 35*, 289-300.

Baugh, W.M., & Groeneveld, D.P. (2008). Empirical proof of the empirical line. *International Journal of Remote Sensing, 29*, 665-672.

Bear, L.M. (1960). *The geology and mineral resources of the Akaki-Lythrodondha area*: Cyprus Geological Survey Department Memoir 3.

Bedini, E. (2009). Mapping lithology of the Sarfartoq carbonatite complex, southern West Greenland, using HyMap imaging spectrometer data. *Remote Sensing of Environment, 113*, 1208-1219.

Belluco, E., Camuffo, M., Ferrari, S., Modenese, L., Silvestri, S., Marani, A., & Marani, M. (2006). Mapping salt-marsh vegetation by multispectral and hyperspectral remote sensing. *Remote Sensing of Environment, 105*, 54-67.

Belt, K., & Paxton, S.T. (2005). GIS as an aid to visualizing and mapping geology and rock properties in regions of subtle topography. *Geological Society of America Bulletin, 117*, 149-160.

Bierwirth, P.N. (1990). Mineral mapping and vegetation removal via data-calibrated pixel unmixing, using multispectral images. *International Journal of Remote Sensing, 11*, 1999-2017.

Bishop, J.L., Pieters, C. M., & Edwards, J. O. (1994). Infrared spectroscopic analyses on the nature of water in Montmorillonite. *Clays and Clay Minerals, 42*, 702-716.

Bishop, J.L., Lane, M.D., Dyar, M.D., & Brown, A.J. (2008). Reflectance and emission spectroscopy study of four groups of phyllosilicates: smectites, kaolinite-serpentines, chlorites and micas. *Clay Minerals, 43*, 35-54.

Boardman, J.W., & Kruse, F.A. (1994). Automated spectral analysis: a geological example using AVIRIS data, North Grapevine Mountains, Nevada. In, *Proceedings of the Tenth Thematic Conference on Geological Remote Sensing* (pp. I407-I418). San Antonio, TX: Environmental Research Institute of Michigan, Ann Arbor, MI.

Boardman, J. (1998). Leveraging the high dimensionality of AVIRIS data for improved sub-pixel target unmixing and rejection of false positives: mixure tuned matched filtering. In, *Summaries of the Seventh Annual JPL Airborne Geoscience Workshop*. Pasadena, California.

Boyle, J.F., & Robertson, A.H.F. (1984). Evolving metallogenesis at the Troodos spreading axis. *Geological Society, London, Special Publications, 13*, 169-181.

Brown, D.G., Lusch, D.P., & Duda, K.A. (1998). Supervised classification of types of glaciated landscapes using digital elevation data. *Geomorphology, 21*, 233-250.

Burns, R.G. (1970). Crystal field spectra and evidence of cation ordering in olivine minerals. *American Mineralogist, 55*, 1608-1632.

Burns, R.G., Huggins, F. E., & Abu-Eid, R. M. (1972). Polarized absorption spectra of single crystals of lunar pyroxenes and olivines. *Earth, Moon, and Planets, 4*, 93-102.

Carranza, E.J.M., & Hale, M. (2002). Mineral imaging with Landsat Thematic Mapper data for hydrothermal alteration mapping in heavily vegetated terrane. *International Journal of Remote Sensing, 23*, 4827-4852.

Cavalli, M., Tarolli, P., Marchi, L., & Fontana, G.D. (2008). The effectiveness of airborne LiDAR data in the recognition of channel-bed morphology. *Catena, 73*, 249-260.

Chabrillat, S., Pinet, P.C., Ceuleneer, G., Johnson, P.E., & Mustard, J.F. (2000). Ronda peridotite massif: methodology for its geological mapping and lithological discrimination from airborne hyperspectral data. *International Journal of Remote Sensing, 21*, 2363-2388.

Chen, C.M., Hepner, G.F., & Forster, R.R. (2003). Fusion of hyperspectral and radar data using the IHS transformation to enhance urban surface features. *ISPRS Journal of Photogrammetry and Remote Sensing, 58*, 19-30.

Chen, Q. (2007). Airborne lidar data processing and information extraction. *Photogrammetric Engineering and Remote Sensing, 73*, 109-112.

Chica-Olmo, M., & Abarca-Hernandez, F. (2000). Computing geostatistical image texture for remotely sensed data classification. *Computers & Geosciences*, *26*, 373-383.

Chini, M., Pacifici, F., Emery, W.J., Pierdicca, N., & Del Frate, F. (2008). Comparing statistical and neural network methods applied to very high resolution satellite images showing changes in man-made structures at rocky flats. *IEEE Transactions on Geoscience and Remote Sensing, 46*, 1812-1821.

Clark, I. (1979). *Practical Geostatistics*. London: Applied Science Publishers.

Clark, R.N. (1981). Water Frost and Ice - the near-Infrared Spectral Reflectance 0.65-2.5 µm. *Journal of Geophysical Research, 86*, 3087-3096.

Clark, R.N., Swayze, G.A., Gallagher, A., King, T.V.V., & Calvin, W.M. (1993). *The U. S. Geological Survey Digital Spectral Library:* Version 1: 0.2 to 3.0 microns, U.S. Geological Survey Open File Report, pp. 93-592.

Clark, R.N. (1999). Spectroscopy of rocks and minerals, and principles of spectroscopy. In A.N. Rencz (Ed.), *Manual of Remote Sensing, Volume 3, Remote Sensing for the Earth Sciences* (pp. 3-58). New York: John Wiley and Sons.

Clark, R.N., Swayze, G.A., Livo, K.E., Kokaly, R.F., Sutley, S.J., Dalton, J.B., McDougal, R.R., & Gent, C.A. (2003). Imaging spectroscopy: Earth and planetary remote sensing with the USGS Tetracorder and expert systems. *Journal of Geophysical Research, 108*, 5.1-5.44.

Clark, R.N., King, T.V.V., Klejwa, M., Swayze, G.A., & Vergo, N. (1990). High Spectral Resolution Reflectance Spectroscopy of Minerals. *Journal of Geophysical Research-Solid Earth and Planets, 95*, 12653-12680.

Clark, R.N., & Roush, T.L. (1984). Reflectance Spectroscopy - Quantitative-Analysis Techniques for Remote-Sensing Applications. *Journal of Geophysical Research, 89,* 6329-6340.

Cloutis, E.A., Asher, P. M., & Mertzman, S. A. (2002). Spectral reflectance properties of zeolites and remote sensing implications. *Journal of Geophysical Research, 107*, 5.1-5.19.

Congalton, R.G. (1991). A review of assessing the accuracy of classifications of remotely sensed data. *Remote Sensing of Environment, 37*, 35-46.

Congalton, R.G., & Green, K. (1999). *Assessing the accuracy of remotely sensed data: principles and practices*. Boca Raton, FL: CRC Press, Inc.

Constantinou, G. (1972). The geology and genesis of the sulphide ores of Cyprus. PhD thesis, Royal School of Mines, Imperial College, London.

Constantinou, G. (1980). Metallogenesis associated with Troodos ophiolite. In A. Panayiotou (Ed.), *Ophiolites: Proceedings of the International Ophiolite Symposium, Cyprus* (pp. 663-674). Nicosia, Cyprus: Geological Survey Department.

Constantinou, G., & Govett, G.J.S. (1973). Geology, geochemistry and genesis of Cyprus sulfide deposits. *Economic Geology, 68,* 843-858.

Copley, V.R., & Moore, J.M. (1993). Debris provenance mapping in braided drainage using remote sensing. *Geological Society, London, Special Publications, 75,* 405-412.

Corgne, S., Magagi, R., Yergeau, M., & Sylla, D. (2010). An integrated approach to hydro-geological lineament mapping of a semi-arid region of West Africa using Radarsat-1 and GIS. *Remote Sensing of Environment, 114*, 1863-1875.

Crouvi, O., Ben-Dor, E., Beyth, M., Avigad, D., & Amit, R. (2006). Quantitative mapping of arid alluvial fan surfaces using field spectrometer and hyperspectral remote sensing. *Remote Sensing of Environment, 104*, 103-117.

Crowley, J.K., Williams, D.E., Hammarstrom, J.M., Piatak, N., Chou, I-M., & Mars, J.C. (2003). Spectral reflectance properties (0.4–2.5 μm) of secondary Fe-oxide, Fe-hydroxide, and Fe-sulphate-hydrate minerals associated with sulphide-bearing mine wastes. *Geochemistry: Exploration, Environment, Analysis, 3*, 219-228.

Cunningham, D., Grebby, S., Tansey, K., Gosar, A., & Kastelic, V. (2006). Application of airborne LiDAR to mapping seismogenic faults in forested mountainous terrain, southeastern Alps, Slovenia. *Geophysical Research Letters, 33*, L20308.

De Leeuw, J., Jia, H., Yang, L., Liu, X., Schmidt, K., & Skidmore, A.K. (2006). Comparing accuracy assessments to infer superiority of image classification methods. *International Journal of Remote Sensing, 27*, 223-232.

Dong, P., & Leblon, B. (2004). Rock unit discrimination on Landsat TM, SIR-C and Radarsat images using spectral and textural information. *International Journal of Remote Sensing, 25*, 3745-3768.

Drăguț, L., Tiede, D., & Levick, S.R. (2010). ESP: a tool to estimate scale parameter for multiresolution image segmentation of remotely sensed data. *International Journal of Geographical Information Science, 24*, 859-871.

Drury, S.A. (1987). *Image Interpretation in Geology* (pp. 64-88). London: Allen & Unwin.

Drury, S.A. (2001). *Image Interpretation in Geology*, *Third edition*. Cheltenham: Nelson Thornes Ltd.

Ehsani, A.H., & Quiel, F. (2008a). Geomorphometric feature analysis using morphometric parameterization and artificial neural networks. *Geomorphology, 99*, 1-12.

Ehsani, A.H., & Quiel, F. (2008b). Application of self organizing map and SRTM data to characterize yardangs in the Lut desert, Iran. *Remote Sensing of Environment, 112*, 3284-3294.

Ferrier, G. (1995). Evaluation of Apparent Surface Reflectance Estimation Methodologies. *International Journal of Remote Sensing*, *16*, 2291-2297.

Ferrier, G., & Wadge, G. (1996). The application of imaging spectrometry data to mapping alteration zones associated with gold mineralization in southern Spain. *International Journal of Remote Sensing*, *17*, 331-350.

Fitton, N.C., & Cox, S.J.D. (1998). Optimising the application of the Hough transform for automatic feature extraction from geoscientific images. *Computers & Geosciences, 24*, 933-951.

Fitzpatrick-Lins, K. (1981). Comparison of sampling procedures and data analysis for a land-use and land-cover map. *Photogrammetric Engineering and Remote Sensing*, *47*, 343-351.

Flood, M., & Gutelius, B. (1997). Commercial implications of topographic terrain mapping using scanning airborne laser radar. *Photogrammetric Engineering and Remote Sensing*, *63*, 327.

Foody, G.M. (2004). Thematic map comparison: evaluating the statistical significance of differences in classification accuracy. *Photogrammetric Engineering and Remote Sensing*, *70*, 627-633.

Foody, G.M. (2009). Sample size determination for image classification accuracy assessment and comparison. *International Journal of Remote Sensing*, *30*, 5273-5291.

Franke, R., & Nielson, G. (1980). Smooth interpolation of large sets of scattered data. *International Journal for Numerical Methods in Engineering*, *15*, 1691-1704.

Franke, R. (1982). Scattered Data Interpolation - Tests of Some Methods. *Mathematics of Computation*, *38*, 181-200.

Frankel, K.L., & Dolan, J.F. (2007). Characterizing arid region alluvial fan surface roughness with airborne laser swath mapping digital topographic data. *Journal of Geophysical Research-Earth Surface, 112.*

Fraser, S.J., & Green, A.A. (1987). A software defoliant for geological analysis of band ratios. *International Journal of Remote Sensing*, *8*, 525-532.

Gad, S., & Kusky, T. (2007). ASTER spectral ratioing for lithological mapping in the arabian-nubian shield, the neoproterozoic Wadi Kid area, Sinai, Egypt. *Gondwana Research*, *11*, 326-335.

Gass, I.G. (1960). *The geology and mineral resources of the Dhali area*: Cyprus Geological Survey Department Memoir 4.

Gass, I.G., & Masson-Smith, D. (1963). The geology and gravity anomalies of the Troodos Massif, Cyprus. *Philosophical Transactions of the Royal Society of London A, 255*, 417-467.

Gass, I.G. (1968). Is the Troodos massif of Cyprus a fragment of Mesozoic ocean crust? *Nature, 220*, 39-42.

Glenn, N.F., Streutker, D.R., Chadwick, D.J., Thackray, G.D., & Dorsch, S.J. (2006). Analysis of LiDAR-derived topographic information for characterizing and differentiating landslide morphology and activity. *Geomorphology, 73*, 131-148.

Goetz, A.F.H., Hauff, P., Shippert, M., & Maecher, A. G. (1991). Field identification of OH-bearing minerals in the 0.9-1.0 micron region. In, *IEEE IGARSS Proceedings of the 11th Annual International Geoscience and Remote Sensing Symposium* (pp. 2065-2068). Espoo, Finland.

Goryniuk, M.C., Rivard, B. A., & Jones, B. (2004). The reflectance spectra of opal-A (0.5–25 μm) from the Taupo Volcanic Zone: Spectra that may identify hydrothermal systems on planetary surfaces. *Geophysical Research Letters, 31*, L24701.

Govett, G.J.S., & Pantazis, T.M. (1971). Distribution of Cu, Zn, Ni and Co in the Troodos Pillow Lava Series, Cyprus. *Transactions of the Institution of Mining and Metallurgy, Section B: Applied Earth Science, 80*, 27-46.

Grebby, S., Cunningham, D., Naden, J., & Tansey, K. (2010). Lithological mapping of the Troodos ophiolite, Cyprus, using airborne LiDAR topographic data. *Remote Sensing of Environment, 114*, 713-724.

Grebby, S., Naden, J., Cunningham, D., & Tansey, K. (2011). Integrating airborne multispectral imagery and airborne LiDAR data for enhanced lithological mapping in vegetated terrain. *Remote Sensing of Environment*, *115*, 214-226.

Green, A.A., Berman, M., Switzer, P., & Craig, M.D. (1988). A transformation for ordering multispectral data in terms of image quality with implications for noise removal. *IEEE Transactions on Geoscience and Remote Sensing, 26*, 65-74.

Grunsky, E., Harris, J., & McMartin, I. (2009). Predictive mapping of surficial materials, Schultz Lake Area (NTS 66A), Nunavut, Canada. *Reviews in Economic Geology, 16*, 177-198.

Guibas, L., & Stolfi, J. (1985). Primitives for the Manipulation of General Subdivisions and the Computation of Voronoi Diagrams. *Acm Transactions on Graphics, 4*, 74-123.

Harding, D.J., & Berghoff, G.S. (2000). Fault scarp detection beneath dense vegetation cover: airborne lidar mapping of the Seattle fault zone, Bainbridge Island, Washington State. In, *Proceedings of the American Society of Photogrammetry and Remote Sensing Annual Conference*. Washington, D.C.

Harris, A., Bryant, R.G., & Baird, A.J. (2006). Mapping the effects of water stress on Sphagnum: Preliminary observations using airborne remote sensing. *Remote Sensing of Environment, 100*, 363-378.

Harris, J.R., Wilkinson, L., Heather, K., Fumerton, S., Bernier, M. A., Ayer, J., & Dahn, R. (2001). Application of GIS processing techniques for producing mineral prospectivity maps — a case study: Mesothermal Au in the Swayze Greenstone Belt, Ontario, Canada. *Natural Resources Research, 10*, 91-124.

Harris, J.R., Rogge, D., Hitchcock, R., Ijewliw, O., & Wright, D. (2005). Mapping lithology in Canada's Arctic: application of hyperspectral data using the minimum noise fraction transformation and matched filtering. *Canadian Journal of Earth Sciences, 42*, 2173-2193.

Harsanyi, J.C., & Chang, C.I. (1994). Hyperspectral Image Classification and Dimensionality Reduction - an Orthogonal Subspace Projection Approach. *IEEE Transactions on Geoscience and Remote Sensing*, *32*, 779-785.

Haselwimmer, C.E., Riley, T.R., & Liu, J.G. (2010). Assessing the potential of multispectral remote sensing for lithological mapping on the Antarctic Peninsula: case study from eastern Adelaide Island, Graham Land. *Antarctic Science*, *22*, 299-318.

Haugerud, R.A., & Harding, D.J. (2001). Some algorithms for virtual deforestation (VDF) of lidar topographic survey data. *International Archives of Photogrammetry and Remote Sensing, 34(3/W4)*, 211-217.

Haugerud, R.A., Harding, D.J., Johnson, S.Y., Harless, J.L., Weaver, C.S., & Sherrod, B.L. (2003). High-resolution Lidar topography of the Puget Lowland, Washington — A bonanza for earth science. *GSA Today, 13,* 4-10.

Hill, R.A., Wilson, A.K., George, M., & Hinsley, S.A. (2010). Mapping tree species in temperate deciduous woodland using time-series multi-spectral data. *Applied Vegetation Science*, *13,* 86-99.

Hsiao, K., Lui, J., Yu, M., & Tseng, Y. (2004). Change detection of landslide terrains using ground based lidar data. In, *Proceedings of the 20th ISPRS Congress*. Istanbul, Turkey: Commission V, WG VII/5.

Huete, A.R. (1988). A soil-adjusted vegetation index (SAVI). *Remote Sensing of Environment, 25*, 295-309.

Hui, L., Di, L., Xianfeng, H., & Deren, L. (2008). Laser intensity used in classification of Lidar point cloud data. In, *IEEE proceedings of IGARSS '08, Geoscience and Remote Sensing Symposium, 2008* (pp. 1140-1143). Boston, MA.

Huising, E.J., & Pereira, L.M.G. (1998). Errors and accuracy estimates of laser data acquired by various laser scanning systems for topographic applications. *ISPRS Journal of Photogrammetry and Remote Sensing*, *53*, 245-261.

Hunt, G.R., & Salisbury, J. W. (1970). Visible and near infrared spectra of minerals and rocks, I: Silicate minerals. *Modern Geology, 1*, 283-300.

Hunt, G.R. (1977). Spectral signatures of particulate minerals in visible and near infrared. *Geophysics, 42*, 501-513.

Hunt, G.R., & Ashley, R.P. (1979). Spectra of altered rocks in the visible and near-Infrared. *Economic Geology*, *74*, 1613-1629.

Hutchinson, C.F. (1982). Techniques for combining Landsat and ancillary data for digital classification improvement. *Photogrammetric Engineering and Remote Sensing, 48*, 123-130.

Jensen, J.R. (2005). *Introductory digital image processing: a remote sensing perspective*. New Jersey: Prentice Hall.

Ji, C.Y. (2000). Land-use classification of remotely sensed data using Kohonen Self-Organizing Feature Map neural networks. *Photogrammetric Engineering and Remote Sensing, 66,* 1451-1460.

Jianwen, M., & Bagan, H. (2005). Land-use classification using ASTER data and self-organized neutral networks. *International Journal of Applied Earth Observation and Geoinformation, 7,* 183-188.

Jordan, G., & Schott, B. (2005). Application of wavelet analysis to the study of spatial pattern of morphotectonic lineaments in digital terrain models. A case study. *Remote Sensing of Environment, 94,* 31-38.

Kähler, G., & Stow, D.A.V. (1998). Turbidites and contourites of the Palaeogene Lefkara Formation, southern Cyprus. *Sedimentary Geology, 115,* 215-231.

Karnieli, A., Meisels, A., Fisher, L., & Arkin, Y. (1996). Automatic extraction and evaluation of geological linear features from digital remote sensing data using a Hough transform. *Photogrammetric Engineering and Remote Sensing, 62*, 525-531.

Kavzoglu, T., & Mather, P.M. (2002). The role of feature selection in artifial neural network applications. *International Journal of Remote Sensing, 23,* 2919-2937.

Kennelly, P.J. (2008). Terrain maps displaying hill-shading with curvature. *Geomorphology, 102*, 567-577.

King, T.V.V., & Clark, R. N. (1989). Spectral characteristics of chlorites and Mg-serpentines using high-resolution reflectance spectroscopy. *Journal of Geophysical Research, 94*, 13,997-14,008.

King, T.V.V., & Ridley, W.I. (1987). Relation of the spectroscopic reflectance of olivine to mineral chemistry and some remote sensing implications. *Journal of Geophysical Research, 92*, 11,457-11,469.

Kohonen, T. (1982). Self-organized formation of topologically correct feature maps. *Biological Cybernetics, 43*, 59-69.

Kohonen, T. (1990). The self-organizing map. *Proceedings of the IEEE, 78*, 1464-1480.

Kohonen, T. (2001). *Self-Organizing Maps, Third edition*. Berlin: Springer.

Koike, K., Nagano, S., & Kawaba, K. (1998). Construction and analysis of interpreted fracture planes through combination of satellite-image derived lineaments and digital elevation model data. *Computers & Geosciences, 24*, 573-583.

Koike, K., Nagano, S., & Ohmi, M. (1995). Lineament analysis of satellite images using a Segment Tracing Algorithm (STA). *Computers & Geosciences*, *21*, 1091-1104.

Koroneos, C., Fokaidis, P., & Moussiopoulos, N. (2005). Cyprus energy system and the use of renewable energy sources. *Energy, 30*, 1889-1901.

Kraus, K., & Pfeifer, N. (1998). Determination of terrain models in wooded areas with airborne laser scanner data. *ISPRS Journal of Photogrammetry and Remote Sensing, 53*, 193-203.

Kresic, N. (1995). Remote sensing of tectonic fabric controlling groundwater flow in Dinaric Karst. *Remote Sensing of Environment, 53*, 85-90.

Kressler, F.P., Bauer, T. B., & Steinnocher, K. T. (2001). Object-oriented per-parcel land use classification of very high resolution images. In, *Proceedings of IEEE/ISPRS Joint Workshop on Remote Sensing and Data Fusion over Urban Areas* (pp. 164-167).

Kruse, F.A., Lefkoff, A.B., Boardman, J.W., Heidebrecht, K.B., Shapiro, A.T., Barloon, P.J., & Goetz, A.F.H. (1993). The Spectral Image-Processing System (Sips) - Interactive Visualization and Analysis of Imaging Spectrometer Data. *Remote Sensing of Environment, 44*, 145-163.

Kühni, A., & Pfiffner, O.A. (2001). The relief of the Swiss Alps and adjacent areas and its relation to lithology and structure: topographic analysis from a 250-m DEM. *Geomorphology, 41*, 285-307.

Landis, J.R., & Koch, G.G. (1977). The measurement of observer agreement for categorical data. *Biometrics, 33*, 159-174.

Lapierre, H. (1968). Nouvelle observations sur la série sédimentaire Mamonia (Chypre). *Comptes Rendus de l'Académie des Sciences, Paris, 268*, 32-35.

Lapierre, H., Bosch, D., Narros, A., Mascle, G.H., Tardy, M., & Demant, A. (2007). The Mamonia Complex (SW Cyprus) revisited: remnant of Late Triassic intra-oceanic volcanism along the Tethyan southwestern passive margin. *Geological Magazine, 144*, 1-19.

Latypov, D. (2005). Effects of laser beam alignment tolerance on lidar accuracy. *ISPRS Journal of Photogrammetry and Remote Sensing, 59*, 361-368.

Leckie, D.G. (1987). Factors affecting defoliation assessment using airborne multispectral scanner data. *Photogrammetric Engineering and Remote Sensing, 53*, 1665-1674.

Lee, D.T., & Schachter, B. J. (1980). Two algorithms for constructing a Delaunay Triangulation. *Journal of Computer and Information Sciences*, *9*, 219-242.

Leprieur, C., Verstraete, M. M., & Pinty, B. (1994). Evaluation of the performance of various vegetation indices to retrieve vegetation cover from AVHRR data. *Remote Sensing Reviews, 10*, 265-284.

Leverington, D.W. (2010). Discrimination of sedimentary lithologies using Hyperion and Landsat Thematic Mapper data: a case study at Melville Island, Canadian High Arctic. *International Journal of Remote Sensing*, *31*, 233-260.

Li, L.F., Wang, J.F., & Leung, H. (2009). A knowledge-based similarity classifier to stratify sample units to improve the estimation precision. *International Journal of Remote Sensing*, *30*, 1207-1234.

Li, P., Li, Z., & Moon, W. (2001). Lithological discrimination of Altun area in northwest China using Landsat TM data and geostatistical textural information. *Geosciences Journal, 5*, 293-300.

Li, P.J., & Moon, W.M. (2004). Land cover classification using MODIS-ASTER airborne simulator (MASTER) data and NDVI: a case study of the Kochang area, Korea. *Canadian Journal of Remote Sensing, 30*, 123-136.

Li, Z., & Eastman, J.R. (2006). The nature and classification of unlabelled neurons in the use of Kohonen's self-organizing map for supervised classification. *Transactions in GIS*, *10*, 599-613.

Li, Z., & Eastman, J.R. (in press). Commitment and typicality measures for the Self-Organizing Map. *International Journal of Remote Sensing*.

Liberti, M., Simoniello, T., Carone, M.T., Coppola, R., D'Emilio, M., & Macchiato, M. (2009). Mapping badland areas using LANDSAT TM/ETM satellite imagery and morphological data. *Geomorphology, 106*, 333-343.

Lohani, B., & Mason, D.C. (2005). A case study on error identification and minimisation in airborne altimetric LiDAR data. *International Journal of Geoinformatics*, *1*, 53-61.

Loughlin, W.P. (1991). Principal Component Analysis for alteration mapping. *Photogrammetric Engineering and Remote Sensing, 57*, 1163-1169.

Mallet, C., & Bretar, F. (2009). Full-waveform topographic lidar: State-of-the-art. *ISPRS Journal of Photogrammetry and Remote Sensing, 64*, 1-16.

Marsh, S.E., & Mckeon, J.B. (1983). Integrated Analysis of High-Resolution Field and Airborne Spectroradiometer Data for Alteration Mapping. *Economic Geology, 78*, 618-632.

Masoud, A., & Koike, K. (2006). Tectonic architecture through Landsat-7 ETM+/SRTM DEM-derived lineaments and relationship to the hydrogeologic setting in Siwa region, NW Egypt. *Journal of African Earth Sciences*, *45*, 467-477.

Mather, P.M., Tso, B., & Koch, M. (1998). An evaluation of Landsat TM spectral data and SAR-derived textural information for lithological discrimination in the Red Sea Hills, Sudan. *International Journal of Remote Sensing, 19*, 587-604.

Mazzarini, F., Pareschi, M.T., Favalli, M., Isola, I., Tarquini, S., & Boschi, E. (2007). Lava flow identification and aging by means of lidar intensity: Mount Etna case. *Journal of Geophysical Research-Solid Earth*, *112*, B02201.

McKean, J., & Roering, J. (2004). Objective landslide detection and surface morphology mapping using high-resolution airborne laser altimetry. *Geomorphology, 57*, 331-351.

Mitchell, J.J., & Glenn, N. F. (2009). Subpixel abundance estimates in mixture-tuned matched filtering classifications of leafy spurge (*Euphorbia esula* L.). *International Journal of Remote Sensing, 30*, 6099-6119.

Moore, G.K., & Waltz, F.A. (1983). Objective Procedures for Lineament Enhancement and Extraction. *Photogrammetric Engineering and Remote Sensing, 49*, 641-647.

Moores, E.M., & Vine, F.J. (1971). Troodos Massif, Cyprus and other ophiolites as oceanic crust: evaluation and implications. *Philosophical Transactions of the Royal Society of London A, 268*, 443-467.

Morris, R.V., Lauer, H.V., Lawson, C.A., Gibson, E.K., Nace, G.A., & Stewart, C. (1985). Spectral and other physicochemical properties of submicron powders of hematite (Alpha-Fe2o3), maghemite (Gamma-Fe2o3), magnetite (Fe3o4), goethite (Alpha-Feooh), and lepidocrocite (Gamma-Feooh). *Journal of Geophysical Research-Solid Earth and Planets, 90*, 3126-3144.

Morris, R.V., Neely, S.C., & Mendell, W.W. (1982). Application of Kubelka-Munk Theory of Diffuse Reflectance to Geologic Problems - the Role of Scattering. *Geophysical Research Letters, 9*, 113-116.

Mountrakis, D., Pavlides, S., Zouros, N., Astaras, T., & Chatzipetros, A. (1998). Seismic fault geometry and kinematics of the 13 May 1995 Western Macedonia (Greece) earthquake. *Journal of Geodynamics, 26*, 175-196.

Mundt, J., Streutker, D., & Glenn, N. (2007). Partial unmixing of hyperspectral imagery: theory and methods. In, *Proceedings of the American Society for Photogrammetry and Remote Sensing*. Tampa, Florida: Curran Associates, Inc.

Murphy, R.J., & Wadge, G. (1994). The effects of vegetation on the ability to map soils using imaging spectrometer data. *International Journal of Remote Sensing, 15*, 63-86.

Mutlu, M., Popescu, S.C., Stripling, C., & Spencer, T. (2008). Mapping surface fuel models using lidar and multispectral data fusion for fire behavior. *Remote Sensing of Environment, 112*, 274-285.

O'leary, D.W., Friedman, J.D., & Pohn, H.A. (1976). Lineament, linear, lineation - some proposed new standards for old terms. *Geological Society of America Bulletin, 87*, 1463-1469.

Pacifici, F., Chini, M., & Emery, W.J. (2009). A neural network approach using multi-scale textural metrics from very high-resolution panchromatic imagery for urban land-use classification. *Remote Sensing of Environment*, *113*, 1276-1292.

Palamara, D.R., Nicholson, M., Flentje, P., Baafi, E., & Brassington, G.M. (2007). An evaluation of airborne laser scan data for coalmine subsidence mapping. *International Journal of Remote Sensing*, *28*, 3181-3203.

Paradella, W.R., Bignelli, P.A., Veneziani, P., Pietsch, R.W., & Toutin, T. (1997). Airborne and spaceborne Synthetic Aperture Radar (SAR) integration with Landsat TM and gamma ray spectrometry for geological mapping in a tropical rainforest environment, the Carajas Mineral Province, Brazil. *International Journal of Remote Sensing*, *18*, 1483-1501.

Parsons, A.J., & Yearley, R. J. (1986). An analysis of geologic lineaments seen on LANDSAT MSS imagery. *International Journal of Remote Sensing, 7*, 1773-1782.

Pashiardis, S., & Michaelides, S. (2008). Implementation of the Standard Precipitation Index (SPI) and the Reconnaissance Drought Index (RDI) for regional drought assessment: a case study for Cyprus. *European Water*, 57-65.

Pavlis, T.L., & Bruhn, R.L. (2011). Application of LIDAR to resolving bedrock structure in areas of poor exposure: An example from the STEEP study area, southern Alaska. *Geological Society of America Bulletin, 123*, 206-217.

Peña, S.A., & Abdelsalam, M.G. (2006). Orbital remote sensing for geological mapping in southern Tunisia: Implication for oil and gas exploration. *Journal of African Earth Sciences, 44*, 203-219.

Philip, G., Ravindran, K.V., & Mathew, J. (2003). Mapping the Nidar Ophiolite Complex of the Indus Suture Zone, Northwestern-Trans Himalaya using IRS-1C/1D data. *International Journal of Remote Sensing, 24*, 4979-4994.

Pignatti, S., Cavalli, R.M., Cuomo, V., Fusilli, L., Pascucci, S., Poscolieri, M., & Santini, F. (2009). Evaluating Hyperion capability for land cover mapping in a fragmented ecosystem: Pollino National Park, Italy. *Remote Sensing of Environment, 113*, 622-634.

Pike, R.J., & Wilson, S.E. (1971). Elevation-Relief Ratio, Hypsometric Integral, and Geomorphic Area-Altitude Analysis. *Geological Society of America Bulletin, 82*, 1079-1084.

Poole, A.J., & Robertson, A.H.F. (1991). Quaternary uplift and sea-level change at an active plate boundary, Cyprus. *Journal of the Geological Society, London, 148*, 909-921.

Prentice, C.S., Crosby, C.J., Harding, D.J., Haugerud, R.A., Merritts, D.J., Gardner, T.W., Koehler, R.D., & Baldwin, J.N. (2003). Northern California LIDAR data: A tool for mapping the San Andreas Fault and pleistocene marine terraces in heavily vegetated terrain. In, *American Geophysical Union Fall Meeting*. Abstract G12A-06.

Price, J.C., Anger, C. D., & Mah, S. (1995). Preliminary evaluation of casi preprocessing techniques. In, *Proceedings of the 17th Canadian Symposium on Remote Sensing* (pp. 649-697). Saskatoon, Canada: Canadian Remote Sensing Society & Canadian Aeronautics and Space Institute).

Priddy, K.L., & Keller, P.E. (2005). *Artificial neural networks: an introduction*. Bellingham, WA: SPIE Press.

Prima, O.D.A., Echigo, A., Yokoyama, R., & Yoshida, T. (2006). Supervised landform classification of Northeast Honshu from DEM-derived thematic maps. *Geomorphology, 78*, 373-386.

Qari, M.Y.H.T. (1991). Application of Landsat TM data to geological studies, Al-Khabt Area, Southern Arabian Shield. *Photogrammetric Engineering and Remote Sensing, 57*, 421-429.

Ricchetti, E. (2000). Multispectral satellite image and ancillary data integration for geological classification. *Photogrammetric Engineering and Remote Sensing, 66*, 429-435.

Ricchetti, E., & Palombella, M. (2005). Application of Landsat 7 ETM+ imagery for geological lineament analysis of Southern Italy. In, *IEEE Proceedings of IGARSS '05, Geoscience and Remote Sensing Symposium 2005* (pp. 5200-5203).

Richards, J.A. (1994). *Remote sensing digital image analysis: an introduction*. Berlin: Springer-Verlag.

Roberts, D.A., Yamaguchi, Y., & Lyon, R. J. P. (1985). Calibration of airborne imaging spectrometer data to percent reflectance using field spectal measurements. In, *Proceedings of 19th International Symposium on Remote Sensing of Environment* (pp. 679-688). Ann Arbor, Michigan.

Robertson, A.H.F., & Woodcock, N. H. (1979). Mamonia Complex, southwest Cyprus: Evolution and emplacement of a Mesozoic continental margin. *Geological Society of America Bulletin, 90*, 651-665.

Robertson, A.H.F., & Xenophontos, C. (1997). Cyprus. In E.M. Moores, & Fairbridge, R. W. (Ed.), *Encyclopedia of European and Asian regional geology* (pp. 160-171). London: Chapman & Hall.

Rogge, D.M., Rivard, B., Harris, J., & Zhang, J. (2009). Application of hyperspectral data for remote predictive mapping, Baffin Island, Canada. *Reviews in Economic Geology*, *16*, 209-222.

Rondeaux, G., Steven, M., & Baret, F. (1996). Optimization of soil-adjusted vegetation indices. *Remote Sensing of Environment*, *55*, 95-107.

Rosenfield, G.H., & Fitzpatricklins, K. (1986). A Coefficient of Agreement as a Measure of Thematic Classification Accuracy. *Photogrammetric Engineering and Remote Sensing*, *52*, 223-227.

Rothery, D.A. (1987). Improved discrimination of rock units using Landsat Thematic Mapper imagery of the Oman ophiolite. *Journal of the Geological Society*, *144*, 587-597.

Rowan, L.C., & Mars, J.C. (2003). Lithologic mapping in the Mountain Pass, California area using Advanced Spaceborne Thermal Emission and Reflection Radiometer (ASTER) data. *Remote Sensing of Environment*, *84*, 350-366.

Rowan, L.C., Simpson, C.J., & Mars, J.C. (2004). Hyperspectral analysis of the ultramafic complex and adjacent lithologies at Mordor, NT, Australia. *Remote Sensing of Environment*, *91*, 419-431.

Roy, R., Launeau, P., Carrere, V., Pinet, P., Ceuleneer, G., Clenet, H., Daydou, Y., Girardeau, J., & Amri, I. (2009). Geological mapping strategy using visible near-infrared-shortwave infrared hyperspectral remote sensing: Application to the

Oman ophiolite (Sumail Massif). *Geochemistry Geophysics Geosystems, 10*, Q02004.

Saha, A.K., Gupta, R. P., & Arora, M. K. (2002). GIS-based landslide hazard zonation in the Bhagirathi (Ganga) Valley, Himalayas. *International Journal of Remote Sensing*, *23*, 357-369.

Schetselaar, E.M., Chung, C.J.F., & Kim, K.E. (2000). Integration of Landsat TM, gamma-ray, magnetic, and field data to discriminate lithological units in vegetated granite-gneiss terrain. *Remote Sensing of Environment, 71*, 89-105.

Schiefer, S., Hostert, P., & Damm, A. (2006). Correcting brightness gradients in hyperspectral data from urban areas. *Remote Sensing of Environment*, *101*, 25-37.

Searle, D.L. (1972). Mode of occurrence of the cupriferous pyrite deposits of Cyprus. *Transactions of the Institution of Mining and Metallurgy, Section B: Applied Earth Science*, *81*, B189-B197.

Siegal, B.S., & Goetz, A.F.H. (1977). Effect of vegetation on rock and soil type discrimination. *Photogrammetric Engineering and Remote Sensing, 43*, 191-196.

Singer, R.B.M., T. B. (1979). Mars: Large scale mixing of bright and dark surface materials and implications for analysis of spectral reflectance. In, *Proceedings of the 10th Lunar and Planetary Science Conference* (pp. 1835-1848). Houston, Texas: New York, Pergamon Press, Inc.

Singer, R.B. (1981). Near-Infrared Spectral Reflectance of Mineral Mixtures - Systematic Combinations of Pyroxenes, Olivine, and Iron-Oxides. *Journal of Geophysical Research, 86*, 7967-7982.

Sithole, G. (2001). Filtering of laser altimetry data using a slope adaptive filter. *International Archives of Photogrammetry and Remote Sensing, XXXIV*, 203-210.

Smewing, J.D., Simonian, K.O., & Gass, I.G. (1975). Metabasalts from Troodos Massif, Cyprus - Genetic Implication Deduced from Petrography and Trace-Element Geochemistry. *Contributions to Mineralogy and Petrology, 51*, 49-64.

Smith, G.M., & Milton, E.J. (1999). The use of the empirical line method to calibrate remotely sensed data to reflectance. *International Journal of Remote Sensing, 20*, 2653-2662.

Smith, S.L., Holland, D.A., & Longley, P.A. (2005). Quantifying Interpolation Errors in Urban Airborne Laser Scanning Models. *Geographical Analysis, 37*, 200-224.

Song, J.-H., Han, S.-H., Yu, K., & Kim, Y.-I. (2002). Assessing the Possibility of Land-cover Classification Using Lidar Intensity Data. *International Archives of Photogrammetry and Remote Sensing, XXXIV*, 259–262.

South, S., Qi, J.G., & Lusch, D.P. (2004). Optimal classification methods for mapping agricultural tillage practices. *Remote Sensing of Environment, 91*, 90-97.

Staley, D.M., Wasklewicz, T.A., & Blaszczynski, J.S. (2006). Surficial patterns of debris flow deposition on alluvial fans in Death Valley, CA using airborne laser swath mapping data. *Geomorphology, 74*, 152-163.

Strahler, A.N. (1952). Hypsometric (area-altitude) analysis of erosional topography. *Geological Society of America Bulletin, 63*, 1117-1142.

Strahler, A.H., Logan, T.L., & Bryant, N.A. (1978). Improving forest cover classification accuracy from Landsat by incorporating topographic information. In, *Proceedings of the Twelfth International Symposium on Remote Sensing of Environment* (pp. 927-942): Environmental Research Institute of Michigan, Ann Arbor, MI.

Sultan, M., Arvidson, R.E., Sturchio, N.C., & Guinness, E.A. (1987). Lithologic mapping in arid regions with Landsat thematic mapper data: Meatiq Dome, Egypt. *Geological Society of America Bulletin, 99*, 748-762.

Süzen, M.L., & Toprak, V. (1998). Filtering of satellite images in geological lineament analyses: an application to a fault zone in Central Turkey. *International Journal of Remote Sensing, 19*, 1101-1114.

Swarbrick, R.E., & Robertson, A. H. F. (1980). Revised stratigraphy of the Mesozoic rocks of southern Cyprus. *Geological Magazine, 117*, 547-563.

Tortora, R.D. (1978). A note on sample size estimation for multinomial populations. *American Statistician, 32*, 100-102.

Tripathi, N.K., Gokhale, K.V.G.K., & Siddiqui, M.U. (2000). Directional morphological image transforms for lineament extraction from remotely sensed images. *International Journal of Remote Sensing, 21*, 3281-3292.

van der Meer, F. (1996). Spectral mixture modelling and spectral stratigraphy in carbonate lithofacies mapping. *ISPRS Journal of Photogrammetry and Remote Sensing, 51*, 150-162.

van der Meer, F., & Bakker, W. (1997). Cross correlogram spectral matching: application to surface mineralogical mapping by using AVIRIS data from Cuprite, Nevada. *Remote Sensing of Environment, 61*, 371-382.

van der Meer, F., Vazquez-Torres, M., & Van Dijk, P.M. (1997). Spectral characterization of ophiolite lithologies in the Troodos Ophiolite complex of Cyprus and its potential in prospecting for massive sulphide deposits. *International Journal of Remote Sensing, 18*, 1245-1257.

Varga, R.J., & Moores, E.M. (1985). Spreading structure of the Troodos ophiolite, Cyprus. *Geology, 13*, 846-850.

Verikas, A., & Bacauskiene, M. (2002). Feature selection with neural networks. *Pattern Recognition Letters, 23*, 1323-1335

Wallace, J.A. (2005). LiDAR altimetry and hyperspectral imaging: new technologies for geological and mineralogical mapping. PhD thesis, University of Waterloo, Ontario.

Wallace, J., Morris, B., & Howarth, P. (2006). Identifying structural trend with fractal dimension and topography. *Geology, 34*, 901-904.

Webster, T.L., & Dias, G. (2006). An automated GIS procedure for comparing GPS and proximal LIDAR elevations. *Computers & Geosciences, 32*, 713-726.

Webster, T.L., Murphy, J.B., & Gosse, J.C. (2006a). Mapping subtle structures with light detection and ranging (LIDAR): flow units and phreatomagmatic rootless cones in the North Mountain Basalt, Nova Scotia. *Canadian Journal of Earth Sciences, 43*, 157-176.

Webster, T.L., Murphy, J.B., Gosse, J.C., & Spooner, I. (2006b). The application of lidar-derived digital elevation model analysis to geological mapping: an example from the Fundy Basin, Nova Scotia, Canada. *Canadian Journal of Remote Sensing, 32*, 173-193.

Webster, T.L., Forbes, D.L., MacKinnon, E., & Roberts, D. (2006c). Flood-risk mapping for storm-surge events and sea-level rise using lidar for southeast New Brunswick. *Canadian Journal of Remote Sensing, 32*, 194-211.

Wehr, A., & Lohr, U. (1999). Airborne laser scanning - an introduction and overview. *ISPRS Journal of Photogrammetry and Remote Sensing, 54*, 68-82.

Wilson, R.A.M. (1959). *The geology of the Xeros-Troodos area*: Cyprus Geological Survey Department Memoir 1.

Wladis, D. (1999). Automatic lineament detection using digital elevation models with second derivative filters. *Photogrammetric Engineering and Remote Sensing, 65*, 453-458.

Wood, J.D. (1996). The geomorphological characterisation of digital elevation models. PhD thesis, University of Leicester, Leicester.

Zhang, K.Q., Chen, S.C., Whitman, D., Shyu, M.L., Yan, J.H., & Zhang, C.C. (2003). A progressive morphological filter for removing nonground measurements from airborne LIDAR data. *IEEE Transactions on Geoscience and Remote Sensing, 41*, 872-882.

Zhang, J.K., Rivard, B., & Sanchez-Azofeifa, A. (2005). Spectral unmixing of normalized reflectance data for the deconvolution of lichen and rock mixtures. *Remote Sensing of Environment, 95*, 57-66.